

## INFORMATION TO USERS

The most advanced technology has been used to photograph and reproduce this manuscript from the microfilm master. UMI films the text directly from the original or copy submitted. Thus, some thesis and dissertation copies are in typewriter face, while others may be from any type of computer printer.

The quality of this reproduction is dependent upon the quality of the copy submitted. Broken or indistinct print, colored or poor quality illustrations and photographs, print bleedthrough, substandard margins, and improper alignment can adversely affect reproduction.

In the unlikely event that the author did not send UMI a complete manuscript and there are missing pages, these will be noted. Also, if unauthorized copyright material had to be removed, a note will indicate the deletion.

Oversize materials (e.g., maps, drawings, charts) are reproduced by sectioning the original, beginning at the upper left-hand corner and continuing from left to right in equal sections with small overlaps. Each original is also photographed in one exposure and is included in reduced form at the back of the book. These are also available as one exposure on a standard 35mm slide or as a 17" x 23" black and white photographic print for an additional charge.

Photographs included in the original manuscript have been reproduced xerographically in this copy. Higher quality 6" x 9" black and white photographic prints are available for any photographs or illustrations appearing in this copy for an additional charge. Contact UMI directly to order.



University Microfilms International  
A Bell & Howell Information Company  
300 North Zeeb Road, Ann Arbor, MI 48106-1346 USA  
313/761-4700 800/521-0600



Order Number 9018973

**Volcanic evolution of the Koolau dike complex: Determined  
from intrusive magma flow, anisotropy of magnetic susceptibility,  
and remanent magnetization directions**

**Knight, Michael Don, Ph.D.**

University of Hawaii, 1989

**U·M·I**

300 N. Zeeb Rd.  
Ann Arbor, MI 48106



**VOLCANIC EVOLUTION OF THE KOOLAU DIKE COMPLEX:  
DETERMINED FROM INTRUSIVE MAGMA FLOW,  
ANISOTROPY OF MAGNETIC SUSCEPTIBILITY, AND  
REMANENT MAGNETIZATION DIRECTIONS**

**A DISSERTATION SUBMITTED TO THE GRADUATE DIVISION OF THE  
UNIVERSITY OF HAWAII IN PARTIAL FULFILLMENT OF THE  
REQUIREMENTS FOR THE DEGREE OF**

**DOCTOR OF PHILOSOPHY  
IN GEOLOGY AND GEOPHYSICS**

**DECEMBER 1989**

**By**

**MICHAEL D. KNIGHT**

**Dissertation Committee:**

**George P.L. Walker, Chairman**

**John M. Sinton**

**Barry R. Lienert**

**John P. Lockwood**

**Rollin C. Jones**

**c Copyright by Michael Don Knight 1988**

**All Rights Reserved**

## ACKNOWLEDGEMENTS

I have great admiration for my advisor Dr. George Walker. He not only assisted me in the field, but also had keen insights into the major questions to be addressed in this study. His advice, encouragement, and persevering patience in my persistent determination to use paleomagnetic techniques to further our understanding of volcanic flow features is greatly appreciated. This investigation was greatly aided by Dr. Walker's previous indepth studies of the Koolau dike complex. This project was supported under National Science Foundation grant EAR 82-06655 and grant NAGW-1084 from the Mars Evolution of Volcanism, Tectonism and Volatiles Project, principal investigator Dr. Peter Mougini-Mark. I would like to specially thank Dr. Barry Lienert for writing and revising the necessary computer software programs for the AMS measurements, and for keeping the balanced bridge susceptibility spinner in correct working order. I would like to thank the other members of my committee Dr. John Sinton, Dr. Jack Lockwood, and Dr. Rollin Jones for their editorial comments and thoughtful questions during my defence. I would also like to thank Chuck Helsley and Barbara Keating for allowing me unlimited use of the paleomagnetic equipment, micro-computers, printers and the like at the paleomagnetic laboratory, Hawaii Institute of Geophysics (HIG). The field work would have been nearly impossible if it were not for the help of many of my student colleagues at HIG, particularly Bryon Stevens, Scott Rowland, Michael Jackson, and Glenn Brown. I would also like to thank three visiting students who helped with field work and/or laboratory measurements of the remanent magnetization (AF demagnetization) for a number of sites, particularly Alan Mathews from Michigan Technological University, Iwan Willimans from the University of Lancaster, United Kingdom, and Katherine Hughes from the University of Waikato, New Zealand. Finally I would like to thank my aunt Fran Roberts for her encouragement and financial support, and my mother and father for their endearing devotion.

## ABSTRACT

I measured the magnetic fabric in 71 dikes, a sill, a filled lava tube associated with the Koolau Volcano, as well as four young to recent lava flows from the Island of Hawaii. Anisotropy of magnetic susceptibility (AMS) was determined for nearly 670 specimens drilled in situ from 77 sites, and statistically significant AMS clusters were found in all but 10. 35 of the dikes show a macroscopic surface lineation; the mean maximum AMS direction ( $\chi_1$ ) coincides with this lineation direction to within  $25^\circ$  in 22 and to within  $15^\circ$  in 12. Based on a magnetic imbrication the AMS technique was used to infer the absolute magma flow directions in 17 dikes. In these the maximum AMS axis of samples from one side of the dike form a tight cluster on an equal area plot, and those from the other side of the dike form another tight cluster. These two clusters form a pair symmetrically disposed on either side of the plane of the dike and are inferred to be the result of an imbrication of the ferrimagnetic crystals (anisotropic ones) against each margin of the dike during deposition in a velocity gradient, and hence indicate the absolute flow direction. Based on surface lineations, AMS magma flow directions, thermal remanent magnetization (TRM) directions, and morphology and cross-cutting features of the dikes I infer that there were three magma sources, 1–2 km below the present erosional surface, which fed the Koolau Dike Complex. The oldest center was below the NW-end of Kaneohe Bay, and is unique in that it is the only area in which all the measured dikes exhibits very steep plunge directions in the maximum  $\chi_1$  AMS axes and it is the only area to have normally magnetized dikes (after alternating field demagnetization in a peak field of 150 Oe the TRM direction is Declination= $3.26^\circ$ , Inclination= $10.34^\circ$ ,  $\kappa=25.0$ ,  $\alpha_{95}=19.8^\circ$ ). Previously the exposed portion of the Koolau volcano was thought to have formed entirely during the early Matuyama Reversed Chron, but this new TRM data suggests that the earliest dikes formed during the Gauss Normal Chron ( $>2.43$  Ma). The next oldest center is 12 km to

the SE below the S-end of Kaneohe Bay. The youngest center is below the Kawainui Swamp (6 km farther SE), and is the location of a +310 milligal Bouguer anomaly. A hot-spot trace may, thus, be marked by a progression of eruptive centers within a single volcano as well as a progression of volcanoes.

## TABLE OF CONTENTS

	Page
ACKNOWLEDGEMENTS .....	iv
ABSTRACT .....	v
LIST OF TABLES .....	x
LIST OF ILLUSTRATIONS .....	xi
<b>CHAPTER 1. VOLCANIC EVOLUTION OF THE KOOLAU DIKE COMPLEX: DETERMINED FROM INTRUSIVE MAGMA FLOW, AMS, and REMANENT MAGNETIZATION DIRECTIONS .....</b>	
<b>Purpose .....</b>	<b>1</b>
<b>Introduction .....</b>	<b>2</b>
<b>KNOWLEDGE OF RIFT ZONE PROCESSES IN ACTIVE HAWAIIAN VOLCANOES .....</b>	
<b>Background .....</b>	<b>5</b>
<b>Structure and the Internal Plumbing System .....</b>	<b>6</b>
<b>Neutral Buoyancy as a Control on Dike Emplacement .....</b>	<b>19</b>

KNOWLEDGE OF KOOLAU VOLCANO AND ITS DIKE COMPLEX .....	22
Climate .....	22
Previous Investigations .....	23
Koolau Dike Morphology and Intrusive Magma Flow .....	31
OBJECTIVES AND TECHNIQUES USED IN THE PRESENT STUDY OF THE KOOLAU COMPLEX .....	37
Macroscopic Surface Lineations .....	37
Lateral Fractures .....	38
Radial Fractures .....	47
Cone Fractures .....	50
Magma Flow Structures .....	50
Crystal and Vesicle Orientations .....	51
Magnetic Fabric of Dikes .....	51
Density of Koolau Dikes .....	53
Natural Remanent Magnetization of the Koolau Dikes .....	56
Stability of Remanent Magnetization .....	60
CHAPTER 2. THEORY OF ANISOTROPY OF MAGNETIC SUSCEPTIBILITY	69
Introduction .....	69
Theory of AMS .....	72
Shape Anisotropy and the Demagnetizing Factor .....	74
Evaluation of the Susceptibility Ellipsoid .....	82
AMS Parameters .....	85

<b>AMS INSTRUMENTATION AND MEASUREMENTS</b> .....	90
<b>Background</b> .....	90
<b>AMS Measurements</b> .....	91
<b>Statistics</b> .....	98
<b>CHAPTER 3. AMS RESULTS FOR THE KOOLAU DIKE COMPLEX</b> .....	103
<b>Basic Principles of AMS</b> .....	103
<b>AMS Data for the Koolau Dike Complex</b> .....	112
<b>Summary and Interpretation of the AMS Data</b> .....	159
<b>CHAPTER 4. MAGMA FLOW DIFFERENTIATION IN DIKES</b> .....	170
<b>Introduction</b> .....	170
<b>Flow Differentiation and Crystal Content Across the Dike</b> .....	176
<b>Relation of AMS to Imbrication Fabric</b> .....	189
<b>Role of Turbulence</b> .....	191
<b>Vesicle Orientation During Magma Flow</b> .....	196
<b>Bubble Dynamics and Rheology during intrusion</b> .....	204
<b>CHAPTER 5. VOLCANIC EVOLUTION AND MAGMA FLOW IN THE KOOLAU DIKE COMPLEX</b> .....	208
<b>Discussion</b> .....	208
<b>Conclusion</b> .....	210
<b>APPENDIX A</b> .....	217
<b>APPENDIX B</b> .....	296
<b>REFERENCES</b> .....	298

## LIST OF TABLES

Tables	Page
1.1 Natural remanent magnetization directions for the Koolau dikes.....	61
2.1 Initial mass susceptibility of rocks and minerals of interest .....	71
2.2 Some anisotropy of magnetic susceptibility parameters .....	88
3.1 Summary of anisotropy of magnetic susceptibility and macroscopic surface lineations for 76 sites .....	113
3.2 Description of 73 sampled sites, comparison of plunge to $\chi_1$ direction and inferred magma flow direction .....	115
4.1 Vesicle shape classification scheme .....	198

## LIST OF ILLUSTRATIONS

Figures	Page
1.1 Hypocenters of shallow earthquakes during 1970–1983 near Kilauea caldera .....	8
1.2a Model of magma ascent path into Kilauea primary conduit .....	11
1.2b Model of dike injection path, honeycomb structure .....	11
1.3 Bouguer gravity map for the Koolau Volcano .....	14
1.4 Histogram of dike trends for the Koolau Volcano .....	26
1.5 Equal area plot of mean $\chi_1$ axes for 62 Koolau dikes .....	28
1.6a Photograph of macroscopic surface lineations .....	40
1.6b Photograph of bumps and ridges along an irregular dike surface .....	40
1.7 Rose diagram of macroscopic surface lineation plunge direction for 38 Koolau dikes .....	42
1.8a Photograph of dike margin with slickenside-like grooves .....	44
1.8b Photograph of dike margin with slickenside-like grooves .....	44
1.9 Schematic drawing of en echelon dike offsets .....	46
1.10a Photograph of imbricated sheet joints along dike margins .....	49
1.10b Photograph of zeolite filled pipe-vesicles along dike margin .....	49
1.11 Histogram of bulk density of 70 Koolau dikes .....	55

1.12	Plot of dike density versus the plunge direction of inferred magma flow azimuth for 62 dikes .....	58
1.13a	Equal area plot of NRM directions for normally magnetized dikes .....	65
1.13b	Equal area plot of NRM directions for reversely magnetized dikes .....	65
1.13c	Equal area plot of remanent directions for normally magnetized dikes after AF-demagnetization .....	65
1.13d	Equal area plot of remanent directions for reversely magnetized dikes after AF-demagnetization .....	65
1.14a	Plot of the step-wise progressive alternating field demagnetization .....	68
1.14b	Zijderveld plot of the step-wise progressive AF demagnetization .....	68
2.1a	Cartoon of observed AMS susceptibility vector direction for an isotropic mineral in a uniform low external magnetic field .....	77
2.1b	Cartoon of observed maximum AMS susceptibility direction for an ellipsoidal-shaped magnetite grain in a low external field .....	77
2.1c	Cartoon of the susceptibility ovaloid .....	77
2.2	Plot of the anisotropy factor against the dimension ratio .....	80
2.3	Graphic representation of the two-dimensional surface of the susceptibility ovaloid plotted in the xy-plane .....	84
2.4	Plot of logarithmic mean of the AMS axial ratios for 70 Koolau dikes .....	87
2.5a	Photograph of the Balance Bridge Susceptibility Spinner .....	94

2.5b	Schematic layout of the Balanced Bridge Susceptibility Spinner .....	94
2.6a	Cartoon of core specimen orientation within cubic sample holder .....	96
2.6b	Schematic of sample spin direction and orientation of applied field .....	96
2.7	Unit circle of the error ellipse normal to the mean maximum AMS direction .....	102
3.1	Block diagram of idealized AMS axes relative to the inferred magma flow direction along the dike walls .....	107
3.2	AMS plot of a recent lava flow from Kilauea's East Rift Zone .....	110
3.3a	Plot of Graham's V versus Total percent anisotropy for 525 AMS measurements .....	121
3.3b	Flinn diagram .....	121
3.4	Equal area plots for six major categories of AMS axial distributions .....	125
3.5a	Pie diagram of the agreement between the plunge direction of the macroscopic surface lineations and the $\chi_1$ AMS plunge direction .....	161
3.5b	Pie diagram showing the percentage of Koolau dikes which fall within the six major categories of the AMS axial distributions .....	161
3.6a	Plot of distance from the Kailua caldera verses dike width for 71 dikes ....	165
3.6b	Plot of distance from the Kailua caldera verses total anisotropy .....	165
3.7	Pie diagram summarizing the AMS magma flow directions in 71 dikes ....	167

4.1a	Cartoon of velocity profile of a Newtonian fluid under laminar flow in a dike	173
4.1b	Cartoon of vertical magma flow in a dike .....	173
4.1c	Cartoon of horizontal magma flow in a dike .....	173
4.2	Variation in olivine crystal content across the dike width .....	179
4.3a	Grain orientation of 565 grains .....	182
4.3b	Grain orientation of 607 grains .....	183
4.3c	Grain orientation for 553 grains .....	184
4.4a	Cartoon of forces acting on a spherical particle during upward laminar flow	186
4.4b	The forces acting on a spherical particle during downward laminar flow ...	187
4.4c	Equal area plot of the AMS axial distributions for dike KD58 .....	187
4.5a	Idealized drawing showing imbrication of anisotropic tablet-shaped phenocrysts and microphenocrysts during upward laminar flow .....	193
4.5b	Idealized drawing showing oblate ellipsoidal shaped crystals imbricated along both margins .....	193
4.5a	Idealized drawing showing prolate ellipsoidal shaped magnetite grains imbricated along the dike margin .....	193
4.6a	Vesicle, microvesicle, and microphenocryst orientation for an infilled lava tube .....	201

4.6b	Vesicle, microvesicle, and microphenocryst orientation for an infilled lava tube .....	202
4.6c	Vesicle, microvesicle, and microphenocryst orientation for an infilled lava tube .....	203
5.1	Idealized summary diagram of the three magma centers and their associated dikes which formed during the evolution of the Koolau shield volcano ....	212
 Plates		
I	Map of dike localities measured for AMS .....	314
II	Map of mean maximum AMS directions of dikes measured .....	315

**CHAPTER 1**  
**VOLCANIC EVOLUTION OF THE KOOLAU DIKE COMPLEX:**  
**DETERMINED FROM INTRUSIVE MAGMA FLOW, AMS, AND**  
**REMANENT MAGNETIZATION DIRECTIONS**

**PURPOSE**

One of the most important and often asked questions in any volcanological study dealing with Hawaiian shield volcanoes is: what was the position of the eruptive fissure(s) or source vent(s), and in what way was it related to the underlying magma reservoir? Interpretation of the magma flow directions in dikes of eroded shield volcanoes offers an opportunity to study the movement of magma through its subsurface feeder-conduit system. This study addresses the problem of how the dynamics of magma movements and fluid rheology within dikes are related to the structure and dynamics of the shallow magma reservoir(s) and whether or not the absolute magma flow azimuths within dikes can be used to constrain the depth and location of their source reservoir(s). Other specific questions addressed in this study include the following: After ascent into the shield, what factors are responsible for the subsequent intrusion directions into the shallow rift zones? Do the magnetic flow characteristics, mechanics, and bulk densities of the Koolau dikes support the "*bulk-density zonation*" model of Walker [1986] and similarly the "*neutral buoyancy*" model of Ryan [1987]? How did the effects of magma intrusion into the different rift zones influence the growth of the Koolau shield? Because the exposed Koolau dike complex is best seen in the more deeply eroded parts of the Koolau shield at about one kilometer below the original constructional surface, it is an ideal subject for understanding how the internal plumbing system in a rift zone is related to the overall morphology of a large shield volcano.

One approach to answering these questions is to elucidate the behavior of silicate fluids in motion. Interpretation of the magma flow directions in dikes of eroded shield volcanoes

offers an opportunity to study the movement of magma through its subsurface feeder-conduit system.

The Hawaiian-Emperor volcanic chain is perhaps the best known and most intensely studied hot spot trace, postulated to have formed as the oceanic lithosphere moved over a stationary mantle plume [Wilson, 1963a, b; Morgan, 1971, 1972]. The mid-ocean plate Hawaiian volcanoes are isolated from the complications of oceanic spreading ridges and oceanic/continental subduction zones, and their apparent lithologic and structural simplicity implies that, if there is a hope of really understanding how the internal plumbing system of a volcano works, Hawaii seems to be the ideal place. Hence, the present investigation is aimed at better constraining the spatial and temporal evolution of a single hotspot volcano, the Koolau shield volcano on the island of Oahu, by studying in detail the magnetic fabrics of 71 dikes, one sill, and an infilled lava tube associated with its major dike complexes.

## INTRODUCTION

Lateral magma intrusions into the rift zones of active Hawaiian volcanoes, for example Kilauea's east rift and Mauna Loa's southwest rift, have long been inferred to occur [Hitchcock, 1900; Stearns and Vaksvik, 1935; Stearns, 1939; Wentworth and Jones, 1940; Wentworth and Winchell, 1947; Wright, 1971; Swanson et al., 1976; Lipman, 1980; Epp et al., 1983; Pollard et al., 1983; Dzurisin et al., 1984; Dorak et al., 1986; Holcomb, 1980, 1987; Klein et al., 1987; Ryan, 1987a, b; Koyanagi et al., 1987], but few details have been known of the underground magma movements.

Stearns [1939], during the first systematic geologic survey of Oahu, recognized the existence of a zone of numerous dikes, paralleling the major axis of the Koolau volcano, which he referred to as a *dike complex* (including the entire mass of country rock and dikes). Similar dike complexes were mapped on Waianae Volcano in Oahu [Stearns, 1939; Macdonald, 1940; Zbinden and Sinton, 1988], on East Molokai Volcano [Stearns

and Macdonald, 1947; Holcomb, 1981], on West Maui Volcano [Stearns and Macdonald, 1942; Macdonald et al., 1983; Diller, 1982] and on other Hawaiian volcanoes.

The chemical histories of intrusive and extrusive rocks are largely controlled by factors that govern the magma flow paths, the transport times and the dynamics of the rheological processes operating during flow. The dike morphology and magma flow trajectories record the history of magma rise which is influenced by the relationships between the system's *internal magma pressure*, *rock stresses*, and *fracture toughness* or ability of *external fracture* to induce flow paths. Commonly these dikes propagate at shallow depths (inferred to be  $\approx 350$  m) for tens of kilometers without erupting at the surface. Occasionally intrusive bodies will propagate upward to feed surface lava flows, e.g. the initiation of the 1959 Kilauea Iki fissure eruption in which *Delaney and Pollard* [1982] estimated the upward flow velocity of magma to be  $0.1 \text{ m s}^{-1}$ . Their cooling rate calculations, for basaltic magma flowing at initial velocities of  $1 \text{ m s}^{-1}$  in 2 m wide dikes, predict complete solidification within only a few hours. *Wilson and Head* [1981] predicted that for a given magma flux, the flow velocity is proportional to the square-root of the dike width. According to *Wilson and Head* [1981] and *Delaney and Pollard* [1982] an eruptive conduit or dike will remain open if the magma flux is high enough to replenish heat lost through cooling of the country rock by conduction and to a minor extent by convection. Thus, when the flow rate becomes so small as to be unable to replenish heat lost to the country rock the dike freezes and no steady state equilibrium between magma flux and dike width is attained. These predictions could explain why the narrowest dikes found closest to Hawaiian volcanic centers tend to have the most irregular morphologies.

The time taken to freeze a dike of a given width has also been estimated by *Wilson and Head* [1989] using the method and physical properties given by *Turcotte and Schubert* [1982]. *Wilson and Head's* [1989] results, for an intrusive event along Kilauea's East Rift Zone, predict that a 1-m-wide dike freezes in a time ranging from one week to several months depending on the time since the most recent previous intrusion and temperature of

the surrounding country rock. In addition, they indicate that a 5-m-wide dike, which represents the upper limit for the widest observed dikes in Hawaii (e.g. the widest Hawaiian-dike observed by the author is an East Molokai dike measuring 530 cm), can remain partly liquid from 4 months to 2.5 years.

The hydrostatic pressure at any depth in an erupting magma is not likely to be greatly different from the local lithostatic pressure once steady flow to the surface has been reached, and has been assumed equal in most of *Wilson and Head's* [1981] calculations. It is generally accepted [*Pollard and Muller, 1976; Fedotov, 1978; Delaney and Pollard, 1982; Pollard et al., 1983; Rubin and Pollard, 1987*] that a dike will propagate if the *internal pressure* minus the *remote stress* (i.e. the stress-intensity factor at the dike tip) exceeds a critical value of the fracture toughness of the host rock. As suggested by Rubin and Pollard [1987] the factors influencing the stress intensity along the dike perimeter can be divided into two categories: those factors pertaining to dike morphology include: dike size; shape (parallel versus irregular walls); and depth beneath the surface; and those factors related to the distribution of the driving pressure (magma pressure minus the remote stress) within the dike are controlled by: magma-reservoir pressure; magma density (influenced by the presence of phenocrysts); presence of vesiculated magma or gas at the dike top; pressure gradients due to viscous flow (e.g., flow differentiation, crystal interactions and crystal/vesicle interactions). The remote stress contributors are: density stratification of the rift zone [*Walker, 1987, 1989*]; gravitational loading of the edifice [*Fiske and Jackson, 1972*]; intrusions of earlier dikes; faulting (internal structure of the volcanic edifice); and the regional tectonic stress field. Regarding density, many concur that the surface density of  $2.3 \text{ g cm}^{-3}$  for the upper 1–2 km corresponds to an average density for vesiculated lava flows [*Kinoshita et al., 1963*], and a density of  $2.9 \text{ g cm}^{-3}$  at depths of more than 2–3 km represent submarine lavas [*Moore and Fiske, 1969; Swanson et al., 1976*], solidified intrusions [*Hill and Zucca, 1987*], or flows with vesicles now filled with hydrothermal minerals (zeolites).

In summary, dike propagation directions within the complexes are controlled by a number of factors, of which the following can be considered some of the most important.

- (i) The external pressure due to the *remote stress field*.
- (ii) The *weight of the volcanic edifice* above the magma reservoir, manifested in both vertical and horizontal lithostatic pressures.
- (iii) The *hydrostatic pressure of the magma* as a fluid having a density that is dependent on composition, volatile content, and crystal content.
- (iv) The *host rock mechanics* (e.g. fracture toughness and compressibility) and any structural anisotropy in the rocks.
- (v) The magmatic *pressure due to gas expansion*, in which buoyancy induced magma rise resulting from exsolved volatiles may be a significant factor only in the uppermost (100–300 m) portion of the active volcano.
- (vi) *Bulk-rock density zonation* also influences dike propagation direction.

Furthermore, *Dieterich* [1988] indicates that other factors are required to generate the appropriate dike-trapping stress field within the linear rift zones of Hawaiian shields where thousands of individual dikes can be concentrated (e.g. the linear rift zone of the Koolau complex has an estimated 7400 or more individual dikes [*Walker*, 1987]). For continued multiple-dike injection within the swarms, localized tectonic factors such as extensional faulting, and gravitational downsagging of the volcanic center must also play a role in the evolutionary history of the the dike complexes.

## KNOWLEDGE OF RIFT ZONE PROCESSES IN ACTIVE HAWAIIAN VOLCANOES

### BACKGROUND

The first crustal structure and process-oriented model for Hawaiian shield development was proposed by *Eaton* [1962] who described the magma ascent, storage, and rift zone intrusion processes. During the last 15 years detailed seismic and geodetic studies have

indicated that an interconnected dike complex occurs below the active rift zones of Hawaiian volcanoes and that the dikes are commonly intruded laterally from a shallow central magma reservoir, typically as blade-like intrusions [Wright, 1971; Ryan *et al.*, 1983; Pollard *et al.*, 1983; Dvorak *et al.*, 1986; Klein *et al.*, 1987; Rubin and Pollard, 1987; Ryan, 1988; Wilson, 1988]. Structural models based on seismicity have refined earlier models for the internal structure of the active Hawaiian shields (Figure 1.1) [Hill, 1969; Zucca and Hill, 1980; Zucca *et al.*, 1982; Klein *et al.*, 1987; and Hill and Zucca, 1987]. Seismic studies have suggested that the ultimate source lies well below the base of the oceanic crust in the upper mantle at depths of at least 40 or 60 km [Eaton, 1962; Ellsworth and Koyanagi, 1977; Ryan, 1988].

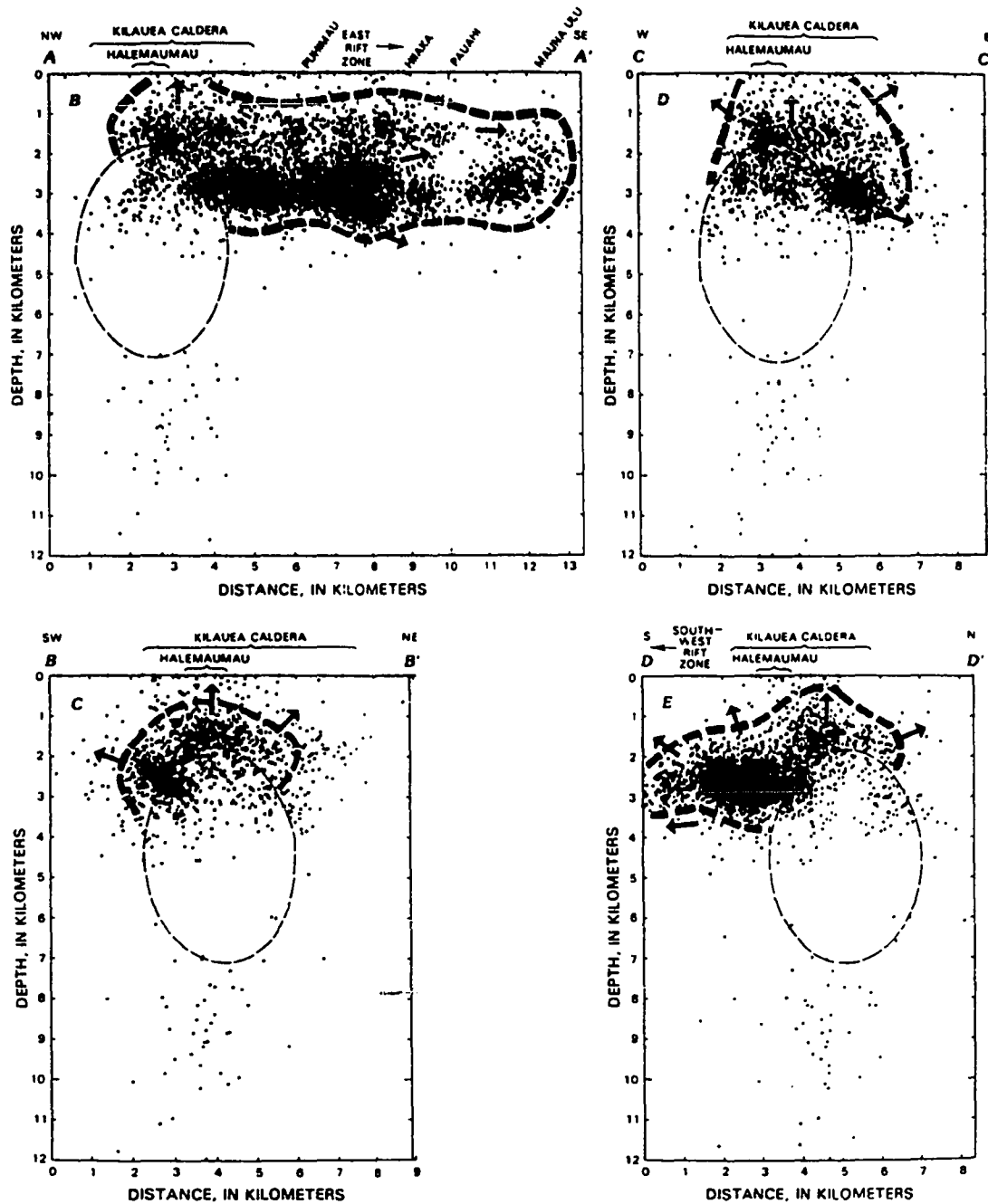
Lipman *et al.* [1985] described the dramatic geodetic and geologic changes associated with the largest seismic events (e.g. the 1975 Kalapana earthquake,  $M = 7.2$ ) thereby constraining the basal structure of the active Mauna Loa and Kilauea shields. They suggested that the shallow dipping sediment/volcanic interface at the base of the shield has permitted a seaward migration of the unbuttressed side of these volcanoes so making space for major rift zones.

## STRUCTURE AND THE INTERNAL PLUMBING SYSTEM

Active Hawaiian shield volcanoes characteristically have well-defined *rift zones* within which most of their eruptions are concentrated. Extinct and eroded shield volcanoes characteristically have *dike complexes*, these being regarded as the subsurface equivalent of the active rift zones. Much can be learned about the origin of Hawaiian shield volcanoes by studying their dike complexes. Swanson *et al.* [1976] used the results of trilateration and geologic surveys to derive a model emphasizing the role of forceful intrusion of magma to produce the observed displacements.

Pollard *et al.* [1983] derived a model for estimating the geometry and depth of intrusion of dike-like bodies from the surface displacement profiles and surficial structures presumed

Figure 1.1 A modified version of Figure 43.10B–E; page 1045; *Klein et al.* [1987]. These cross sections show the hypocenters of shallow earthquakes during 1970–1983 near Kilauea caldera. The mostly aseismic region below the most intense cluster of hypocenters is interpreted by *Klein et al.* [1987] to represent the approximate position of the magma reservoir (shown as thin dashed oval). Also shown, are the inferred shapes and possible extent of the major intrusive bodies (area encompassed by thick dashed line) represented here by the region of most intense seismicity; small arrows are inferred magma flow directions resulting from forceful dike injection and directed away from the presumed magma reservoir. Note that magma flow is interpreted to be mostly horizontal over a wide 1–3 km deep zone, but can also be either upward or downward depending on the relative depth of intrusion, in compliance with models of neutral buoyancy [*Ryan*, 1987] and bulk-density zonation [*Walker*, 1987].



[modified from Klein et al., 1987]

to form above the shallow feeder system. *Shaw* [1980] considered the role of fluid pressure in the stability of magma-charged fractures within the crust and upper mantle to predict the effective principal stress above the Hawaiian hotspot. In a recent study *Chevallier and Verwoerd* [1988] compared a model derived from observed volcanological features of intraplate volcanoes in the Indian Ocean, with a corresponding computed stress field model. They suggest that there is a coherent stress pattern associated with five principal structural elements (or levels) of their geological model; namely *rift fracture*, *tension fracture*, *conical shear fracture*, *radial hydraulic fracture*, and *conical fracture* at the summit caldera.

Magma generated at the Hawaiian hotspot rises to accumulate in shallow central reservoirs (2–7 km) beneath the summit calderas of these volcanoes, and then moves out into the rift zones via a network of feeder dikes [*Wright*, 1971; *Ellsworth and Koyanagi*, 1977; *Klein et al.*, 1987]. Seismic and geodetic data suggest that the dikes in the rift zones of Kilauea Volcano and Krafla Volcano are intruded laterally from a shallow central magma reservoir and are typically blade-like in form. *Klein et al.* [1987] infer that the shallow intrusion pattern and subsurface structure of Kilauea Volcano is a multitiered complex of interconnected dikes. These magma storage reservoirs have even been referred to as *honeycomb* structures of interconnected fluid-filled parcels from different deformation centers [*Eaton*, 1962; *Kinoshita*, 1969; *Dieterich and Decker*, 1975; *Hill*, 1977; *Ryan et al.*, 1983; *Dvorak et al.*, 1983; *Ryan*, 1988]. Figures 1.2a and b depict the inferred deeper (sub-conduit) structure for the internal plumbing system of Hawaiian shield volcanoes.

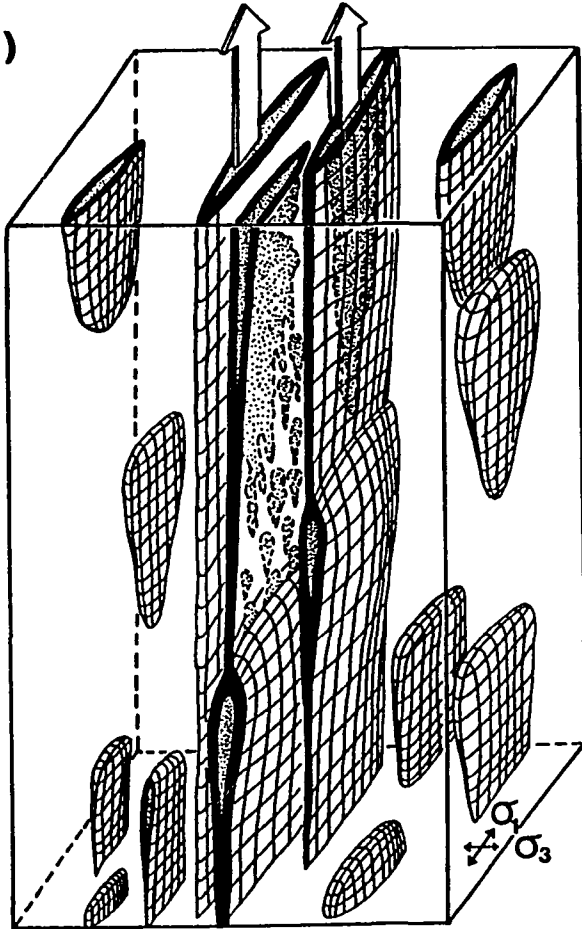
The concept of a *dike complex* stems from early work done on the older dissected Hawaiian shields, and is defined as a mappable body that may be related to a specific volcano or volcano-tectonic structure in which dikes generally form more than 50% of the total rock body [*Stearns*, 1939; *Stearns and Macdonald*, 1946; *Wentworth and Jones*, 1940], and differs from a *dike swarm*, a concept which predates work done in Hawaii, and is defined as a group of dikes, which may be in radial, parallel, subparallel, or en

Figure 1.2(a) Revised from Figure 24B, page 4245; *Ryan* [1988]. Illustrates the inferred magma ascent path within the core and margins of Kilauea's primary conduit, and is consistent with the geometry and mechanics of fluid-filled ascending fractures developed by *Weertman* [1971a, b], *Pollard* [1973], and *Weertman and Chung* [1977]. *Ryan* [1988] indicates that both the core and conduit margins are active during periods of relatively high supply, and that isolated parcels of melt-filled fractures within the three-dimensional meshwork may or may not be interconnected. The ascent path of these parcels is governed by the the internal stress field and laws of neutral buoyancy and bulk density zonation (in both figures  $S_1$  and  $S_3$  represent the maximum and minimum principal effective stresses, respectively).

(b) Schematic geometry of dike sets (applies to either horizontal or vertical magma lenses) giving a "honeycomb" structure of interconnected fluid-filled fractures. Two types of crack propagation due to extensional shear failure near dike tips as described by *Pollard* [1973] are shown (A and B).

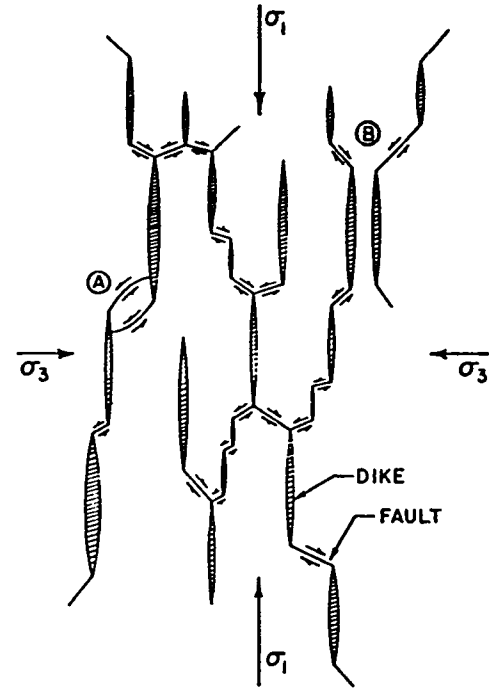
**Magma Ascent into Kilauea Primary Conduit**

**(a)**



**(from Ryan, 1988)**

**(b) Honeycomb Structure of Interconnected Fluid Packets**



**(from Hill, 1977)**

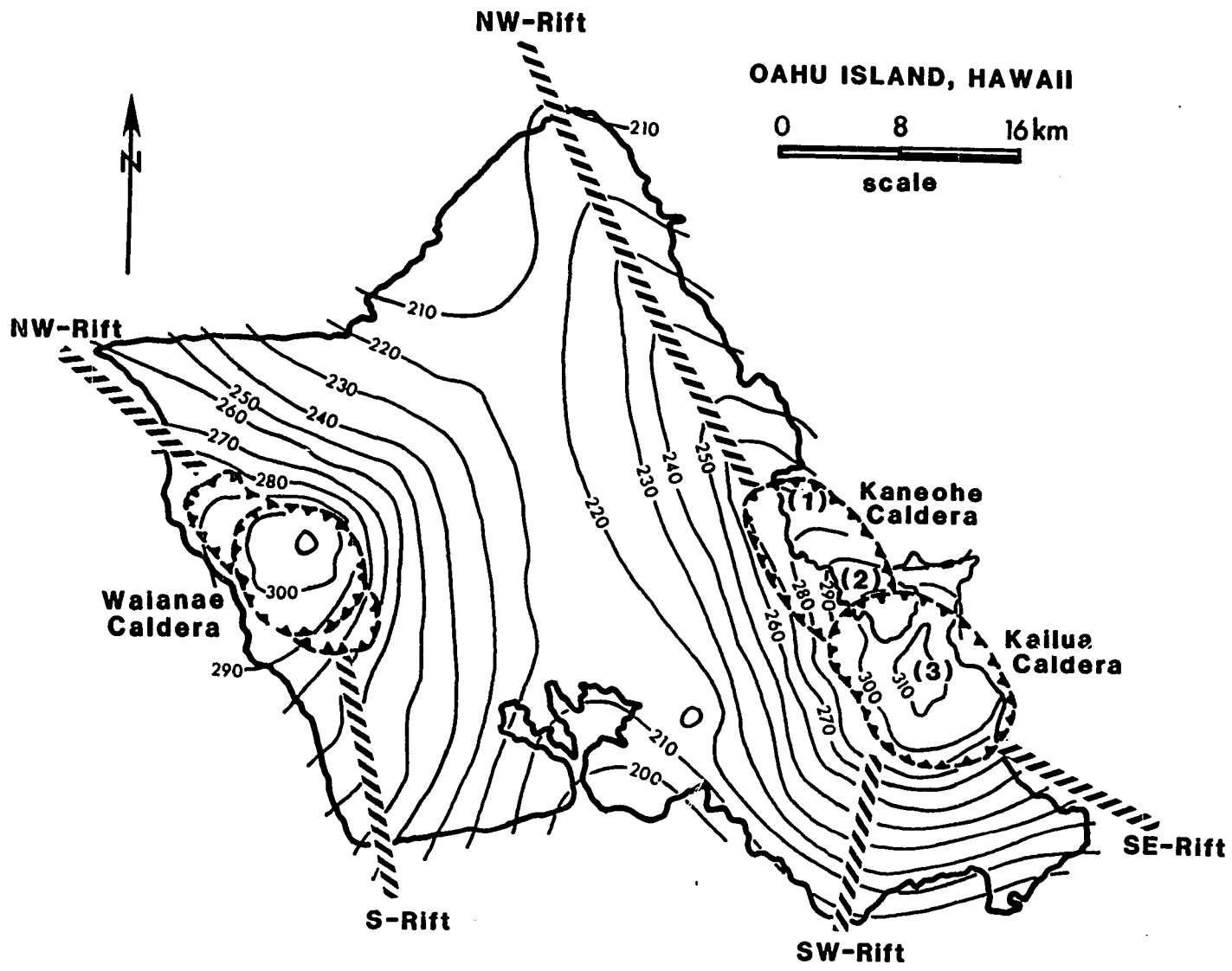
echelon arrangement that are compositionally, spatially and temporally related, making up 80–100% of the total rock body. *Wentworth* [1951] further restricts the usage of the term dike complex to those areas where there are 100 or more dikes per mile, and *Takasaki et al.* [1969] applied it to areas where dikes constitute more than 5% of the rock. In the most recent study of the Koolau dike complex, *Walker* [1987] estimated the *total dike intensity* at a great many localities within the eroded parts of the volcanic shield based on detailed quantitative measurements of the percentage of the total volume of dike rock to country rock.

Like other Hawaiian shields the rift zones coincide with very high positive Bouguer gravity anomalies that reach a maximum where the calderas are located (Figure 1.3). These anomalies are thought to represent a much higher proportion of dense intrusive rocks associated with the magma chambers and central conduit system, as well as relatively dense ponded intracaldera lavas. Paradoxically these gravity highs coincide with areas where the intensity of the dike complex drops to a very low value. *Walker* [1987] suggests that the subsidence of the calderas and their environs was very rapid: so rapid, that the dike complex had no opportunity of building up to a high intensity. Subsidence and formation of the calderas was possibly by downward creep into a thermally-weakened lithosphere above a hotspot.

Of the active Hawaiian shield volcanoes the best possible surface analog for Koolau's deeply eroded dike complex is Kilauea's East Rift system, which is buttressed along its northern flank by the larger Mauna Loa and Mauna Kea volcanoes. The major structures of the active Hawaiian rift zones include *linear eruptive fissures* with or without *spatter ramparts*, elongate and semicircular *spatter* and *cinder cones*, coalesced and nested *collapse pit craters*, and *open cracks* parallel to the main rift axes [*Wentworth and Macdonald, 1953; Macdonald, 1953*].

Individual fissure vents range from a few tens of meters to several tens of kilometers long (e.g. the great 1950 vent system of Mauna Loa), they open due to magmatic pressures

Figure 1.3 Bouguer gravity map (after *Strange et al.*, 1965), shows the inferred main Koolau caldera, herein referred to as the Kailua caldera, located at the +310 mgal contour (in the general vicinity of the Kawainui Swamp), also shown is an inferred older center, the Kaneohe caldera. Note that three separate magma source reservoirs (labelled 1 to 3) for the Koolau Dike Complex are also shown. Similar to other Hawaiian shields the caldera centers coincide with large positive Bouguer anomalies (highest anomalies are observed at Kauai and Mauna Kea, +330 and +320 mgal). The volcanic centers associated with Positive Bouguer Anomalies are thought to result from thick subsided sequences of ponded lava flows and abundant high density intrusive bodies. The major rift axes of the Koolau Dike Complex are oriented NW-SE and a minor one trends SW-NE (shown by thick hatched line). Also shown are the caldera center and rifts of the older Waianae Volcano.



and serve as conduits during initial stages of most Hawaiian eruptions. Fissure vents are typically open at the surface, and their lips are commonly draped by agglutinated spatter and lava that flowed back into the vent during late stages of the eruption [Lipman, 1980]. At depth these vents must be represented by dikes. Surface drainback structures provide physical evidence for possible downward oriented magma flow; such a mechanism has been suggested by *Easton and Lockwood* [1983] for some unusual dikes along the Hilina Fault zone, Kilauea Volcano, and *Knight and Walker* [1988] have inferred similar gravitationally induced downward flow directions based on the AMS fabrics of some shallow intrusives of the Koolau dike complex. After the initial stage, activity on fissure vents typically becomes restricted to a single or a few closely spaced centers, where continued activity produces spatter or cinder cones, and their distribution can be interpreted as the surface manifestation and evolution of the rift zone and hence the underlying dike complex.

Cracks mostly occur in clusters parallel to the rift zone and are thought to be unrelated to specific vent systems; they are typically less than several meters wide, and generally lack vertical or lateral shearing. Based on well-documented geodetic studies at Kilauea, *Swanson et al.* [1976] indicate that some surface cracks are the result of simple extension related to dilation of the rift zone accompanying intrusion of basaltic magma at shallow depths. Furthermore, *Swanson et al.* [1976] suggest that considerable horizontal dilation (mostly perpendicular to the rift axis) is associated with the presumed *forceful* injection of magma, which is manifested at the surface by gaping cracks and fissures that parallel the main rift axes. They also argue that gravity sliding occurs in response to oversteepening of the flanks due to the accumulation of many intrusions and that these slides occur on shallow listric faults that do not intersect the rift zone. Movement along the Hilina fault exemplifies this tectonic environment which is parallel to the ERZ but 5–10 km outboard of it. In contrast to this "*active*" dike injection model for the horizontal growth of Hawaiian rift zones, is the idea that gravity faults may act to open the rift and permit "*passive*"

intrusion at the head of the slump [Dieterich, 1988]. A passive intrusion model is somewhat supported by Moore and Krivoy [1964], who have proposed that gravity slumps would initiate at the base of shallow rift intrusions that dip with the slope of the volcano flank. The motion on these gravity faults acts to open the rift zones to permit passive intrusion. Interpretation of the seismic data associated with the November 29<sup>th</sup> Kalapana earthquake [Furumoto and Kovach, 1979; Crosson and Endo, 1982] indicates that a roughly horizontal fault plane intersects the base of the rift zone. This fault plane is presumed to be the interface between the sediment covered Cretaceous oceanic crust and the overlying volcanic shield. In a recent seismic investigation of the crustal structure under the Hawaiian Islands between Kauai and Molokai, Lindwall (in press) indicates that there is some uncertainty in locating the interface between the volcanic edifice and the oceanic crust in this region, and that this could be a result of a low-velocity zone associated with a very thin sediment layer.

As indicated by Knight and Walker [1988] for the Koolau Volcano, similar orientations of rift zones in terms of progressive growth of the volcanoes from northwest to southeast parallel to the Pacific plate motion vector, have also been interpreted for the island of Hawaii [Fiske and Jackson, 1972; Lipman, 1980]. According to Fiske and Jackson [1972] the orientation of Kilauea's rift zones were controlled by "buttressing effects" of the southeast flank of Mauna Loa. Similarly, the orientations of Mauna Loa's two rift zones were controlled by its location adjacent to the flanks of the older volcanoes of Hualalai and Mauna Kea [Lipman, 1980].

Based on several lines of evidence, the locus of active vents of the ERZ has migrated several kilometers downrift and southward with time. Kilauea's southwest rift zone and summit caldera also show some evidence of southward migration. Lipman [1980] suggests that the anomalous details of Mauna Loa's structure, particularly the southwest rift, reflects changing interplay between the growth of this volcano and concurrent growth at differing rates of Mauna Kea, Hualalai, and Kilauea. Based on similar arguments, the

complexities in the rift structures of both the Waianae Volcano (e.g. *Zbinden and Sinton* [1988] infer that the south rift zone may have migrated over a broad area from west to east) and to a lesser extent the secondary rifts of the Koolau Volcano (the minor NE-SW dike complex) could also reflect changing interplay between these two volcanoes.

The majority of the Hawaiian and Icelandic dikes are nearly vertical and occur within swarms and rift zones, that are mostly narrower than 10 km and greater than 100 km long and contain hundreds to thousands of dikes [*Lipman, 1980; Walker, 1959, 1987; Gudmundsson, 1984*]. By comparison to other Hawaiian rifts, the main NW-SE rift zone of the Koolau Volcano (65 km), Mauna Loa's southwest rift zone (100 km), and along with the east rift zones of Kilauea and East Maui volcanoes, makes these the longest in Hawaii. For the Hawaiian lava shields, those dikes which strike parallel to the rift axis tend to dip at high angles toward the crest of the dome.

*Jackson [1968], Hill [1969], and Ryan [1987]* to explain the roughly cylindrical core of ultramafic cumulates inferred on the basis of seismic evidence within active and extinct Hawaiian volcanoes, suggested that as these volcanoes grow upward, their summit magma reservoirs must also rise progressively to higher levels. *Decker et al. [1983]* have geodetically confirmed this trend of upward reservoir growth, by demonstrating that Mauna Loa's magma reservoir is presently at a shallow elevation approximately the same level as the summit of its younger neighbor, Kilauea (i.e. the magma reservoir roof lies at  $\approx 2-3$  km depth below the 4,169 m summit of Manua Loa).

*Swanson et al. [1976]* infer that the shallow magma reservoir 2-5 km beneath Kilauea's summit caldera is an intricate plexus of dikes, sills, and irregular shaped chambers which are in a constant state of flux. As magma pressure exceeds the strength of the reservoir rocks, leakage from the system results in a shallow intrusion and usually in an eruption. According to *Swanson et al. [1976]*, displacement and seismic events on the south flank of Kilauea Volcano take place soon after intrusive activity, indicating that the displacement is the result of forceful intrusion in the rift zones. At Kilauea, virtually all

eruptions and shallow intrusions occur either in the summit area or along the two major rift zones. During rift eruptions the summit area subsides due to the migration of magma outward from the central reservoir into a rift zone. *Swanson et al.* [1976] indicates that during many east rift eruptions few earthquakes occur between the source reservoir and the vent site, suggesting a virtually unobstructed interconnecting conduit feeder system. Hence, the aseismic nature of these "slow leaks" into the ERZ suggests that they are not accompanied by the formation of new dikes [*Epp et al.*, 1983]. *Hoffman* [1988] modeled the ground deformation associated with the recent activity along Kilauea's East Rift Zone near Pu'u O'o vent (for phases 1-48, from 1983–1986). He suggests that the best fit for the ground deformation data and associated volume flux of erupted magma ( $1-10 \text{ m}^3 \text{ s}^{-1}$ ) is a single open feeder dike dipping at a high angle to the south and measuring 2 m wide by 3 km high and 2 km long (in the vicinity of Pu'u O'o) that connects with the main feeder system associated with the central magma reservoir beneath the Kilauea Caldera. He also indicates that seismic activity was confined to the early eruptive phases and that once the dike had established itself future seismic activity was very limited. *Swanson et al.* [1976] indicate that particularly during the initial magma injection stage of an eruption in which many shallow earthquakes commonly occur in the immediate vicinity of the eruption, that either the magma is forcibly wedging its way towards the surface along a new fissure or that it is clearing obstructions or closures in the previously formed one.

*Epp et al.* [1983] demonstrated that the amount of deflation of the summit reservoir during an eruption can be related to the elevation of the eruptive vents on the ERZ, and that there appears also to be a general relationship between volume of erupted lava and vent elevation. The rates of magma injection (volume flux) into the East Rift Zone (ERZ) are quite variable. They range from high volume fluxes of about 100 to  $1000 \text{ m}^3 \text{ s}^{-1}$ , that are commonly accompanied by shallow seismic swarms presumably related to the formation of new dikes, to low values of  $1-10 \text{ m}^3 \text{ s}^{-1}$ , that are largely aseismic and have been interpreted to suggest that continuous magma conduits exist in the mid to lower levels of the dike

complex [Epp *et al.*, 1983]. It appears that the most recent eruptions at Kupaianaha (i.e. the period July 1986–1988: represents continuous low flux) also follow this paradigm in which most of the eruptions were aseismic and of low volume flux [Hoffman, 1988; Wilson, 1988]. The initial eruptive style at Pu'u O'o during the period January 1983– July 1986 represented paroxysmal eruptions with high volume flux.

Shallow lateral dike intrusion is a valid mechanism of magma transport based on seismicity and other geophysical evidence of the active rift zones in both Hawaii and Iceland [Klein *et al.*, 1987; Walker, 1954]. At Kilauea and Mauna Loa geodetic and seismic data suggest that the upper part of the volcano expands elastically as magma rises from a deep source and inflates a summit reservoir system located approximately 2–7 km below the surface [Koyanagi *et al.*, 1976]. Recent studies [e.g., Lipman, 1980; Lockwood *et al.*, 1987; Hill and Zucca, 1987; Klein *et al.*, 1987; Dvorak and Okamura, 1987] infer that the rapid subsidence of the summit region overlying a shallow magma reservoir is associated with the lateral flow of magma for up to several tens of kilometers into adjacent rift zones. Figure 1.1 after Klein *et al.* [1987] shows that the assumed position of the magma reservoir below Kilauea caldera (dashed line) is marked by an aseismic region determined from the epicenter and hypocenter data of shallow earthquakes during 1970–1983. The upper part of the reservoir can be viewed as the fluid column whose top level fluctuates with changes in stored magma volume. Dikes propagate because the magmatic pressure is greater than the confining lithostatic pressure, thus causing the rock to fail or fracture ahead of the magma front or forcing precession fractures (e.g. cooling joints) or through-going rift-zone extension cracks to widen.

## NEUTRAL BUOYANCY AS A CONTROL ON DIKE EMPLACEMENT

Ryan [1987] defines the level of "*neutral buoyancy*" as the depth at which the *in situ* density of magma is in approximate mechanical equilibrium (at both the macroscopic and microscopic scale) with its surrounding host country rock. Therefore the horizon level

of neutral buoyancy, where the near vertical driving force is zero, is that depth interval within which the magma density is equal to the aggregate country rock density ( $\rho_{\text{magma}} = \rho_{\text{country rock}}$ ). Hence, neutral buoyancy imposes constraints on the geometry, location and fluid dynamics of dike emplacement. In *Ryan's* model, the zone of neutral buoyancy is expected to have a narrow vertical extent, and wide lateral extent, similar to that envisioned for a typical dike morphology (blade-like). Thus, a melt will rise vertically into an intrusive dike as long as the magma is in a state of *positive buoyancy* ( $\rho_{\text{melt}} < \rho_{\text{environment}}$ ). This rising magma will experience a continuous reduction in its buoyancy until either it is erupted at the surface as a lava flow or until it eventually stops rising and is intruded laterally at the point of *neutral buoyancy*. Above this horizon is the region of *negative buoyancy*, where a denser magma will flow downward under the influence of gravitational forces ( $\rho_{\text{melt}} > \rho_{\text{environment}}$ ).

At the magma reservoir margins, beneath the rift system axis, the horizon of neutral buoyancy is generally coincident with the peak in the available magma driving pressure. If a magma experiences a positive buoyancy, the available excess pressure can do the work of rock (hydraulic) fracturing at the propagating dike tip. In other words, if an eruption is initiated by an excess pressure at the magma reservoir the overlying rocks will fail when their tensile strength or shear strength is exceeded (i.e. active dike injection model).

According to *Wilson and Head* [1981] wall failure will occur if the pressure gradient exceeds the stress in the surrounding country rocks by a sufficient amount (i.e. the upper limit of pressure difference is ~200 bars at any depth). They contend that magma will not reach the surface through a fissure that is narrower than a certain width, and that this limit is determined by cooling effects or the presence of a yield strength in the magma. *Ryan* [1987] suggests that rupture of the magma reservoir by failure of the confining wall rock should be a recurring phenomenon at the same preferred depth. From seismic evidence at Kilauea Volcano, this depth level is inferred to be at about 3 km, beneath the caldera floor within the region of presumed neutral buoyancy. *Ryan* contends that along the level of

neutral buoyancy lateral dike propagation continues until the fluid pressure falls below that required to meet and exceed the *in situ* tensile strength of the host rock at the advancing magma fracture front. Similar reasoning has been used to infer that the most common dike injection mechanism is one favoring lateral rather than vertical magma injection [Rubin and Pollard, 1987], and that the volume-ratio of intrusives to lava flows may exceed 2:1 for Kilauea and at mid-ocean spreading ridges [Dzurisin *et al.*, 1984; Ellwood, 1978]. However, for deeply dissected shield volcanoes such as the Koolau, this ratio is only about 1:2 or 1:4 at the one kilometer erosional level. Knight and Walker [1988] contend that oblique magma flow directions may be even more important during the formation of the Koolau shield nearest to the volcanic center.

Based on seismic and geodetic evidence, Ryan [1987] recognizes three modes of neutral buoyancy-controlled dike formation.

- (i) Slow initial leakage with a gradually enlarging magma fracture front along the horizon of neutral buoyancy causes the dike top that rise progressively towards the surface, while the keel simultaneously descends.
- (ii) Abrupt initial magma leakage with a rapidly propagating dike tip under inferred positive and negative buoyancy forces quickly return magma parcels below and above the horizon of neutral buoyancy to positions of mechanical equilibrium.
- (iii) Harmonic oscillations of the top and bottom of the extending dike lens correspond to momentary buildup of inferred pressure differentials resulting in vertical expansions and contractions during magma injection.

This kind of dike necking (narrowing) related to large, intermittent magma pulses is dependent on *reservoir volume*, rates of *isostatic recovery of pressure* at the source, and *near-field inhomogeneities* in the stress environment (e.g. differential extensional shear failure at the dike tip due to dilatancy or contractancy of the country rock; Pollard, 1983; Ryan, 1987). These factors can result in constrictions of the magma flow velocity along the horizon of neutral buoyancy, thus resulting in a dike morphology

that resembles a knife blade with a doubly-serrated edge. *Ryan* [1987], *Hoffman* [1988], and *Wilson and Head* [1989] and others have inferred a similar harmonic dike structure formed during the initial stages of the January 1983–July 1986 Pu'u O'o eruptive sequence along the middle East Rift Zone of Kilauea Volcano. They model a single, continuous, open, 2–3 m wide dike that was directly connected to the reservoir structure beneath Kilauea Caldera, and was able to transfer magma batches to a still-molten region of the rift zone storage system via a small number of long, narrow discrete compartments (as many as five) and ultimately find its way to the surface at Pu'u O'o vent during very short repose periods of the order of several weeks to months. These models are a first attempt to describe the complexities of magma flow through intrusive bodies, suggesting that magma may not always rise upward away from their presumed source reservoirs. These complex flow mechanisms must be kept in mind when inferring magma flow azimuths in dikes based on magnetic fabric studies.

## KNOWLEDGE OF THE KOOLAU VOLCANO AND ITS DIKE COMPLEX

### CLIMATE

The subaerially exposed portion of the Koolau Volcano lies between 21°15'N and 21°45'N latitude and 157°35'W and 158°5'W longitude within the northeasterly tradewind belt. The present climate is tropical to subtropical with a mean annual temperature of 23.7°C in Honolulu, and is characterized by an annual average rainfall of as much as 5,100 mm on the upper slopes of the windward (northeast) flank of the Koolau Range falling to under 500 mm in the arid regions along the southwest (leeward) flank of the volcano. In general, there is an average decrease of approximately 2.2°C in mean temperature with each increase of 300 m in elevation [*Stearns and Vaksvik*, 1935]. Furthermore, the paleoclimate several million years ago may have been drastically different during the initial shield building stage as suggested by *Stearns* [1939]. Based on the number of tree molds found between basaltic flow units for both the Koolau and Kilauea volcanoes, *Walker* (personal

communication) suggests that a general lack of tree-molds in the Koolau lava seems to support the notion of a much more arid paleoclimate covering a much wider region for the early history of the Koolau Volcano (pre-Pleistocene). An alternative explanation for this lack of tree molds in the Koolau lavas could be a higher eruptive rate or increased mass-flux, thus inhibiting the development of large trees.

## PREVIOUS INVESTIGATIONS

The Koolau volcano forms the eastern two-thirds of Oahu, and is the erosional remnant of a deeply dissected large-volume tholeiitic lava-shield in an oceanic intraplate tectonic environment. Of the 107 volcanic shields forming the Hawaiian-Emperor chain, the Koolau is ranked twelfth overall in total volume [23,000 km<sup>3</sup>; *Bargar and Jackson, 1974*]. The shield remnant is an asymmetrical elongate dome extending northwest-southeast. In plan view the main ridge of the lava-shield has an elongate elliptical shape (slightly convex towards the Waianae volcano), in which its major northwest-southeast axis has a subaerial length of 57 km and parallels the main trend of the Hawaiian-Emperor Ridge. Based on bathymetric evidence the dimensions of the original subaerial edifice of the shield may have been nearly 70 km by 25 km. Following the shield-building stage there was a long period of erosion which developed more than 600 m of relief along the northeastern part of the Koolau Range (the windward side), in which the original topographic crest of the range was shifted towards the southwest [*Winchell, 1947; Walker, 1987*].

During the Wilkes Expedition *Dana* [1840] recognized the general volcanic structure of the Koolau Range as representing the erosional remnant of a volcano and he and later workers showed that the island of Oahu was formed by the coalescence of two overlapping and eroded large tholeiitic lava shields in which the younger Koolau volcano forms the eastern two-thirds and the older Waianae volcano forms the western third of the island (Figure 1.2). *Stearns* [1939] was first to describe the major rift zone of the Koolau shield,

giving it the name *dike complex*, and geologists began to understand how the rift zones and their feeder dikes were inter-related.

As pointed out by *Dana* [1889] the slopes of the southern, western, and northwestern sides of the Koolau shield remain intact but the northeastern (windward) slopes are cut by a 32 km long escarpment concave toward the northeast, referred to as the *Pali* cliffs (the Hawaiian word *Pali* means cliff or precipice). *Dutton* [1884] discussed the contrast between the windward and leeward slopes, concluding that more intense erosion on the rainier, windward slopes was the cause of the present morphology.

Two main co-linear rift zones in the Koolau volcano, having a NW-SE trend along the longitudinal axis of the shield and parallel to the Hawaiian chain, were mapped by *Stearns* [1939], *Takasaki et al.* [1969], *Takasaki and Mink* [1982], and *Walker* [1986, 1987]. A minor southwest rift zone also occurs [*Wentworth*, 1951; *Takasaki and Mink*, 1982; *Bigelow*, 198] (Figure 1.3). The subaerial length of the main rift zone is 57 km and its maximum width is 7 km [*Walker*, 1987]. Figure 1.4 after *Walker* [1987] is a histogram of the strike of 2554 dikes in which 70 percent of all measured dikes have strikes between 100° and 150°. For comparison, Figure 1.5 is an equal-area plot of the mean maximum  $\chi_1$  (AMS) directions of 62 Koolau dikes. This figure shows a slight bimodal distribution subparallel to the strike of the major and the minor rift axes (320° and 60° from east, respectively).

The net long-term effect of the many thousands of dike-induced dilations within the dike complex was a significant widening (at least 4 km) of the Koolau Volcano. According to *Moore* [1964] the volcano was also undergoing synchronous denudation by seaward movement on systems of normal faults and great landslides along the unbuttressed sides of the lava-shield. *Moore's* [1964] interpretation for the origin of the Pali cliff-line of the Koolau is based on topographic and bathymetric evidence, in which he envisions giant submarine landslide-collapse events that resulted in catastrophic seaward displacement of a major portion (20–30 km wide zone) of the northeastern coastline and exposing the

Figure 1.4 Histogram showing the trend of 2554 dikes from the Koolau dike complex (after *Walker*, 1987). Note that the majority of dikes (57%) have trends between 100–150°, showing the dominantly parallel trend for the dikes within the Koolau complex.

**Histogram of 2554 Dike Strikes**

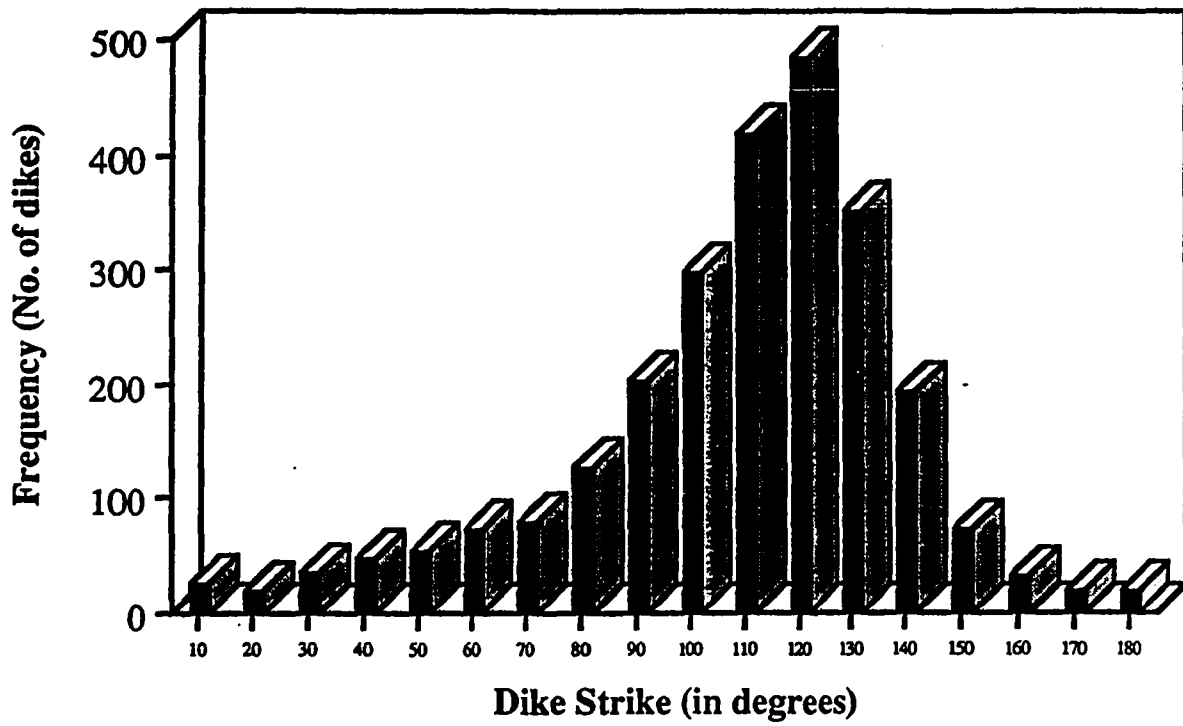
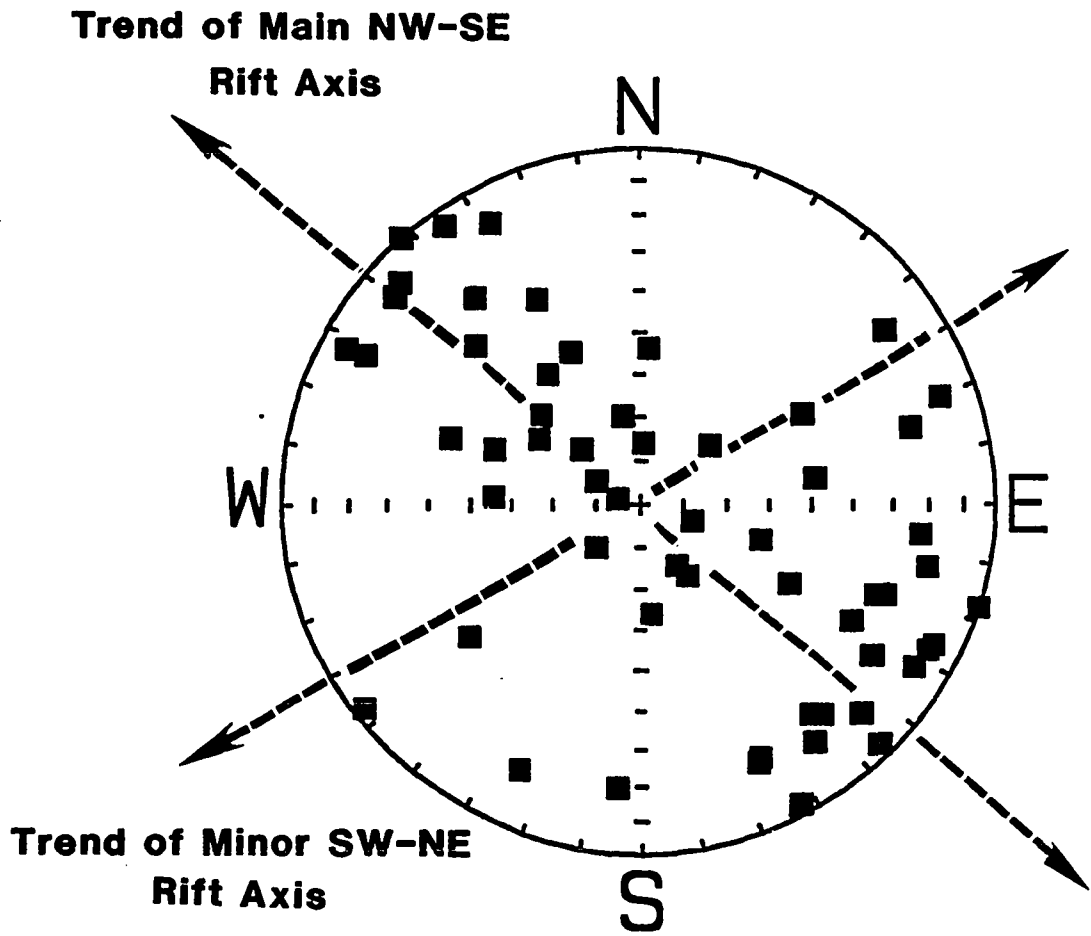


Figure 1.5 An equal-area plot of mean  $\chi_1$  axes for 62 Koolau dikes that show good to moderate clustering of the AMS directions. Note that the mean maximum  $\chi_1$  AMS direction closely approximates (within  $10^\circ$ ) the trend of the major NW- SE dike complexes. There is also a small percentage of the sampled dikes (8%), in which the mean maximum AMS directions plot at right angles to the main dike complex. The AMS fabrics of these dikes are thus in better agreement with the trend of the minor SW- NE dike complex.



**Plot of the Mean Maximum  $X_1$   
Susceptibility Directions of 62 Dikes**

underlying dike complex. *Moore's* [1964] "landslide" hypothesis seems to suggest that the Koolau must have had a mobile northeast flank analogous to Kilauea's mobile south flank.

*Moore* [1964] bases his landslide model mostly on bathymetric evidence, in which a large area of rough submarine topography (nearly 50 km wide by 150 km long) occurs off of the northeastern coast of Oahu. He also suggests that major submarine faulting (listric normal faults) would have caused large horizontal displacements of many tens of kilometers along the interface of the volcanic edifice and underlying oceanic crust.

The presumed apex and highest part of the shield rises 900 m with the summit at Konahuanui (3,105 ft) near the head of Nuuanu Valley. Based on detailed topographic and bathymetric maps, there is some evidence that the windward slopes of the Koolau shield may have extended 12-14 km northeast of the present summit.

The subaerial part of the Koolau volcano was formed almost entirely after the formation of the Waianae volcano in the western part of Oahu, but overlapped with the formation of the late-stage (2.4 Ma) alkalic cap of the Waianae. *Jackson and Wright* [1970] indicate that the total volume of the subaerial and submarine Koolau edifice is 45,000 km<sup>3</sup>, which is nearly twice the volume estimate by *Bargar and Jackson* [1974]. Using this larger volume estimate, and assuming that the eruption rates during the formation of the Koolau volcano were similar to historical eruption rates at Mauna Loa and Kilauea volcanoes, then the entire Koolau tholeiitic shield could have been constructed in only 0.8 m.y. [*Doell and Dalrymple*, 1973]. The very recent (mostly less than 0.3 m.y.) small-volume and highly alkalic rejuvenation-stage Honolulu Series formed long after the main shield building and caldera forming stages.

Radiometric (K-Ar) dating of the Koolau lavas indicates that volcanic activity occurred before 2.6 Ma to about 1.8 Ma, thus overlapping with the youngest dated Waianae activity at 2.4 Ma [*Doell and Dalrymple*, 1973]. *McDougall and Tarling* [1963] reported only reversed polarity rocks from eight sites from the Koolau, of which five gave K-Ar ages that

range from 2.2–2.5 Ma. Thus analyzed exposed lavas of the Koolau volcano were erupted entirely during the early Matuyama reversed polarity chron. In *Tarling's* [1965] study only one dike from the Koolau complex was measured for NRM, its initial direction was reversely magnetized, with a mean declination of  $173^\circ$  and inclination of  $5^\circ$ . After partial demagnetization in an alternating field to 150 Oersted (peak) this site gave a mean declination of  $180^\circ$  and an inclination of  $-17^\circ$  (i.e. reversed polarity direction).

The Koolau lavas comprise only tholeiitic basalt flows, about half of which are aa and half are pahoehoe [*Wentworth and Macdonald*, 1953]. These lava flows are virtually identical in texture, mineralogy, and composition to the intrusive dikes of the Koolau feeder system. Unlike the Waianae volcano, the Koolau did not enter the alkalic-cap stage; the abundant tuff cones, tuff rings and maar volcanoes and associated (silica-undersaturated) nephelinitic lavas of the rejuvenation-stage "*post-erosional*" lavas [*Stearns and Vaksvik*, 1935; *Wentworth and Jones*, 1940], apparently formed much later (1.5 m.y. after the Koolau volcano became inactive), probably over a time span from about 500 k.y. to less than 10 k.y.

The Koolau volcano gives a strong positive Bouguer gravity anomaly [*Strange et al.*, 1965], the axis of which coincides with the axis of the dike complex. The youngest feature and center of the Koolau volcano is identified as the Kailua Caldera (near the Kawainui Swamp; Figure 1.4), where there is good evidence for a caldera [*Walker*, 1987, 1988] and where the Bouguer anomaly reaches its maximum value of +310 mgal. Seismic refraction studies by *Adams and Furumoto* [1965] revealed the existence of rocks having a high seismic velocity ( $7.7 \text{ km s}^{-1}$ ), presumably representing major intrusions, at a shallow (1 km) depth below the caldera.

*Fiske and Jackson* [1972] postulated that dike propagation in Hawaiian volcanic edifices is determined by gravitational stresses and is influenced by the buttressing effect of adjacent volcanoes. According to this model, the dominant NW–SE orientation of the Koolau dike complex, and thus the overall shield morphology, was controlled by the pre-

existing topographic edifice of the older Waianae volcano. *Walker* [1986] postulated that the rock-density zonation established by formation of the dike complex guided the position of later-injected dikes. He pointed out that the complex has an intensity mostly of 50–65%, and suggested that, at this intensity, the bulk-rock density of the complex became equal to or greater than that of basaltic magma, so inhibiting further dike injection into it. Therefore, the initial dike propagation direction (perpendicular to the minimum remote stress field), and hence the overall morphology of the complex must evolve under the constraint of both the neutral buoyancy forces acting on the magma and the gravitationally induced stress field of the edifice.

The Koolau lavas are composed mainly of olivine- and hypersthene-bearing basalts, slightly more silicic than most Hawaiian basalts [*Winchell*, 1947] with locally a few interstratified pyroclastic deposits [*Walker*, 1987a]. The general dip of the lava flows outside the caldera complex is quite shallow, 3–6°, and mostly less than 10° away from the rift axis. In contrast, lavas dip much more steeply (up to 35°–50°) inside the Kailua caldera and are locally associated with massive caldera collapse breccias composed of lavas and dike rock [*Walker*, 1987a and 1987b]. *Walker* [1987a] suggests that these anomalously high-angle basalt flows within the Kailua Caldera are related to centripetal downsagging formed by many incremental subsidence events. He infers that where the great positive Bouguer anomaly is centered, below the Kawainui Swamp area inside the presumed Kailua Caldera, the dike injection rate could not keep pace with subsidence and collapse of the shield, hence the low intensity of observed dikes and the general lack of a well defined dike swarm at the center of the Koolau caldera.

## **KOOLAU DIKE MORPHOLOGY AND INTRUSIVE MAGMA FLOW**

Koolau dikes are commonly narrower than the basaltic dikes found in other volcanic provinces (e.g. British Tertiary Province, Deccan Traps, Iceland, and the Columbia River Plateau). This narrowness is thought to reflect the generally lower viscosity of Koolau

magmas, the closer proximity of the dikes to their volcanic centers or shallow source reservoirs, and the generally lower volume flux of individual eruptive events, particularly when compared to the exceptionally large volume and very thick individual flows (30–100 m) of the great flood basalt provinces. *Walker* [1987] and *Knight and Walker* [1988] find that the narrow (75 cm wide), near vertical ( $\geq 80^\circ$ ), dikes form proximal to the major eruptive centers. The less common circumferential, non-vertical, shallow-dipping ( $65^\circ$ – $75^\circ$ ) dikes form at or very near the major caldera margins (e.g. the Castle Junction and Keolu Hills dike swarms). The dikes at the margins of the major rift axes and outside the caldera centers (e.g. Mokulua Islands), particularly along the unbuttressed northeast side of the volcano, tend to be oriented parallel to the major rift axes and dip steeply ( $75^\circ$ – $85^\circ$ ) away from the rift axis, in agreement with the "bulk-density zonation" model of *Walker* [1987].

The two major rift zones extend northwest and southeast from the Kailua caldera. These major dike complexes are presumed to have formed at right angles (tangential) to the minimum stress direction, in which the unbuttressed side of the Koolau Volcano was decoupled from the pre-existing topographic edifice of the Waianae Volcano. Hence, the feeder dike system evolved in a neutrally buoyant gravitationally induced remote stress field in which dike propagation was parallel to the maximum stress direction and tangential to the Waianae Volcano. The general non-vertical nature of the dikes in this complex, and the non-horizontal orientation of their dilation vectors, implies that injection of the dikes resulted in considerable vertical movement; for every 1 km of horizontal extension in the Koolau complex there was 0.3 km of vertical displacement. The precise significance of this is not fully understood.

As already mentioned Koolau dikes, have a median width of less than 100 cm and are narrower than the basaltic dikes commonly found in many other volcanic areas such as Iceland [*Gudmundsson*, 1983]. Widths of the dikes that were sampled in this study for AMS vary from 17 to 408 cm, with a median value of 125 cm (this higher median width is

a result of sampling bias during this investigation). The widest dikes (>3 m) are most abundant at the farthest distances from the caldera complex, to the far north in the Koloa, Kaipapau, and Mokulua gulches some 18 to 22 km away from the Kailua center. The wider dikes, which are inferred to have formed at greater depth in the edifice, tend to be dense and commonly doleritic, except at or very near their chilled margins. Some are porphyritic and may grade to picrite (with >30% modal olivine) in the central best-crystallized portions. They range from highly vesicular centers to completely nonvesicular, and are commonly cut by prismatic cooling joints oriented perpendicular to the margins. The thinner dikes commonly have irregular surface morphology; they have many small offshoots, are aphyric, flow-banded, and vesicular, and locally contain pipe vesicles/amygdales infilled with zeolites and other secondary minerals near their margins. These narrow dikes commonly have a less conspicuous (finer scale) jointed structure or lack prismatic jointing. Some dikes contain discrete layers of coarser-grained crystals or vesicles that form parallel to the dike margins, and are referred to as crystal or vesicle segregation layers (refer to the subsequent chapter on Grain Orientations and Vesicle Distributions). *Wentworth and Jones [1940]* and *Walker [1987]* suggest that the occurrence of vesicles and banding in intrusive bodies occurs only at very shallow depths less than several hundred meters. Excentric vesicularity banding and crystal segregation zones are also prominent features displayed by some filled lava tubes (e.g. KT38) which to some degree must be considered as intrusive.

Three zones of systematic layering can be identified in most well-developed dikes: a *central zone* of finely crystalline rock (feldspar or olivine phyric), comprising most of the thickness of the medium and wide dikes; this zone locally grading into massive coarse grained picritic centers in some of the widest dikes (e.g., dike KD39); a *glassy selvage* (commonly this selvage is altered to an oxidized rust-brown color) that is usually several millimeters thick on each of the margins; and a *subselvage* inside the glassy selvage on each margin usually composed of multiple coloration bands parallel to the margins. The

subselvage is commonly several centimeters to a decimeter wide and is the least constant of the zones. These zones appear to be wholly related to the history of cooling and crystallization, and the processes of magma flow differentiation. There is little evidence that such banding is related to successive intrusion of varying liquids, though multiple dikes are known.

Jointing in the Koolau dikes and sills can be described as occurring in a trifold dimensional array: ideally the primary joint sets consist of large polygonal prisms with individual prisms up to 100 cm across and oriented orthogonal to the margins. Only a few of the columns are hexagonal, and many are five sided to irregular in form. Jointing of the subselvage is similar and grades into that of the central zone, except that the polygons are smaller size (often 2–10 cm wide); jointing of the glassy selvage is still closer (typically 0.5 cm across). The polygonal joints that cut the central part of the dike are the most prominent in the selvage and subselvage [*Wentworth and Jones, 1940*].

Dominantly upward dike propagation can occur if magmas are significantly vesiculated and hence strongly buoyant. The seismic and geodetic record [*Klein et al., 1987; Dvorak et al., 1986*] of Kilauea shows that at least 50 percent of the magma excursions from the chamber give rise to surface eruptions, thereby promoting upward rather than horizontal growth.

The maximum length of individual dikes is difficult to establish because: (1) most good exposures occur along short roadcuts that are generally not parallel with the dike strike; (2) areas where the dike outcrops extend across country tend to lie in the heavily forested river valleys where access is difficult, and are interrupted by alluvium; and (3) younger basalt flows tend to mantle the ridges between deeply dissected stream valleys not permitting continuous correlation of the dike outcrops between valleys. However, in the outer reaches of the rift axis away from eruptive centers where the dike intensity is lowest (dropping off to less than 10-15% per 100 meters of outcrop) and individual dikes tend to be much wider (>300 cm) than the median width of 53 cm [*Walker, 1987*] the dikes tend to cluster in sets

of five or less, and the widest dikes can possibly be traced to adjacent stream valleys. For example, some 35–50 km northwest of the main eruptive centers of the Koolau dome two such dike sets, one in the Maakua Gulch and the other in the Koloa Gulch, occur nearly three kilometers apart. Based on several lines of evidence, these dike sets have been inferred to represent discontinuous segments of the same dikes. Thus, the widest dike in each set is 315–365 cm and is adjacent to a narrow one 110–145 cm wide; these dikes have similar morphology; and the maximum AMS directions, particularly for the narrower dikes (KD65 and KD69) have very similar flow azimuths which plunge shallowly (26° and 17°, respectively) to the northwest away from their presumed source. If this correlation is valid then at least some of the Koolau dikes, particularly those farthest from their source, may be continuous for tens of kilometers.

*Baer and Reches* [1987] studied the surface features of many dike segments to deduce flow patterns of magma in dikes from Makhtesh Ramon, Israel, and found that, in general, magma flow was neither vertical nor horizontal but was at low oblique angles. They pointed out that corrugated dike walls are common when well-stratified host rocks cause magma channelization. However this kind of surface occurs when the dike cuts through well-bedded sediments, and such corrugations are not good indicators of flow direction. Alignment of elongated bumps and ridges (fingers) on the irregular surfaces of some dikes also give a sense of flow direction [*Pollard et al.*, 1975; *Baer and Reches*, 1987]. Host rocks composed of alternating successions of relatively dense flow interiors and porous, clinkery, flow tops (aa-type flow units) constitute a primary source of mechanical anisotropy within the Koolau volcanic shield, and may provide the tool for the formation of grooves observed on many of the dike walls. Flow banding marked by a streaky coloration occurs in the outermost few centimeters of the dikes, as well as in the interiors of some, and is easily seen in some dike cross-sections and sample cores. The coloration bands are sometimes stretched out to produce a lineation. Slickenside-like grooves are occasionally seen on a sheet joint a few centimeters inside and parallel to the dike margin,

but they may not always be related to primary magma flow. For example, they may be formed by post-depositional tectonic deformation. A few dikes display imbricated sheet joints (in a zone 10–20 cm wide) along their margins and this imbrication seems to indicate the flow azimuth. Pipe vesicles occur in the marginal parts of a few dikes and may also indicate the flow azimuth. Occasionally spindle-shaped vesicles elongated in the flow direction are also found in the dike margins (refer to subsequent section on "Objectives and techniques used...").

Surface lineations are quite common on the Koolau dikes but were measured on fewer than 10% of the dikes examined because they are seen only where a sufficiently broad dike surface is bared and is not so weathered that the outer few millimeters have been stripped off [Walker, 1987]. The plunge direction of the lineations used in this study and compared with the AMS magnetic fabric are therefore based on averages of at least three measurements along the dike margin.

Most surface lineations plunge toward Kailua (or to the Kawainui Swamp area southwest of Kailua), but the lineations of a number of older dikes (inferred from crosscutting features) plunge toward a second center under Kaneohe Bay (refer to Figure 41.14; Walker, 1987). These two centers were interpreted by Walker [1987] to be source regions of the dike complex, at a depth of about 1.5 or 2 km below present sea level.

A limited comparative study of the dike swarm in the Kolekole Pass roadcuts in the central caldera area of the Waianae Volcano, following the recent broad survey by Zbinden and Sinton, 1988], reveals many differences between them and the Koolau dikes. The Waianae dikes have a much more variable chemical composition [Zbinden and Sinton, 1988], were evidently intruded at a higher elevation within the edifice (based on their irregular morphology and abundant vesicle segregation zones, in which many dikes contain pipe vesicles), and are narrower (48 cm median width compared to 65 cm for the Koolau dikes). They also have a more nearly radial distribution, a generally lower dip angle (commonly  $<70^\circ$ ), and a generally steeper dilation vector (direction of opening; commonly

plunging >30°). Older dikes in the Waianae swarm tend to be more steeply dipping and are often cut by more shallow dipping ones. The central Waianae complex presumably formed in a dominantly radial stress field following and/or contemporaneous with the formation of intra-caldera breccias.

## OBJECTIVES AND TECHNIQUES USED IN THE PRESENT STUDY OF THE KOOLAU COMPLEX

Mapping out the flow trajectory of intrusive bodies can be extremely useful for inferring the depth and emplacement mechanism of otherwise inaccessible magma source reservoirs. Also, by incorporating the spatial and temporal relationships of the dike emplacement within deeply dissected shield volcanoes it should be possible to constrain the dynamics and mechanics of magma transport within the dikes as they enter the rift zones, and the kinematic evolution of the storage system(s) associated with these volcanoes. A number of different methods can be used to infer magma flow directions through basaltic dikes (e.g., surface lineations, fracture propagation patterns, echelon offset patterns, flow banding structures, groove molds and elongate finger terminations, microscopic crystal orientations, orientation of spindle, or pipe-shaped vesicles, etc.)

### MACROSCOPIC SURFACE LINEATIONS

*Surface lineations* and elongate vesicles were apparently first employed to determine magma flow directions by *Harker* [1904] and more recently by *Walker and Leedal* [1956], *Ui et al.* [1984], *Gartner and Delaney* [1985], *Shelley* [1985], and *Baer and Reches* [1987]. As part of an extensive study of the deeply-eroded dike complex of the Koolau volcano on Oahu, *Walker* [1987] mapped macroscopic surface lineations on over 100 dikes and found that they plunge toward two areas several kilometers apart, one of which occurs below Kaneohe Bay and the other below Kawainui Swamp in the center of the Koolau

caldera. He inferred that magma rose obliquely toward the surface from shallow magma sources situated in these two areas [Walker, 1987, p. 974, Figure 41.14]. The study of magma-flow direction using macroscopic surface lineations has several shortcomings: (1) not all dikes show lineations; (2) many outcrops, particularly those in road cuts, are unfavorable for revealing the lineations; (3) the lineations give the sense of direction (Figures 1.6a and 1.7), but not the azimuth of flow (i.e., the absolute flow direction); (4) surface lineations on dike margins record the movement only of the initial magma pulse, which may differ from the movement of the main magma body; (5) surface lineations may vary as much as 50° in short distances along the same dike margin (Figure 1.6b), and many measurements must be made to give an average flow direction; and (6) the flow lineations can be confused with slickenside-like grooves carved mechanically on the margins of some dikes subsequent to magma intrusion, possibly related to tectonic subsidence (Figure 1.8a and b).

## LATERAL FRACTURES

*Lateral fracture propagation patterns* based on field relationships between dikes and joint sets (as well as the distribution pattern of microfaults and brecciation zones), and *en echelon offset patterns* have been used to infer the horizontal dike propagation directions (Figures 1.9a and b), the near-field principal paleostress pattern [Stevens, 1911; Nakamura, 1977; Zoback and Zoback, 1980; Gartner and Delaney, 1985], and emplacement patterns of the presumed shallow near-surface feeder systems [Delaney and Pollard, 1981; Tsunakawa, 1983; Delaney et al., 1986; Rubin and Pollard, 1987]. *Tension cracks* develop under a high deviatoric stress field in which crack propagation is parallel to the principal compressive stress  $\sigma_1$ . However, a major problem with such an interpretation based solely on the lateral fracture pattern, is distinguishing whether or not the magma has passively invaded along older fractures to form dikes [Billings, 1972; Currie and Ferguson, 1970; Wilson, 1970] or whether the excess magma pressure has

Figure 1.6(a) Photograph of a chilled margin of a dike from Mokolua Island showing macroscopic surface lineations (MSL). These MSL's are thought to represent the initial magma flow direction (or dike injection direction), here shown to plunge at  $35^{\circ}$ – $40^{\circ}$  toward the Kailua caldera. They consist of millimeter-high wrinkles projecting out from the glassy surfaces or from planes within the glassy selvage of the dike margins. It is believed that they form from mechanical interaction of the intruding lava with its host rock (scale is 15 cm).

(b) Photograph of bumps and ridges (fingers) making up the irregular dike surfaces (margins); note that the plunge direction of the macroscopic surface lineations diverge and curve to accommodate the irregularities in the chilled margin and can vary by as much as  $50^{\circ}$  over very short distances. Therefore many measurements over a large lateral extent of the dike's margin must be averaged to determine the initial magma flow direction (scale is 15 cm).

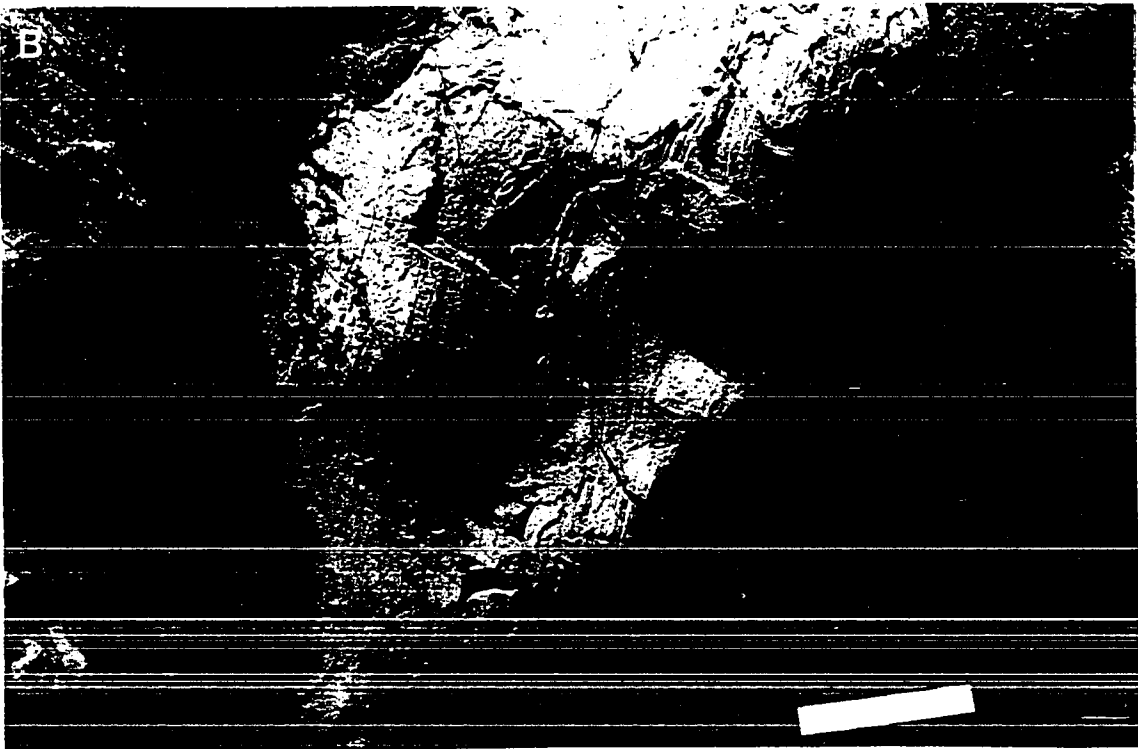
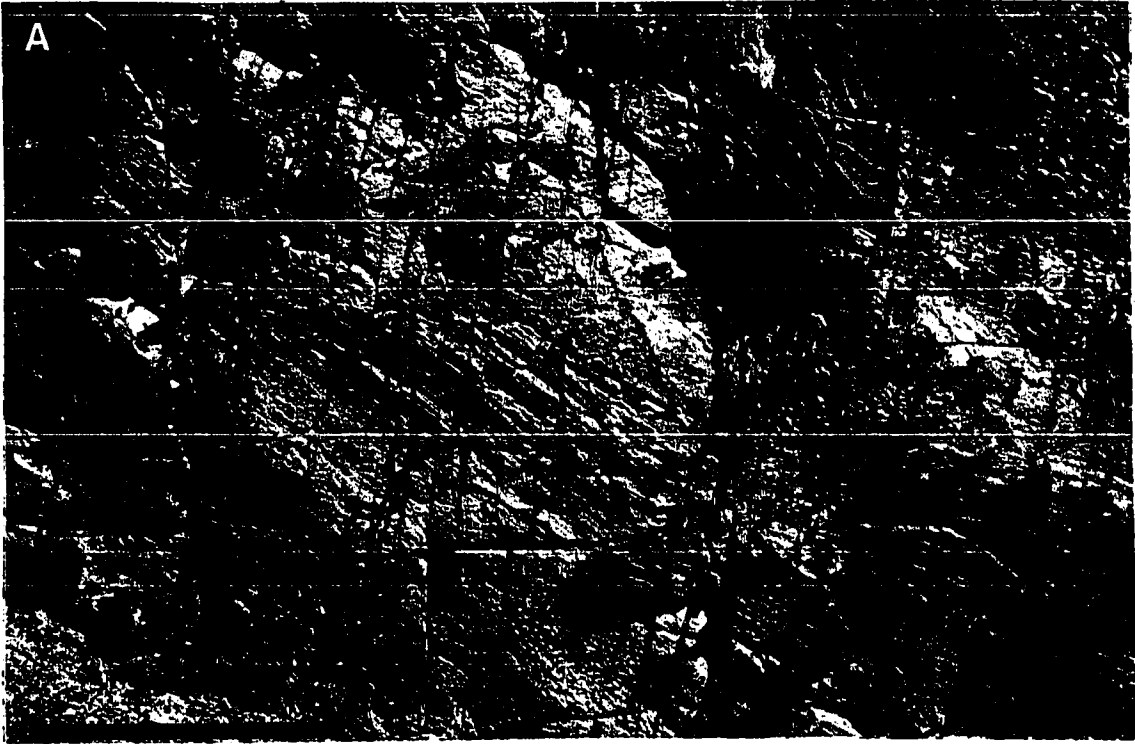


Figure 1.7 Rose diagram of the macroscopic surface lineation (MSL) plunge direction for 38 Koolau dikes; dips are projected along the main NW-SE trend of the dike complex. Note that there are three main groupings of the MSL: (1) the majority of the dikes have shallow (0–40°) oblique plunge directions towards the southeast; (2) a second group with steep (50–70°) oblique plunge directions towards the southeast; (3) and another with shallow (0–50°) oblique plunge towards the northwest.

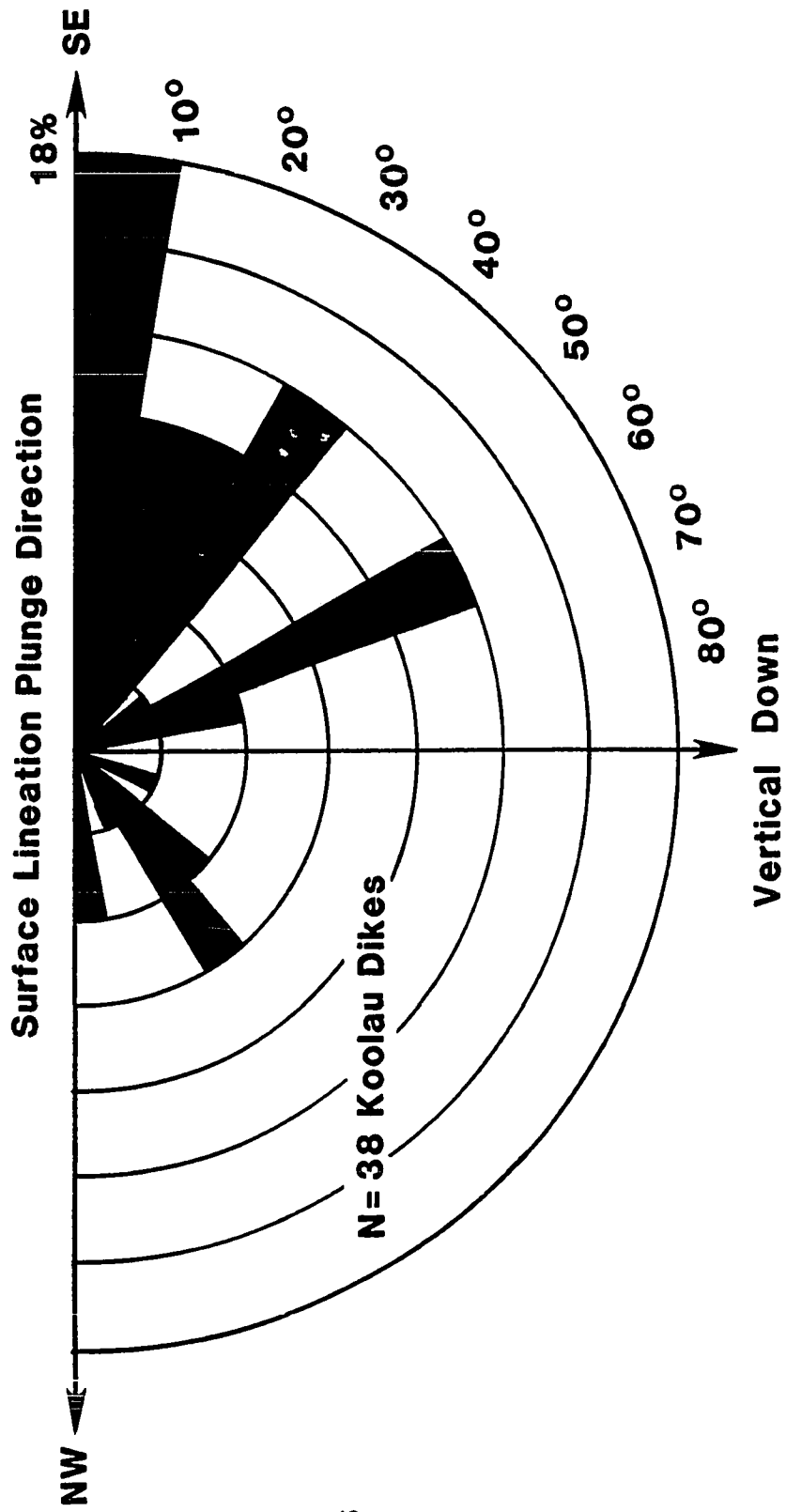


Figure 1.8(a) Photograph of slickenside-like grooves on the margin of a dike from Mokolua Island (note geologic rock hammer for scale). The very shallow plunge direction of the grooves (NW) is towards the Kailua caldera, and may support the notion that these structures are related to dike injection and not related to post-emplacement tectonism, since faulting in this area is suggested to be high-angle normal faulting [Moore, 1964].

(b) Photograph of similar groove-like structures along the oxidized chilled-margin of a dike from Keolu Hills. Their interpretation as a primary magma flow indicator is somewhat dubious, in that their form is accentuated (or overprinted) by a fine-scale jointing and weathering of the chilled-margin (scale equals 20 cm).

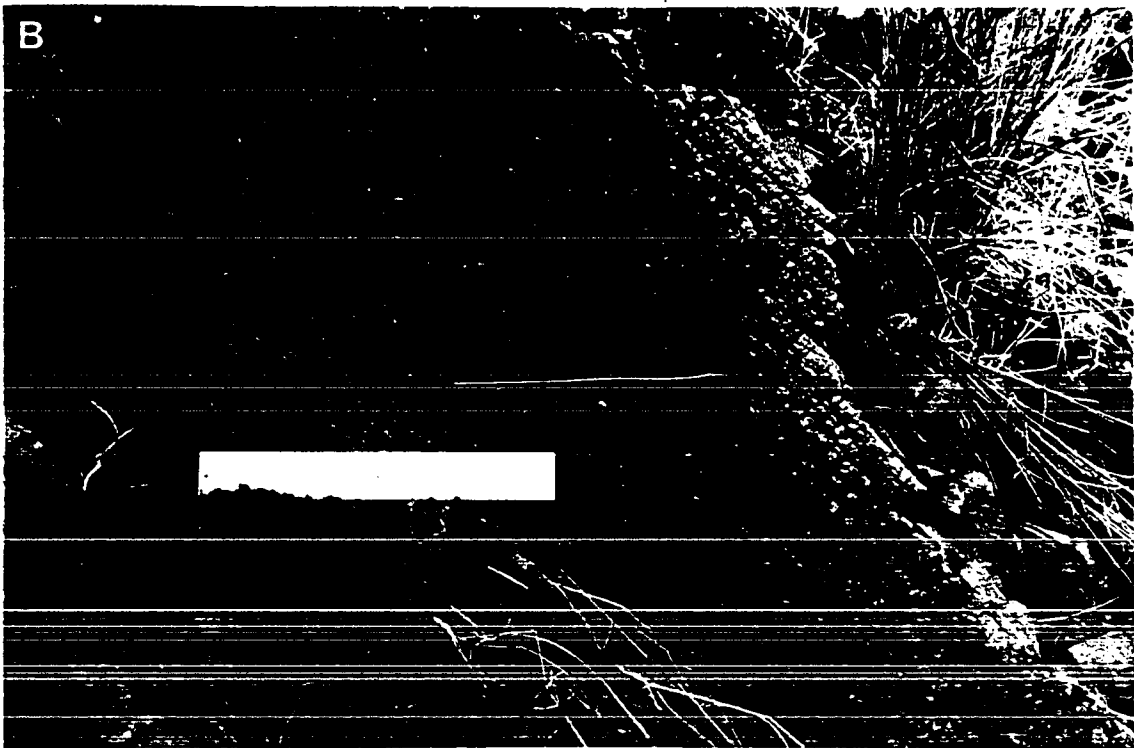
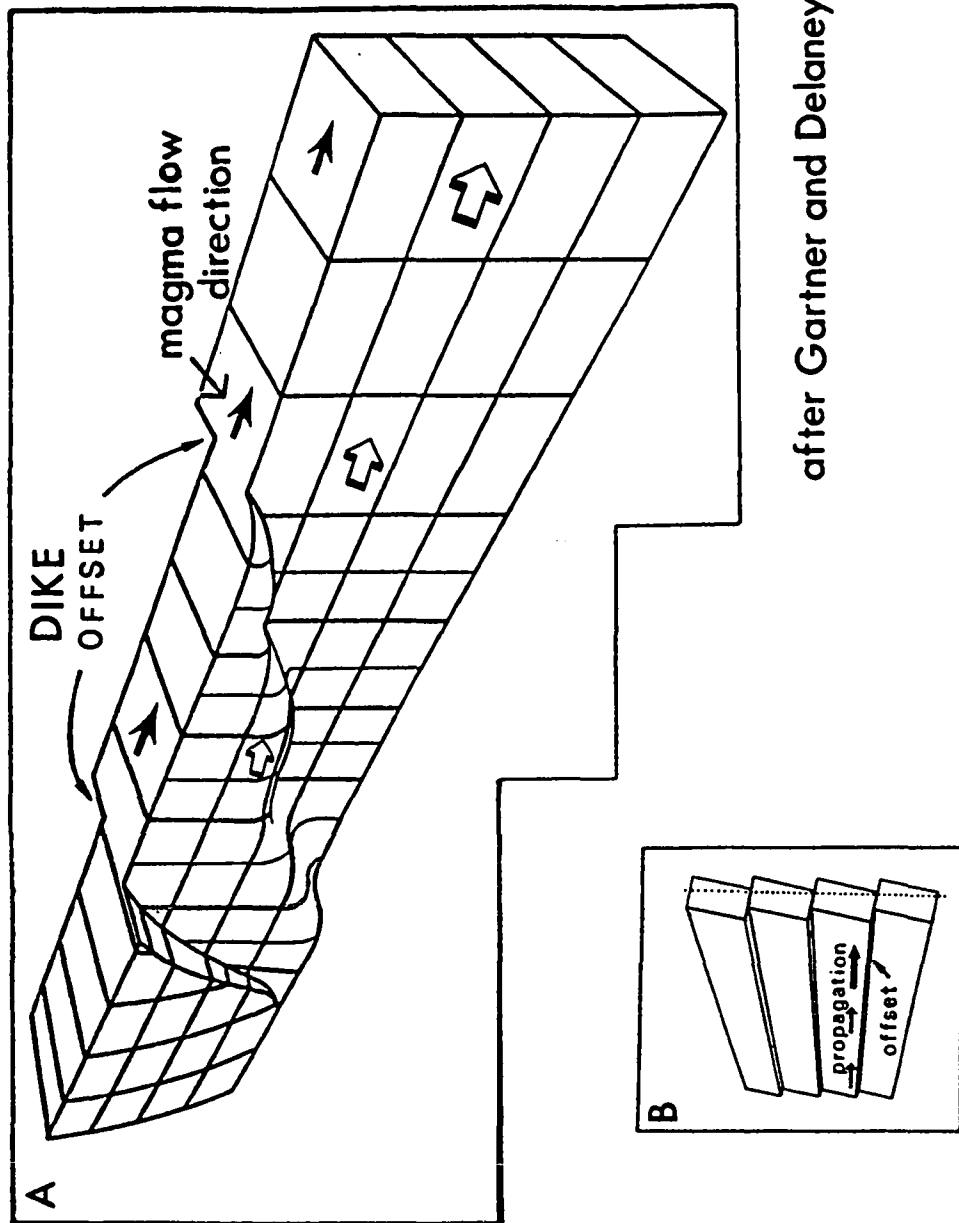


Figure 1.9 Is a schematic drawing (after *Gartner and Delaney*, 1986) of an echelon dike offsets or steps observed in the San Rafael diabasic dike swarm exposed near the northwestern margin of the Colorado Plateau. *Gartner and Delaney* [1986] indicate that these offsets are a measure of the local direction of fracture propagation.



after Gartner and Delaney, 1985

forcibly generated new tension cracks beyond the dike tip in which magma could then invade [Anderson, 1938, 1951]. *Delaney et al.* [1986] suggest that where dike-parallel adjacent joints and regional joints are both present, particular care should be exercised in inferring dike emplacement mechanisms. They also indicate that it is important to determine if the joints are stratigraphically or geographically continuous throughout the region where dikes are present; if the local joints are discontinuous, the magma could not have invaded the entire region along them, and thus the dike is a good indicator of stress direction, at least in those strata that lack local joints.

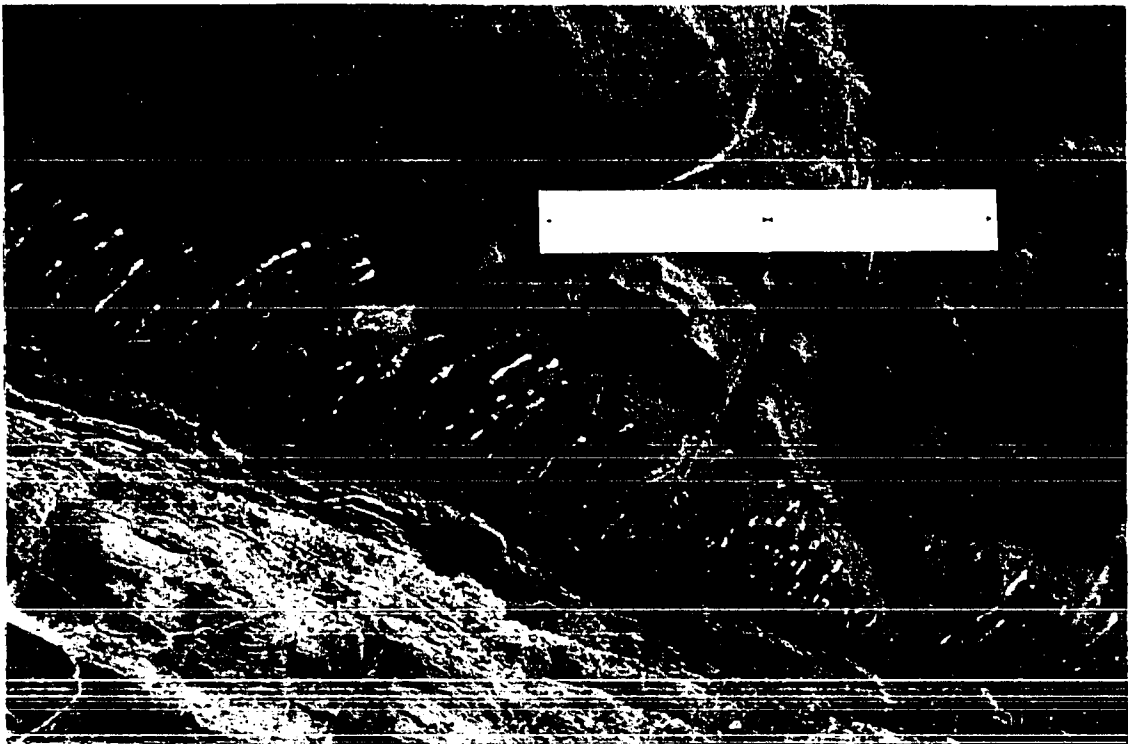
Somewhat different in their mode of formation are imbricated sheet-joints which form along the margins of some dikes (Figure 1.10a). The imbrication angle is thought to give the absolute flow direction during initial dike injection. The mode of formation of these sheet-joints could be related to internal shearing during a more mature stage in the dike's cooling history, in which an already nearly completely solidified dike is forcibly reactivated along its (thermally weakened) center due to increased or renewed magma supply. At any rate marginal imbricated sheet-joints are very likely reliable recorders of the overall magma flow direction in these dikes.

## **RADIAL FRACTURES**

*Radial hydraulic fractures* develop when the pressurized magma is forcefully injected into the discontinuities of the country rock. This type of fracturing will form only when the magma pressure is higher than the combined magnitude of the tangential component of the least compressive stress ( $\sigma_3$ ) and the tensile strength of the rock *Chevallier and Verwoerd* [1988]. Radial fractures and radial dike propagation are most common in the isolated non-interactive cones and shield volcanoes (e.g. Spanish Peaks [Ode, 1957; Muller, 1986], Kauai Volcano), but can also easily form within the central cone or caldera (e.g. Caldera de Taburiente, La Palma [Staudigel et al., 1986], and the central calderas of the Waianae [Zbinden and Sinton, 1988] and Koolau volcanoes).

Figure 1.10 (a) Imbricated sheet joints are occasionally seen along the margins of some dikes; in this example they suggest dike injection was from left to right. The direction of imbrication for this dike sampled near Makapuu Head at the distal end of the southeast rift of the Koolau Volcano agrees quite well with the flow direction inferred from its AMS fabric (note, holes are sampling sites for paleomagnetic measurements; they are 2.5 cm in diameter).

(b) Zeolite filled pipe-vesicles (up to 10 cm long) bent in the direction of magma flow are occasionally seen along the margins of some dikes. The inferred magma flow direction for this dike was from left to right. This photo is of a dike from the southern Mokolua Island, about one kilometer offshore from Kailua (scale = 20 cm).



## CONE FRACTURES

*Cone fractures* or *cone sheets* are suggested to form as a result of uplifting of the roof of the magma chamber in the central part of the volcano [Anderson, 1936; Phillips, 1974]. Cone fractures represent shear planes along a zone of weakness as shown by Robson and Barr [1964]. Macdonald and Abbott [1979] specify two areas in Hawaii where low-angle dikes are common. These are near the junction of the Koolau caldera with the northwest rift zone in the vicinity of Castle Junction, on Oahu (refer to Figure 2, page 4217; Ryan [1988]), and around the periphery of the main Kauai shield volcano, found principally along the Napali Coast. In both, the low-angle dikes dip toward the center of the caldera. However, at least for the Koolau volcano, based on their irregular morphology, vesicularity, and narrow widths, these dikes are thought to represent relatively shallow levels of dike intrusion associated with caldera collapse episodes [Ryan, 1988], and are not cone sheets generated by major conical fracture episodes during uplifting by the central magma body.

## MAGMA FLOW STRUCTURES

*Flow banding structures* (streaky coloration bands) often occur in the outermost few centimeters of the dike, as well as in the interiors of some, and are easily seen in some dike cross sections. These coloration bands are sometimes stretched out to produce a lineation, and when exposed in three-dimensions can give clues to the sense of magma flow direction, although the magma flow azimuth cannot be determined. Alignment of *groove molds* on host walls that form parallel to and between elongated bumps and ridges (*fingers*) on the margins of some dikes are oriented parallel to the local direction of dike propagation (attributed to host rock inhomogeneity) and are inferred to indicate the initial magma flow direction (Figure 1.6b) [Pollard et al., 1975; Gartner and Delaney, 1985]. However, the magma flow direction subsequent to finger coalescence and formation of dike offsets may not necessarily be parallel to the main flow direction.

Furthermore, these small-scale flow indicators have been noted to have abrupt changes over short distances [Gartner and Delaney, 1985; Baer and Reches, 1987]. Some dikes are characterized by offsets and small dikelets (*horns*) along their margins which also indicate the dike propagation direction [Pollard et al., 1975]. Since these flow indicators are preserved only along the interfaces between the dike and its country rock, good exposures of large portions of well preserved dike walls (not too highly fractured and jointed so as to make interpretation of the structures incomprehensible) and/or adjacent country rock are required for averaging the inferred initial magma flow directions.

### CRYSTAL AND VESICLE ORIENTATIONS

*Crystal and grain orientations* based on elongated grains within the groundmass fabric (with aspect-ratios of  $\geq 1:2$ ) that are subparallel to the dike walls probably indicate the flow direction, and their sense of obliquity (imbrication) relative to each dike wall provides a unique determination of the absolute magma flow azimuth [Roberts and Sanderson, 1971; Smith, 1978; Shelley, 1985]. *Pipe vesicles* occur in the marginal parts as well as the centers of a few dikes and are elongated in the flow direction (Figure 1.10b). The best examples of pipe vesicles in Oahu are found along the shore of the Mokolua Islands, Koolau volcano, and within the central caldera of the Waianae volcano near Kolekole Pass. *Spindle shaped, strongly elongated, vesicles* also occur in some dikes and can be used in the same way as crystals.

### MAGNETIC FABRIC OF DIKES

One method that has great potential for resolving the magma flow direction through intrusive bodies, and therefore diagnosing the possible location of the source reservoir, is the anisotropy of magnetic susceptibility (AMS) technique. This technique can be used to define the magnetic fabric and hence the petrofabric formed by the mechanics of motion and suspension of dispersed magnetic (titanomagnetite) minerals oriented prior to solidification of the silicate fluids in igneous bodies (e.g. dikes, sills, lava flows, ignimbrites, and filled

lava tubes), which in turn can be correlated with their associated surface structures. This method can give important constraints on the rheology, flow velocity, and flow regime, and most importantly for present purposes can indicate the absolute magma flow directions.

I applied the AMS technique to study the magnetic fabric in 71 dikes, one sill, and two infilled lava tubes of the Koolau volcano to investigate its possible usefulness as a method of studying magma flow direction (refer to Locality Map; Plate I). I also applied this technique to a nephelinitic dike and associated aa lava flow from the Koko Crater rift system on Oahu (from the Honolulu Volcanics), and to four tholeiitic lava flows from Kilauea Volcano and Mauna Loa Volcano, Hawaii.

The AMS technique was first applied to lava flows and dikes by *Khan* [1962], with somewhat ambiguous results. *Stacey* [1960a] used the AMS method to determine the magnetic fabric of a Tasmanian dolerite sill and more recently this technique was employed to determine the flow direction in basalts (both extrusive and intrusive) by *Ellwood* [1975, 1978] and *Ellwood and Fisk* [1977]. *Ellwood* [1982] also used the AMS method to relate magnetofabric flow lineations of pyroclastic flow deposits (ignimbrites) with their known source vents in the central San Juan Mountains. *Knight et al.* [1986] determined the flow direction for three separate cooling units of the Toba Tuff in north central Sumatra, and *Incoronato et al.* [1983] used a similar method to determine the flow direction of base surge deposits from the Phlegrean Fields in Italy.

The AMS measurements refer to the variation of magnetic susceptibility with direction in a material and can be expressed by defining three principal orthogonal axes of the maximum, intermediate, and minimum susceptibility; hence the magnitudes and azimuths of these principal axes define the orientation of the magnetic fabric or petrofabric of the sample. Furthermore, if it is correct to assume that under laminar flow conditions the elongate magnetic grains will preferentially align parallel to the flow direction, then the

AMS technique can be used to infer magma flow directions based on the magnetic lineation direction in igneous rocks.

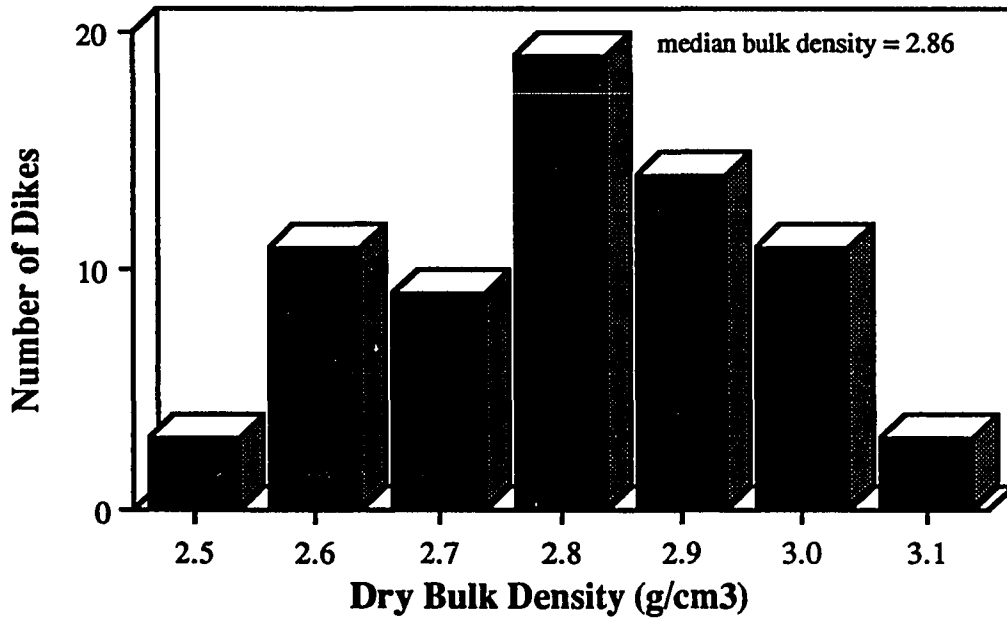
AMS develops either from anisotropy within the crystal lattice of magnetic minerals (i.e., *magnetocrystalline anisotropy*) or from the non-equant shape of individual mineral particles (i.e. *shape anisotropy*). In low magnetic fields, magnetocrystalline anisotropy is not observed in cubic minerals, and because titanomagnetite is the dominant magnetic carrier in the Koolau dikes, shape rather than crystalline anisotropy should have the most important effect on the AMS fabric. Most rocks contain grains with irregular shapes, and therefore the most important effect for AMS is related to shape anisotropy and results from the inequality of the demagnetizing factors in three mutually perpendicular directions across a non-equidimensional grain.

## DENSITY OF KOOLAU DIKES

Densities were determined from cylindrical core specimens that showed the least alteration or fracturing, and generally lacked open vesicles. The average bulk density at each site is thought to represent a minimum value, since many of the specimens show variable degrees of secondary chemical alteration (oxidation, chloritization, or hydrothermal alteration), and some specimens contain abundant amygdaloidal zeolites which tend to alter (raise) the original bulk density. The average bulk density determined for 70 dikes from the Koolau complex is  $2.86 \text{ g cm}^{-3}$  and ranges from  $2.54$  to  $3.17 \text{ g cm}^{-3}$  (Figure 1.11). Two-thirds of the measured dikes have densities  $\geq 2.80 \text{ g cm}^{-3}$  which is in good agreement with the  $2.9 \text{ g cm}^{-3}$  estimate by *Hill and Zucca* [1987] for inferred intrusives at 1–3 km depth below Kilauea Volcano. The densest dike (KD60;  $\rho = 3.17 \text{ g cm}^{-3}$ ) is a fresh aphyric rock from Mokolii Island (Chinaman's Hat), and the least dense dike (KD56;  $\rho = 2.54 \text{ g cm}^{-3}$ ) is from Haipuu, near Molii Pond and is one of only two dikes that are highly vesiculated, brecciated, and normally magnetized. In general, low density dikes tend to be more vesicular and/or chloritized, and the denser ones tend to be more porphyritic and

**Figure 1.11 Histogram of the average dry-rock bulk density of 70 sites in the Koolau Dike Complex. The mean bulk density is 2.86 g cm<sup>-3</sup>, and ranges from 2.54 to 3.17 g cm<sup>-3</sup>.**

**Histogram of Bulk Density for 70 Koolau Dikes**



contain abundant coarse-grained olivine phenocrysts. These relationships are discussed in greater detail in Chapter 3.

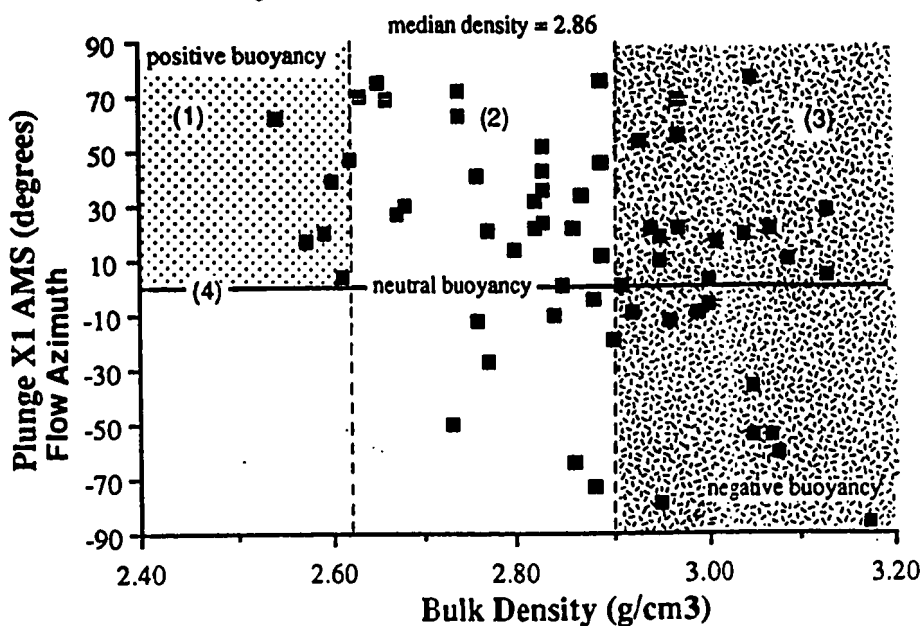
Figure 1.12 is a plot of the dike bulk density versus the plunge direction of the inferred magma flow azimuth for 62 dikes (maximum AMS axis plunge direction is positive for upward directed flow and negative for downward directed flow azimuths, refer to Chapter 3). Three density fields and a line of neutral buoyancy are shown in this figure. *Field "1"* represents the flanks of Hawaiian basaltic shields, which may have densities ranging from  $\rho = 2.40\text{--}2.62 \text{ g/cm}^3$ , note that only six dikes fall in this region, all exhibiting upward directed flow azimuths. The lower limit of this field represents the densities of volcanic and marine sediments, or pyroclastic tuffs, while the upper limit represents the average density of summit-differentiated olivine tholeiite basalt [Ryan, 1988; Dieterich, 1988]. *Field "2"* representing a slightly higher density level of the shield, in which vesiculated basaltic lava flows, and nonvesiculated flows and dikes range from  $\rho = 2.62\text{--}2.90 \text{ g/cm}^3$ . More than half of the intrusive dikes fall in field "2". *Field "3"* represents the highest density zone ( $\rho \geq 2.9 \text{ g/cm}^3$ ) at the deepest erosional level of the dike complex where dike intensities are greatest. Dikes which fall in this field are mainly nonvesicular and the least weathered or altered. Ten out of 26 dikes (38%) that fall within field "3" have downward plunging  $\chi_1$  directions, and nearly half of these tend to be located 10-22 km from the Kailua center (refer to Chapter 3). The level of neutral buoyancy labeled "4" in Figure 1.12 is here suggested to be a region of horizontal magma flow within the dikes, i.e. to satisfy this category dike injection must be neither positively or negatively buoyant.

#### NATURAL REMANENT MAGNETIZATION DIRECTION OF KOOLAU DIKES

The natural remanent magnetization (NRM) direction of 71 sites from the Koolau dike complex is presented in order: (1) to assess the magnetic stability of the intrusive bodies before and after partial demagnetization in an alternating field (AF); (2) to compare these results with those of previous investigators; (3) to detect any difference between *in situ*

Figure 1.12 Plot of dike bulk density versus the plunge direction of the inferred magma flow azimuth for 62 dikes from the Koolau Volcano. Three density fields are shown (labeled 1–3), the solid horizontal line represents the zero plunge direction of the mean  $\chi_1$  AMS direction or the neutral buoyancy layer, positive buoyancy zone is inferred for upward directed  $\chi_1$  flow azimuths and the negative buoyancy zone is below the horizontal line (downward directed  $\chi_1$  flow azimuths).

## Bulk Density of Koolau Dikes vs X1 (AMS) Plunge



- (1) bulk density of volcano flanks 2.4-2.62 g/cm<sup>3</sup>
- (2) density of nonvesiculated basalt >2.65 g/cm<sup>3</sup>
- (3) bulk density of dike complex (diabase 2.9 g/cm<sup>3</sup>)
- (4) level of neutral buoyancy  
(magma density was in equilibrium with surrounding host rock)

dikes and possible anomalous (stable) NRM directions (in order to interpret possible tectonic readjustments of the dike complex related to subsidence or denudation of the shield); (4) to investigate the usefulness of the site-mean NRM directions as an aid in distinguishing between the relative intrusive ages (e.g. normal versus reverse remanent magnetization directions); and (5) to detect inconsistencies of individual samples in order to evaluate possible poor field orientations or laboratory preparation errors, and thus be able to weight reliability of the specimens for future AMS fabric studies.

*McDougall and Tarling* [1963] reported only reverse polarity rocks from eight sites from the Koolau volcanics, of which five gave K-Ar ages that ranged from 2.2 to 2.5 Ma. In their study only one dike from the Koolau complex was measured for NRM. Its initial mean declination=  $173^{\circ}$  and inclination=  $5^{\circ}$ , and after partial demagnetization in an AF to 150 oersted (peak) this site gave a mean declination of  $180^{\circ}$  and an inclination of  $-17^{\circ}$ . *Tarling* [1965] reports a  $D= 180^{\circ}$  and  $I= -17^{\circ}$  for one dike treated in 150 Oe peak field, which compares fairly well with my results for 53 dikes (Table 1.1). He also presents paleomagnetic data for seven lava flows treated under similar conditions, which have mean  $D= 179^{\circ}$  and  $I= -33^{\circ}$ . *Doell and Dalrymple* [1973] indicate that exposed lavas of the Koolau volcano were erupted entirely during the early Matuyama reversed polarity chron at about 2.6 to 1.8 Ma. They indicate that the Koolau shield became inactive about 1.8 Ma (K-Ar); the Koolau lavas are reversely magnetized, and represent a series of flows from the most southerly (SE) portion of the shield near Makapuu Head. The average paleomagnetic data for 24 sites (lava flows) from Makapuu Head is presented in *Doell and Dalrymple* [1973]. Their Makapuu Head lava flows give an average  $D= 173.5^{\circ}$  and  $I= -15.2^{\circ}$ , which compares moderately well with the mean  $D= 187.64^{\circ}$  and  $I= -21.88^{\circ}$  for a filled lava tube at Makapuu Head (KT38). It is also interesting to note that three dikes sampled at Makapuu Head (KD35-37) gave notably different (stable) paleomagnetic directions, with positive inclination angles (refer to, Table 1.1). It is not known if these dike have suffered post-

emplacement tectonic tilting or whether these paleomagnetic directions are truly representative of the youngest intrusive events of the Koolau shield.

### STABILITY OF REMANENT MAGNETIZATION

Between 4 to 20 cores were drilled from each intrusive body and filled lava tube by means of a portable gasoline rock drill and oriented by means of a Brunton compass and sun compass. The NRM of 554 specimens was measured with a Schonstedt Spinner Magnetometer on line with a micro-computer at the Hawaii Institute of Geophysics paleomagnetism laboratory. The site-mean NRM directions based on 423 specimens are shown in Figures 1.13*a* and *b* and summarized in Table 1.1. The scatter in the NRM directions from a single dike must not be excessive, and the limiting value of dispersion in the mean NRM directions was arbitrarily chosen as those dikes that had a precision parameter ( $\kappa$ ) of greater than 14 and an  $\alpha_{95}$  less than  $20^\circ$  (refer to Figures 1.13 *a* and *b*). 51 sites (399 specimens) fit this criteria and have reversed polarity directions very similar to *Tarling's* [1964] direction after AF demagnetization. For the reversed sites the mean NRM direction is declination =  $183.8^\circ$  and inclination =  $-26.9^\circ$  (Figure 1.13*b* and Table 1.1). Of special interest are two dikes (KD56 and 61 from northern Kaneohe Bay, at Haipuu and Mokolii Island respectively; that also fit this criteria, but are normally magnetized. The mean NRM direction for these two sites is  $D = 5.4^\circ$  and  $I = 19.5^\circ$  (Figure 1.13*a*).

Following the NRM measurements the low coercivity (soft unstable magnetization) components were removed from all specimens by treatment on 150 Oe (peak) AF. The results of this blanket AF demagnetization using a three-axis tumbler and magnetic induction levels to at least 150 Oe for 54 stable dikes gave a mean  $D = 184.6^\circ$  and  $I = -30.1^\circ$  for the reversely magnetized sites, and  $D = 3.3^\circ$  and  $I = 10.3^\circ$  for the two normally magnetized dikes (refer to Figures 1.13*c* and *d*, and Table 1.1). If there are no Koolau lavas significantly younger than the youngest dates of *Doell and Dalrymple's* (1973; 1.8 Ma), then the two normally magnetized dikes from northern Kaneohe Bay must have formed

**Table 1.1**

MRM Data for (stable) Reversely Magnetized Koolau Dikes

Site	N	Decl	Incl	l	m	n	K	a95
KD1	9	189.32	-30.68	-0.85	-0.14	-0.51	92.2	4.9
KD3	4	171.58	-36.51	-0.80	0.12	-0.59	19.1	16.0
KD4	4	193.28	-20.28	-0.91	-0.22	-0.35	14.9	18.1
KD5	9	209.05	-21.72	-0.81	-0.45	-0.37	37.0	7.7
KD6	7	149.37	-9.31	-0.85	0.50	-0.16	17.2	12.8
KD7	4	169.36	-19.37	-0.93	0.17	-0.33	37.4	11.4
KD8	4	201.87	-22.86	-0.86	-0.34	-0.39	24.9	14.0
KD12	6	184.24	-7.01	-0.99	-0.07	-0.12	14.1	15.2
KD13	12	183.67	-31.97	-0.85	-0.05	-0.53	34.6	6.9
KD15	5	212.62	-36.72	-0.68	-0.43	-0.60	25.9	12.3
KD18	8	190.21	-31.80	-0.84	-0.15	-0.53	58.2	6.5
KD19	5	176.83	-27.40	-0.89	0.05	-0.46	27.9	11.9
KD20	7	187.58	-19.08	-0.94	-0.12	-0.33	41.5	8.2
KD22	10	203.63	-32.56	-0.77	-0.34	-0.54	136.4	3.8
KD24	7	146.19	-12.59	-0.81	0.54	-0.22	24.9	10.6
KD25	7	168.26	-24.62	-0.89	0.19	-0.42	24.4	10.7
KD26	10	166.87	-41.86	-0.73	0.17	-0.67	133.9	3.8
KD27	9	174.27	-36.42	-0.80	0.08	-0.59	199.4	3.3
KD28	10	161.36	-35.10	-0.78	0.26	-0.57	22.8	9.3
KD30	9	194.52	-6.38	-0.96	-0.25	-0.11	14.9	12.1
KD31	7	255.55	-63.80	-0.11	-0.43	-0.90	58.6	6.9
KD32	12	173.71	-43.04	-0.73	0.08	-0.68	137.6	3.4
KD34	7	182.28	-43.18	-0.73	-0.03	-0.68	203.3	3.7
KD35	13	189.80	41.72	-0.74	-0.13	0.67	42.2	6.0
KD36	4	192.11	20.78	-0.91	-0.20	0.35	27.9	13.2
KD37	8	177.30	24.26	-0.91	0.04	0.41	118.4	4.5
KD38	19	191.10	-20.15	-0.92	-0.18	-0.34	202.0	2.3
KD39	13	206.39	-26.39	-0.80	-0.40	-0.44	175.2	2.9
KD40	6	206.70	-24.89	-0.81	-0.41	-0.42	16.1	14.2
KD42	6	174.99	-45.85	-0.69	0.06	-0.72	24.9	11.4
KD44	7	176.80	-31.68	-0.85	0.05	-0.53	185.9	3.9
KD45	6	232.32	-60.64	-0.30	-0.39	-0.87	61.9	7.3
KD46	7	180.01	-44.78	-0.71	0.00	-0.70	470.6	2.4
KD48	4	174.37	-1.48	-0.99	0.10	-0.03	303.3	4.0
KD51	8	184.44	-13.74	-0.97	-0.08	-0.24	62.0	6.3
KD52	6	189.85	-18.45	-0.93	-0.16	-0.32	124.2	5.1
KD53	8	183.18	-38.72	-0.78	-0.04	-0.63	112.2	4.7
KD54	7	184.23	-24.94	-0.90	-0.07	-0.42	272.5	3.2
KD55	6	188.48	-21.05	-0.92	-0.14	-0.36	24.6	11.5
KD57	6	184.96	-61.51	-0.48	-0.04	-0.88	534.4	2.5
KD58	7	167.27	-21.90	-0.91	0.20	-0.37	52.4	7.3
KD59	5	195.36	14.44	-0.93	-0.26	0.25	72.0	7.4
KD60	9	177.89	-66.85	-0.39	0.01	-0.92	74.3	5.4
KD62	6	171.92	-34.89	-0.81	0.12	-0.57	139.1	4.8
KD63	5	169.13	-19.91	-0.92	0.18	-0.34	22.1	13.3
KD64	10	166.96	-20.97	-0.91	0.21	-0.36	57.5	5.8
KD65	9	164.16	-30.08	-0.83	0.24	-0.50	217.0	3.2
KD66	9	186.24	-23.58	-0.91	-0.10	-0.40	123.0	3.2
KD69	11	182.35	-44.98	-0.71	-0.03	-0.71	96.4	4.3
KD70	11	187.45	-46.83	-0.68	-0.09	-0.73	258.9	2.6
KD71	11	200.53	-5.03	-0.93	-0.35	-0.09	32.8	7.4
<b>Average</b>	<b>8</b>							
<b>Sum</b>	<b>399</b>	<b>n =</b>	<b>51</b>	<b>-41.04</b>	<b>-2.70</b>	<b>-20.85</b>		
		<b>-176.23</b>	<b>-26.89</b>	<b>R =</b>	<b>46.11</b>	<b>k =</b>	<b>10.2</b>	
						<b>a95 =</b>	<b>6.1</b>	
<b>Koolau Dikes with Scattered MRM Data</b>								
	<b>N</b>	<b>Decl</b>	<b>Incl</b>	<b>l</b>	<b>m</b>	<b>n</b>	<b>k</b>	<b>a95</b>
KD2	6	190.47	-44.60	-0.70	-0.13	-0.70	1.0	58.4
KD9	5	130.35	-31.31	-0.55	0.65	-0.52	5.6	26.5
KD10	9	184.86	5.03	-0.99	-0.08	0.09	9.7	15.0
KD11	11	180.00	1.89	-1.00	0.00	0.03	8.4	14.5
KD14	6	162.71	47.52	-0.64	0.20	0.74	2.9	33.3
KD16	8	177.18	-14.75	-0.97	0.05	-0.25	7.5	18.1
KD17	7	76.76	69.59	0.08	0.34	0.94	1.6	42.4
KD21	9	134.15	44.54	-0.50	0.51	0.70	4.6	21.7
KD23	8	141.95	-14.64	-0.76	0.60	-0.25	7.5	18.1
KD29	8	195.14	-6.67	-0.96	-0.26	-0.12	5.5	21.2
KD33	10	41.06	-5.98	0.75	0.65	-0.10	1.2	39.9
ED41	6	206.89	-10.30	-0.88	-0.44	-0.18	8.6	19.4
ED43	11	302.76	-78.16	0.11	-0.17	-0.98	1.5	34.8
ET47	13	194.25	-52.02	-0.60	-0.15	-0.79	2.0	27.4
KD49	8	303.09	-59.25	0.28	-0.43	-0.86	1.4	42.1
ED50	6	225.05	-3.76	-0.71	-0.71	-0.07	3.4	31.0
<b>Sum</b>	<b>131</b>	<b>H =</b>	<b>16</b>	<b>-8.03</b>	<b>0.62</b>	<b>-2.32</b>		
<b>Average</b>		<b>175.56</b>	<b>-16.09</b>	<b>R =</b>	<b>8.38</b>	<b>k =</b>	<b>2.0</b>	
						<b>a95 =</b>	<b>24.9</b>	

**Table 1.1 (continued)**

Sites	N	NRM Data for Normally Magnetized Koolau Dikes						a95
		Decl	Incl	l	m	n	k	
KD56	8	-5.82	9.63	0.98	-0.10	0.17	249.4	3.1
KD61	16	18.08	28.66	0.83	0.27	0.48	118.5	3.2
Sum	24	M =	2	1.81	0.17	0.65		
Average		5.42	19.54	R =	1.93	k =	15.3	
						a95 =	25.3	

**Blanket AF-Desmagnetisation (150 Oe) Peak Field, (stable) Reversely Magnetized Dikes**

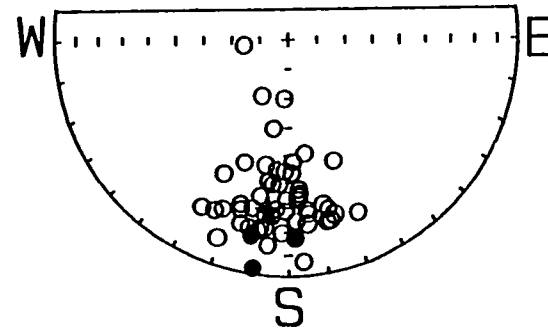
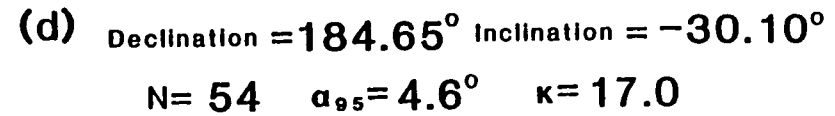
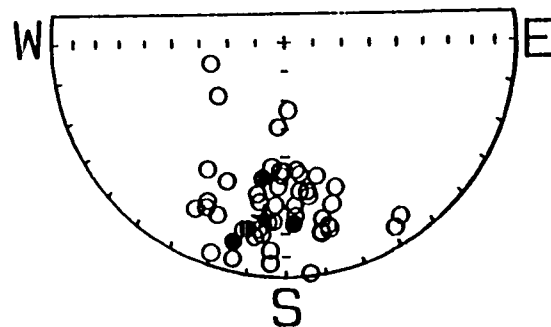
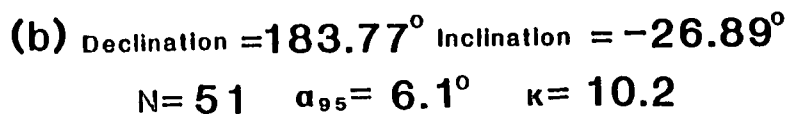
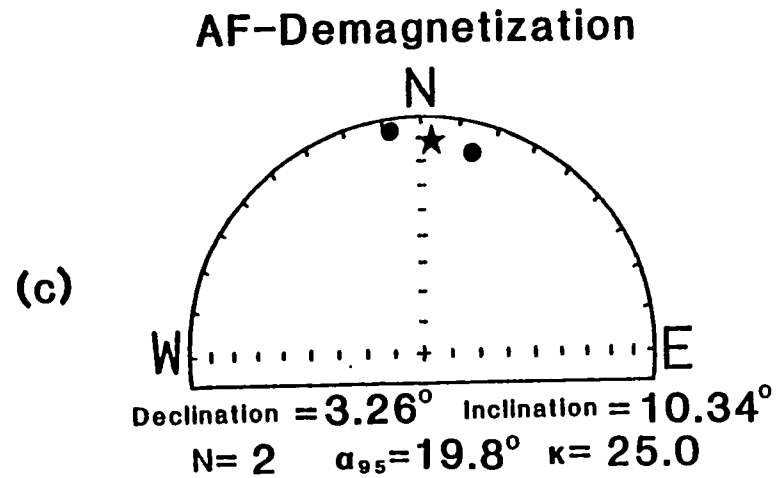
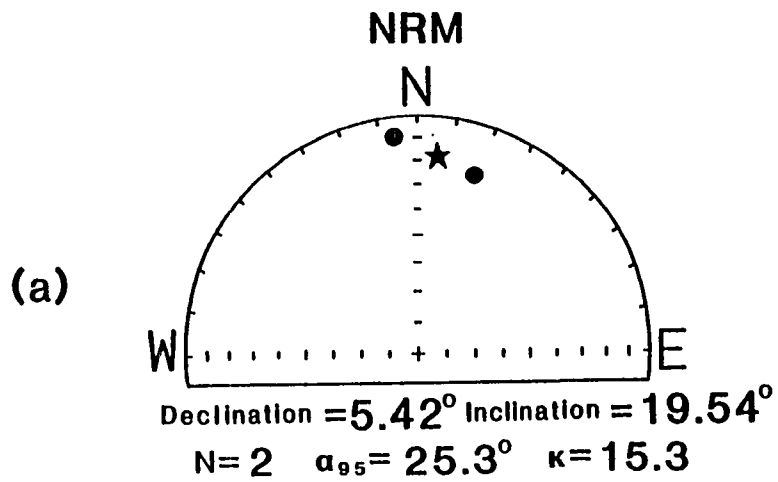
Sites	N	Decl	Incl	l	m	n	k	a95
KD1	8	184.80	-29.58	-0.87	-0.07	-0.49	298.1	2.9
KD3	5	176.98	-36.91	-0.80	0.04	-0.60	40.7	9.8
KD4	5	202.06	-25.40	-0.84	-0.34	-0.43	774.8	2.2
KD5	7	204.63	-23.65	-0.83	-0.38	-0.40	56.1	7.1
KD6	7	157.34	-22.06	-0.86	0.36	-0.38	106.6	5.1
KD7	3	166.67	-28.01	-0.86	0.20	-0.47	92.2	8.4
KD8	3	197.34	-29.71	-0.83	-0.26	-0.50	170.7	6.2
KD9	5	173.61	-29.80	-0.86	0.10	-0.50	55.4	8.4
KD10	7	167.78	-23.43	-0.90	0.19	-0.40	180.5	3.9
KD11	9	177.74	-24.13	-0.91	0.04	-0.41	643.9	1.8
KD12	5	182.13	-19.91	-0.94	-0.03	-0.34	58.7	8.2
KD15	6	207.10	-37.47	-0.71	-0.36	-0.61	163.0	4.5
KD16	6	192.05	-27.43	-0.87	-0.19	-0.46	155.8	4.6
KD18	7	191.67	-31.90	-0.83	-0.17	-0.53	185.3	3.9
KD19	3	195.11	-21.58	-0.90	-0.24	-0.37	652.8	3.2
KD20	6	191.87	-22.49	-0.90	-0.19	-0.38	115.4	5.3
KD22	7	200.56	-35.54	-0.76	-0.29	-0.58	63.0	6.7
KD24	7	165.17	-24.39	-0.88	0.23	-0.41	44.6	7.9
KD25	7	180.64	-28.37	-0.88	-0.01	-0.48	167.4	4.1
KD26	7	171.51	-40.30	-0.75	0.11	-0.65	75.6	6.1
KD27	8	177.45	-36.35	-0.80	0.04	-0.59	296.1	2.9
KD28	8	186.12	-38.88	-0.77	-0.08	-0.63	61.2	6.3
KD30	9	188.97	-20.23	-0.93	-0.15	-0.35	41.6	7.2
KD31	6	263.52	-64.48	-0.05	-0.43	-0.90	367.6	3.0
KD32	8	178.63	-43.10	-0.73	0.02	-0.68	151.1	4.0
KD34	6	187.87	-40.12	-0.76	-0.10	-0.64	363.2	3.0
KD35	13	191.21	17.48	-0.94	-0.19	0.30	130.6	3.4
KD36	4	189.83	3.00	-0.98	-0.17	0.05	66.6	8.6
KD37	8	178.07	17.54	-0.95	0.03	0.30	240.7	3.2
KT38	9	187.64	-21.88	-0.92	-0.12	-0.37	436.6	2.2
KD39	13	208.31	-22.11	-0.82	-0.44	-0.38	286.5	2.3
KD42	6	175.83	-47.81	-0.67	0.05	-0.74	203.0	4.0
KD43	4	158.34	-35.30	-0.76	0.30	-0.58	97.9	7.1
KD44	7	176.67	-33.47	-0.83	0.05	-0.55	163.6	4.1
KD45	8	205.82	-59.16	-0.46	-0.22	-0.86	106.1	4.8
KD46	7	182.46	-45.49	-0.70	-0.03	-0.71	324.7	2.9
KD48	4	176.37	-6.81	-0.99	0.06	-0.12	220.9	4.7
KD50	4	196.41	-27.14	-0.85	-0.25	-0.46	139.1	5.9
KD51	9	185.91	-14.25	-0.96	-0.10	-0.25	41.3	7.3
KD52	6	189.72	-20.61	-0.92	-0.16	-0.35	320.8	3.2
KD53	8	183.26	-39.26	-0.77	-0.04	-0.63	144.5	4.1
KD54	8	185.68	-26.83	-0.89	-0.09	-0.45	154.6	4.0
KD55	8	189.02	-21.96	-0.92	-0.15	-0.37	50.6	7.0
KD57	5	190.04	-59.40	-0.50	-0.09	-0.86	1075.0	1.9
KD58	7	173.59	-27.58	-0.88	0.10	-0.46	230.0	3.5
KD60	9	182.79	-59.55	-0.51	-0.02	-0.86	144.0	3.9
KD62	5	177.40	-35.08	-0.82	0.04	-0.57	171.6	4.8
KD63	5	165.94	-21.55	-0.90	0.23	-0.37	21.3	13.6
KD64	10	173.69	-24.11	-0.91	0.10	-0.41	251.3	2.8
KD65	9	168.18	-30.04	-0.85	0.18	-0.50	146.5	3.9
KD66	9	188.84	-28.73	-0.87	-0.13	-0.48	169.9	3.6
KD69	10	185.24	-44.67	-0.71	-0.06	-0.70	100.6	4.4
KD70	10	190.00	-46.48	-0.68	-0.12	-0.73	165.3	3.4
KD71	10	200.87	-13.80	-0.91	-0.35	-0.24	274.0	2.7
Sum	380	N =	54	-43.88	-3.57	-25.52		
Average	7	-175.35	-30.10	R =	50.89	k =	17.0	
						a95 =	4.6	

**Table 1.1 (continued)**

Sites	N	AF-Demagnetisation (150 Oe)			Peak Field, unstable dikes			a95
		Decl	Incl	l	m	n	k	
KD2	3	188.96	-37.52	-0.78	-0.12	-0.61	20.0	18.1
KD13	8	180.51	-32.72	-0.84	-0.01	-0.54	31.9	8.2
KD14	2	200.15	-5.57	-0.93	-0.34	-0.10	12.5	28.0
KD17	4	189.99	-17.76	-0.94	-0.17	-0.31	31.2	12.5
ED21	5	173.66	-12.02	-0.97	0.11	-0.21	34.3	10.7
ED23	8	166.93	-30.10	-0.84	0.20	-0.50	34.0	8.5
KD29	7	193.54	-23.40	-0.89	-0.21	-0.40	17.3	12.9
KD33	9	43.95	-27.20	0.64	0.62	-0.46	1.4	39.3
ED40	8	190.47	-24.30	-0.90	-0.17	-0.41	14.6	12.9
ED41	6	216.74	-8.65	-0.79	-0.59	-0.15	4.4	27.2
ED49	8	181.36	-45.10	-0.71	-0.02	-0.71	1.3	43.6
Sum	68	N =	11	-7.96	-0.71	-4.39		
Average		-174.93	-28.77	R =	9.11	k =	5.3	
						a95 =	18.3	

Sites	N	AF-Demagnetisation (150 Oe)			Peak Field, (stable) Normally Magnetized Dikes			a95
		Decl	Incl	l	m	n	k	
KD56	8	-7.48	6.00	0.99	-0.13	0.10	195.8	3.5
KD61	11	14.28	14.32	0.94	0.24	0.25	62.9	5.3
Sum	19	N =	2	1.93	0.11	0.35		
Average		3.26	10.34	R =	1.96	k =	25.0	
						a95 =	19.8	

Figure 1.13(a-d) Equal-area plots of the remanent magnetization directions before and after alternating demagnetization remanence. Star is the resulting mean remanent magnetization direction, and the magnetic parameters are defined in the text and Table 1.2.



- Upper Hemisphere Projection
- Lower Hemisphere Projection

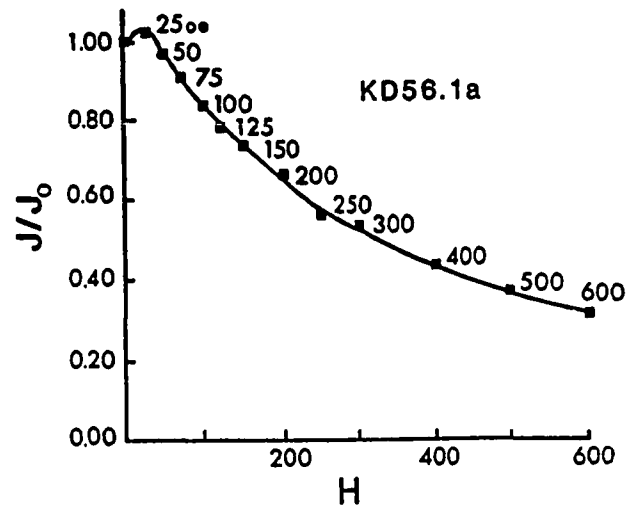
during the Gauss normal polarity chron (>2.54 Ma) and probably did not form during the later Brunhes normal polarity chron.

In general, after AF demagnetization 54 dikes and one filled lava tube gave a precision parameter ( $\kappa$ ) of 40 or more and an  $\alpha_{95}$  less than  $10^\circ$ . For the dikes with high magnetic stability the original NRM directions agree to within  $5^\circ$  with the directions after AF demagnetization in more than 75% of the dikes. In summary, the dikes seem to fall into two categories, one that is magnetically stable and the other magnetically unstable, similar to findings reported by *Graham* [1953] and *Larson and Strangway* [1969]. However, most samples have been affected to some degree by a low intensity secondary magnetization component that is a present day overprint and is viscous in origin. This secondary magnetization when present was easily removed in most cases by 75 to 100 Oe AF. In this study a pilot group of 8 specimens were subjected to step-wise progressive AF demagnetization to peak fields of 600 Oe, two of the results are presented in the orthogonal vector plots (Figure 14a and b; *Zijderveld*, 1967). In general after the present day viscous overprinting is removed at about 100 Oe peak field these specimens show a linear trend towards the origin on these vector plots.

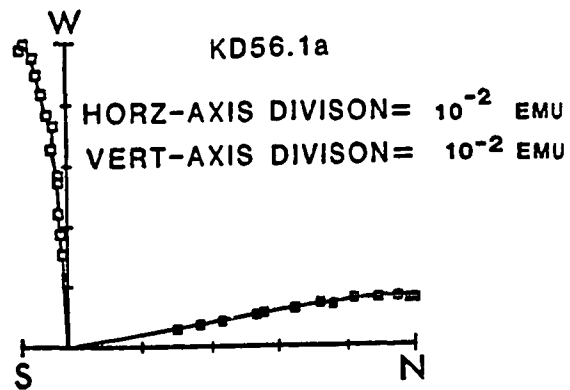
Figure 1.14(a) Plot of the step-wise progressive alternating field demagnetization to peak fields of 600 Oe for dike KD56, the normally magnetized dike; showing that there is a low intensity ( $\leq 50$  Oe) secondary magnetization component that is a present day overprint and is viscous in origin.

(b) Zijderveld Plot of dike KD56 subjected to step-wise progressive AF demagnetization to peak fields of 600 Oe. Note that after the low intensity magnetic component is removed there is a nearly linear progression towards the origin.

(a) AF-Demagnetization



(b)



## CHAPTER 2

### THEORY OF ANISOTROPY OF MAGNETIC SUSCEPTIBILITY

#### INTRODUCTION

Thirty-five years ago, *Graham* [1953] first discussed the usefulness of magnetic anisotropy in rocks as an aid in petrofabric analysis, but only in the last 10 years has renewed interest in applying the anisotropy of magnetic susceptibility (AMS) technique to geologic problems become evident in the literature [*Ellwood*, 1975, 1978, 1982; *Ellwood and Fisk*, 1977; *Kligfield et al.*, 1977; *Rees*, 1979; *Taira and Lienert*, 1979; *Incoronato et al.*, 1983; *Ellwood and Wolff*, 1985; *Knight et al.*, 1986; *Knight and Walker*, 1988; *Cogne and Perroud*, 1988; *Hrouda, et al.*, 1988; *MacDonald and Ellwood*, 1988].

Before describing the measurement technique used it is desirable to clarify some of the physical basis of AMS. The AMS technique is concerned with *initial susceptibility*, which depends on the *size, composition, and abundance of ferro- or ferrimagnetic minerals*. Note that iron for example, is ferromagnetic since the magnetic atoms within domains have their (spin) moments aligned in the same direction, while magnetite is ferrimagnetic since the magnetic ions at different crystal lattice sites are opposed.

It is instructive first to discuss susceptibility in terms of a magnetically isotropic medium before proceeding to the special anisotropic case. From a rock magnetism perspective *idealized rocks* are ones in which a small quantity (generally  $\leq 1\%$ ) of fine ferromagnetic particles with ellipsoidal shape are uniformly dispersed in random orientation and the particles are spaced far enough apart as to exert no mutual magnetic interaction. In magnetically isotropic rocks the induced magnetization ( $M$ ) is always parallel to the applied field ( $H$ ), and the susceptibility is a scalar quantity dependent on the magnitude of  $H$ . Generally, rocks that show an increase in susceptibility with increased field contain ferromagnetic particles of smaller size and hence greater coercivity [*Nagata*, 1961].

Although, the initial magnetic susceptibility of rocks in weak magnetic fields depends on the size, composition, and abundance of ferromagnetic minerals there is the general tendency for volcanic rocks to have susceptibilities that range from  $10^{-4}$  to  $10^{-2}$  emu/cm<sup>3</sup>, in plutonic rocks from  $10^{-4}$  to  $5.0 \times 10^{-3}$  emu/cm<sup>3</sup>, in metamorphic rocks from  $10^{-5}$  to  $3.0 \times 10^{-4}$  emu/cm<sup>3</sup>, and in sedimentary rocks less than  $10^{-5}$  emu/cm<sup>3</sup> [Nagata, 1961]. The *initial mass susceptibility* ( $\chi_o = \text{intrinsic}$ , or *bulk susceptibility*) of rocks and minerals of interest in this study are shown in Table 2.1 (after Collinson, 1983). Furthermore, there is a linear relationship between susceptibility and the composition of magnetite. Titanomagnetite forms a complete solid solution series from magnetite (Fe<sub>3</sub>O<sub>4</sub>), one iron end-member to ulvospinel (Fe<sub>2</sub>TiO<sub>4</sub>) the iron-titanium end-member, hence, basic and ultrabasic rocks generally have a relatively higher magnetic susceptibility than say hematite (Fe<sub>2</sub>O<sub>3</sub>), because of their higher iron content, and the tholeiitic basalts of the Koolau dike complex are no exception, with susceptibility values that range from  $10^{-3}$  to  $10^{-2}$  emu/cm<sup>3</sup>.

Before proceeding to the fundamental theories of magnetic susceptibility it is important first to review the fundamental terms that can be used to describe how magnetized a material may be and how these quantities are related in the two standard systems of units, namely the Gaussian cgs (centimeters-grams-seconds) units and the internationally recommended SI (Système Internationale) units. The three fundamental terms are:  $B$ , the magnetic induction (or magnetic flux intensity);  $H$ , the magnetic field strength; and  $M$ , the magnetic dipole moment or magnetization per unit volume [Shive, 1986]. In the cgs system

$$B = H + 4\pi M \quad (1)$$

In the SI system

$$B = \mu_o H + M \quad (2)$$

**Table 2.1 Initial mass susceptibility of rocks and minerals of interest in this study (after Collisson, 1983)**

<i>Rocks and Minerals</i>	<i>Initial Mass Susceptibility</i> (m <sup>3</sup> kg <sup>-1</sup> )
Magnetite <sup>a</sup>	5.7 x 10 <sup>-4</sup>
Maghemite <sup>a</sup>	
Pyrrhotite	~1 x 10 <sup>-7</sup> -10 <sup>-5</sup>
Ilmenite	1 x 10 <sup>-6</sup>
Hematite	6 x 10 <sup>-7</sup> -10 <sup>-6</sup>
Orthopyroxene <sup>b</sup>	5 x 10 <sup>-7</sup>
Igneous rocks	~1 x 10 <sup>-6</sup> -10 <sup>-4</sup>
Red sediments	~5 x 10 <sup>-9</sup> -10 <sup>-8</sup>
Limestones	~2 x 10 <sup>-9</sup> -10 <sup>-8</sup>

<sup>a</sup>Observed value for isolated, spherical grains

<sup>b</sup>Average value

Where  $\mu_0 = 4\pi \times 10^{-7}$  H/m is the permeability of free space [Shive, 1986]. In SI units,  $B$  is expressed in tesla (T), while  $M$  and is expressed in amperes per meter ( $A\ m^{-1}$ ).

A fifth important term is used to describe how magnetized an object may become under the influence of a (low) magnetic field, referred to as the *magnetic susceptibility* ( $k$ ), which is defined by the equation:

$$M = kH \quad (3)$$

where a magnetization per unit volume  $M$  is induced in a material of *volume susceptibility*  $k$  or *mass susceptibility*  $\chi$  by an applied field  $H$  (i.e.  $B = \mu_0 H$ ; Collinson [1983]). Therefore, in SI units, using  $B = \mu_0(H + M)$  [Sears et al., 1982],  $k$  is in  $emu\ cm^{-3}$  and the units of  $\chi$  are in  $emu\ g^{-1}$ . Thus in both systems, volume susceptibility is a dimensionless quantity in which 1 cgs unit of susceptibility equals  $4\pi$  SI units of susceptibility [Shive, 1986]. The relationship between  $k$  and  $\chi$  is,  $\chi = k/\rho$  where  $\rho$  is the samples density in  $kg\ m^{-3}$ .

## THEORY OF AMS

By definition, anisotropy of magnetic susceptibility describes the variation of magnetic susceptibility with direction within a material, and differs from isotropic susceptibility since the susceptibility varies with the direction along which the sample is measured. In theory, most rocks placed in a magnetic field will acquire an induced magnetic moment. The magnetic susceptibility per unit mass,  $\chi_{ij}$  is then equal to the magnitude of the induced moment  $J_j$ , divided by the inducing field  $H_i$ . AMS measurements are approximated by the second-rank symmetric tensor  $\chi_{ij}$ , which can be thought of as a combination of the effects of all the magnetic grains within a specimen (i.e. the tensor relates the different vector fields  $H_i$  and  $J_j$ ). The three principal components (*eigenvectors*) of the tensor  $\chi_{ij}$  are the *maximum* ( $k_1$ ), *intermediate* ( $k_2$ ), and *minimum* ( $k_3$ ) *susceptibility directions* [Nye, 1969]. In a magnetically isotropic medium the induced magnetization  $M$  is always

parallel to the applied field and  $\chi_1 = \chi_2 = \chi_3$ , however, in an anisotropic medium  $M$  is not in general parallel to the applied field. Thus the field  $H_i$  and the induced magnetization  $M_j$  have components  $H_1, H_2$ , and  $H_3$  and  $M_1, M_2$ , and  $M_3$  along  $x, y$ , and  $z$ -axes, and the net magnetization  $M$  resulting from both an inducing field  $H$  and a remanent magnetization  $R$  can be expressed in tensor form:

$$\begin{bmatrix} M_1 \\ M_2 \\ M_3 \end{bmatrix} = \begin{bmatrix} k_{11} & k_{12} & k_{13} \\ k_{21} & k_{22} & k_{23} \\ k_{31} & k_{32} & k_{33} \end{bmatrix} \begin{bmatrix} H_1 \\ H_2 \\ H_3 \end{bmatrix} + \begin{bmatrix} R_1 \\ R_2 \\ R_3 \end{bmatrix} \quad (4)$$

where the  $k$  tensor is the susceptibility tensor. From Equation (6), take for example  $k_{31}$  to be the volume susceptibility appropriate to the contribution to the magnetization  $M_3$  along the  $z$ -axis resulting from  $H_1$  acting along the  $x$ -axis.

Alternatively the volume susceptibility tensor  $k_{ij}$  can be expressed in terms of a mass susceptibility ( $\chi$ ), and can be expressed in the more convenient form of a column matrix, provided  $\chi$  is symmetric (i.e.  $\chi_{31} = \chi_{13}$ ):

$$\chi = [\chi_{11} \chi_{22} \chi_{33} \chi_{12} \chi_{23} \chi_{31}] \quad (5)$$

I will assume that there are no interactions between the remanent and induced magnetizations. That is,  $\chi$  is independent of  $R$ . Generally this statement will be true for low applied magnetic fields and as long as the susceptibility differences are very small ( $\ll 10\%$ ) the remanent directions should not be affected. The basic assumption is, that as the sample is placed in a number of different orientations, the remanence moves with the sample. The magnetic field  $H$ , however, does not. It is fixed in the coordinate system of the balanced bridge, and shall be referred to as the measurement direction and shall be represented as  $(i,j,k)$ . The net induced magnetization  $M$  is measured in this same direction. Equations (3 and 4) can be expressed in the general form:

$$M_j = \chi_{ij} H_i \quad (i = 1,2,3) \quad (6)$$

where  $\chi_{ij}$  is a symmetric second-order (mass) susceptibility tensor having  $\chi_{12} = \chi_{21}$ ,  $\chi_{23} = \chi_{32}$ , and  $\chi_{31} = \chi_{13}$ . In an anisotropic sample, three orthogonal axes are defined along which the susceptibility takes on a maximum ( $\chi_1$ ), intermediate ( $\chi_2$ ), and minimum ( $\chi_3$ ) magnitude.

There are two quadric surfaces which are useful in discussing AMS, namely, the *representation ellipsoid* and the *magnitude ovaloid*. The most widely accepted convention for expressing anisotropic susceptibility is in terms of the representation ellipsoid; henceforth I will follow this convention for describing the AMS surfaces.

In the anisotropic case when  $\chi_1 > \chi_2 \approx \chi_3$ , then the susceptibility ellipsoid is *prolate* (i.e. cigar or needle shaped) and represents a lineated magnetic fabric; if  $\chi_1 \approx \chi_2 > \chi_3$ , then the ellipsoid is *oblate* (i.e. pancake shaped) and the corresponding fabric is foliated. The representation ellipsoid has the general form:

$$\frac{x_1^2}{\chi_a^2} + \frac{x_2^2}{\chi_b^2} + \frac{x_3^2}{\chi_c^2} = 1 \quad (7)$$

Note that the square root of the denominator in each term is the length of the semi-axes of the ellipsoid. As demonstrated by *Nagata* [1961] the loci of the ends of the vectors representing the susceptibility parallel to the applied magnetic field,  $H_i$ , do not form an ellipsoid but an ovaloid.

## SHAPE ANISOTROPY AND THE DEMAGNETIZING FACTOR

In low fields, magnetocrystalline anisotropy is not observed in cubic minerals, and since titanomagnetite is the dominant magnetic carrier in the Koolau dikes, shape rather than crystalline anisotropy should have the most important effect on the AMS fabric. Since elongated nonequant magnetic grains are more readily magnetized along their long axis, shape anisotropy may result as the internal magnetic field induced by the magnetostatic

poles at their surfaces is weakest in this direction [Stoner, 1945]. In spherical grains the separation of the surface poles is the same for all directions, resulting in no shape anisotropy (Figure 2.1a). All other shapes can be essentially represented as ellipsoids or ovaloids [Stacey, 1960 a, b; Uyeda et al., 1963] and will be more readily magnetized along their long axes than in any other direction. Acicular or rod-shaped magnetic crystals tend to have very high susceptibility anisotropy, in which  $\chi_1 \gg \chi_2 = \chi_3$ .

Consider now the effect of intrinsic susceptibility ( $k_i$  or  $\chi_i$ ) on shape anisotropy of a single elongated ellipsoidal magnetite grain. Anisotropy of magnetic susceptibility resulting from grain shape arises from the dependence of demagnetizing factor  $N$  on particle shape.  $N$  is the demagnetizing factor due to the separation of the surface magnetostatic poles (Figure 2.1b). For an applied field  $H$  the effective magnetic field ( $H_i$ ) inside an anisotropic (elongate) particle is:

$$H_i = H - NM \quad (8)$$

where  $M$  is the volume intensity of induced magnetization and  $N$  is the demagnetizing factor of the particle along the direction of the applied field. From the above equations

$$H_i = H - N\chi_i H_i \quad (9)$$

leading to the general form:

$$\chi_o = \frac{\chi_i}{1 + N\chi_i} \quad (10)$$

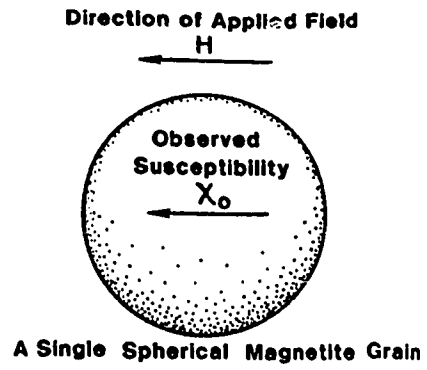
where  $\chi_i$  and  $\chi_o$  are the intrinsic (bulk susceptibility) and the observed susceptibility, respectively. The observed susceptibility is equivalent to the apparent susceptibility ( $k_a$ ) of Uyeda et al. [1963]. In the  $xy$ -plane the difference in susceptibility  $\Delta\chi$ , can be expressed by the following [Stacey, 1963]

Figure 2.1(a) Cartoon of the observed AMS susceptibility ( $\chi_o$ ) vector direction resulting from a single spherical-shaped magnetite grain under the influence in a uniform low external magnetic field ( $H$ ). Note that the direction of  $H$  is always parallel to the ( $\chi_o$ ) vector direction. Thus no shape anisotropy results and the observer susceptibility is isotropic.

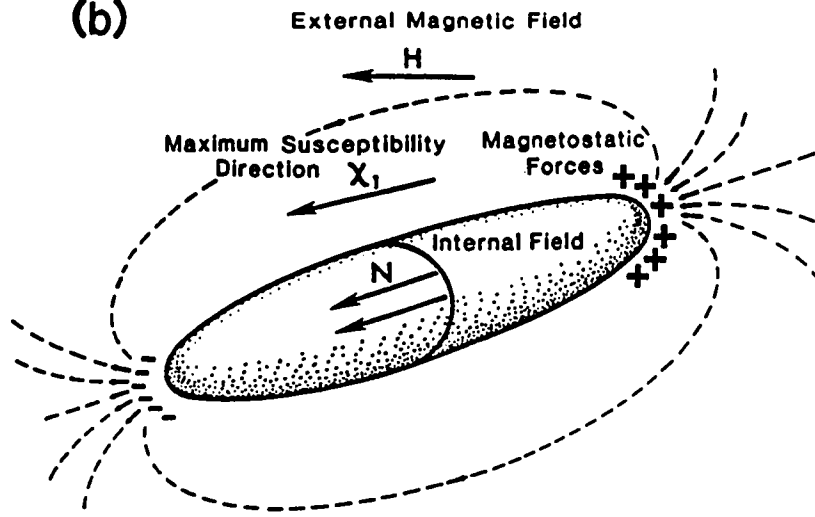
(b) Cartoon of the observed maximum AMS susceptibility direction ( $\chi_1$ ) resulting from a single elongate ellipsoid-shaped magnetite grain under the influence of a uniform low external magnetic field ( $H$ ).  $N$  is the demagnetizing factor due to the separation of the surface magnetostatic poles (shown by "+" and "-"). In this example the internal field is weakest parallel to the elongation direction, because the magnetostatic forces are weakest in this direction. The  $\chi_1$  AMS susceptibility direction will tend to parallel this elongation direction, and its magnitude will be a maximum when the applied field ( $H$ ) is oriented along this direction. Hence,  $\chi_1$  will vary depending on the direction in which it is measured in a non-spherical particle.

(c) Cartoon of the presumed physical shape of the "*susceptibility ovaloid*", resulting from a single prolate shaped magnetite grain (with a dimension ratio  $m= 2.5$ ) suspended on a homogeneous non-magnetic rock core specimen and placed in a low external field.

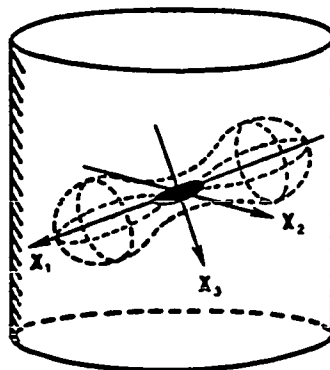
(a)



(b)



(c)



$$\Delta\chi = \frac{\chi_i^2(N_a - N_b)}{(1 + N_a\chi_i)(1 + N_b\chi_i)} \quad (11)$$

The observed susceptibility is anisotropic when  $N$  varies with direction [Uyeda *et al.*, 1963]. By considering a single magnetically isotropic (homogeneous) grain of spheroidal shape (e.g. prolate) in which  $\chi_{ia} \neq \chi_{ib} = \chi_{ic}$  (Figure 2.1b), Uyeda *et al.* [1963] defines the anisotropy factor,  $P$  as:

$$P = \frac{1 + \chi_i N_b}{1 + \chi_i N_a} \quad (12)$$

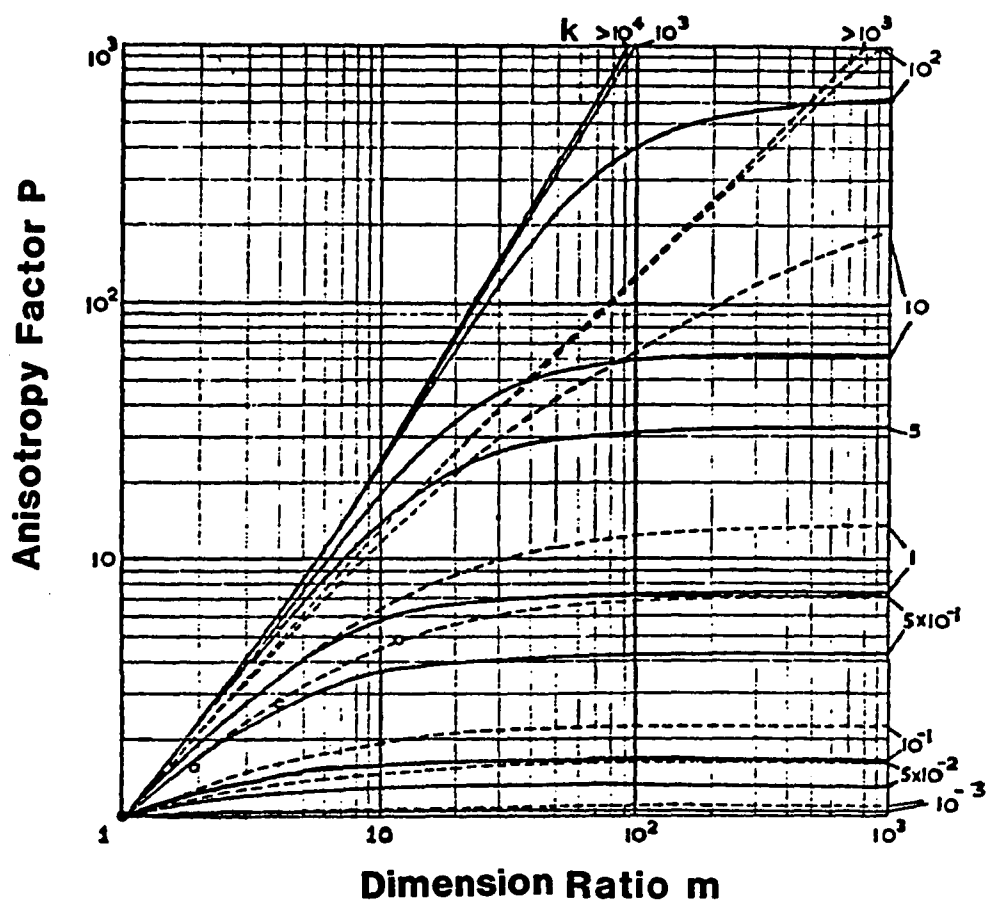
Stoner [1945] tabulated the numerical values  $N_a$  and  $N_b$  for prolate and oblate ellipsoids of revolution. Uyeda *et al.* [1963] used these values to plot a family of curves which relates the dimension ratios of the ellipsoid of revolution to the observed (apparent) maximum to minimum susceptibility ratios. Figure 2.2 (after Uyeda *et al.*, 1963) is a plot of the anisotropy factor ( $P$ ) against the dimension ratio ( $m$ ), where  $m = a/b$ . Two important conclusions relative to this study can be drawn from this plot.

- (1) If bulk susceptibility is less than  $10^{-3}$  emu  $\text{cm}^{-3}$ , then the shape effect is very small because samples having dimension ratios of  $10^3$ , will only show susceptibility anisotropies of 10% or less of the shape anisotropy.
- (2) A single homogeneous magnetite grain, with an intrinsic susceptibility of  $2.0 \times 10^{-1}$  emu  $\text{cm}^{-3}$  [Parry, 1965], will exhibit a susceptibility anisotropy which is considerably less than its actual shape anisotropy.

For example, Taira [1976] calculated that an ellipsoidal magnetite grain with a dimension ratio of  $m=2$  (i.e. a typical aspect ratio for grains observed in the Koolau dike samples) and a bulk susceptibility of  $0.5$  emu/ $\text{cm}^3$  will give a susceptibility anisotropy of about 1.7 percent. Hence, the apparent susceptibility anisotropy due to shape is very small when the bulk susceptibility is small. It is not until the susceptibility approaches that of

Figure 2.2 A plot of the anisotropy factor (P) against the dimension ratio (m), where  $m = a/b$  (maximum /minimum ellipsoid dimension) (revised from *Uyeda et al.*, 1963). Note that typical susceptibility values of the Koolau dike samples fall in the  $5 \times 10^{-2}$  eum/cm<sup>3</sup> range, and therefore have very low shape anisotropy factors (P= 1.7%). Note that typical values for the total susceptibility anisotropy of the Koolau dike specimens fall in the 1.0 to 6.0% range, which is similar to this low "P" factor.

**Bulk Susceptibility ( $k$ , in  $\text{emu}/\text{cm}^3$ )**



pure magnetite ( $5.0 \times 10^{-1} \text{ emu/cm}^3$ ; shown as open circles in Figure 2.2) that the anisotropy factor becomes significant.

Since  $N_a + N_b + N_c = 4\pi$ , and considering the special case when  $N_b = N_c$ , P becomes:

$$P = \frac{1 + \chi_i^{1/2}(4\pi - N_a)}{1 + \chi_i N_b} \quad [\text{Uyeda et al., 1963}] \quad (13)$$

By substituting in the appropriate bulk susceptibility values for the Koolau dike rocks ( $\chi_i = 10^{-2} \text{ emu cm}^{-3}$ ), the P-factor reaches a maximum ( $P = 1.062$ ) when  $N_a$  is zero.  $N_a$  becomes zero when the dimension ratio of a prolate ellipsoid is infinite (needle-shaped), and a closely analogous argument is also appropriate to oblate spheroids. Therefore, no matter what shape a crystal of hematite has, the shape effect should be unimportant because of its very low intrinsic susceptibility (refer to Table 2.1).

The apparent susceptibility is anisotropic when  $N$  is a directional quantity [Uyeda et al., 1963]. Thus, the dependence of the observed susceptibility ( $\chi_o$ ) on  $N$  implies variation in  $\chi_o$  according to the direction in which it is measured in a non-spherical particle. Figure 2.1b, after Stacey [1960a, 1963], Uyeda et al. [1963], and Bhathal [1971], is a cartoon depicting the presumed maximum susceptibility direction (due to shape anisotropy) resulting from a single elongate ellipsoidal-shaped magnetite grain placed in a low external magnetic field. In this hypothetical example the maximum  $\chi_1$  AMS direction always aligns parallel to the direction of maximum grain elongation as a result of the inequality of the demagnetizing factors in this direction, where  $N_j$  represents the demagnetizing factor along the  $x_j$ -axis of the magnetite grain ( $H$  and  $\chi_1$  are as previously defined). Therefore in summary, shape anisotropy arises as a result of the inequality of the demagnetizing factors along different directions in a non-equidimensional grain.

## EVALUATION OF THE SUSCEPTIBILITY ELLIPSOID

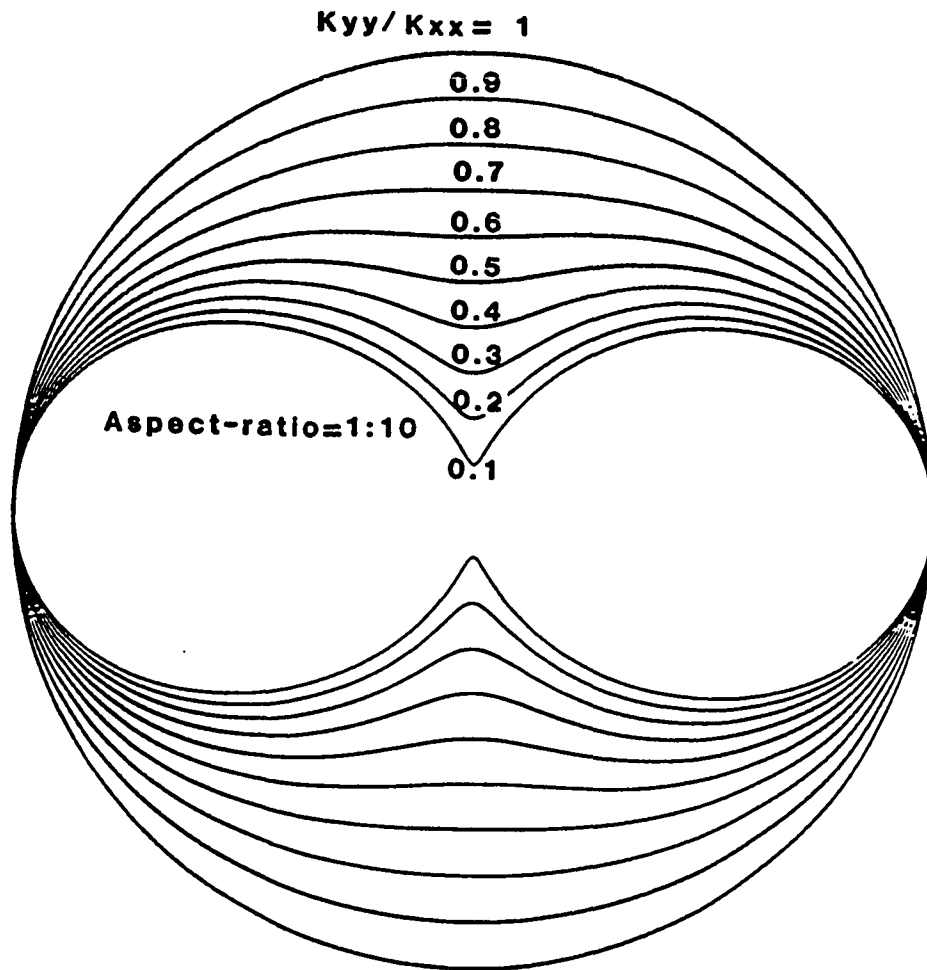
As mentioned previously the three-dimensional shape of the AMS tensor, an ovaloid (its physical representation), is mathematically defined as one over the square root of the susceptibility and is commonly, though incorrectly, referred to by most authors as the susceptibility ellipsoid, magnitude ellipsoid, equivalent magnetic ellipsoid, or AMS ellipsoid [Khan, 1962; Ney, 1969; Bhathal, 1971; Ellwood, 1981; Knight *et al.*, 1986]:

If we assume that susceptibility variation with direction can be represented by a symmetric second-rank tensor [Ney, 1969], then the magnitude surface of this tensor is an *ovaloid*, with principal axes corresponding to the maximum, intermediate, and minimum susceptibility directions. Figure 2.1c, is a cartoon depicting the physical shape of the *susceptibility ovaloid* resulting from a single prolate-shaped magnetite grain with a low dimension ratio ( $m= 2.5$ ) suspended in a homogeneous rock core specimen. Figure 2.3 graphically depicts the two-dimensional surface of the representation ellipsoid (ovaloid), plotted in the  $xy$ -plane for ten different ratios of the intermediate:maximum axes,  $k_{yy}/k_{xx}$  or  $\chi_2/\chi_1$ . It is interesting to note that it is not until  $k_{yy}/k_{xx}$  approaches 7:10 ( $\chi_2/\chi_1 = 0.7$ ) that the surface of the susceptibility tensor finally approaches an ellipse-like form. The representation quadric of the tensor given by:

$$|\chi_{ij}| = 0 \quad (14)$$

is an ellipsoid whose principal axes also coincide with the maximum, intermediate, and minimum susceptibility directions. By convention the representation quadric in most AMS studies is referred to as the susceptibility ellipsoid, in which the magnitudes of the maximum, intermediate, and minimum susceptibilities are the eigenvalues of the susceptibility tensor, and their directions are the eigenvectors. Therefore, in the special case when  $H$  is directed along one of the principal axes of susceptibility of the specimen, the magnitude of the tensor is expressed by:

Figure 2.3 Is a graphic representation of the two-dimensional surface of the *susceptibility ovaloid* (representation ellipsoid), plotted in the  $xy$ -plane for ten different ratios of the intermediate:maximum axes,  $k_{yy}/k_{xx}$  or  $\chi_2/\chi_1$ . Note that as the dimension ratio reaches 1.43 ( $k_{yy}/k_{xx} = 0.7$ ) the surface of the susceptibility tensor finally approaches an ellipse shape.



**OVALOID SURFACES IN THE XY-PLANE**

$$M_j = \lambda H_i \quad (15)$$

where  $\lambda$  is the eigenvalue corresponding to this principal axis. In summary, the eigenvectors of the susceptibility tensor give the orientation of the maximum ( $\chi_1$ ), intermediate ( $\chi_2$ ), and minimum ( $\chi_3$ ) susceptibility axes, and its eigenvalues give the magnitude of  $\chi_1$ ,  $\chi_2$ , and  $\chi_3$ , from which are derived the shape and intensity parameters of the representation ellipsoid or susceptibility ovaloid. The most useful AMS parameters for this investigation are discussed in the following section.

### AMS PARAMETERS

*Ellwood et al.* [1988] strongly recommends that at the very least, all papers report mean or bulk susceptibilities and provide enough information so that the principal susceptibilities can be determined. Because many authors of AMS studies have somewhat arbitrarily chosen their own (biased) set of susceptibility parameters, and because there is no universal standard, reviewing the literature can easily confuse the obvious quantitative comparisons. Because of this over-abundance of parameters, and to avoid such confusion, *Ellwood et al.* [1988] suggest that each parameter used should be carefully defined and the original reference given. Furthermore, *Jelinek* [1979] indicates that the fact that grain sizes and susceptibilities have a log normal distribution suggests that comparisons should be made on the basis of logarithmic rather than arithmetic values (refer to Figure 2.4 and Table 2.2).

The magnetic anisotropy parameters currently being used can be divided into three main groups.

- (1) Parameters that are based on *ratios of the principal susceptibilities*.
- (2) Parameters that are based on *susceptibility differences*.
- (3) Parameters that use *combinations of ratios and differences* of principal susceptibilities.

Figure 2.4 Plot of the logarithmic mean of the AMS axial ratios;  $\log[\chi_2/\chi_3]$  versus  $\log[\chi_1/\chi_2]$  for 70 Koolau dikes. This plot of the log(axial ratios) shows that the shape of the mean susceptibility tensor is slightly more oblate (pancake-shaped) than prolate (cigar-shaped); similar to figure 3.2*b*, Chapter 3 which shows the strain ellipsoid "Flinn" diagram for 660 individual dike specimens. Note that the logarithmic mean susceptibility tensor is oblate shaped in 40 (56%) of Koolau dikes and is prolate shaped in the other 31 (44%).

**PLOT of log (X2/X3) vs log (X1/X2) for 70 Koolau dikes**

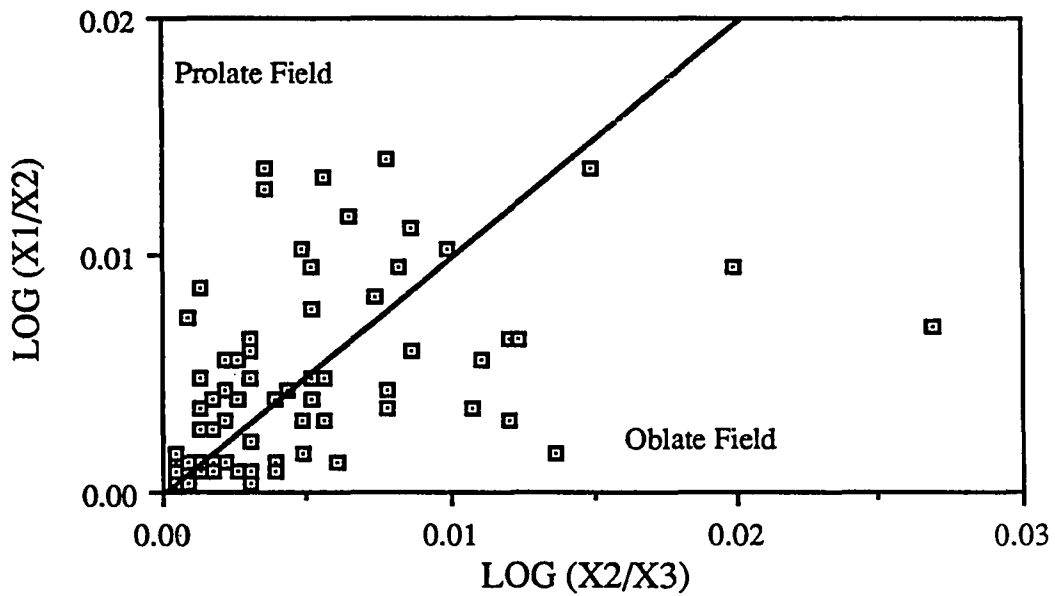


**Table 2.2** Some anisotropy of magnetic susceptibility parameters

Term	AMS axes	References
<b>Magnitudes of Anisotropy</b>		
Anisotropy degree, <i>P</i>	* $k_1/k_3$	<i>Nagata</i> , 1953; 1961
Degree or Percent Anisotropy, <i>h</i>	* $(k_1 - k_3)/k_2 \times 100$	<i>Howell et al.</i> , 1958
Total Anisotropy, <i>H</i>	* $(k_1 - k_3)/k_{\text{mean}}$	<i>King and Rees</i> , 1962; <i>Owen</i> , 1974
<b>Lineation</b>		
Lineation, <i>L</i>	* $k_1/k_2$	<i>Balsley and Buddington</i> , 1958; 1960
Magnetic Lineation, <i>l</i>	* $(k_1 - k_2)/k_{\text{mean}}$	<i>Khan</i> , 1962
Lineation	$(k_1 + k_3)/2k_2$	<i>Urrutis-Fucugauchi</i> , 1980a
Lineation degree	$2k_1/(k_2 + k_3)$	<i>Hrouda et al.</i> , 1971a
<b>Foliation</b>		
Foliation, <i>F</i>	* $k_2/k_3$	<i>Stacey et al.</i> , 1960; 1961
Magnetic Foliation, <i>f</i>	* $(k_2 - k_3)/k_{\text{mean}}$	<i>Khan</i> , 1962
Foliation	$(k_1 + k_2)/2k_3$	<i>Balsley and Buddington</i> , 1960
Foliation degree	$2k_2/(k_1 + k_3)$	<i>Urrutis-Fucugauchi</i> , 1980a
Lineation/Foliation	$(k_1k_3 - k_2k_3)/(k_1k_2 - k_1k_3)$	<i>Stacey</i> , 1960
Strain indicator	$(k_1k_3 - k_2k_3)/(k_2^2 - k_1k_3)$	<i>Flinn</i> , 1962
<b>Shape, Prolateness, Oblateness</b>		
Prolateness, <i>L/F</i>	$(k_1 - k_2)/(k_2 - k_3)$	<i>Khan</i> , 1962
Prolateness	$(2k_1 - k_2 - k_3)/(k_2 - k_3)$	<i>Urrutis-Fucugauchi</i> , 1980b
Oblateness, <i>F/L</i>	$(k_2 - k_3)/(k_1 - k_2)$	<i>Khan</i> , 1962
Oblateness	$(k_1 + k_2 - 2k_3)/(k_1 - k_2)$	<i>Urrutis-Fucugauchi</i> , 1980b
Eccentricity, <i>E</i>	* $k_2^2/k_1k_3$	<i>Hrouda et al.</i> , 1971a
Ellipsoid Shape	$(k_1 - k_2)(2k_1 - k_2 - k_3)/(k_2 - k_3)$	<i>Urrutis-Fucugauchi</i> , 1980b
Shape Indicator	$(k_1k_2 - k_2^2)/(k_1k_2 - k_1k_3)$	<i>Urrutis-Fucugauchi</i> , 1980a
<i>q</i> Factor	$(k_1 - k_2)/[(k_1 + k_2)/2 - k_3]$	<i>Granar</i> , 1958
<i>Graham's V</i> angle	* $\sin^{-2}[(k_2 - k_3)/(k_1 - k_3)]$	<i>Graham</i> , 1966
<i>Jelinek's T</i> Factor	$2 \ln(k_2/k_3) / \ln(k_1/k_3) - 1$	<i>Jelinek</i> , 1981

\* magnetic susceptibility parameters used in this study

The fundamental method used here for determining the anisotropy of susceptibility in weak magnetic fields is the A.C. bridge susceptibility spinner method described by *Graham* [1966] and *Taira* [1976], and now modified and revised by Barry R. Lienert at the Hawaii Institute of Geophysics (the AMS procedure is outlined in the following section). Instruments like the one used in this study measure susceptibility differences with the initial susceptibility magnitude being measured independently. In this respect, differences are more precisely determined than total magnitude since errors in the initial susceptibility measurements may be reflected in the calculated ratios [*Ellwood et al.*, 1988]. Therefore those parameters that are based on susceptibility differences are more accurately determined with this equipment.

At least three parameters are required to describe the shape of the observed magnetic anisotropy. I have taken these as the total magnitude of the anisotropy ( $H$  in percent), the degree of lineation ( $L$ ), and the degree of foliation ( $F$ ). In this study the magnetic susceptibility was measured in terms of susceptibility per unit mass ( $\chi$ ), where the mass susceptibility is represented by:

$$\bar{\chi} = \frac{(\chi_1 + \chi_2 + \chi_3)}{3} \quad (16)$$

For convenience the eigenvalues have also been normalized with respect to  $\chi_1 = 1.000$  (refer to the statistical data of each site presented in Appendix A, and summarized in Table 3.1 of Chapter 3).

The total anisotropy ( $H$ ), not to be confused with  $H_i$  (the magnetic field) defined in the previous section is represented by the equation [Table 2.2; *Owens*, 1974]

$$H = [(\chi_1 - \chi_3) / \bar{\chi}] \quad (17)$$

The parameter  $V$  [Graham, 1966] is a convenient index of shape:  $<45^\circ$  for a prolate ellipsoid;  $>45^\circ$  for an oblate ellipsoid.  $V$  is given by the following relationship:

$$\sin^2 V = (\chi_2 - \chi_3) / (\chi_1 - \chi_3) \quad (18)$$

Two additional parameters considered very useful in evaluating the susceptibility tensor's shape, i.e. the representation ellipsoid, are the magnetic lineation ( $L$ ) and foliation ( $F$ ) given by Khan [1962], where

$$L = (\chi_1 - \chi_2) / \chi_{mean} \quad (19)$$

$$F = (\chi_2 - \chi_3) / \chi_{mean} \quad (20)$$

Table 2.2 shows some additional anisotropy parameters, as well as the ones used in this study. It should be emphasize, however, that even these parameters do not adequately parameterize all the magnetic fabric features.

## AMS INSTRUMENTATION AND MEASUREMENTS

### BACKGROUND

There are several reliable techniques for determination of AMS, of which the author has used two, namely the torsion-fiber balance [King and Rees, 1962; Stone, 1963; Ellwood, 1984] and the balanced bridge susceptibility spinner [Graham, 1966]. In this study all the samples were measured for AMS using a modified balanced bridge susceptibility spinner at the University of Hawaii, originally constructed by Graham [1966]. The instrument used consists basically of an A.C. bridge whose output balance is influenced by the sample, and a system on line with a mini-computer which analyzes the bridge balance signal and automatically detects the various component phase shifts and then calculates and records the eigenvalues and eigenvectors of the susceptibility ellipsoid.

In this study the AMS fabrics of dikes are used to decipher magma rheology in hopes of interpreting the flow behavior during dike intrusion. Ultimately, the magnetic fabrics

can be used to infer the general location of the magma reservoir and hence the magmatic evolution of the Koolau dike complex. Therefore, we have to obtain the resultant principal directions and ratios of the principal susceptibilities defined as best as possible. Therefore we should not study the fluctuation of the mean susceptibilities of the specimens, but as *Jelinek* [1978] indicates, we should use the mean tensor method to infer the structural geology, since the variability of the mean susceptibility would increase the variability of the results. For example, in the present investigation in which the geological object is an intrusive body of a single rock type the susceptibility is caused by ferrimagnetic grains distributed *sparsely* throughout ( $\leq 1\%$  of the bulk sample). Since these tholeiitic basaltic dike rocks in most cases contain a very small amount of magnetite the mean susceptibility will fluctuate severely depending on the number of grains contained in the individual specimens, whereas the variability of the principal directions and the ratios of the principal susceptibilities may be considerably less variable.

In the following section I will briefly discuss *Jelinek's* [1978] method to calculate the susceptibility tensor on a group of specimens, originating from a single geological body (intrusive or extrusive lava flow). *Jelinek's* [1978] mathematical approach, gives an estimate of the mean normalized tensor, an estimate of the principal susceptibilities derived from it, and a reasonable estimate of the principal susceptibility directions together with their respective ellipsoidal confidence regions. The susceptibilities along chosen directions in the specimen are measured and used to compute the elements of the susceptibility tensor, the principal susceptibilities and the principal directions. I will also show how a group of specimens of dike rock, and thus simultaneously a single intrusive body, can be assigned a certain "*mean*" tensor along with ellipsoidal estimates of its variability.

## AMS MEASUREMENTS

The following is a brief outline of the AMS system used at the Hawaii Institute of Geophysics' paleomagnetic laboratory.

(1) The core sample is mounted in a plastic cube holder on a drive shaft (~1m long) that passes through the center of two coils forming one arm of a balanced four arm A.C. bridge (see Figures 2.5 and 2.6a and b). The A.C. bridge balance is sensitive to the slight changes in the inductance of the two coils on either side of the sample due to the component of the sample along the coils axis. The A.C. bridge is driven at 3 KHz by a high stability oscillator producing a small magnetic field (~5 mT) which is uniform to about 1% over a volume of 10.8 cm<sup>3</sup> [Graham, 1966]. The shaft rotates the sample at 5 hz and the susceptibility anisotropy in the plane of the sample at right angles to the drive shaft imparts a 10 hz amplitude modulation to the 3 KHz signal from the bridge. The bridge balance signal is isolated by synchronous detection at 3 KHz and, after appropriate amplification, is synchronous detected at twice the spin frequency (10 hz) using a reference signal generated by a photo-diode and shutter attached to the sample-drive shaft.

(2) Both in-phase and out-of-phase components of the specimen's AMS are then measured normal to four tetrahedral axes of the cubic sample holder (Figure 2.6a). The two AMS components about each axis are also measured with the sample rotated 180° about the reference direction (e.g. the directions marked A and A' on the sample holder; Figure 2.5a). The in-phase component should then remain the same while the out-of-phase component should change sign allowing visual confirmation that the equipment is operating correctly. Before each spin the A.C. bridge is re-balanced, then the in-phase and out-of-phase bridge balance signals are recorded after enough data has been averaged to give satisfactory signal to noise ratios. The eight orientations result in 16 components of susceptibility differences, i.e. eight in-phase and eight out-of-phase components (i.e. *I* and *Q*'s). After the eighth spin (orientation) the bulk susceptibility is measured along with the reference direction. It is easy to show that the bulk susceptibility measurement has no effect on the resulting eigenvector directions. However, it is needed in the calculation of such parameters as the magnetic lineation and foliation.

Figure 2.5(a) Photograph of the Balance Bridge Susceptibility Spinner used at the University of Hawaii paleomagnetism laboratory. Photo is taken looking along the measured susceptibility direction perpendicular to the spin axis, the sample is mounted in a plastic cube holder on a drive shaft that passes through the center of two coils (Helmholtz coils) forming one arm of a balanced four arm A.C. bridge.

(b) Schematic layout of the Balanced Bridge Susceptibility Spinner. Showing the four arms of the A.C. Bridge, The sample centered within one arm of the balanced bridge, the balancing system, 3 Khz oscillator, and the balance signal pickup



## Balanced Bridge System

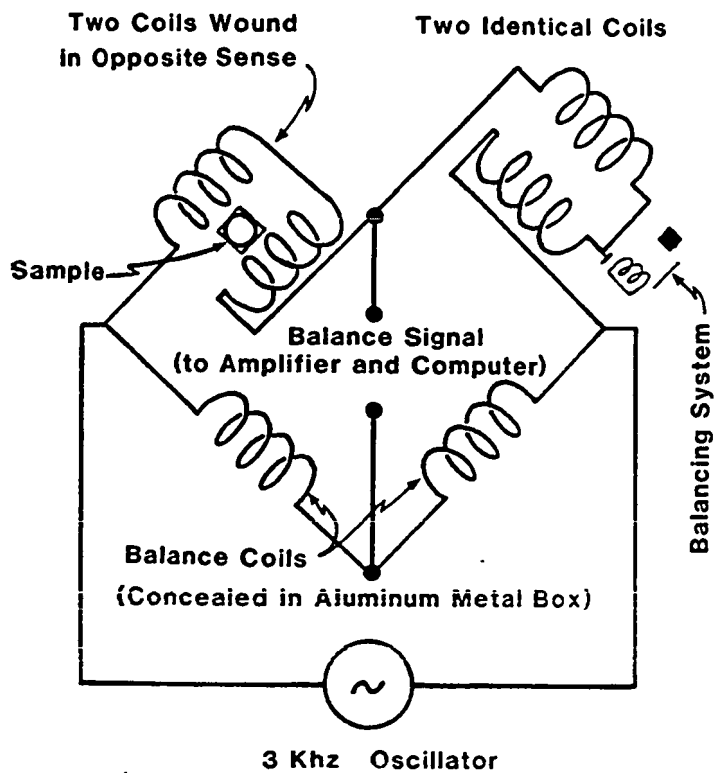
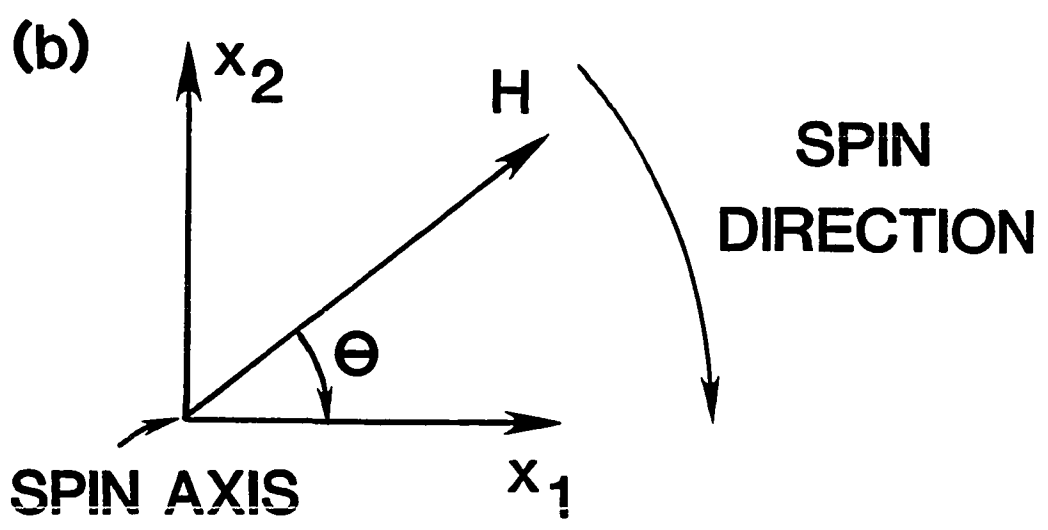
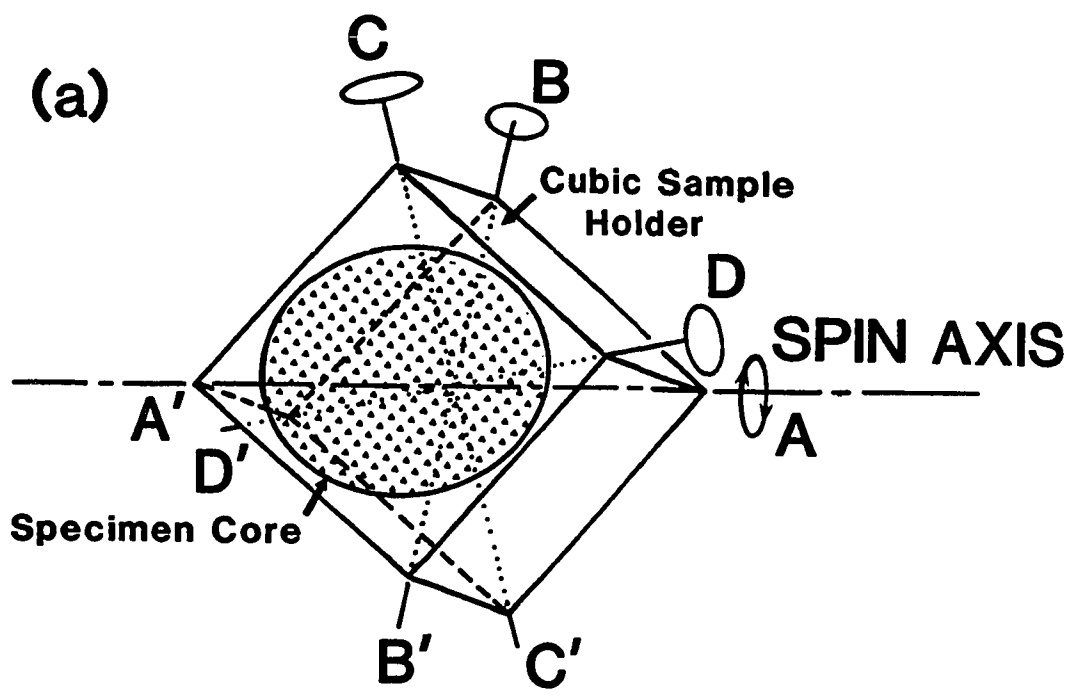


Figure 2.6(a ) Cartoon showing the core specimen mounted within the cubic sample holder, and the specimen's eight orientations (taken along the vertices of the sample holder referred to as the four tetrahedral spin axes) in which the AMS is measured.

(b) A schematic of the sample spin direction, and the orientation of the applied field ( $H$ ), which can be resolved into two components  $x_1$  and  $x_2$ . The A.C. bridge balance is sensitive to the slight changes in the components measured normal to the spin axis (e.g. in the plane of the paper).



(3) The known susceptibility tensor of the sample is then calculated by a program written in MS-Quick Basic [Lienert, 1988] for a PC-compatible microcomputer that inverts the 17 x 6 matrix set of equations (i.e. 17 sets of equations and 6 unknowns) relating the 17 measured components to the six elements of the susceptibility tensor. Briefly, let the components measured in the spin plane (Figures 2.6a and b) be  $x_1, x_2$  and the inducing field  $H$  is applied at an angle  $\theta$  to  $x_1$ . The components of  $H$  along the two axes will be

$$H x_1 = H \cos\theta \quad (21)$$

$$H x_2 = H \sin\theta \quad (22)$$

The induced magnetization  $M_j$  (from the generalized form of Equation 4) along  $x_1$  and  $x_2$  will be

$$M x_1 = (\chi_{11} H \cos\theta + \chi_{12} H \sin\theta) \rho \quad (23)$$

$$M x_2 = (\chi_{12} H \cos\theta + \chi_{22} H \sin\theta) \rho \quad (24)$$

Combining Equations 25 and 26 gives

$$M = \rho H \left[ \frac{1}{2} (\chi_{11} - \chi_{22}) \cos 2\theta + \chi_{12} \sin 2\theta + \frac{\chi_{11} + \chi_{22}}{2} \right] \quad (25)$$

The angle  $\theta$  is varying with time by rotating at an angular frequency,  $\omega t + \phi$  where  $\phi$  is a fixed phase angle, and corresponds to the angle between  $H$  and the instantaneous position of the  $x_1$  axis (Figure 2.6b). In practice  $\phi$  can be set by adjusting the phase of the reference signal used to synchronously detect the resulting output. The two values used are adjusted using a reference sample and are set at  $\phi = 0$  (the in-phase component,  $I$ ) and  $\phi = -\pi/4$  (the out-of-phase quadrature) relative to a reference direction on the sample holder. Thus the measured output  $I$  and  $Q$  are:

$$I = 1/2 (\chi_{11} - \chi_{22}) \quad (26)$$

and

$$Q = \chi_{12} \quad (27)$$

where  $\chi_{11}$ ,  $\chi_{22}$ , and  $\chi_{12}$  are the components of the susceptibility tensor along the two reference directions corresponding to  $I$  and  $Q$ .  $I$  and  $Q$  components are measured for eight spins about the diagonals of the cubic sample holder.

(4) The measured  $I$ 's and  $Q$ 's, as well as the bulk susceptibility are related to  $\chi$ , the six components of susceptibility relative to the common sample holder axis are related by the matrix equation

$$d = R\chi \quad (28)$$

where,  $d$  is the column of measured components, and  $R$  is a  $17 \times 6$  matrix of coefficients calculated from the fixed set of angles representing the directions of each measured component.  $\chi$  is then obtained from  $d$  using the least squares inverse

$$\chi = (R^T R)^{-1} R^T d \quad (29)$$

The covariance matrix for  $\chi$  is then

$$\text{Cov}(\chi) = (R^T R)^{-1} \sigma d^2 \quad (30)$$

where,  $\sigma d^2$  is the mean square misfit between observed and predicted values of the data,  $d$ . (Refer to Appendix B for the actual values of  $R$  and its least squares inverse).

## STATISTICS

(1) The method used to eliminate the effect of fluctuating mean susceptibility in a group of AMS samples is to normalize each susceptibility tensor of each individual specimen by

dividing it by its mean susceptibility. The normalized tensor of a specific specimen will then be

$$\chi_{\text{norm}} = \chi / \bar{\chi} \quad (31)$$

where,

$$\bar{\chi} = \frac{\chi_{11} + \chi_{22} + \chi_{33}}{3} \quad (32)$$

Since all the operations will deal exclusively with normalized tensors, we shall omit the index "norm". From *Jelinek* [1978], the principal susceptibilities and principal directions, derived from the normalized mean tensor, will be denoted by  $\chi_1, \chi_2, \chi_3$ , and the eigenvectors  $p_1, p_2, p_3$ , respectively.

(2) It is now desirable to calculate the mean tensor for  $N$  individual specimens from a particular geological body or locality. A problem that has plagued this analysis, as well as those of previous investigations, has been to choose a suitable statistical parameter which represents the scatter in these  $N$  tensors and which could be estimated from the AMS measurements. One approach that has a certain amount of appeal because it is illustrative and easy to effect, is to calculate the mean values of the principal susceptibility directions and their circular (cone) confidence regions for directed data, i.e. *Fisherian statistics* [*Fisher*, 1953]. This approach was used by *Knight and Walker* [1988], in which the  $\alpha_{95}$ 's in their Table 1, page 4308, are computed by *Fisher's* method for the  $N$  eigenvectors for each of  $\chi_1, \chi_2$ , and  $\chi_3$ . However, there are a number of objections to using *Fisher's* method.

- (i) The regions of confidence of the resultant principal directions on a unit sphere are assumed to be circles (i.e.  $\alpha_{95}$  represents the projection of the half angle of 95% cone of confidence; [*Fisher*, 1953]), and therefore do not describe the directional character of the uncertainty in the determination of the mean principal directions of the representation ellipsoid.

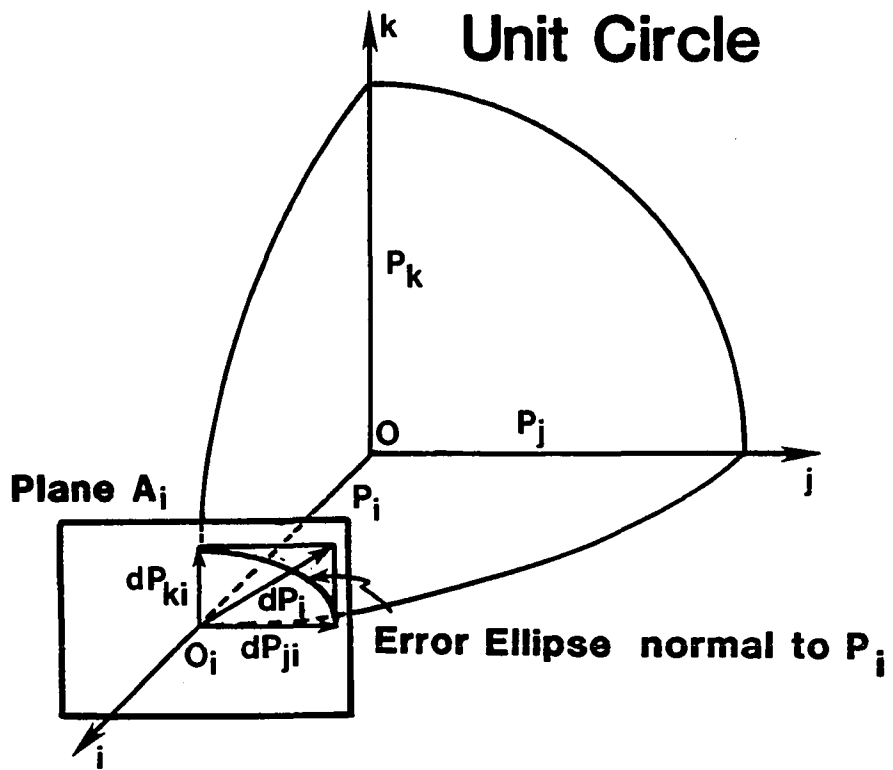
(ii) Fisher statistics assumes that each eigenvector is independent of the other two, whereas the three eigenvectors for each tensor (and the mean) must be orthogonal. For a prolate tensor this method will tend to over estimate the uncertainty in determining the minimum principal direction while under estimating the confidence interval for the maximum principal direction.

(3) It is now desirable to calculate the mean normalized tensor for a sample of  $N$  specimens, having tensors  ${}^1\chi_i, {}^2\chi_i, \dots, {}^N\chi_i$  which is given by:

$$\hat{\chi} = N^{-1} \sum_{k=1}^N \chi_k \quad (33)$$

The interpretation of the variability of the principal directions for the mean normalized tensor is determined using *Jelinek's* [1978] statistical approach to construct error ellipses for the mean normalized tensors. Of most interest are the regions of confidence about the mean principal susceptibility directions  $\hat{P}_1, \hat{P}_2, \hat{P}_3$ . Figure 2.7 shows the ellipsoidal confidence region of the  $i$ -th principal direction normal to  $P_i$ . The ellipse is considered to be an approximate  $(100 - \alpha)\%$  ellipse, and we have chosen the 95% confidence interval for constructing the lengths of the semi-axes of the ellipse on the unit sphere, e.g. the ellipse  $\xi_i$  in plane  $A_i$  and centered about the  $O_i$  end point is shown in Figure 2.7. The ellipse of 95% confidence about each mean tensor is projected centrally onto a unit sphere, and denoted by the maximum and minimum confidence angles of vector  $P_i$  (the other two mutually perpendicular error ellipses are also projected on the unit sphere, refer to appendices A and B). The three error ellipses at the 95% confidence interval are defined by the half angles (maximum and minimum axes) of the cones of confidence based on the mean directions for  $N$  specimens.

Figure 2.7 Depicts the unit circle of the equal-area AMS plots and the interpretation of the variability of the principal AMS directions (at the 95% confidence interval) after *Jelinek* [1978]. In this example the error ellipse is taken normal to the vector  $P_i$  (e.g. the variability of the mean maximum AMS direction)



## CHAPTER 3

### AMS RESULTS FOR THE KOOLAU DIKE COMPLEX

#### BASIC PRINCIPLES OF AMS

AMS develops either from anisotropy within the crystal lattice of magnetic minerals (i.e., magnetocrystalline anisotropy) or from nonsphericity of shape of individual mineral particles. A strong magnetocrystalline anisotropy arises primarily from samples containing hematite (rhombohedral crystal structure) as the spontaneous magnetization along the c-axis is very low, and from shape alignments in samples containing magnetite (cubic crystal structure). The crystallographic axes along which the spontaneous magnetization tends to lie are called the *easy* directions while the axes along which it is hard to produce magnetic saturation are called *hard* directions (*Bhathal*, 1971). In magnetite the easy directions lie along the [111] axes. The magneto-crystalline energy can be defined as the work required to make the spontaneous magnetization lie along a certain direction compared to an easy direction. For cubic minerals such as magnetite this energy is significant, and can only be observed in the presence of high magnetic fields, because their intrinsic susceptibilities are isotropic. Hematite on the other hand is ferromagnetic only in the basal plane (which is therefore a plane of high susceptibility), and similarly other non-cubic minerals like pyrrhotite, and members of the ilmenite-hematite series owe their susceptibility anisotropy to the alignment of their crystal axes (i.e. *magnetocrystalline anisotropy*) [*Uyeda et al.*, 1963; *Bhathal*, 1971].

*Grabovsky and Brodskaya* [1958] suggested additional anisotropy can occur if the magnetic grains occur in rows or planes and are close enough to each other, preferably in contact, that they can create a significant *textural anisotropy* (which is a special case of shape anisotropy) even if individual magnetic grains are isotropic. Textural anisotropy occurs when rocks contain a high concentration of magnetite.

*Bhathal and Stacey* [1969] and *Bhathal* [1971] describe another kind of susceptibility anisotropy which is due to *domain alignment*. It occurs when the intrinsic magnetic susceptibility of any ferro- or ferrimagnetic mineral is a function of the orientation of the applied field with respect to the domain directions. *Bhathal and Stacey* [1969] showed that for some basalt samples an induced anisotropy arises from domain alignment which is produced by treating stationary specimens in a strong alternating field. *Bhathal* [1971] noticed that it is easier to enhance the intrinsic anisotropy by aligning the domains with the long axes of the grains than it is to reduce the intrinsic anisotropy by a perpendicular alignment of domains. He found that the domains are harder to align in smaller grains (e.g. grains approaching single or pseudo-single domain size) due to their higher coercive forces and hence a larger field is required to move (roll-over) the domain walls in them. Anisotropy due to domain alignment will therefore be important in rocks that contain a significantly higher percentage of larger multi-domain magnetite grains. Based on limited petrographic studies, large multi-domain magnetite grains do not seem to make up a significant proportion of the Koolau specimens, that is, most of the magnetite is very fine-grained ( $\leq 0.1$  mm diameter), homogeneous, and generally lacks exsolution lamella.

In summary, *Bhathal* [1971], *Taira* [1976] and *Taira and Lienert* [1979] show that AMS can be related to any one or a combination of the following five effects:

- (1) *Shape of individual magnetic grains.*
- (2) *Shape of the bulk sample.*
- (3) *Distribution of magnetic minerals within the sample (textural anisotropy).*
- (4) *Magnetocrystalline anisotropy of individual magnetic grains.*
- (5) *Domain alignment.*

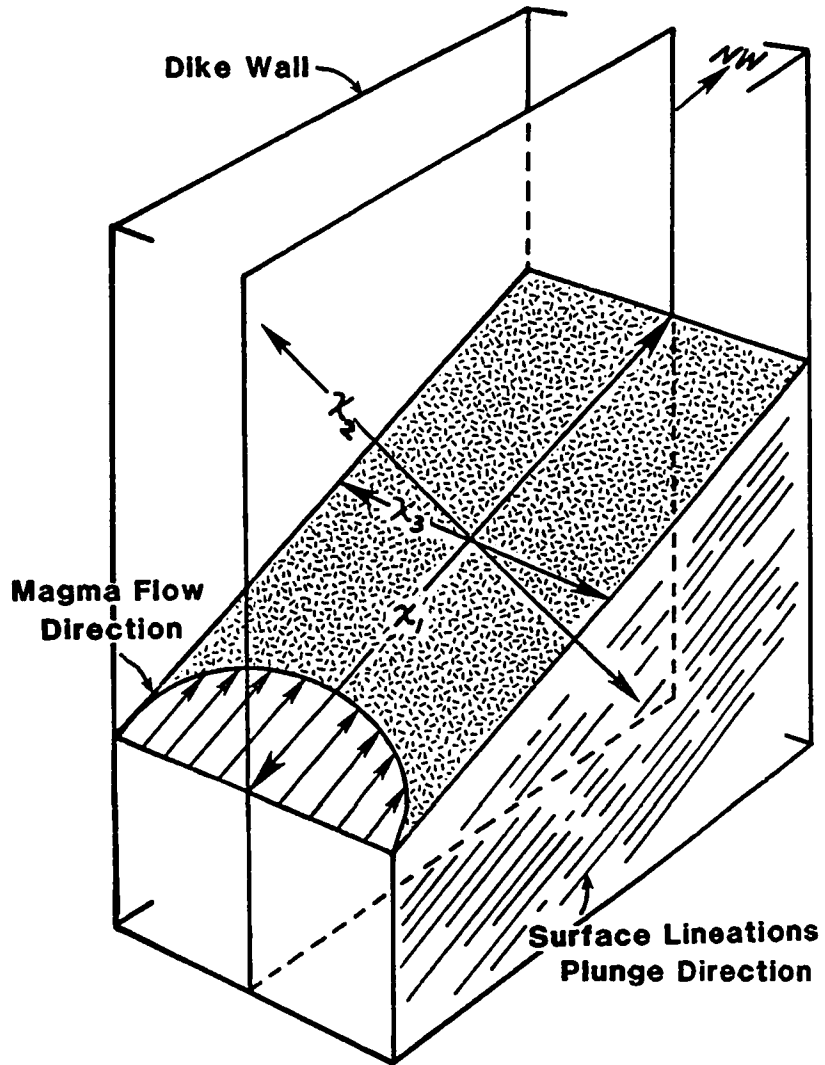
Since most rocks contain grains with irregular shapes, the most important effect for AMS is related to shape anisotropy and is a result of the demagnetizing factors in three mutually perpendicular directions across a non-equidimensional grain (refer to Chapter 2,

Figure 2.1b). Shape anisotropy due to aligned elongate (prolate) particles or to planer or linear distributions of particles seems to be the most common cause of AMS in rocks. These prolate or oblate grains can be aligned by simple gravitational settling of platy or elongated grains during sediment deposition, or by flow mechanisms in intrusive igneous bodies, lava flows, and ash flow tuffs (ignimbrites). However, this primary fabric is often modified to a lesser or greater extent by a large number of factors. In sedimentary rocks these factors include: alignment in the presence of the geomagnetic field, current flow, bottom slope angle, grain size and shape, vertical compaction, bioturbation, and particle aggregation or flocculation [Ellwood, 1988]. Factors that can alter the primary fabric in igneous rocks include: post-emplacement crystallization, gravitational settling (particularly in low viscosity melts), applied stresses, chemical or hydrothermal alteration, compaction, and metamorphism. Other factors that may appear to modify the primary fabric are experimental problems encountered during sample preparation, and measurement.

The conclusion that can be derived from measurements made on various rock types is that in general the maximum magnetic susceptibility lies in the bedding or foliation plane for sediments [Rees, 1965; Taira and Lienert, 1979; Ellwood, 1988], some igneous rocks (e.g. ignimbrites; Ellwood and Fisk, 1977; Knight et al., 1986), and metamorphic rocks [Kligfield et al., 1977]. Furthermore, most sediments, some pyroclastic deposits (e.g. ignimbrites), and possibly also some lava flows tend to exhibit an oblate-shaped magnetic fabric, that is slightly imbricated in the direction of flow. In volcanic and intrusive rocks alignment of already crystallized (anisotropic) minerals may occur during laminar magma flow, in which gravity and hydrodynamic forces normally result in elongated and platy minerals being orientated within the flow plane. Depending on the velocity profile across the dike width, and its propensity toward turbulent flow, the elongate minerals will be further constrained into orientations either parallel or perpendicular to the flow direction along the plane of maximum shearing (Figure 3.1). It is generally thought that grain orientations resulting from primary igneous flow are generally weak unless the magma has

Figure 3.1. Block sketch of idealized arrangement of AMS axes relative to the inferred magma flow direction based on the orientation of macroscopic surface lineations along the dike walls. The maximum  $\chi_1$  AMS axis is thought to align in the dike foliation plane (this is an  $\chi_1/\chi_2$  foliation, not a foliation of platy minerals as ordinarily defined) and parallel to the magma flow azimuth. The intermediate  $\chi_2$  axis is normal to  $\chi_1$  and is also in the dike foliation plane, while the minimum  $\chi_3$  axis is aligned parallel to the dike pole.

## Orientation of the Principal Susceptibilities

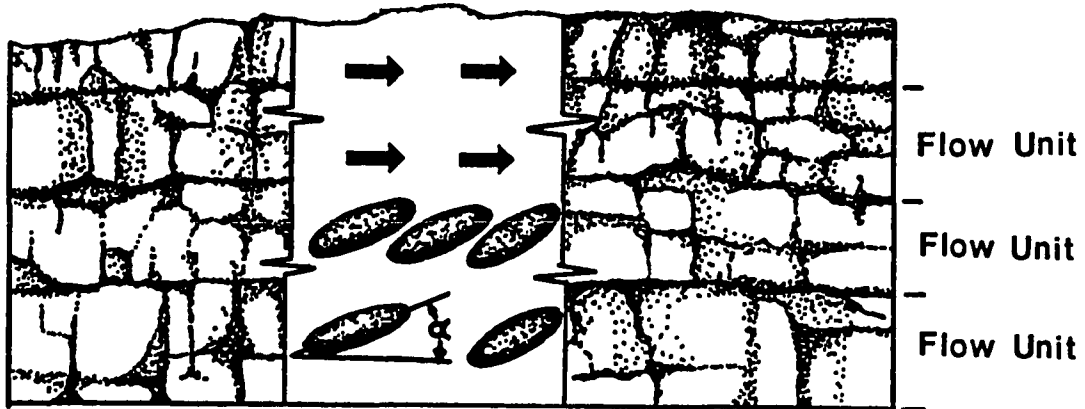


a relatively high viscosity. For low-viscosity pahoehoe lava flows this corollary seems to be substantiated, since they commonly have low total susceptibility anisotropy (e.g. Hawaiian lava flows typically have  $H \leq 0.5\%$ ) and thus have most random AMS fabrics. Out of four pahoehoe lava flows sampled, only one (CV67) shows moderate clustering of the  $\chi_1$  axes, and is inferred to have a magnetic imbrication of  $24^\circ$  parallel to the presumed flow direction (Figure 3.2). Only one aa-lava flow was sampled. It also shows a good clustering of the  $\chi_1$  axes very near the presumed lava flow direction, and has a much higher total susceptibility anisotropy ( $H = 1.35\%$ ) than the pahoehoe lava flows. Two factors that might be responsible for the aa-lava flow having a higher anisotropic susceptibility and non-random AMS fabric are: (1) a generally higher flow velocity, in which laminar flow forces are greater than the gravitational effects and topographic irregularities encountered during flow; (2) the slightly higher susceptibilities probably represent a higher modal percentage of titanomagnetite grains present. One possible explanation for the presumed difference in the amount of titanomagnetite present in pahoehoe- versus aa-type flows erupted from the same fissure could be that aa-lavas are sometimes erupted cooler, and therefore might be more crystalline, and hence more magnetic. Though inconclusive (based on the limited number of lava flows), this study suggests that aa lava flows may be better suited for future AMS fabric studies. Their apparent higher viscosities and flow velocities have resulted in higher susceptibility, total susceptibility anisotropy ( $H > 1.0\%$ ), and better degrees of clustering of their axial distributions.

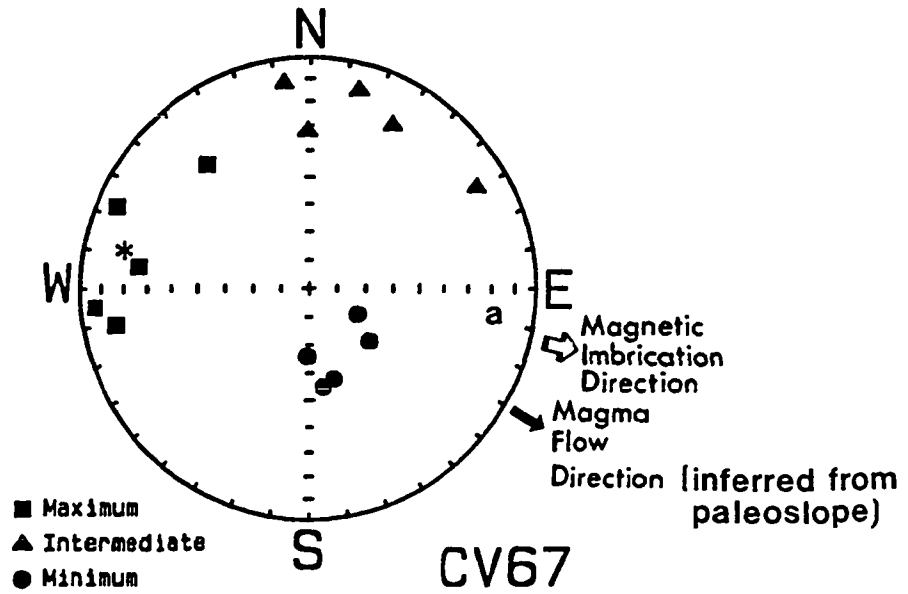
In the magnetic fabric study of intrusive igneous bodies one might expect that in near-vertical dikes, viscosities are high enough to counterbalance the gravitational buoyancy forces that would tend to rotate the anisotropic grains parallel to the downward directed gravity component once the magma has stopped flowing. The mostly fine-grained doleritic to aphyric texture of the Koolau dikes suggests that they formed mainly from (primitive) low-viscosity tholeiitic magmas. Because the alignment of primary magnetic grains can represent a significant shape anisotropy in the Koolau dikes (the mean total percent

Figure 3.2 AMS plot of a recent lava flow from Kilauea's East Rift Zone. The minimum AMS axes are slightly inclined (mean= 24°) to the vertical direction and are inferred to be an imbrication near the base of the flow unit, hence the imbrication direction of this tholeiitic lava flow (CV67) is 100° and plunges 24° toward the presumed source (i.e. the magnetic imbrication angle  $\alpha = 90^\circ - \text{plunge of minimum } \chi_3 \text{ axis}$ ). Note that there is close agreement between the magma flow direction inferred from the paleoslope and the magnetic imbrication direction.

# PAHOEHOE LAVA FLOWS



$\alpha$  = Imbrication Angle



anisotropy  $H = 2.4\%$ , and can commonly be as high as 4–8%), and since 90% of the time the maximum ( $\chi_1$ ) AMS plunge direction is non-vertical (i.e. with a  $\chi_1$  plunge of  $<70^\circ$ ), then it seems safe to argue that gravitational forces did not dominate over the rheological forces. Also, AMS fabrics agree well with the presumed magma flow directions inferred from the mean plunge directions of macroscopic surface lineations, particularly for samples collected along the dike margins, and this supports the idea that the dike magmas freeze in the direction of initial magma flow before gravitational stresses could realign the grains. Since the thinner dikes (1–2 m wide) should have the shortest cooling histories, on the order of days to weeks [Fedotov, 1978; Delaney and Pollard, 1982], they are thought to be the best candidates for AMS fabric studies. This may also be valid for samples collected near the quenched margins of wider dikes ( $>2$  m), where cooling is quickest. However, samples collected from the centers of a number of dikes show anomalous AMS directions when compared to the mean axial distributions of samples collected from the dike margins. This variation in AMS fabric across the dike width could suggest that the gravitational effects or other factors (e.g. such as a longer cooling history) might be significant along the centers of the wider dikes ( $>2$  m).

For the Koolau dikes the AMS representation ellipsoid is assumed to be due to the preferred alignment of the magnetic grains resulting from either emplacement of a partially crystallized magma, crystal growth during or following magma emplacement, and/or realignment in a stress field. Though the dike specimens are only slightly anisotropic (many have  $H$  values near 2–4%), the AMS data obtained from these dikes do exhibit significant axial clustering. Hence a slight prolate component in the plane of foliation, perpendicular to the velocity gradient, is interpreted to indicate the initial magma flow direction during dike injection or the early stages of dike propagation.

## AMS DATA FOR THE KOOLAU DIKE COMPLEX

The following section is a brief discussion of the AMS measurements for 660 samples from 71 dikes and an infilled lava tube of the Koolau volcano (refer to Figure 1.11 for the sample sites and Tables 3.1 and 3.2 for a summary of the AMS measurements). Also presented is a preliminary study of the AMS fabric of 4 recent lava flows from the Island of Hawaii.

$H$  varies between 0.2% and 14.1% with a mean value of 2.4% (standard deviation 1.82), which is well within the experimental precision of the balanced bridge susceptibility spinner used in this study. An anisotropy of more than 10% may influence the directions of remanent magnetization [Uyeda *et al.*, 1963]; only 13 samples exceeded this value. It is also noted that the mean total anisotropy ( $H$ ), calculated from the mean tensor, is not necessarily equivalent to the arithmetic mean of the  $H$  values for each specimen (refer to the statistical data in Appendix A). As discussed earlier, the AMS tensor is defined by three orthogonal vectors with lengths and magnitudes. Therefore the mean  $H$  value will generally be less than the arithmetic *mean* total anisotropy (i.e. if its standard deviation is high), unless the susceptibility tensors for the individual specimens are tightly clustered.

A plot of  $V$  versus  $H$  for 525 AMS measurements is shown in Figure 3.3a. In this figure, 48% of the samples fall in the prolate ellipsoid field, 50% fall in the oblate field, and 2% have  $V=45^\circ$ ; 77% of the samples have Graham's  $V$  values between  $30^\circ$  and  $60^\circ$ . Another type of two-axis ratio plot used to classify the shape of individual grains and describe the form of the AMS ellipsoid, following the convention of Flinn [1962] for strain ellipsoids, is shown in Figure 3.3b and plots the ratio of  $\chi_2/\chi_3$  against the ratio of  $\chi_1/\chi_2$ . Of the 527 samples plotted, 48% fall in the prolate ellipsoid field, 46% in the oblate field, and 6% have  $a=b$  (the threshold between oblate and prolate grains). As shown in Table 3.1, the mean  $L$  is less than  $F$  at 56 sites, implying that the magnetic fabrics of the Koolau dikes are mainly foliate (80%). Also shown in Table 3.1 is the mean  $E$  factor or eccentricity for each dike (defined by Hrouda *et al.* [1971] as,  $\chi_2^2/\chi_1\chi_3$ ). Hrouda *et al.*

TABLE 3.1 Summary of Anisotropy of Magnetic Susceptibility (AMS) and Macroscopic Su

Site	N <sub>1</sub> /N <sub>2</sub>	Macroscopic Flow Lineation DIKE			$\bar{\chi}_1$			$\bar{\chi}_2$			$\bar{\chi}_3$		
		Azimuth (deg)	Plunge, $\chi \times 10^{-3}$ (deg)	$\chi \times 10^{-3}$ (emu/gm)	D <sub>max</sub>	I <sub>max</sub>	$\alpha_{95}$ (max:min)	D <sub>int</sub>	I <sub>int</sub>	$\alpha_{95}$ (max:min)	D <sub>min</sub>	I <sub>min</sub>	$\alpha_{95}$ (max:min)
KD1	11/11	136	75SE	2.408	320.7	-64.9	74:36	98.4	-19.1	74:36	13.9	15.6	56:37
KD2	6/4	126	25SE	2.557	312.7	-11.4	11:3	199.0	-63.4	15:6	47.8	-23.7	13:5
KD3	6/4	120	7SE	2.572	303.3	11.1	25:1	231.6	-58.0	34:4	26.8	-29.6	26:2
KD4	8/5	130	30SE	2.675	302.3	-6.9	14:13	196.7	-65.8	15:13	35.2	-23.0	17:10
KD5	10/8	140	6SE	2.249	327.6	-31.1	21:9	115.3	-54.5	65:10	48.0	15.4	65:15
KD6	9/9	130	24SE	2.331	324.8	-0.6	9:6	233.8	-59.7	13:7	55.1	-30.3	14:6
KD7	7/7	125	61SE	2.865	355.8	75.2	14:6	140.1	12.1	21:7	51.9	-9.4	17:6
KD8	4/3	105	63ESE	2.265	332.7	59.2	40:4	108.3	23.1	40:4	26.8	-19.3	7:5
KD9	5/5			3.645	76.0	23.3	23:9	165.2	-1.9	58:5	70.7	-66.6	58:11
KD10	12/12	100	38ESE	4.428	49.5	9.9	37:9	143.5	21.8	38:16	296.8	65.8	20:11
KD11	11/11	305	10NW	5.416	298.3	0.8	24:12	207.2	54.3	33:21	28.9	35.7	33:12
KD12	8/6	140	25SE	4.436	19.2	63.1	21:5	198.9	26.9	45:17	289.0	0.1	45:4
KD13	12/12			2.198	314.7	-31.3	23:16	132.1	-58.7	24:10	44.0	1.2	19:16
KD14	6/6			6.145	47.7	49.4	53:21	128.4	-7.9	56:27	31.7	-39.5	43:25
KD15	6/6	50	40NE	2.222	58.7	24.5	24:8	153.7	10.8	44:20	85.6	-62.9	43:8
KD16	8/6	230	40SW	2.714	66.7	-13.0	22:13	211.2	-74.2	29:18	334.6	-8.9	27:13
KD17	7/7	120	9SE	2.955	285.7	-16.2	19:6	152.7	-67.0	48:8	20.4	-15.9	48:13
KD18	10/9			2.268	314.2	-28.3	22:13	149.5	-61.1	18:11	50.0	-5.2	20:10
KD19	5/4			0.887	331.1	-14.2	27:13	147.0	-75.8	27:3	60.8	1.0	17:6
KD20	7/4			2.038	4.3	-21.2	10:3	179.9	-68.8	23:8	273.7	-1.5	24:6
KD21	9/7	331	25NW	5.311	320.3	28.6	9:8	133.0	61.2	28:7	48.6	-3.1	27:9
KD22	13/7	215	68SW	2.559	50.6	-37.3	22:8	187.7	-43.9	24:22	301.7	-23.0	24:8
KD23	9/9	310	70NW	3.586	302.2	72.4	17:9	142.4	16.5	15:12	50.7	5.7	18:11
KD24	6/6	311	45NW	5.779	8.5	52.3	16:5	244.3	23.5	17:4	321.2	-27.6	11:5
KD25	8/7	315	32NW	5.080	306.2	62.2	16:4	150.8	24.6	46:9	56.3	9.8	46:13
KD26	12/10			3.841	294.2	16.8	16:10	113.5	73.2	20:11	24.2	-0.2	24:6
KD27	9/9			1.852	69.4	70.0	39:6	142.4	-6.1	39:10	50.3	-19.0	11:6
KD28	10/10	120	5SE	7.393	275.9	-17.8	21:6	156.3	-57.0	20:5	15.2	-26.8	9:4
KD29	10/10			4.507	40.3	53.2	19:14	114.9	-11.2	19:13	17.1	-34.5	18:4
KD30	10/10			5.817	299.4	17.5	52:17	225.2	-40.9	51:19	11.7	-43.9	23:18
KD31	7/7	125	10SE	3.915	320.0	23.1	23:6	123.0	65.9	15:4	47.3	-6.3	23:10
KD32	13/9	270	0	4.452	289.2	8.8	11:3	266.1	-80.5	12:7	18.6	-3.7	10:4
KD33	10/10	260	75W-SW	2.647	57.7	-72.5	27:9	107.6	11.5	27:8	14.9	13.0	10:5
KD34	7/7	90	56E	4.222	301.4	-48.7	19:7	91.4	-37.3	17:7	13.4	15.2	12:6
KD35	14/14			1.212	329.5	-20.7	17:15	130.1	-68.2	20:16	57.0	6.6	23:10
KD36	4/4	125	20SE	0.641	289.1	-26.7	20:4	118.5	-63.0	15:4	21.1	-3.8	21:6
KD37	8/6			0.332	324.8	-67.5	17:8	132.0	-22.0	44:17	43.8	4.5	44:8
KT38	16/16			0.877	339.8	1.5	14:6	246.9	61.8	70:8	70.6	28.1	70:10
KD39	14/13			1.036	308.7	51.3	53:8	124.8	38.7	53:15	36.3	-1.9	16:8
KD40	9/6	140	74SE	0.477	333.3	50.9	24:8	123.8	35.2	24:9	44.5	-14.7	11:8
KD41	6/6			0.732	299.9	-59.3	48:29	115.3	-30.7	48:25	26.5	2.0	36:11
KD42	8/8	120	15SE	4.605	304.5	-24.3	19:11	123.4	-65.7	23:13	34.3	0.4	20:6
KD43	11/11	145	23SE	4.741	305.5	-24.8	15:13	140.2	-64.5	14:4	38.1	-5.7	15:7
KD44	7/7			1.818	317.3	4.4	13:10	225.0	27.8	42:9	55.6	61.8	42:12
KD45	8/8			3.896	351.3	-26.3	27:14	253.9	-14.7	32:16	317.7	59.4	25:13
KD46	7/7	135	39SE	5.683	293.3	56.9	16:5	141.0	30.0	7:5	43.5	12.7	16:5

ic Susceptibility (AMS) and Macroscopic Surface Lineations for 76 Sites

		$\bar{\chi}_2$		$\bar{\chi}_3$											
max	$\alpha_{95}$	Dint	Iint	$\alpha_{95}$	Dmin	Imin	$\alpha_{95}$	H	V	L	F	$\chi_1/\chi_2$	$\chi_2/\chi_3$	E	width, dip,
(max:min)			(max:min)			(max:min)	(%)	(deg)	(%)	(%)				(cm)	(deg)
74:36	98.4	-19.1	74:36	13.9	15.6	56:37	0.75	38.6	0.3	0.5	1.003	1.005	1.002	76	90
11:3	199.0	-63.4	15:6	47.8	-23.7	13:5	1.86	57.4	1.3	1.2	1.013	1.005	0.992	72	77NE
25:1	231.6	-58.0	34:4	26.8	-29.6	26:2	4.40	57.1	3.1	2.8	1.031	1.013	0.983	17	75NE
14:13	196.7	-65.8	15:13	35.2	-23.0	17:10	3.46	55.7	2.4	2.3	1.024	1.011	0.988	105	82NE
21:9	115.3	-54.5	65:10	48.0	15.4	65:15	1.37	64.0	1.1	0.8	1.011	1.003	0.992	115	83NE
9:6	233.8	-59.7	13:7	55.1	-30.3	14:6	4.19	54.1	2.7	2.8	1.027	1.015	0.988	90	80NE
14:6	140.1	12.1	21:7	51.9	-9.4	17:6	3.24	29.1	0.8	2.7	1.008	1.025	1.033	50	78NE
40:4	108.3	23.1	40:4	26.8	-19.3	7:5	1.54	31.3	0.4	1.3	1.004	1.011	1.007	65	85NE
23:9	165.2	-1.9	58:5	70.7	-66.6	58:11	2.14	54.7	1.4	1.4	1.014	1.007	0.993	33	15SE
37:9	143.5	21.8	38:16	296.8	65.8	20:11	2.15	41.5	0.9	1.7	1.009	1.012	1.003	74	75NE
24:12	207.2	54.3	33:21	28.9	35.7	33:12	2.53	62.4	2.0	1.5	1.020	1.005	0.986	48	85NE
21:5	198.9	26.9	45:17	289.0	0.1	45:4	3.56	46.4	1.9	2.6	1.019	1.017	0.999	31	85NE
23:16	132.1	-58.7	24:10	44.0	1.2	19:16	1.78	39.0	0.7	1.4	1.007	1.011	1.004	57	90
53:21	128.4	-7.9	56:27	31.7	-39.5	43:25	1.98	45.3	1.0	1.5	1.010	1.010	1.000	248	90
24:8	153.7	10.8	44:20	85.6	-62.9	43:8	0.5	57.6	0.4	0.3	1.004	1.001	0.998	42	75SE
22:13	211.2	-74.2	29:18	334.6	-8.9	27:13	2.26	43.9	1.1	1.7	1.011	1.012	1.001	275	75NW
19:6	152.7	-67.0	48:8	20.4	-15.9	48:13	1.94	69.7	1.7	1.1	1.017	1.002	0.986	83	70NE
22:13	149.5	-61.1	18:11	50.0	-5.2	20:10	1.77	46.2	0.9	1.3	1.009	1.009	0.999	230	90
27:13	147.0	-75.8	27:3	60.8	1.0	17:6	1.16	39.3	0.5	0.9	1.005	1.007	1.002	175	90
10:3	179.9	-68.8	23:8	273.7	-1.5	24:6	2.94	50.9	1.8	2.0	1.018	1.012	0.994	200	80NE
9:8	133.0	61.2	28:7	48.6	-3.1	27:9	4.02	63.6	3.2	2.4	1.032	1.008	0.977	45	75NE
22:8	187.7	-43.9	24:22	301.7	-23.0	24:8	1.20	40.9	0.5	0.9	1.005	1.007	1.002	45	75NW
17:9	142.4	16.5	15:12	50.7	5.7	18:11	3.39	54.5	2.2	2.3	1.022	1.012	0.989	20	85NE
16:5	244.3	23.5	17:4	321.2	-27.6	11:5	4.07	47.1	2.2	3.0	1.022	1.019	0.997	200	80NE
16:4	150.8	24.6	46:9	56.3	9.8	46:13	2.13	56.5	1.5	1.4	1.015	1.007	0.992	97	85NE
16:10	113.5	73.2	20:11	24.2	-0.2	24:6	3.72	63.0	2.9	2.2	1.030	1.008	0.979	85	85SW
39:6	142.4	-6.1	39:10	50.3	-19.0	11:6	7.61	27.5	6.9	1.6	1.016	1.064	1.047	97	80NE
21:6	156.3	-57.0	20:5	15.2	-26.8	9:4	6.74	35.2	2.3	5.7	1.022	1.047	1.024	85	75NE
19:14	114.9	-11.2	19:13	17.1	-34.5	18:4	4.64	45.7	2.4	3.5	1.024	1.023	0.999	75	60NE
52:17	225.2	-40.9	51:19	11.7	-43.9	23:18	3.44	27.0	0.7	3.1	1.007	1.028	1.035	101	60NE
23:6	123.0	65.9	15:4	47.3	-6.3	23:10	4.57	48.9	2.6	3.3	1.026	1.020	0.994	125	80NE
11:3	266.1	-80.5	12:7	18.6	-3.7	10:4	5.03	54.2	3.3	3.4	1.033	1.018	0.985	40	85S
27:9	107.6	11.5	27:8	14.9	13.0	10:5	4.19	36.5	1.5	3.5	1.015	1.028	1.013	43	80SE
19:7	91.4	-37.3	17:7	13.4	15.2	12:6	6.61	44.2	3.2	5.0	1.032	1.035	1.003	22	85S
17:15	130.1	-68.2	20:16	57.0	6.6	23:10	2.84	37.3	1.0	2.3	1.010	1.018	1.008	121	82SW
20:4	118.5	-63.0	15:4	21.1	-3.8	21:6	3.82	35.4	1.3	3.2	1.013	1.026	1.013	45	90
17:8	132.0	-22.0	44:17	43.8	4.5	44:8	1.04	50.6	0.6	0.7	1.006	1.004	0.998	35	90
14:6	246.9	61.8	70:8	70.6	28.1	70:10	3.63	69.0	3.1	2.0	1.032	1.005	0.974	250	
53:8	124.8	38.7	53:15	36.3	-1.9	16:8	0.97	29.7	0.2	0.9	1.002	1.007	1.005	358	80NE
24:8	123.8	35.2	24:9	44.5	-14.7	11:8	2.57	32.9	0.8	2.2	1.008	1.018	1.011	130	90
48:29	115.3	-30.7	48:25	26.5	2.0	36:11	3.51	19.1	0.4	3.3	1.004	1.032	1.028	230	90
19:11	123.4	-65.7	23:13	34.3	0.4	20:6	1.87	45.4	0.9	1.4	1.009	1.009	1.000	150	85NE
15:13	140.2	-64.5	14:4	38.1	-5.7	15:7	1.90	55.9	1.3	1.2	1.013	1.006	0.993	50	88NE
13:10	225.0	27.8	42:9	55.6	61.8	42:12	1.10	60.6	0.8	0.7	1.008	1.003	0.994	85	80NE
27:14	253.9	-14.7	32:16	317.7	59.4	25:13	0.84	54.5	0.6	0.6	1.006	1.003	0.997	35	75SW
16:5	141.0	30.0	7:5	43.5	12.7	16:5	4.34	36.2	1.5	3.6	1.015	1.029	1.014	155	87NE

TABLE 3.1 (Con't)

Site	Macroscopic Flow Lineation DIKE			$\bar{\chi}_1$			$\bar{\chi}_2$			$\bar{\chi}_3$			
	$N_1/N_2$	Azimuth (deg)	Plunge, $\chi \times 10^{-3}$ (deg)	$D_{max}$	$I_{max}$ (max:min)	$\alpha_{95}$	$D_{int}$	$I_{int}$ (max:min)	$\alpha_{95}$ (max:min)	$D_{min}$	$I_{min}$ (max:min)	$\alpha_{95}$ (max:min)	
KD47	13/12			1.217	284.5	-10.8	24:19	249.6	76.9	43:23	13.1	7.3	43:19
KD49	8/8	95	8E	4.508	325.4	3.6	49:16	239.9	-51.4	50:22	52.5	-38.4	30:12
KD50	6/6			2.616	336.9	44.5	31:17	103.9	31.5	25:12	33.8	-29.1	27:15
KD51	10/10	135	40SE	3.216	303.0	-33.9	49:5	201.4	-16.7	50:15	89.5	-51.2	23:5
KD52	6/6	123	10SE	3.601	291.9	-45.8	34:10	157.2	-34.4	34:22	49.4	-24.1	35:24
KD53	9/6			3.313	316.3	-71.7	16:5	193.9	-10.1	39:12	281.2	15.2	39:6
KD54	8/5	115	40E-SE	3.453	271.9	-42.3	26:6	180.0	-2.0	22:9	87.8	-47.6	17:9
KD55	8/8			3.450	330.0	-74.0	46:20	115.6	-13.3	46:8	27.7	8.7	20:10
KD56	8/8			1.545	307.3	54.2	30:16	113.6	35.0	30:7	28.2	-6.5	16:7
KD57	10/8			0.582	355.3	65.3	14:9	129.8	18.5	25:13	45.2	-15.8	26:7
KD58	9/6			0.608	3.5	-66.0	21:5	184.2	-24.0	20:17	274.1	0.3	19:9
KD59	6/5	295	35NW	3.415	290.8	38.2	19:8	116.1	51.7	12:8	22.8	2.6	21:9
KD60	12/9	290	35NW	0.495	324.9	78.6	16:8	117.6	10.2	24:10	28.5	-5.1	25:12
KD61	15/15			1.158	0.2	62.3	30:7	131.5	19.1	30:11	48.4	-19.3	11:7
KD62	8/4			1.256	297.4	74.3	10:5	126.9	15.5	16:1	36.2	2.5	14:5
KD63	8/5			1.517	22.9	59.6	30:24	125.6	7.4	34:26	39.8	-29.3	36:8
KD64	14/14			0.749	329.2	16.6	40:28	92.7	61.7	46:23	52.2	-22.3	36:28
KD65	9/9			0.650	312.0	26.3	23:6	116.0	62.8	23:11	38.8	-6.5	12:5
KD66	9/6			1.832	300.9	-9.0	17:4	177.4	-74.0	17:15	33.0	-13.1	15:5
CV67	6/5			0.826	281.1	14.6	39:9	196.0	-18.1	39:19	334.4	-66.4	21:8
SW68	8/8			0.490	17.3	12.1	44:24	121.5	48.9	62:22	277.5	38.6	63:24
KD69	11/11			1.532	322.7	16.7	15:14	116.3	71.5	14:6	50.4	-7.8	15:6
KD70	11/11			2.002	59.1	2.9	52:18	145.1	-54.5	50:39	331.1	-35.3	40:28
KD71	8/8			1.046	322.0	18.0	26:19	135.2	71.9	27:13	51.4	-2.0	23:6
CV73	8/8			0.458	10.1	-37.0	67:25	250.2	-33.4	67:23	312.4	35.3	38:19
KD74	13/10			2.126	309.4	1.5	21:6	216.2	63.7	32:9	40.1	26.2	34:15
KD75	13/13	310	20SE	3.328	358.0	75.2	17:10	189.3	14.5	65:13	278.6	-2.8	64:9
KD76	13/13	315	44NW	4.258	298.8	-49.9	19:12	162.0	-31.5	69:14	57.6	-22.1	69:15
KD77	7/7			4.502	312.7	34.5	14:7	147.6	54.6	7:3	47.6	7.0	14:3
KD78	6/5			0.507	35.4	-36.2	27:7	108.3	21.9	26:14	354.0	45.7	15:12

Mean AMS data for Koolau dike samples collected in 1986-1988 and measured at University of Hawaii over the number of samples used in the final AMS mean results (e.g.,  $N_1/N_2 = 6/5$  indicates calculations);  $\chi_1$ ,  $\chi_2$ ,  $\chi_3$  are the mean maximum, intermediate, and minimum susceptibility directions and  $I_{int}$ ,  $D_{min}$  and  $I_{min}$  are the declination and inclination of the mean susceptibility direction axes of (ellipse) cone of 95% confidence about the mean, in degrees;  $H$  is the mean total anisotropy value at each site;  $L$  and  $F$  are the quantitative measures of the mean lineation and foliation, respectively;  $R$  and  $E$  are the axial magnitude ratios;  $E$  is ellipticity (shape factor where  $E < 1.000$  represents susceptible oblate ones).

		$\bar{\chi}_2$		$\bar{\chi}_3$													
	max $\alpha_{95}$ (max:min)	D <sub>int</sub>	I <sub>int</sub>	$\alpha_{95}$ (max:min)	D <sub>min</sub>	I <sub>min</sub>	$\alpha_{95}$ (max:min)	H (%)	V (deg)	L (%)	F (%)	$\chi_1/\chi_2$	$\chi_2/\chi_3$	E	width, (cm)	dip, (deg)	
3	24:19	249.6	76.9	43:23	13.1	7.3	43:19	0.18	54.3	0.1	0.1	1.001	1.001	0.999	850		
5	49:16	239.9	-51.4	50:22	52.5	-38.4	30:12	0.52	38.5	0.2	0.4	1.002	1.003	1.001	100	88NE	
5	31:17	103.9	31.5	25:12	33.8	-29.1	27:15	1.17	50.9	0.7	0.8	1.007	1.005	0.998	145	80NE	
9	49:5	201.4	-16.7	50:15	89.5	-51.2	23:5	0.45	35.8	0.2	0.4	1.002	1.003	1.001	56	88NE	
3	34:10	157.2	-34.4	34:22	49.4	-24.1	35:24	0.74	42.0	0.3	0.6	1.003	1.004	1.001	120	77NE	
7	16:5	193.9	-10.1	39:12	281.2	15.2	39:6	0.43	58.4	0.3	0.3	1.003	1.001	0.998	140	90	
3	26:6	180.0	-2.0	22:9	87.8	-47.6	17:9	0.45	53.4	0.3	0.3	1.003	1.002	0.999	64	90	
0	46:20	115.6	-13.3	46:8	27.7	8.7	20:10	1.15	28.1	0.3	1.0	1.003	1.009	1.006	167	85NE	
2	30:16	113.6	35.0	30:7	28.2	-6.5	16:7	1.02	24.0	0.2	0.9	1.002	1.009	1.007	305	90	
3	14:9	129.8	18.5	25:13	45.2	-15.8	26:7	1.88	51.2	1.1	1.3	1.011	1.007	0.996	70	90	
0	21:5	184.2	-24.0	20:17	274.1	0.3	19:9	1.29	55.1	0.9	0.9	1.009	1.004	0.996	136	65SW	
2	19:8	116.1	51.7	12:8	22.8	2.6	21:9	1.54	50.1	0.9	1.1	1.009	1.006	0.997	102	90	
6	16:8	117.6	10.2	24:10	28.5	-5.1	25:12	1.46	54.4	1.0	1.0	1.010	1.005	0.995	82	90	
3	30:7	131.5	19.1	30:11	48.4	-19.3	11:7	0.38	25.1	0.1	0.3	1.003	1.003	1.002	222	90	
3	10:5	126.9	15.5	16:1	36.2	2.5	14:5	2.33	42.9	1.1	1.8	1.011	1.013	1.002	372	90	
6	30:24	125.6	7.4	34:26	39.8	-29.3	36:8	1.71	26.2	0.3	1.5	1.003	1.014	1.011	241	80NE	
6	40:28	92.7	61.7	46:23	52.2	-22.3	36:28	0.33	38.7	0.1	0.3	1.001	1.002	1.001	160	88NE	
3	23:6	116.0	62.8	23:11	38.8	-6.5	12:5	3.44	40.3	1.4	2.7	1.014	1.020	1.006	110	90	
0	17:4	177.4	-74.0	17:15	33.0	-13.1	15:5	2.07	36.9	0.7	1.7	1.007	1.013	1.006	305	75NE	
6	39:9	196.0	-18.1	39:19	334.4	-66.4	21:8	0.14	27.6	0.0	0.1	1.000	1.001	1.001		(Lava)	
1	44:24	121.5	48.9	62:22	277.5	38.6	63:24	0.05	49.6	0.0	0.0	1.000	1.000	1.000		(Lava)	
7	15:14	116.3	71.5	14:6	50.4	-7.8	15:6	0.74	30.3	0.2	0.6	1.002	1.006	1.004	145	90	
9	52:18	145.1	-54.5	50:39	331.1	-35.3	40:28	0.26	45.8	0.1	0.2	1.001	1.001	1.000	365	90	
0	26:19	135.2	71.9	27:13	51.4	-2.0	23:6	0.61	33.0	0.2	0.5	1.002	1.004	1.002	408	90	
0	67:25	250.2	-33.4	67:23	312.4	35.3	38:19	0.09	24.4	0.0	0.1	1.000	1.001	1.001		(Lava)	
5	21:6	216.2	63.7	32:9	40.1	26.2	34:15	0.28	58.4	0.2	0.2	1.002	1.001	0.999	55	80NE	
2	17:10	189.3	14.5	65:13	278.6	-2.8	64:9	0.52	65.5	0.4	0.3	1.004	1.001	0.997	60	75NE	
9	19:12	162.0	-31.5	69:14	57.6	-22.1	69:15	0.73	17.3	0.1	0.7	1.001	1.007	1.006	65	80NE	
5	14:7	147.6	54.6	7:3	47.6	7.0	14:3	1.93	44.7	1.0	1.4	1.010	1.010	1.000	84	90	
2	27:7	108.3	21.9	26:14	354.0	45.7	15:12	1.35	35.0	0.4	1.1	1.004	1.009	1.005		(Lava)	

ed in 1986-1988 and measured at University of Hawaii:  $N_1/N_2$  is the total number of samples per site  
AMS mean results (e.g.,  $N_1/N_2 = 6/5$  indicates that one sample was rejected from the mean  
intermediate, and minimum susceptibility directions as described in the text;  $D_{max}$  and  $I_{max}$ ,  $D_{int}$   
inclination of the mean susceptibility directions;  $\alpha_{95}$  (max:min) is the half radius of the semi-  
me mean, in degrees; H is the mean total anisotropy at each site; V in degrees is the mean Graham's  
measures of the mean lineation and foliation, respectively, as defined in the text;  $\chi_1/\chi_2$  and  $\chi_2/\chi_3$   
(shape factor where  $E < 1.000$  represents susceptibility ellipsoids that are prolate, while  $E > 1.000$

TABLE 3.2 Description of 73 Sampled Sites, Comparison of Plunge of Lineations to  $\chi_1$  (AMS) Direction and Direction

Plunge of the Location and Description	Site	Dike Description	Macroscopic Lineation Compared with $\chi_1$ (AMS)	Degree and Type of Cluster of $\chi_1$	AMS
Cut on H3 Highway, 50' north of Mokapu Road	KD1	Irregular chilled margins; slightly oxidized; this dike intruded the middle of an older dike	15° more	good; moderately lineated	
Natural outcrop near 1	KD2	Slightly chloritized; abundant amygdales; lacks own cooling joints	12° more	excellent; highly lineated	
	KD3	Narrow dike; porphyritic; very irregular; margins flow banded	12° less	good; moderately lineated	
Makapu Saddle Road just northeast of H3 Highway overpass	KD4	Amygdales have maximum diameter of 5 mm, average is 1 mm	24° more	excellent-good; bimodal	
	KD5	Chilled margin slightly oxidized to an iron oxide color	24° less	moderate; bimodal	
	KD6	Very fresh; nonglassy chilled margins; cuts breccia.	25° more	excellent; foliated to slightly bimodal	
	KD7	Very fresh; nonglassy chilled margins; separated from site 6 by an 11-cm screen of breccia.	38° less	good/moderate; slightly lineated	
Mokapu Saddle Road 55 m northeast of sites 6 and 7	KD8	Moderately weathered; highly jointed and fractured; has irregular surface morphology		poor; random	
	KD9	Moderately weathered; low-angle intrusive sheet; variable dip		good; slightly lineated	
South side of Mokapu Saddle Road 180 m west of H3 overpass	KD10	Chloritized; contains sparse amygdales and many carbonate veins	26° more	moderate/poor; bimodal along foliation plane	
	KD11	Chloritized; relatively old, contains amygdales; irregular	12° more	good; bimodal	
	KD12	Chloritized; variable lineation plunge 5-60°; younger than adjacent dike 11		poor; random	
Coast at Kealahi Point (Heeia State Park)	KD13	Weathered to a rust-brown color; highly jointed; slightly porphyritic		good; bimodal	
	KD14	Weathered to a rust-brown color; abundant fine-scale cross joints; irregular margins		poor; random	
Cut at north end of Apokula Street (Keolu Hills)	KD15	Fresh; nonglassy chilled margins; dike sidesteps to the southeast; separated by pyroclastic screen	24° more	good; foliated to slightly bimodal	
	KD16	Fresh nonglassy chilled margins; lineations vary 10- 65°; crosscuts older dikes	24° more	good; bimodal	
	KD17	Irregular; moderately weathered; separated by well-indurated pyroclastic screen	20° less	good; slightly lineated	
Path cuts on southern side of interfluvium between Waikeke and Uwau valleys	KD18	Fresh, nonglassy chilled margins; large (0.5 cm) amygdales in the center		good; bimodal	
	KD19	Fresh nonglassy chilled margins; extremely vesicular in the center; massive to slightly jointed		good; moderately lineated	

on of 73 Sampled Sites, Comparison of Plunge of Lineations to  $\chi_1$  (AMS) Direction and Inferred Magma Flow

Site	Dike Description	Macroscopic Lineation Compared with $\chi_1$ (AMS)	Degree and Type of Cluster of $\chi_1$	AMS Magma Flow Azimuth
KD1	Irregular chilled margins; slightly oxidized; this dike intruded the middle of an older dike	15° more	good; moderately lineated	321° and up at 65°
KD2	Slightly chloritized; abundant amygdalae; lacks own cooling joints	12° more	excellent; highly lineated	313° and up at 11°
KD3	Narrow dike; porphyritic; very irregular; margins flow banded out in	12° less	good; moderately lineated	303° and down at 11°
KD4	Amygdalae have maximum diameter of 5 mm, average is 1 mm	24° more	excellent-good; bimodal	302° and up at 7°
KD5	Chilled margin slightly oxidized to an iron oxide color	24° less	moderate; bimodal	327° and up at 31°
KD6	Very fresh; nonglassy chilled margins; cuts breccia.	25° more	excellent; foliated to slightly bimodal	325° and up at 1°
KD7	Very fresh; nonglassy chilled margins; separated from site 6 by an 11-cm screen of breccia.	38° less	good/moderate; slightly lineated	176° and up at 75°
KD8	Moderately weathered; highly jointed and fractured; has irregular surface morphology		poor; random	
KD9	Moderately weathered; low-angle intrusive sheet; variable dip		good; slightly lineated	256° and up at 23°
KD10	Chloritized; contains sparse amygdalae and many carbonate veins	26° more	moderate/poor; bimodal along foliation plane	230° and up at 10°
KD11	Chloritized; relatively old, contains amygdalae; irregular	12° more	good; bimodal	298° and up at 1°
KD12	Chloritized; variable lineation plunge 5-60°; younger than adjacent dike 11		poor; random	
KD13	Weathered to a rust-brown color; highly jointed; slightly porphyritic		good; bimodal	315° and up at 31°
KD14	Weathered to a rust-brown color; abundant fine-scale cross joints; irregular margins		poor; random	
KD15	Fresh; nonglassy chilled margins; dike sidesteps to the southeast; separated by pyroclastic screen	24° more	good; foliated to slightly bimodal	239° and up at 24°
KD16	Fresh nonglassy chilled margins; lineations vary 10- 65°; crosscuts older dikes	24° more	good; bimodal	67° and up at 13°
KD17	Irregular; moderately weathered; separated by well-indurated pyroclastic screen	20° less	good; slightly lineated	106° and down at 16°
KD18	Fresh, nonglassy chilled margins; large (0.5 cm) amygdalae in the center		good; bimodal	317° and up at 28°
KD19	Fresh nonglassy chilled margins; extremely vesicular in the center; massive to slightly jointed		good; moderately lineated	335° and up at 21°

TABLE 3.2 (continued)

Plunge of the Location and Description	Site	Dike Description	Macroscopic Lineation Compared with $\chi_1$ (AMS)	Degree and Type of Cluster of $\chi_1$
	KD20	Moderately weathered; well jointed and fractured; some amygdales; dip is variable (45- 80° NE)		excellent; well lineated
Northernmost deep cut in H3 Highway	KD21	Chloritized; lacks own cooling joints; abundant amygdales	15° less	excellent; bimodal
	KD22	Altered to a greenish color; crosscut by a younger dike; irregular margins	38° more	good; slightly foliated
	KD23	Altered to a greenish color; lacks own cooling joints; very irregular	4° less	excellent/good; well lineated
	KD24	Slightly altered; cuts massive lava	42° less	excellent; well lineated
	KD25	Slightly altered; follows center of older dike	32° less	good; moderately well lineated
Cut at join of Kamahamaha Highway with Kahakili Highway	KD26	Altered to dark rust brown color; slightly porphyritic; well jointed and moderately fractured		good; bimodal
	KD27	Slightly weathered; porphyritic, rich in olivine and plagioclase phenocrysts		moderate/poor; well foliated
Northernmost deep cut in H3 Highway	KD28	Fresh; nonglassy chilled margins; lacks own jointing pattern; slightly porphyritic	26° less	excellent/good; bimodal
	KD29	Weathered to rust-brown color; well jointed; slightly porphyritic		good; slightly foliated
	KD30	Weathered to dark rust color; abundant amygdales in the center		poor; slightly bimodal foliated
Cut at Pohakea Point	KD31	Slightly weathered nonglassy chilled margins; moderately jointed	39° more	good; bimodal
	KD32	Weathered nonglassy chilled margins; irregular; dike offset and feeder present	18° more	good/moderated; slightly bimodal
	KD33	Weathered nonglassy chilled margins; dilation vector plunging 20° NE; lineations vary between 65° and 85°	3° more	moderate/good; bimodal foliated
	KD34	Dark rust-brown color; irregular; dilation vector plunges 35° NE	15° more	good; well foliated
Cut in Kailua Road south of join with Kaelepulu Street	KD35	Fresh; nonglassy chilled margins display imbricated sheet joints (in a zone 10- 20 cm wide)		moderate; bimodal
	KD36	Fresh glassy chilled margins; slightly porphyritic, cut by younger dike 37	14° more	good; slightly lineated
	KD37	Very fresh glassy chilled margins; porphyritic, containing large olivine phenocrysts (0.5 cm); relatively young		good; moderately well lineated
	KT38	Lava tube (diameter 2- 2.5 m); concentric crystal and vesicle segregation layers, vesicles tend to coarsen inward and flatten toward base		excellent/good; bimodal
	KD39	Moderately weathered; chilled margins highly oxidized; center extremely olivine porphyritic		poor; random foliated
Cut above Sea Life Park near Makapuu Point Relay Station	KD40	Moderately weathered; highly jointed	52° less	good; foliated
	KD41	Slightly weathered; well jointed; slightly porphyritic		poor; random

Dike Description	Macroscopic Lineation Compared with $\chi_1$ (AMS)	Degree and Type of Cluster of $\chi_1$	AMS Magma Flow Azimuth
Moderately weathered; well jointed and fractured; some amygdalae; dip is variable (45- 80° NE)		excellent; well lineated	5° and up at 20°
Chloritized; lacks own cooling joints; abundant amygdalae	15° less	excellent; bimodal	140° and up at 29°
Altered to a greenish color; crosscut by a younger dike; irregular margins	38° more	good; slightly foliated	51° and up at 37°
Altered to a greenish color; lacks own cooling joints; very irregular	4° less	excellent/good; well lineated	122° and up at 72°
Slightly altered; cuts massive lava	42° less	excellent; well lineated	188° and up at 52°
Slightly altered; follows center of older dike	32° less	good; moderately well lineated	126° and up at 63°
Altered to dark rust brown color; slightly porphyritic; well jointed and moderately fractured		good; bimodal	294° and down at 17°
Slightly weathered; porphyritic, rich in olivine and plagioclase phenocrysts		moderate/poor; well foliated	
Fresh; nonglassy chilled margins; lacks own jointing pattern; slightly porphyritic	26° less	excellent/good; bimodal	276° and up at 18°
Weathered to rust-brown color; well jointed; slightly porphyritic		good; slightly foliated	115° and up at 11°
Weathered to dark rust color; abundant amygdalae in the center		poor; slightly bimodal foliated	119° and up at 18°
Slightly weathered nonglassy chilled margins; moderately jointed	39° more	good; bimodal	140° and up at 23°
Weathered nonglassy chilled margins; irregular; dike offset and feeder present	18° more	good/moderated; slightly bimodal	109° and up at 9°
Weathered nonglassy chilled margins; dilation vector plunging 20° NE; lineations vary between 65° and 85°	3° more	moderate/good; bimodal foliated	58° and up at 72°
Dark rust-brown color; irregular; dilation vector plunges 35° NE	15° more	good; well foliated	121° and down at 49°
Fresh; nonglassy chilled margins display imbricated sheet joints (in a zone 10- 20 cm wide)		moderate; bimodal	152° and down at 4°
Fresh glassy chilled margins; slightly porphyritic, cut by younger dike 37	14° more	good; slightly lineated	109° and down at 27°
Very fresh glassy chilled margins; porphyritic, containing large olivine phenocrysts (0.5 cm); relatively young		good; moderately well lineated	145° and down at 68°
Lava tube (diameter 2- 2.5 m); concentric crystal and vesicle segregation layers, vesicles tend to coarsen inward and flatten toward base		excellent/good; bimodal	160° and down at 2°
Moderately weathered; chilled margins highly oxidized; center extremely olivine porphyritic		poor; random foliated	
Moderately weathered; highly jointed	52° less	good; foliated	153° and up at 51°
Slightly weathered; well jointed; slightly porphyritic		poor; random	

TABLE 3.2 (continued)

Plunge of the Location and Description	Site	Dike Description	Macroscopic Lineation Compared with $\chi_1$ (AMS)	Degree and Type of Cluster of $\chi_1$	AMS
Kapaa Quarry	KD42	Chloritized; center (30 cm wide) contains abundant amygdales up to 0.5 cm diameter; abundant calcite-filled veins; margins show flow banding	11° less	very good,	30
	KD43	Chloritized; few amygdales; non-glassy with irregular sinusoidal surfaces; abundant calcite-filled veins	17° more	excellent; bimodal lineated	30
	KD44	Chloritized; slightly irregular surface; in contact with dike 43		excellent; well lineated	3
	KD45	Chloritized; narrow (25- 35 cm wide); contains abundant large amygdales; has irregular surfaces; is a relatively old dike, crosscut by younger ones		moderate to poor; slightly lineated	3
	KD46	Chloritized; aphyric, nonvesicular; center (30 cm wide) contains sparse concentration of amygdales (<0.2 cm)	85° less	excellent; bimodal	2
Makapuu Point, 100 m northwest of light-house	KT47	Lava tube (diameter 11 m by 9 m); concentric crystal and vesicle segregation layers; is the northwest extension of lava tube KT38		poor; scattered	
	KD48	Vertical circular pluglike intrusive body (diameter 290 cm); contains vertical columnar joints, radial inward		poor; scattered	
Wailea Point, Lanikai	KD49	Weathered to rust-brown color; contains nonglassy chilled margins; slightly irregular trend; surface lineation plunge varies 2- 8° NW	20° less	good-moderate; bimodal	1
	KD50	Weathered to rust-brown color; highly jointed and fractured; with irregular surface morphology		good; lineated	1
Kapaa Quarry	KD51	Chloritized; nonglassy chilled margin contains flow banding; has associated feeder offshoot (40 cm wide)	10° more	moderate-poor; bimodal foliated	3
	KD52	Chloritized; margins are flow banded; dilation vector dips 20° S-SW	36° less	moderate-poor; foliated	2
	KD53	Weathered to a rust-brown color; margin is flow banded and contains segregation layers of vesicles with few pipe vesicles along the margins; amygdales (0.2- 0.5 cm) concentrated in the center		excellent; lineated	3
	KD54	Moderately weathered; abundant amygdales present; flow banding and pipe vesicles along margins	18° less	good; slightly lineated	2
	KD55	Moderately weathered; contains two amygdaloidal zones (each 20 cm wide and offset 18 cm from the dike center); both margins are cut by younger dikes		moderate-poor; slightly foliated	3
Haipuu, near Molii Pond	KD56	Slightly weathered; contains brecciated zones within its interior; thin vesicle concentration zone (20 cm wide) near each margin; irregular surface		moderate; bimodal foliated	3
Mokolii Island (China-mans Hat)	KD57	Slightly weathered; nonglassy chilled margins; contains cooling joints perpendicular to margins		very good; foliated	1

Di	Dike Description	Macroscopic Lineation Compared with $\chi_1$ (AMS)	Degree and Type of Cluster of $\chi_1$	AMS Magma Flow Azimuth
42	Chloritized; center (30 cm wide) contains abundant amygdaloids up to 0.5 cm diameter; abundant calcite-filled veins; margins show flow banding	11° less	very good,	304° and up at 24°
43	Chloritized; few amygdaloids; non-glassy with irregular sinusoidal surfaces; abundant calcite-filled veins	17° more	excellent; bimodal lineated	306° and up at 25°
44	Chloritized; slightly irregular surface; in contact with dike 43		excellent; well lineated	317° and down at 4°
45	Chloritized; narrow (25- 35 cm wide); contains abundant large amygdaloids; has irregular surfaces; is a relatively old dike, crosscut by younger ones		moderate to poor; slightly lineated	351° and up at 26°
46	Chloritized; aphyric, nonvesicular; center (30 cm wide) contains sparse concentration of amygdaloids (<0.2 cm)	85° less	excellent; bimodal	293° and down at 57°
47	Lava tube (diameter 11 m by 9 m); concentric crystal and vesicle segregation layers; is the northwest extension of lava tube KT38		poor; scattered	
48	Vertical circular pluglike intrusive body (diameter 290 cm); contains vertical columnar joints, radial inward		poor; scattered	
49	Weathered to rust-brown color; contains nonglassy chilled margins; slightly irregular trend; surface lineation plunge varies 2- 8° NW	20° less	good-moderate; bimodal	117° and down at 9°
50	Weathered to rust-brown color; highly jointed and fractured; with irregular surface morphology		good; lineated	154° and up at 36°
51	Chloritized; nonglassy chilled margin contains flow banding; has associated feeder offshoot (40 cm wide)	10° more	moderate-poor; bimodal foliated	303° and up at 34°
52	Chloritized; margins are flow banded; dilation vector dips 20° S-SW	36° less	moderate-poor; foliated	292° and up at 45°
53	Weathered to a rust-brown color; margin is flow banded and contains segregation layers of vesicles with few pipe vesicles along the margins; amygdaloids (0.2- 0.5 cm) concentrated in the center		excellent; lineated	316° and up at 72°
54	Moderately weathered; abundant amygdaloids present; flow banding and pipe vesicles along margins	18° less	good; slightly lineated	272° and up at 42°
55	Moderately weathered; contains two amygdaloidal zones (each 20 cm wide and offset 18 cm from the dike center); both margins are cut by younger dikes		moderate-poor; slightly foliated	330° and up at 74°
56	Slightly weathered; contains brecciated zones within its interior; thin vesicle concentration zone (20 cm wide) near each margin; irregular surface		moderate; bimodal foliated	307° and up at 54°
57	Slightly weathered; nonglassy chilled margins; contains cooling joints perpendicular to margins		very good; foliated	173° and up at 65°

TABLE 3.2 (continued)

Plunge of the Location and Description	Site	Dike Description	Macroscopic Lineation Compared with $\chi_1$ (AMS)	Degree and Type of Cluster of $\chi_1$	AMS Magma
Pali Lookout (near old Pali Highway)	KD58	Slightly weathered; glassy chilled margins; contains cooling joints perpendicular to margins (25- 45 cm wide); center has a vesicle concentration zone (55 cm wide)		excellent-very good; lineated	174° ar
Wailea Point, Lanikai	KD59	Weathered to rust brown color; contains nonglassy chilled margins; highly jointed and fractured; irregular morphology; surface lineation plunge varies 25- 35° NW	2° more	very good; bimodal	111° ar
Mokolii Island (China-mans Hat)	KD60	Moderately weathered; glassy to semi-glassy chilled margin; contains cooling joints slightly bimodal perpendicular to margins; surface lineation plunge varies 30°-40° NW	42° less	very good; slightly bimodal	145° ar
	KD61	Weathered to rust gray color; flow banding and pipe-vesicles along margins, nonglassy; contains brecciated zones within its interior; center is highly vesicular		excellent; lineated; slightly bimodal	180° a
Kaipapau Gulch	KD62	Slightly weathered; massive fine-grained to plagioclase porphyritic in the center; irregular margins; center contains small vesicles (1 mm diameter)		excellent; foliated	297° a
	KD63	Slightly weathered to light gray; contains cooling joints perpendicular to the glassy chilled margins; is massive, aphyric		moderate-poor; random	
Maakua Gulch	KD64	Moderately weathered; flow banded with narrow (4 mm wide) vesicles segregation zones along margins; center is highly vesicular and olivine porphyritic		poor; random	
	KD65	Weathered to light-gray; contains non-glassy chilled margins; is aphyric with few olivine phenocrysts		good; foliated; bimodal	312° a
	KD66	Weathered to a light-gray; massive to slightly porphyritic with few plagioclase phenocrysts; is 305 cm wide		very good; foliated	300° a
Koloa Gulch	KD69	Weathered to a medium dark gray; has slightly irregular margins containing abundant small (1 mm diameter) vesicles		very good; slightly foliated	323° a
	KD70	Moderately weathered; flow banded; has nonglassy chilled margins with many (14 individual stringers) narrow vesicle segregation zones; has elongate irregular vesicles parallel to the dike walls; center is olivine and plagioclase porphyritic; is very wide (365 cm)		poor; random	
	KD71	Weathered to a reddish-brown color; flow banded irregular margins; contains abundant large vesicles concentrated in segregation zones along margins; is very wide (408 cm)		good-moderate; bimodal	322°
Mokolua Island	KD74	Highly altered (chloritized) to a light-greenish gray color; contains zeolite-filled amygdales along the margins; center has an amygdale segregation zone (15 cm wide); pipe vesicles occur subparallel to margins, plunge directions= 38°NW		moderate; bimodal	129°

Dike Description	Macroscopic Lineation Compared with $\chi_1$ (AMS)	Degree and Type of Cluster of $\chi_1$	AMS Magma Flow Azimuth
partly weathered; glassy chilled margins; contains cooling joints perpendicular to margins (25- 45 cm wide); center has a vesicle concentration zone (5 cm wide)		excellent-very good; lineated	174° and down at 64°
altered to rust brown color; contains nonglassy chilled margins; highly jointed and fractured; regular morphology; surface orientation plunge varies 25- 35° NW	2° more	very good; bimodal	111° and up at 38°
partly weathered; glassy to semi-glassy chilled margin; contains cooling joints slightly bimodal perpendicular margins; surface lineation plunges 30°-40° NW	42° less	very good; slightly bimodal	145° and up at 79°
altered to rust gray color; flow banded and pipe-vesicles along margins, non-assy; contains brecciated zones within its interior; center is highly vesicular		excellent; lineated; slightly bimodal	180° and up at 62°
partly weathered; massive fine-grained to agioclase porphyritic in the center; regular margins; center contains small vesicles (1 mm diameter)		excellent; foliated	297° and down at 74°
partly weathered to light gray; contains cooling joints perpendicular to the glassy chilled margins; is massive, aphyric		moderate-poor; random	
partly weathered; flow banded with narrow (1 mm wide) vesicles segregation zones along margins; center is highly vesicular and olivine porphyritic		poor; random	
altered to light-gray; contains non-glassy chilled margins; is aphyric with few olivine phenocrysts		good; foliated; bimodal	312° and down at 26°
altered to a light-gray; massive to slightly porphyritic with few plagioclase phenocrysts; is 305 cm wide		very good; foliated	300° and up at 9°
altered to a medium dark gray; has slightly irregular margins containing abundant small (1 mm diameter) vesicles		very good; slightly foliated	323° and down at 17°
partly weathered; flow banded; has nonglassy chilled margins with many (14 individual stringers) narrow vesicle segregation zones; has longate irregular vesicles parallel to the dike walls; center is olivine and plagioclase porphyritic; is very wide (365 cm)		poor; random	
altered to a reddish-brown color; flow banded irregular margins; contains abundant large vesicles concentrated in segregation zones along margins; is very wide (408 cm)		good-moderate; bimodal	322° and down at 18°
highly altered (chloritized) to a light-greenish gray color; contains zeolite-filled amygdaloids along the margins; center has an amygdale segregation zone (15 cm wide); pipe vesicles occur subparallel to margins, plunge directions= 38°NW		moderate; bimodal	129° and up at 2°

TABLE 3.2 (continued)

Plunge of the Location and Description	Site	Dike Description	Macroscopic Lineation Compared with $\chi_1$ (AMS)	Degree and Type of Cluster of $\chi_1$	AMS
	KD75	Highly weathered to reddish-brown color; nonglassy chilled margins; contains zeolite-filled amygdales; surface lineation plunge shallowly 20°NE	55° less	poor; foliated-random	
	KD76	Weathered reddish-brown gray color; contains zeolite-filled amygdales along the margin; surface lineations plunge 44°NE	6° less	good-moderate; slightly foliated	
	KD77	Moderately weathered dark-gray color; contains zeolite-filled amygdales (2 mm diameter); pipe-vesicles are aligned parallel to margins		excellent; bimodal	

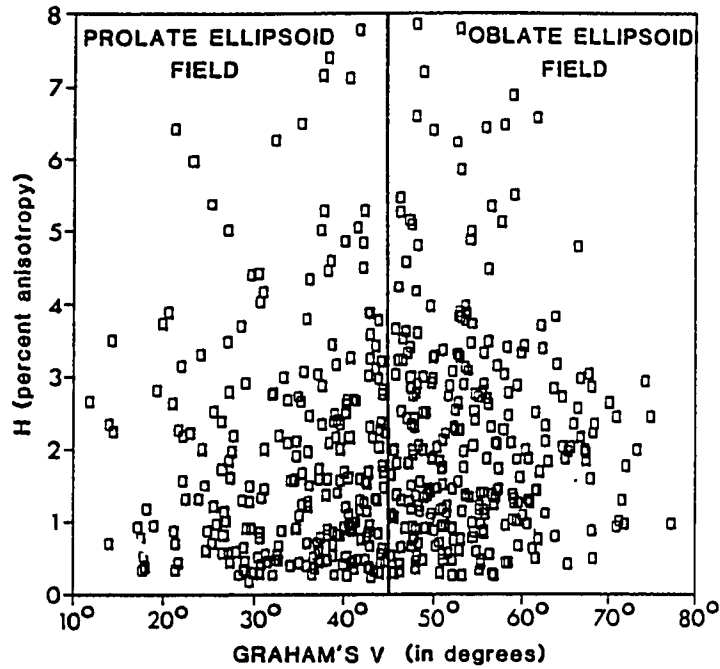
	Dike Description	Macroscopic Lineation Compared with $\chi_1$ (AMS)	Degree and Type of Cluster of $\chi_1$	AMS Magma Flow Azimuth
5	Highly weathered to reddish-brown color; nonglassy chilled margins; contains zeolite-filled amygdaloids; surface lineation plunge shallowly 20°NE	55° less	poor; foliated-random	
6	Weathered reddish-brown gray color; contains zeolite-filled amygdaloids along the margin; surface lineations plunge 44°NE	6° less	good-moderate; slightly foliated	178° and up at 75°
7	Moderately weathered dark-gray color; contains zeolite-filled amygdaloids (2 mm diameter); pipe-vesicles are aligned parallel to margins		excellent; bimodal	133° and up at 34°

Figure 3.3(a) Plot of Graham's  $V$  versus the total susceptibility anisotropy for 525 dike samples from the Koolau complex. *Graham* [1966] defines the susceptibility tensor to be prolate shaped when  $V < 45^\circ$  and oblate shaped when  $> 45^\circ$ . Note that the Koolau dike samples show nearly equal amounts of prolate and oblate ellipsoid shapes, and that there is no systematic variation in ellipsoid shape with increased total susceptibility anisotropy.

(b) Flinn diagram, plot of the axial ratios  $\chi_2/\chi_3$  versus  $\chi_1/\chi_2$  for 527 dike samples. Shows 48% of the Koolau samples have prolate ellipsoid shapes and 46% have oblate shapes, and 6% have  $a=b$ .

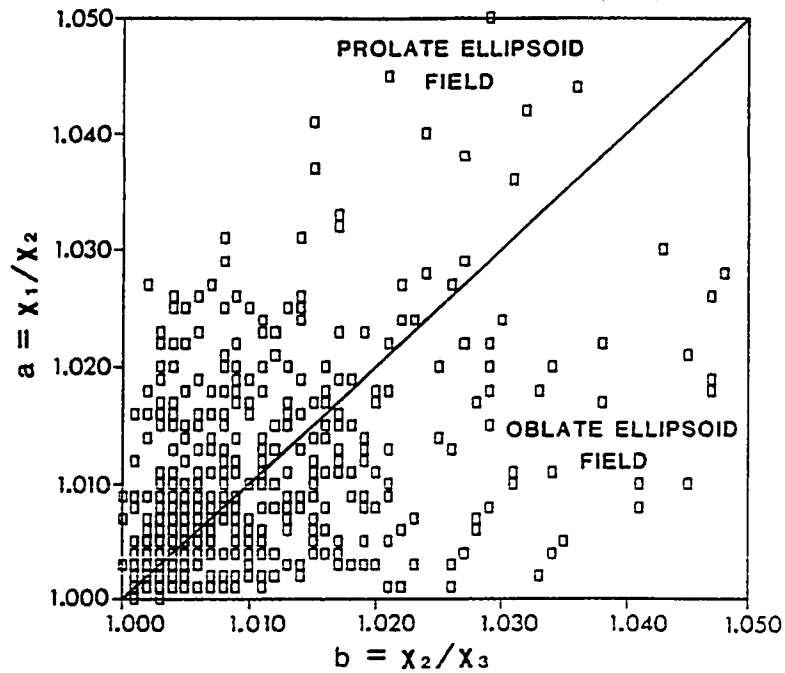
(a) GRAHAM'S V vs % ANISOTROPY

525 dike samples from the Koolau Complex, Oahu



(b) FLINN DIAGRAM

527 dike samples from the Koolau Complex, Oahu



[1971] indicates that the presumed AMS ellipsoid shape is prolate when  $E < 1$ , and for the Koolau dikes this occurs 47% of the time (33 dikes), which is very similar to the results for the magnetic fabric shapes of individual sample represented in the "Flinn diagram" (Figure 3.3b).

Based on *Jelinek's* [1978] statistical analysis (briefly discussed in Chapter 2) the degree of clustering of the AMS axial distributions are drawn as ellipses on all the equal area plots (refer to Appendix A). The 95% confidence interval for the three principal directions specified in Table 4 are represented by two semi-apical (maximum and minimum) half angles. I have arbitrarily categorized the degree of clustering at each site on the  $\chi_1$  maximum angle. Therefore, a conservative estimate of the degree of clustering of the  $\chi_1$  axes is given in Table 3.2 based on the following categories; excellent ( $<15^\circ$ ), very good ( $<20^\circ$ ), good ( $<25^\circ$ ), moderate ( $<30^\circ$ ), moderate to poor ( $<35^\circ$ ), and poor ( $>35^\circ$ ). At each locality, up to five dikes were measured for AMS which, in most instances, represents only a small percentage of the total number of dikes at each outcrop. Note that the  $\alpha_{95}$  error ellipses do not encircle all the principal susceptibility axes. The error ellipses tend to be smaller because they represent the 95% confidence interval over which N samples vary from the mean susceptibility tensor.

Table 3.2 summarizes the description of samples and the comparisons of magma flow based on the AMS measurements with those based on surface lineations and dike morphology. I have followed the convention of *Ellwood et al.* [1988], by plotting the maximum (solid square symbols), intermediate (solid triangles), and minimum (solid circles) susceptibility axes on lower hemisphere equal-area plots (refer to Appendix A). In these figures, the dike trend is shown as a solid line on a great circle; the macroscopic surface lineation plunge direction is plotted as a star, and for comparison, the mean maximum AMS ( $\chi_1$ ) direction is also plotted (asterisk).

Very few samples have been omitted from the equal-area plots in order to give an unbiased representation of the principal susceptibility tensor and its corresponding

directions (refer to Table 3.1). For those sites where sample rejection was needed for calculating the mean susceptibility tensor a number of different criteria was used: (1) samples which have anomalously high or very low total anisotropy values have been omitted because they tend to have a unduly strong influence on the mean tensor calculations; (2) samples with anomalous NRM directions, suggesting that the sample was incorrectly oriented in the field or was magnetically inhomogeneous; and (3) samples collected from the center of the dike that gave anomalous clustering of the AMS axes, possibly due to post-emplacement gravitational realignment of the crystals.

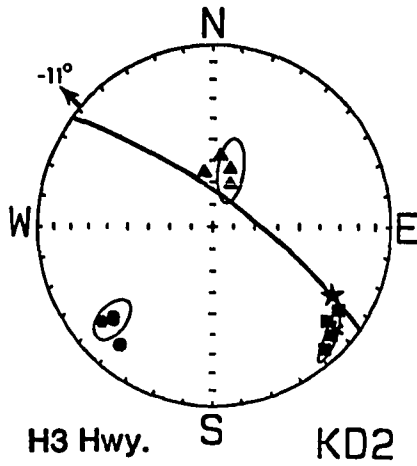
In general, the AMS plots for near-vertical dikes show that the minimum susceptibility ( $\chi_3$ ) directions are well grouped (clustered) in the horizontal direction, perpendicular to the foliation containing  $\chi_1$  and  $\chi_2$  and parallel to the minimum horizontal stress field, near the pole of the dike. The foliation plane containing the maximum and intermediate axes tends to parallel the dike trend, and the plunge of mean pole to this plane ( $\chi_3$ ) is generally less than  $10^\circ$ , which is in close agreement with the near vertical dip of most of the Koolau dikes. When the AMS representation ellipsoid approaches uniaxial shape (i.e., the axial ratio  $\chi_2/\chi_3 \approx 1.000$ ; Table 3), the intermediate and minimum axes may become randomly oriented in a girdle perpendicular to  $\chi_1$ . For this special case the intermediate and minimum axes have similar eigenvalues and can be transposed.

Since the susceptibility tensor represents the summation of all individual magnetic grains, then as the magnetic component changes magnitude or orientation, the shape and orientation of the representation ellipsoid (ovaloid) will also vary, thus allowing an interpretation of the probable nature and origin of the magnetic fabric. Hence the magnetic fabric for the Koolau dike specimens based on the AMS axial distributions, when presented on equal-area projections, can be summarized into the following six major categories (Figure 3.4).

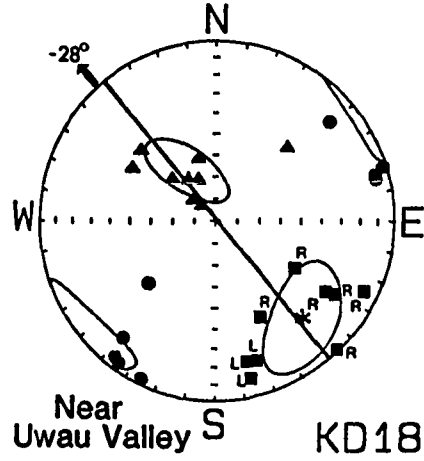
1. *Good clusters of the minimum susceptibility ( $\chi_3$ ) axes near to the pole of the dike or sill, along with good clustering of the maximum susceptibility ( $\chi_1$ ) in the*

Figure 3.4 Equal area plots of six major categories of the AMS axial distributions that describe the magnetic fabric of the Koolau dike complex. The first four categories are used to infer magma flow directions in the Koolau dikes. Refer to the text for a description of the AMS axial distributions for each category.

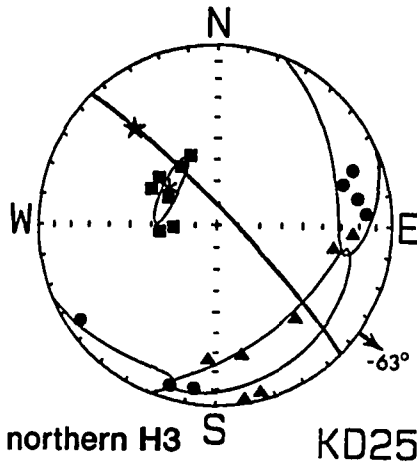
**Category 1**



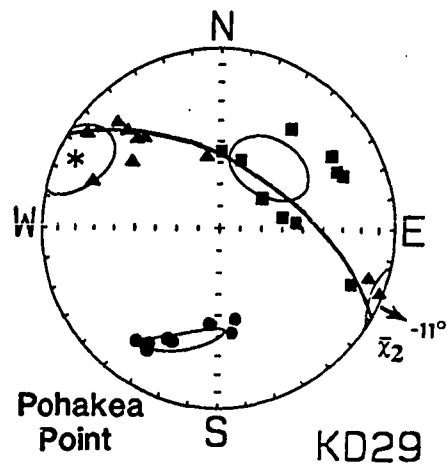
**Category 2**



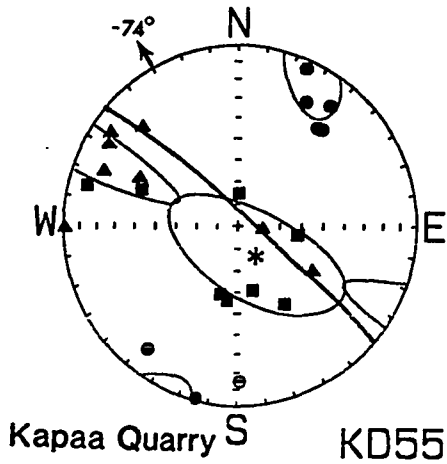
**Category 3**



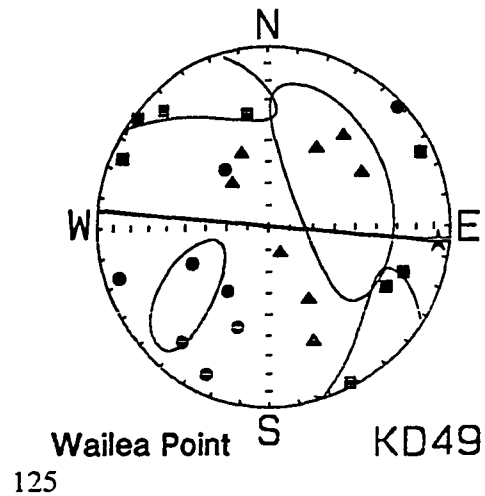
**Category 4**



**Category 5**



**Category 6**



*foliation plane* parallel to the plane of the dike, which indicate that the possible sense of the emplacement direction is most likely a primary feature related to magma flow during dike injection (e.g. KD2).

2. *Well grouped minimum susceptibility ( $\chi_3$ ) axes near the pole of the dike, along with bimodal clustering of ( $\chi_1$ ) axes symmetrically disposed on either side of the dike, which indicate the flow azimuth, i.e., the absolute magma flow direction (e.g. KD18).*
3. *Good clustering of the maximum susceptibility ( $\chi_1$ ) in the foliation plane of the dike along with inclined girdles of the intermediate ( $\chi_2$ ) and minimum susceptibility ( $\chi_3$ ) axes, which may imply that individual magnetic grains resemble prolate ellipsoids (needles) that were aligned during primary magma flow, and that the  $\chi_2$  and  $\chi_3$  axes are of nearly equal dimension, and may have been transposed (e.g. KD25).*
4. *Good clusters of intermediate ( $\chi_2$ ) axes in the foliation plane along with good clustering of the minimum ( $\chi_3$ ) axes along with good clustering of the maximum ( $\chi_1$ ) susceptibility axes oriented at an (anomalous) angle to the dike trend, which may indicate that the intermediate axes are related to primary magma flow and that the magnetic fabric is oblate in nature and/or has an imbricate arrangement of  $\chi_1$  (e.g. KD29).*
5. *Good clusters of minimum ( $\chi_3$ ) axes near the pole of the dike along with random clusters of the maximum ( $\chi_1$ ) and intermediate ( $\chi_2$ ) susceptibility axes along inclined girdles, which indicate that the magnetic fabric resembles a flattened oblate ellipsoid shape or that individual magnetic grains resemble prolate ellipsoids (needles) that are randomly distributed about a foliation plane (e.g. KD55).*
6. *Random orientations of all the susceptibility axes, which may indicate that magma flow was turbulent (with no preferred grain alignment), or that the magnetic fabric is most likely a secondary feature and the magnetic grains crystallized after magma movement had ceased or that they have been altered by weathering or hydrothermal processes (e.g. KD49).*

In the following section all the AMS data is briefly outlined and discussed in terms of individual outcrops composed of dike-sets that contain anywhere from one to ten or more dikes. Each outcrop (at a particular stratigraphic/erosional level within the Koolau

Volcano) may contain several tens to hundreds of dikes, and it is not claimed that the inferred magma flow directions based on the magnetic fabric of sampled dikes are representative of the average magma flow directions of that particular dike swarm. All the equal-area plots discussed in this section are given in Appendix A.

### **Dikes KD1–7; cut on Highway H3; 50 m N. of Mokapu Saddle Road**

These dikes have an average strike of about  $130^\circ$  and dip  $80^\circ\text{NE}$ , they are all exposed at a relatively deep erosional level (110 m above mean sea level). The average bulk density for these seven dikes is high ( $3.00\text{ g cm}^{-3}$ , compared to the average bulk density of  $2.87\text{ g cm}^{-3}$  for 70 of the Koolau dikes in this study; refer to Table 1.1 and Figure 1.12). KD1–3 and 7 are category 1 dikes and KD4–6 are category 2 dikes.

Dike KD1 has macroscopic surface lineations (MSL) that plunge very steeply ( $75^\circ\text{SE}$ ) towards the Kailua Caldera and agree closely with the mean  $\chi_1$  direction of  $141^\circ$  and steep plunge of  $65^\circ\text{SE}$  (asterisk). The  $\chi_2$  and  $\chi_3$  axes fall along a nearly horizontal girdle (foliation plane). The inferred magma flow direction is up at  $-65^\circ$  to the northwest.

The MSL plunge of Dikes KD2–6 are all quite shallow (between  $5^\circ$  and  $30^\circ\text{SE}$ ). The AMS axes for dike KD2 are very well clustered and slightly lineated. The  $\chi_1$  direction is  $133^\circ$  and plunges  $11^\circ\text{SE}$ , and is in good agreement with the MSL plunge ( $10^\circ$  less). The inferred magma flow direction is therefore up at a shallow angle of  $11^\circ$  to the northwest.

Dike KD3, the narrowest dike sampled (17 cm wide), has a very shallow MSL plunge of  $7^\circ\text{SE}$ . The  $\chi_1$  axes are moderately clustered giving a mean direction of  $312^\circ$  and plunge of  $11^\circ\text{NW}$ , and is plunging in the opposite direction to the macroscopic surface lineations ( $18^\circ$  less). Based on the inferred magma source at the other three sites, magma is interpreted to have flowed down at a shallow angle of  $11^\circ$  to the northwest.

In dike KD4 the  $\chi_1$  axes are well clustered in two groups that are offset  $15^\circ$  to either side of the dike trend. (In Appendix A, "L" represents samples collected from the left side of the dike, and "R" represents those collected from the right, as seen by an observer facing

Volcano) may contain several tens to hundreds of dikes, and it is not claimed that the inferred magma flow directions based on the magnetic fabric of sampled dikes are representative of the average magma flow directions of that particular dike swarm. All the equal-area plots discussed in this section are given in Appendix A.

### **Dikes KD1–7; cut on Highway H3; 50 m N. of Mokapu Saddle Road**

These dikes have an average strike of about  $130^\circ$  and dip  $80^\circ\text{NE}$ , they are all exposed at a relatively deep erosional level (110 m above mean sea level). The average bulk density for these seven dikes is high ( $3.00\text{ g cm}^{-3}$ , compared to the average bulk density of  $2.87\text{ g cm}^{-3}$  for 70 of the Koolau dikes in this study; refer to Table 1.1 and Figure 1.12). KD1–3 and 7 are category 1 dikes and KD4–6 are category 2 dikes.

Dike KD1 has macroscopic surface lineations (MSL) that plunge very steeply ( $75^\circ\text{SE}$ ) towards the Kailua Caldera and agree closely with the mean  $\chi_1$  direction of  $141^\circ$  and steep plunge of  $65^\circ\text{SE}$  (asterisk). The  $\chi_2$  and  $\chi_3$  axes fall along a nearly horizontal girdle (foliation plane). The inferred magma flow direction is up at  $-65^\circ$  to the northwest.

The MSL plunge of Dikes KD2–6 are all quite shallow (between  $5^\circ$  and  $30^\circ\text{SE}$ ). The AMS axes for dike KD2 are very well clustered and slightly lineated. The  $\chi_1$  direction is  $133^\circ$  and plunges  $11^\circ\text{SE}$ , and is in good agreement with the MSL plunge ( $10^\circ$  less). The inferred magma flow direction is therefore up at a shallow angle of  $11^\circ$  to the northwest.

Dike KD3, the narrowest dike sampled (17 cm wide), has a very shallow MSL plunge of  $7^\circ\text{SE}$ . The  $\chi_1$  axes are moderately clustered giving a mean direction of  $312^\circ$  and plunge of  $11^\circ\text{NW}$ , and is plunging in the opposite direction to the macroscopic surface lineations ( $18^\circ$  less). Based on the inferred magma source at the other three sites, magma is interpreted to have flowed down at a shallow angle of  $11^\circ$  to the northwest.

In dike KD4 the  $\chi_1$  axes are well clustered in two groups that are offset  $15^\circ$  to either side of the dike trend. (In Appendix A, "L" represents samples collected from the left side of the dike, and "R" represents those collected from the right, as seen by an observer facing

toward the two northern quadrants). The mean  $\chi_1$  direction is  $302^\circ$  and plunges shallowly at  $7^\circ$ SE in the same direction as, but less steeply than, the MSL. The  $\chi_1$  axes of the samples collected from each margin of the dike cluster on opposite sides of the dike trend, this bimodal distribution is inferred to represent an imbrication along each wall of the dike. The absolute magma flow azimuth (large solid arrow) is inferred to be up at  $-7^\circ$  to the northwest.

Dike KD5 also has a wider bimodal distribution of the  $\chi_1$  axes with a mean direction of  $148^\circ$  and plunges  $31^\circ$ SE in the same direction as, but more steeply than the MSL ( $22^\circ$ ). This bimodal distribution, is similar in character to that of dike KD4, hence, it is inferred to represent a magnetic imbrication angle of  $20^\circ$  along each margin of the dike, and thus the absolute magma flow direction is  $328^\circ$  and up at  $-31^\circ$  to the northwest.

Dikes KD6 and 7 are very fresh and very young-looking planer dikes cutting lithified caldera collapse breccias composed of fragments of basalt flows and dike rocks. KD6, is 90 cm wide and shows one of the highest degrees of clustering for all three principal axes, in which the  $\chi_1$  axes have a slightly bimodal distribution offset  $10\text{--}15^\circ$  from the dike trend. Therefore this rather narrow dike has a very small inferred imbrication angle along each margin ( $<10^\circ$ ). The average plunge of the MSL is  $24^\circ$ SE towards the Kailua Caldera and is in the same direction as the plunge of the  $\chi_1$  axes. Based on the AMS fabric the inferred flow azimuth is  $325^\circ$  and up at  $-1^\circ$  to the northwest.

KD7, a 50 cm wide dike with a steep MSL plunge of  $61^\circ$ SE, similar to that of dike KD1, shows very good clustering of AMS axes. The mean  $\chi_1$  direction gives an anomalous trend of  $356^\circ$  and  $75^\circ$ NW plunge. This non-parallel trend of the mean  $\chi_1$  direction could be related to its very steep plunge angle. In summary, these dikes shows very close agreement between the MSL and the maximum  $\chi_1$  directions in all seven dikes; in four the (average) magma flow direction was up at a shallow angle ( $12^\circ$ ), in two the magma flowed up at a steep angle ( $70^\circ$ ), and in one the magma flowed down at a shallow angle ( $11^\circ$ ). *In summary*, the relative young age of these dikes, their high bulk densities

and low vesicularity, and their mainly upward magma flow trajectories, all suggest that this dike-set was emplaced under positive buoyancy forces, and possibly at a relatively great depth. If these dikes were injected very near the end of activity of the Koolau volcano then they could have been injected about 1000 m depth within the volcanic edifice.

#### **Dikes KD8 and 9; N. Mokapu Saddle Road; 55 m NW of sites 6 and 7**

These dikes are from a slightly deeper erosion level than dikes KD1–7 (only about 100 m above sea level). KD8, a moderately weathered dike (category 6), in which only four samples were collected from its southwest margin because of poor exposure and the high degree of jointing and fracturing. Since the AMS fabric is random no interpretation of the magma flow direction is given.

KD9, is a low-angle intrusive sheet (sill-like) with variable dip. All three of the AMS axial distributions show moderate clustering category 1. In this example the  $\chi_3$  axes plot near the pole of the sill while  $\chi_1$  and  $\chi_2$  lie in the foliation plane. The presumed source lies to the east of this site below the Kawaiui Swamp area; thus the inferred magma flow direction is  $256^\circ$  and up at  $-23^\circ$  west-southwest. The  $7^\circ$  difference between the plunge angle of the mean  $\chi_1$  direction and the dip of the intrusive sheet would be consistent with a  $7^\circ$  imbrication angle pointing toward the west.

#### **Dikes KD10–12; S. Mokapu Saddle Road; 180 m W. of the H3 overpass**

These dikes are highly chloritized and contain abundant zeolite-filled amygdales and carbonate veins. The slightly lower than average bulk density ( $2.83 \text{ g cm}^{-3}$ ) of these dikes suggests that hydrothermal alteration can significantly lower the dike density following emplacement (zeolite infilling of vesicles would tend to increase the density, however for these dikes this increase seems to have been offset by secondary alteration). Dike KD10 has an anomalous trend compared to the main rift axis striking  $100^\circ$  and dipping  $75^\circ$  N-NE. The MSL plunges  $38^\circ$  to the east-southeast and does not agree well with the  $50^\circ$  northeast trend and plunge of  $10^\circ$  of the mean  $\chi_1$  direction. The  $\chi_1$  and  $\chi_2$  axes are only moderately or

poorly clustered along an inclined ( $10^\circ$ ) girdle or foliation plane (category 4) with a slight bimodality. Note also that the minimum  $\chi_3$  axes do not cluster near the pole of the dike but are steeply inclined in the foliation plane of the dike. Based on a slight magnetic imbrication the inferred magma flow direction is  $230^\circ$  and up at  $-10^\circ$  to the southwest.

KD11, a 48 cm wide dike, has a MSL that plunges shallowly  $10^\circ$ NW and agrees to within  $12^\circ$  with the mean  $\chi_1$  direction (categories 2 and 3). The maximum  $\chi_1$  axes are well clustered into two groups that are offset  $5\text{--}10^\circ$  to either side of the dike trend. This offset represents an imbrication of the magnetic grains along each wall of the dike. The  $\chi_2$  and  $\chi_3$  axes tend to form a girdle, though there is a tendency for some of them to have nearly equal eigenvalues, hence some of the axes may have been transposed, suggesting that  $\chi_1 \gg \chi_2 \approx \chi_3$ , and thus explaining why the two axes form a girdle. Based on a slight AMS imbrication, the magma flow azimuth is  $298^\circ$  and up at  $-1^\circ$  to the northwest.

Dike KD12 has the lowest bulk density ( $2.66 \text{ g cm}^{-3}$ ) in this set and is adjacent to and younger than KD11 (on the southwest side). The surface lineations plunge  $25^\circ$ SE towards the Kailua Caldera, but due to a poor degree of clustering of the AMS directions no interpretation of the magma flow direction is given (category 6). There is a general tendency for highly chloritized dikes to have very low percent anisotropy. Why this is so is not fully understood, since the mean susceptibility is relatively high ( $4.44 \times 10^{-3} \text{ emu g}^{-1}$ ) (Table 3.1).

### **KD13 and 14; Kealohi Point**

These dikes are nearly vertical and are fairly wide, being 150 cm and 250 cm wide, respectively. They are separated by a screen of lava flows that outcrop along the coast at Kealohi Point (about 1–2 m above sea level). These dikes are moderately weathered to a rust-brown color, they both have fairly unstable and different NRM directions ( $D= 180.5^\circ$ ,  $I= -32.7^\circ$  and  $D= 200.2^\circ$ ,  $I= -5.6^\circ$ , respectively; Table 1.2), and contain abundant fine-scale cross joints. KD13 is vertical and strikes  $125^\circ$  towards the south end of Kaneohe

Bay. It has a fairly high density of  $3.04 \text{ g cm}^{-3}$ , and lacks MSL. Good clustering and a bimodal distribution of the  $\chi_1$  axes (category 2), inferred to represent a magnetic imbrication, indicates that the magma flowed  $315^\circ$  and up at  $-31^\circ$  towards the northwest from a source beneath the south-end of Kaneohe Bay (within the postulated Kaneohe Caldera).

KD14 is a moderately weathered, 248 cm wide dike that contains few zeolite-filled amygdales (1 mm diameter), and has a bulk density of  $2.84 \text{ g cm}^{-3}$ . The AMS fabric is random (category 6). The total anisotropy varies from 0.8–4.8%, and the only apparent explanation is that the dike may have been turbulently emplaced.

#### **Dikes KD15–17; N Apokula Street; Keolu Hills**

These dikes are from a deep-terraced cut about 25 m above sea level, and are moderately weathered. They are irregular, thin, show crosscutting features, and have intruded pyroclastic tuffs, thought to have formed in the upper part of the volcanic edifice. KD15 has a very low bulk density of  $2.77 \text{ g cm}^{-3}$ . Based on these morphological features it is inferred that the dikes formed during multiple stages of shallow intrusion. The Keolu Hills dike swarm marks both the southern and southeastern rim of the Kailua Caldera, where dike intensities locally reach 85% in 100 m traverses; *Walker, 1987*. This dike swarm trends to the northeast (Figure 1.3) subparallel to the minor NE-rift, while the oldest dikes seem to be parallel to the main SE-rift. Dikes KD15 and 16, both strike at  $230^\circ$  normal to the main rift zone and dip at  $75^\circ$  in opposite directions.

Dike KD15 is moderately weathered to a gray color, contains very small ( $<0.1$  mm maximum diameter) zeolite filled amygdales. The dike narrows upwards and also sidesteps to the southeast, and intrudes a hydrothermally altered fine-grained light-gray tuff. The MSL is variable, plunging from  $<30^\circ\text{NE}$  along the arm of the offset to  $65^\circ\text{NE}$  and agrees to within  $24^\circ$  with the plunge of the  $\chi_1$  axes (Table 4). The mean total percent anisotropy is low (0.5%), but, the  $\chi_1$  axes form a good cluster that has a slight bimodality. The  $\chi_2$  and

$\chi_3$  axes plot on a steeply inclined girdle (categories 2 and 3) similar to dike KD11, implying that individual magnetic grains resemble prolate ellipsoids, in which the intermediate and the minimum axes are of nearly equal dimension. The AMS axial ratios and an  $E$  value  $<1.000$  also suggests that the magnetic fabric is prolate (see Table 2.2). For this dike the  $\chi_3$  axes cluster in the vertical foliation plane while the  $\chi_2$  axes cluster near the dike pole, which is opposite to the normal axial distribution for the majority of the Koolau dikes. It seems likely that the  $\chi_2$  and  $\chi_3$  axes have been transposed, suggesting a possible change in the internal stress field at this point of dike injection. This interpretation is also substantiated by the relative closeness of the sample site localities to the dike-offset, suggesting that the magma was undergoing substantial changes in flow direction. The absolute magma flow direction based on the good agreement between the MSL and the AMS imbrication direction is up at  $-24^\circ$  to the southwest.

Dike KD16 crosscuts an older dike, has non-glassy chilled margins, a high bulk density of  $3.0 \text{ g cm}^{-3}$ , and a plunge of the MSL that varies from  $10^\circ$  to  $65^\circ\text{SW}$  (the mean is  $40^\circ$ ). The  $\chi_1$  axes show good clustering with a bimodal distribution that plunges  $13^\circ$  to the southwest and agree to within  $24^\circ$  with the MSL direction (category 2). The absolute magma flow direction is  $67^\circ$  and up  $-11^\circ$  to the northwest (i.e. in the opposite direction to that of dike 15). Based on the relatively high bulk density and inferred magma flow direction, this dike is thought to have been emplaced at moderate depth ( $\sim 1 \text{ km}$ ) along the presumed level of neutral buoyancy.

KD17 is a moderately weathered dike with irregular morphology, a variable strike of about  $120^\circ$ , and a dip of  $70^\circ\text{NE}$ . The MSL plunge shallowly  $9^\circ$  to the southeast and agree very well, to within  $14^\circ$  with the mean  $\chi_1$  direction of  $106^\circ$  and plunge  $16^\circ\text{SE}$ . The  $\chi_2$  and  $\chi_3$  axes form a foliation plane normal to the strike of the dike (category 3), some of the axes seem to be transposed, and are suggested to be related changes in the stress field due to the variability in dike trend. Thus the inferred magma flow direction is down  $16^\circ$  to the southeast, away from the presumed source, the Kailua Caldera. Since this dike is relatively

young, has a slightly higher than average bulk density of  $2.95 \text{ g cm}^{-3}$ , and a magnetic fabric that suggests downward directed magma flow, it is inferred to have been emplaced under negative buoyancy forces. *In summary*, dikes KD14–16 suggest at least two different intrusive events, in which dikes KD15 and 16 are circumferential to the Kailua Caldera and represent the most recent intrusive event with a source to the northeast beneath the Keolu Hills or Kailua Bay.

#### **Dikes KD18–20; between Waikeekee and Uwau valleys**

These dikes are fresh, near vertical, and wide (>175 cm), and lack MSL. They have very low bulk densities averaging  $2.58 \text{ g cm}^{-3}$ , and are located at a moderately high erosional level (280 m above sea level) on the southern side of the interfluvium between Waikeekee and Uwau valleys. Dike KD18 is 230 cm wide, strikes  $140^\circ$ , and is vertical. It is slightly prophyritic, and contains large zeolite-filled amygdales in its center. Some samples contain large (3–5 mm diameter) irregular, elongated vesicles that show elongation parallel to the dike margins. The AMS axial distributions are moderately well clustered. The  $\chi_1$  axes form a bimodal cluster (the type example for category 2), with a mean direction of  $137^\circ$  and plunge of  $28^\circ\text{SE}$  towards the Kaneohe center. The  $\chi_2$  axes plot near vertical, and the  $\chi_3$  axes plot near the pole of the dike. Based on the inferred magnetic imbrication the absolute magma flow direction is  $317^\circ$  and up at  $-28^\circ$ .

Dike KD19 is extremely vesicular and contains large irregular shaped vesicles up to 10 mm diameter. The bulk density was not determined because the samples would have to be destroyed in order to calculate the correct whole rock volume. Only four samples were collected along its southwest margin, however, all axial distributions are moderately-well clustered (category 1). The inferred magma flow direction is  $331^\circ$  and  $-14^\circ$  up.

Dike KD20 strikes  $145^\circ$  with a variable dip of  $45^\circ$  to the  $80^\circ\text{NE}$ , is moderately weathered, well jointed and fractured, and contains amygdales. The average bulk density is  $2.59 \text{ g cm}^{-3}$ . Because of poor exposures all the specimens were collected from the

southwest (left) dike margin. The AMS axial distributions form tight clusters on the equal-area plot (Appendix A). The trend of the mean  $\chi_1$  direction is  $184^\circ$  and plunging  $21^\circ$ –SW,  $\chi_3$  axes plot near to though slightly offset from the dike pole. This apparent offset of the maximum  $\chi_1$  axes to the dike's strike ( $\sim 35^\circ$ ) has several possible explanations: (1) it represents a magnetic imbrication along the left margin of the dike, and thus the absolute magma flow direction was parallel to the dike strike,  $145^\circ$  and up at  $-21^\circ$  towards the northwest; (2) the dip of the dike has preferentially decreased the force producing axial migration of the magnetic particles in the left half of the dike (footwall) because the force exerted by gravity is not exactly opposite the viscous drag acting along the walls, as in the model suggested by *Gibb* [1968] (for a more complete explanation refer to the following section on "Flow Differentiation and Crystal Content...", Chapter 4); or (3) some combination of these two processes was operative during dike injection. The magnetic fabric for dike KD20 is slightly prolate (Table 3.1), and the inferred magma flow direction is  $4^\circ$  and up at  $-21^\circ$  to the north. *In summary*, the dikes of this sub-set all show shall oblique magma flow directions that are consistent with each other and up at  $-14^\circ$  to  $-28^\circ$  towards the northeast.

### **Dikes KD21-28; H3 Highway, northern roadcut**

This dike-set is at an elevation of about 40 m above sea level, and lies half-way between the Kailua and Kaneohe eruptive centers. The dikes are moderately chloritized to a greenish dark-gray color, they have a slightly low average bulk density of  $2.83 \text{ g cm}^{-3}$ , and a very high average (mean) total magnetic anisotropy ( $H= 4.11\%$ ). Five of the dikes have lineated magnetic fabrics, in which the mean susceptibility tensor is prolate shaped (Appendix A). These dikes exhibit crosscutting relationships representing multiple stages of intrusion in which the maximum dike intensity reaches 70%. The MSL for these dikes plunge in opposite directions suggesting the magma rose from two separate source regions, one below Kailua and the other below southern Kaneohe Bay. There is little morphological

evidence for a Kaneohe Caldera. However, based on inferred magma flow directions from MSL plunge directions, *Walker* [1987] suggests that an eruptive center may have existed in southern Kaneohe Bay. Furthermore, since a caldera is specifically a subsidence feature at a center, and Kaneohe Bay represents the only other topographic low with a correspondingly high Bouguer anomaly in this region, it is therefore a likely candidate if two calderas had existed. If this inference is correct, its evidence could have easily been destroyed by huge landslides and debris flows associated with the formation of the Pali cliffline to the southwest as suggested by *Moore* [1964].

Dike KD21 has next to the lowest bulk density ( $2.67 \text{ g cm}^{-3}$ ) of this dike-set, and contains abundant small (1–2 mm) zeolite-filled amygdales that are concentrated along segregation layers parallel to the dike walls. The MSL trend  $331^\circ$  and plunge shallowly  $25^\circ\text{NW}$  towards southern Kaneohe Bay. The  $\chi_1$  AMS axes show excellent clustering. They have a slight bimodal distribution and agree very well within  $15^\circ$  with the MSL trend (category 2). Therefore the absolute magma flow azimuth is  $140^\circ$  and up at  $-29^\circ$  towards the southeast. Furthermore, as suggested for KD20, *Gibb's* [1968] model also seems to explain the slight variation of the mean  $\chi_1$  direction with the dike trend (a  $15^\circ$  shift to the southwest, left) for a right dipping dike (refer to Figure 3.4).

Dike KD22 has the lowest bulk density ( $2.60 \text{ g cm}^{-3}$ ) of this dike-set, it is flow banded along its margin, and has an anomalous strike of  $35^\circ$  and dip of  $75^\circ\text{SE}$ . The MSL plunge steeply  $68^\circ$  to the southwest and vary substantially ( $38^\circ$ ) from the mean plunge of the  $\chi_1$  axes. All three AMS axial distributions are moderately-well clustered and the  $\chi_3$  axes plot near the pole of the dike (category 1). Based on the mean axial ratios the magnetic fabric is slightly oblate. The inferred magma flow direction is  $51^\circ$  and up at  $-37^\circ$  to the northeast.

Dike KD23 strikes  $310^\circ$  and dips  $80^\circ\text{NE}$ . It is moderately weathered to a greenish color, has very irregular margins, and is the narrowest of the dikes sampled (20 cm wide). It has a mean bulk density of  $2.74 \text{ g cm}^{-3}$ . The MSL plunge very steeply at  $70^\circ$  to the northwest towards Kaneohe Bay. The AMS axial distributions are lineated, well clustered,

and have a prolate shape. The mean  $\chi_1$  direction agrees extremely well (within  $4^\circ$ ) with the MSL (category 1). The inferred magma flow direction is  $122^\circ$  and up at  $-72^\circ$  to the southeast from a source below Kaneohe Bay.

Dike KD24 has a similar trend to KD23, but is much wider (200 cm), and also contains abundant zeolite-filled amygdales (1 mm diameter). It has a bulk density of  $2.93 \text{ g cm}^{-3}$ . Only the right margin was exposed well enough to sample. This might explain the large ( $42^\circ$ ) variation between the MSL plunge of  $45^\circ$  to the northwest and the orientation of the  $\chi_1$  axes. The AMS axial distributions are well clustered (category 1), but are offset more than  $50^\circ$  from the dike's strike. This offset could be explained as a magnetic imbrication along the right margin. The inferred magma flow direction is to the south and up at  $-52^\circ$ , and would be in agreement with such an interpretation.

KD25 has a similar trend to dikes KD23 and 24. It is 97 cm wide, and contains abundant zeolite-filled amygdales along its axis (1–2 mm diameter). The MSL plunge  $32^\circ\text{NW}$  and agrees to within  $32^\circ$  (less) with the mean  $\chi_1$  direction. The  $\chi_1$  axes are well clustered in the dike foliation, while the  $\chi_2$  and  $\chi_3$  axes form along a girdle (category 3). The inferred magma flow direction is  $126^\circ$  and up at  $-63^\circ$  from a source beneath Kaneohe Bay.

Dike KD26 lacks surface lineations. It is altered to a light to medium greenish-gray color and is finely porphyritic with very few zeolite-filled amygdales. It has a slightly higher than average bulk density ( $2.92 \text{ g cm}^{-3}$ ), and is massively-well-jointed and moderately fractured. The  $\chi_1$  axes form a good cluster that has a slight bimodality similar to that previously described (categories 2 and 3). In this case the offset is approximately  $15^\circ$  on either side of the dike. The  $\chi_2$  and  $\chi_3$  axes tend to form a slight girdle. However, if two of the  $\chi_2$  and  $\chi_3$  axes (shown by T's, Appendix A) were transposed, then all three axial distributions would be well clustered, with the  $\chi_3$  axes plotting near the pole of the dike. Therefore the magma flow azimuth is  $294^\circ$  and down  $17^\circ$  to the northwest. This

downward plunging flow direction is consistent with this dike's higher than average bulk density of 2.92 g cm<sup>-3</sup>.

Dike KD27 lacks surface lineations and is 97 cm wide. It is coarse-grained porphyritic (subhedral– euhedral phenocrysts ≤3 mm diameter), rich in both olivine and plagioclase phenocrysts and has the highest bulk density of this dike-set (3.08 g cm<sup>-3</sup>). There seems to be a preferred elongation direction of the lath-shaped plagioclase crystals in the plane of the dike. The magnetic fabric is strongly foliate, and oblate shaped ( $E= 1.024$ ). Of all the dikes studied for AMS this one has the highest mean total anisotropy ( $H= 7.61\%$ ). The  $\chi_3$  axes form an excellent cluster near the pole of the dike, while the  $\chi_1$  and  $\chi_2$  axes form a girdle along a foliation plane (category 5). No magma flow direction is inferred from this strongly foliated magnetic fabric.

Dike KD28 strikes 300° and dips 75°NW. This dike is fresh dark greenish-gray and slightly porphyric and has irregular margins. This dike like KD27 is strongly foliated and has the second highest total anisotropy ( $H= 6.74\%$ ). The  $\chi_3$  axes are well clustered near the pole of the dike and the  $\chi_1$  axes are also well clustered and have a slight bimodality, but the mean  $\chi_1$  direction plots at more than 25° from the dike trend and the surface lineations (category 2). This departure seems to be related to the irregular form of the dike. The inferred absolute magma flow direction is 276° and up at -18° away from the Kailua center. *In summary*, the AMS data suggest that the magma source for dikes KD21, and KD23–25 was beneath Kaneohe Bay, and in three of these (KD23–25) the magma flow direction was up at a steep angle between 52–72°. The magnetic fabric in three other dikes (KD22, 26, 28) suggests that their source was located at a second source beneath the Kailua center. The magma flow directions in two of these dikes (KD22 and 28) was up at a shallow angle 18–37°, and in KD26 the magma flowed down at a shallow angle of 17°. Furthermore, amongst the six lineated dikes there is good to moderate agreement between the plunge of surface lineations and the maximum  $\chi_1$  direction, from 4–42°. Based on the abundance of amygdales (zeolite-filled vesicles), the lower average bulk densities, the steeply plunging

MSL and inferred (upward) magma flow directions, these dikes are interpreted to have been emplaced in a positive buoyancy environment possibly very near their source reservoir (within several kilometers).

**Dikes KD29–31; Pohakea Point, S Kaneohe Bay: elevation 20 m**

Dike KD29 is 75 cm wide, strikes  $120^\circ$  and has shallow dip of  $60^\circ\text{NE}$ . This dike is moderately weathered to a light greenish-gray color, is flow-banded on its margins, and contains abundant fine-grained (<1 mm diameter) white zeolite-filled amygdales. It has an average bulk density ( $2.89 \text{ g cm}^{-3}$ ). Since the  $\chi_1$  axes are less well grouped and have a somewhat anomalous trend ( $40^\circ$  and plunge  $53^\circ\text{NE}$ ) the inferred dike-emplacment direction based on the AMS axial distributions seem to be better represented by well clustered  $\chi_2$  axes. In this case the dike emplacement direction is based on the intermediate  $\chi_2$  direction and therefore would agree with the findings of *Ellwood* [1978] for some Icelandic dikes (category 4). The magnetic fabric is slightly foliated and prolate shaped, with a high mean total anisotropy of 4.64%. The inferred magma flow direction (based on the intermediate AMS axial distributions) is  $115^\circ$  and up at  $-11^\circ$ . Furthermore, this interpretation using the  $\chi_2$  axes to infer the magma flow direction is in agreement with the AMS axial distributions of the other dikes. However, for dikes KD30 and KD31 the  $\chi_1$  axes give a flow imbrication in which the azimuth of magma flow is shallow and up toward the SE (Tables 3.1 and 3.2).

Dike KD30 also has a shallow dip  $60^\circ\text{NE}$ , is weathered to a rust color, and contains abundant amygdales in its center. This dike is 101 cm wide and has a slightly lower than average bulk density ( $2.80 \text{ g cm}^{-3}$ ). The  $\chi_3$  axes are well clustered and slightly offset from the dike pole. The  $\chi_1$  and  $\chi_2$  axes are poorly clustered about the dike's foliation plane, and the  $\chi_1$  axes have a slight bimodality inferred to be a magnetic imbrication (categories 2 and 5). The magnetic fabric is strongly foliated and dominated by oblate shaped magnetic

grains ( $E= 1.021$ ). The mean total anisotropy is high; 3.44%. The absolute magma flow direction is  $119^\circ$  and up at  $-18^\circ$  to the southeast.

Dike KD31 strikes  $125^\circ$  and dipping  $80^\circ$ NE. It is 125 cm wide, flow banded, and moderately weathered to a rust brown color along its margins. It is massively grained and sparsely porphyritic, with a bulk density of  $2.83 \text{ g cm}^{-3}$ . MSL are nearly horizontal, plunging  $10^\circ$ SE and vary nearly  $40^\circ$  with the mean maximum AMS axis. The  $\chi_3$  axes are well clustered near the dike pole, the  $\chi_2$  axes are very well clustered in the dike foliation, and the  $\chi_1$  axes have a slight bimodality (category 2). This dike also has a high total anisotropy ( $H= 3.44\%$ ). The absolute magma flow direction is  $140^\circ$  and up  $-23^\circ$  to the southeast from a source beneath Kaneohe Bay. *In summary*, all three dikes of this subset have relatively high total anisotropy (averaging 4.22%), in which the AMS axial distributions are foliated and moderately well clustered. Two dikes (KD30, 31) have an imbricated magnetic fabric, in which the inferred absolute magma flow direction was up toward the southeast at a shallow angle ( $18\text{--}23^\circ$ ), suggesting a source beneath Kaneohe Bay.

#### **Dikes KD32–34; Kailua Road cut S of Kaelepu Street: elevation $\sim 0$ m**

This dike-set is very near the Kawainui Swamp and the high positive Bouguer anomaly. All three dikes strike roughly perpendicular to the main trend of the dike complex. The anomalous dike trends seem to be common feature nearest the proposed caldera margins. KD32 is a narrow 40 cm wide, aphyric dike with an irregular surface morphology. The dike margins are flow banded along a zone several centimeters wide, which is highly altered to a reddish-brown rust color. Both the margins and the center contain abundant small ( $\leq 1$  mm diameter) zeolite-filled amygdales. This dike sidesteps dramatically (2 m) to the north along a narrow feeder and has a dilation plunge of  $23^\circ$  to the north-northeast. The dike strikes approximately  $90^\circ$  and dips  $85^\circ$ S, which is nearly perpendicular to the major trend of the dike complex. Samples were collected just below

the feeder sidestep in hopes of comparing the magnetic fabric with possible complexities in flow rheology that could occur near a dike offshoot. The magnetic fabric is strongly prolate shaped ( $E=0.985$ ), and shows a very tight cluster of the  $\chi_1$  axes in the plane of the dike with only a slight bimodality (category 1 or 2). The mean total anisotropy is high ( $H=4.19$ ). It is interesting to note that all the  $\chi_1$  axes are rotated  $15^\circ$  NW (to the right) of the dike strike, and in the opposite direction of the offshoot. There is a fairly good agreement between the plunge of the surface lineation and the  $\chi_1$  axes (within  $18^\circ$ ), but the bimodality of these axes is so slight that the azimuth of flow is ambiguous. However, the fact that the inferred magnetic imbrication direction agrees well with a presumed magma source reservoir located to the west in the Kawainui swamp as suggested by Walker [1987], adds credence to the above interpretation. Also, if it is correct to infer that dialational opening influenced the orientation of the  $\chi_1$  axes, and assuming that a changing stress field influenced this misalignment (i.e. shifting their orientation  $15^\circ$ ), then the  $\chi_1$  may have been initially parallel to the dike trend farther up source. Therefore the magma flow direction is interpreted to be  $109^\circ$  and up at  $-9^\circ$ .

Dike KD33 is 43 cm wide and strikes  $260^\circ$  and dips  $80^\circ$  SE. It is weathered to a light gray color, is mostly aphyric and contains abundant large ( $\geq 1-2$  mm diameter) zeolite-filled amygdales. The dilation vector plunges shallowly  $20^\circ$  to the northeast. The MSL plunges steeply, though varying between  $65-85^\circ$  W-SW, and agrees extremely well with the mean  $\chi_1$  direction (within  $3^\circ$ ). The minimum  $\chi_3$  susceptibility axes are predominantly well clustered though slightly offset  $25^\circ$  northeast of the dike pole. There is a slight bimodality of the  $\chi_1$  axes (category 2). Both the  $\chi_1$  and  $\chi_2$  axes are moderately clustered and form a girdle subparallel to the dike foliation plane. The total susceptibility anisotropy is high ( $H=4.19\%$ ), and the magnetic fabric is oblate shaped and slightly foliated. The inferred absolute magma flow direction is  $58^\circ$  and up at  $-72^\circ$  to the northeast.

Dike KD34 is 22 cm wide and is weathered to a light pinkish-brown color. It strikes  $90^\circ$  and dips  $85^\circ$  S. It is slightly olivine porphyritic and contains abundant small- and large-

scale zeolite-filled amygdales near its margins and center. The dike margins are irregular with a MSL plunge of  $56^{\circ}\text{E}$ , agreeing well (within  $15^{\circ}$ ) with the mean  $\chi_1$  direction. The dilation vector plunge is  $35^{\circ}$  to the northeast. The AMS axial distributions are very well clustered, and  $\chi_3$  axes plot near the dike pole (category 1). This dike has the third highest mean total percent anisotropy (6.61%). The magnetic fabric is slightly foliated and oblate shaped. The inferred magma flow direction is  $121^{\circ}$  and down  $49^{\circ}$ . *In summary*, the magnetic fabrics of these dikes agree very well with the MSL plunge directions. Furthermore, based on the slight magnetic imbrication in one dike (KD32), and the location of the proposed source relative to the other two (KD33, 34), the inferred magma flow directions for this subset seems to have varied substantially; from obliquely downward, to nearly horizontal or vertical (upward). The abundance of zeolite-filled amygdales suggest that these narrow irregular dikes were intruded at relatively shallow depths in which a buoyant magma was free to flow upward or downward or even horizontally.

#### **Dikes KD35–37, 39, and infilled lava tube KT38, KT47; Makapuu Point**

This dike-set represents the farthest southeast extension of the Koolau dike complex, about 15 km away from the Kailua center. Dikes KD35–37 and the infilled lava tube outcrop along the coast just south of the lighthouse (0–15 m above sea level). Dike KD35 is 121 cm wide and strikes  $165^{\circ}$  and dips  $82^{\circ}\text{SW}$ . It is vesicular (max. diameter= 1 mm) and relatively coarse-grained porphyritic, with large phenocrysts of olivine and plagioclase (max. diameter= 5 mm) inside of the chilled margins. The nonglassy chilled margins display imbricated sheet joints that are interpreted to indicate the absolute flow azimuth (Figure 1.7). The AMS axial distributions are well clustered, with  $\chi_3$  axes plotting near the dike pole. The  $\chi_1$  axes form a good bimodal cluster that is nearly symmetrically disposed to either side of the dike strike (category 2). The inferred magma flow direction based on a magnetic imbrication is in agreement with the sheet joint imbrication ,thus the magma

flowed 150° and shallowly downward 21° to the southeast (compare Appendix A and Figure 1.7).

Dike KD36 is 45 cm wide, strikes 125°, and is vertical. It contains abundant, small spherical vesicles (max.diameter ≤0.5 mm), and is moderately porphyritic, rich in plagioclase crystals (max.diameter= 2 mm). The AMS axes are well clustered with  $\chi_3$  axes plotting near the dike pole (category 1). The MSL plunge is 20°SE and agrees to within 15° with the mean  $\chi_1$  direction. The AMS fabric is foliated and oblate shaped. The magma flow direction is 109° and down 27° to the northwest away from the inferred magma source region (the Kailua center).

Dike KD37 is oriented parallel to and was intruded along a portion of the northeast margin of dike KD36, it is therefore younger. It has fresh, glassy chilled margins and is narrower, coarser grained, and more olivine rich than KD36. It also has abundant large vesicles (up to 1 mm diameter). The  $\chi_1$  axes are well clustered in the dike foliation plane, while  $\chi_2$  and  $\chi_3$  axes are poorly clustered and fall along a girdle (category 3). The inferred magma flow direction is 145° and down 68° to the southeast.

KT38, a lava tube infilling was sampled in order to compare its assumed azimuth of flow to its magnetic fabric, and possibly test the validity of the magnetic imbrication relationship. Samples were collected only from a small portion of the upper part of the tube infilling (250 cm diameter). The lava tube infill contains similar olivine tholeiitic basalt to the dikes sampled at Makapuu Point. The early formed crystals of olivine, plagioclase, and pyroxene tend to be concentrated along segregation layers parallel to the tube walls. The  $\chi_1$  axes have a very tight bimodal distribution, and the flow azimuth derived from it agrees very well (within 10°) with the 6° SE dip of the associated pahoehoe lava flows. The AMS fabric is well lineated and prolate shaped, and represents an imbrication along the margins of the lava tube (category 2). The inferred absolute flow azimuth is 160° and down 2° to the southeast. This interpretation is supported by oriented thin sections collected from the margins of the lower levels of the tube infilling (refer to subsequent section on "Vesicle

Orientations During Magma Flow", Chapter 4), which show similar imbrication of elongated plagioclase crystals and pipe vesicles against the tube walls.

Dike KD39 is one of the widest dikes sampled (358 cm). This dike is located along the surface road to the water storage tanks 400 m above sea level. The dike margins are slightly porphyritic and altered to a red iron-oxidized color. They tend to be irregular and possibly gradational with the country rock. Along the dike margins the host rock lava flows show signs of thermal alteration or erosion (metamorphism). The bulk density is only slightly higher than the average ( $2.90 \text{ g cm}^{-3}$ ). Of the dikes measured for AMS, this is the most olivine-phyric and has a very high concentration of olivine (>60%) in a zone 45 cm wide in its center. The olivine phenocrysts reach a maximum size (max. diameter  $\geq 5$  mm) in this part of the dike. The  $\chi_1$  and  $\chi_2$  AMS axes are scattered along a foliation plane and the  $\chi_3$  axes are well clustered near the dike pole. No flow direction can be inferred (category 6). Note that the mean total susceptibility anisotropy is moderately low ( $H=0.97\%$ ; Table 3.1). It is not possible to determine whether this low value is related to turbulent flow, postemplacement crystal growth, or secondary alteration.

KT47 is the upper part of the infilled lava tube KT38. It is approximately 1 km northwest and approximately 100 m higher in elevation than KT38. KT47 strikes  $162^\circ$  and is 850 cm in diameter. The AMS axes are poorly clustered (random), therefore no interpretation of the magma flow direction is given (category 6). At this locality the infilled lava tube has a larger overall diameter than is observed down at the coastline at site KT38. Its mean total susceptibility anisotropy is very low (0.18%), possibly suggesting that the magma flow was turbulent within this portion of the tube. *In summary*, the magnetic fabric for this dike-set demonstrates a very interesting feature, the inferred magma flow direction of three of the dikes (KD35–37), as well as the infilled lava tube (KT38), was almost certainly away from the Kailua center toward the southeast. This interpretation has important tectonic implications, since it indicates that low on the flanks of the volcanic shield at the extreme outer reaches of the dike complex the magma flowed downward

possibly into pre-existing fractures or cracks. Thus, suggesting that dike injection was not forceful, but instead may have been more passive in nature, at least in the most distal regions, and during the late shield building stage.

#### **Dikes KD40 and 41; Waikane Ridge: elevation 250 m**

Dike KD40 strikes  $140^\circ$  and is vertical. It is 140 cm wide and the MSL plunge  $74^\circ$  to the southeast. Nearest the nonglassy chilled margins the dike is massive or fine-grained, while the center is olivine porphyritic (max.diameter= 2 mm). All the samples were collected from the right (NE) margin. The AMS axial distributions are well clustered, in which the  $\chi_3$  axes plot near the dike pole. The  $\chi_1$  axes plot near the foliation plane of the dike. There is a considerable variation ( $52^\circ$ ) between the  $\chi_1$  direction and the surface lineation plunge. The inferred magma flow direction is  $153^\circ$  and up  $-51^\circ$  to the southeast.

Dike KD41 strikes  $280^\circ$  and is vertical. It is 230 cm wide and contains abundant plagioclase phenocrysts elongated parallel to the dike walls. The mean bulk density is very high ( $3.07 \text{ g cm}^{-3}$ ). The AMS axes are poorly clustered, in which the  $\chi_1$  and  $\chi_2$  axes are randomly distributed along a griddle in the dike foliation plane (category 5). The magma flow direction is poorly constrained but may have flowed  $300^\circ$  and up at  $-59^\circ$ . *In summary*, there seems to be poor agreement for the inferred magma flow directions for the two dikes of this subset.

#### **Dikes KD42-46 and 51-55; Kapaa Quarry: elevation 150–240 m**

The dikes of the first dike-set (KD42–46) were collected near the upper level of the quarry, while the other set represents lower intrusive levels, though there is some overlay at the intermediate sampling levels. All the dikes are to varying degrees hydrothermally altered (chloritized) to a light greenish-gray color. This locality represent one of the higher dike intensities reached in the Koolau complex ( $\geq 55\%$ ). Dike KD42 is 150 cm wide. It strikes  $300^\circ\text{NW}$  and is nearly vertical with a dip of  $85\text{--}88^\circ\text{NE}$ . It is massive, aphyric, and mainly fine grained along its margins and slightly porphyritic at its center. Along the dike

axis is a zone 30 cm wide containing abundant large zeolite filled amygdales (max. diameter= 5 mm). In the hand samples, plagioclase phenocrysts appear to be more abundant than olivine, and the bulk density is slightly lower than the mean ( $2.82 \text{ g cm}^{-3}$ ). The plunge of the MSL is shallow at  $15^\circ\text{SE}$  and agrees excellently with the mean  $\chi_1$  direction (within  $11^\circ$ ). The AMS axes are well clustered, with  $\chi_3$  axes plotting near the dike pole and  $\chi_1$  and  $\chi_2$  axes plotting along the foliation plane of the dike (category 1). The inferred magma flow direction is  $304^\circ$  and up  $-24^\circ$ .

Dike KD43 is 50 cm wide and strikes  $145^\circ$  and is near vertical  $88^\circ\text{NE}$ . It is massive with minor amygdales present, and contains abundant calcite filled cracks. It has a bulk density similar to the mean ( $2.86 \text{ g cm}^{-3}$ ). The MSL surface lineation plunge is  $23^\circ\text{SE}$  and agrees well with the mean  $\chi_1$  direction (within  $17^\circ$ ). All three AMS axes are very well clustered, and the  $\chi_1$  axes show a slight bimodality (category 2). The total susceptibility anisotropy is slightly lower than the mean ( $H= 1.9\%$ ). The magnetic fabric is slightly lineated and prolate shaped. The inferred magma flow direction is  $306^\circ$  and up at  $-25^\circ$  to the northwest.

Dike KD44 strikes  $320^\circ$  and dips  $80^\circ\text{NE}$ , and is adjacent to and wider than KD43 (with a diameter of 85 cm). This dike has a medium dark gray color, and is massively-grained with a slightly higher than average bulk density ( $2.91 \text{ g cm}^{-3}$ ). The  $\chi_1$  axes are very well clustered while the  $\chi_2$  and  $\chi_3$  axes form a slight girdle normal to the dike foliation. In fact the  $\chi_3$  axes plot near the vertical and the  $\chi_2$  axes plot more near the dike pole, opposite to the normal situation (category 3). The inferred magma flow direction is horizontal and slightly down at  $4^\circ$  to the northwest.

KD45 is a very narrow (25–35 cm wide) dike with irregular margins that pinch out at the top. This dike contains abundant zeolite-filled amygdales (max. diameter= 1 mm), and has a very low bulk density of  $2.68 \text{ g cm}^{-3}$ . The AMS axes are moderate to poorly clustered, with the  $\chi_1$  and  $\chi_3$  axes plotting in the dike foliation plane while the  $\chi_2$  axes plot more near the dike pole (category 1?). The mean total susceptibility is low ( $H= 0.84\%$ ),

and magnetic fabric is slightly lineated. The inferred magma flow direction is  $351^\circ$  and up -  $26^\circ$  to the north.

Dike KD46 is 155 cm wide, strikes  $315^\circ$  and its dip is nearly vertical  $87^\circ$ NE. This dike is slightly weathered to a dark-gray color, and is very dense (bulk density is  $3.07 \text{ g cm}^{-3}$ ). It is aphyric, mostly non-vesicular, except along the dike center, in which a 30 cm wide zone contains infrequent small zeolite-filled amygdales (max. diameter  $<1 \text{ mm}$ ). The MSL plunge is  $39^\circ$ SE and varies greatly from the  $\chi_1$  mean direction ( $85^\circ$ ). The AMS axes are very well clustered, in which the  $\chi_3$  axes plot near the dike pole, while  $\chi_1$  and  $\chi_2$  axes plot in the dike foliation plane. The  $\chi_1$  axes have a bimodal distribution (category 2), hence the absolute flow direction is  $293^\circ$  and up at  $-57^\circ$  to the northwest. However, it is worth noting that the  $\chi_2$  direction is in much better agreement with the MSL plunge, thus making this dike fall into category 4. Compared to the other dikes in this subset KD46 has a much higher total susceptibility anisotropy ( $H=4.34\%$ ). The magnetic fabric is foliated and oblate shaped. *In summary*, the inferred magma flow direction is well constrained by the AMS fabric for this dike-set. Magma flow was mostly up toward the northwest at an oblique angle ranging from  $-24^\circ$  to  $57^\circ$  (average is  $33^\circ$ ), and only in one (KD44) did it flow horizontally. The slightly irregular morphology and vesiculated nature of these dikes suggest that they probably were intruded at relatively shallow depths. Furthermore, the oblique upward flow directions suggest that they were also emplaced under positive buoyancy forces.

Dike KD51 is 56 cm wide, and strikes  $135^\circ$  and has a vertical dip. It has irregular nonglassy chilled margins that are flow-banded. It is weathered to a medium gray color, and contains abundant zeolite-filled amygdales (1 mm diameter). The MSL plunge at  $40^\circ$ SE and agree well with the mean  $\chi_1$  direction (within  $10^\circ$ ). The  $\chi_3$  axes form a moderate cluster near the dike foliation, while the  $\chi_1$  and  $\chi_2$  are randomly distributed along a girdle normal to the plane of the dike (category 5?, the intermediate and minimum axes are

transposed). The mean total susceptibility anisotropy is low ( $H=0.45\%$ ). The inferred magma flow direction is  $303^\circ$  and up at  $-34^\circ$ .

Dike KD52 is 120 cm wide, and strikes  $123^\circ$  and dips shallowly  $77^\circ$ NE. This dike is massive, aphyric, and has the highest bulk density of this sub-set ( $3.13 \text{ g cm}^{-3}$ ). The MSL plunge direction agrees moderately well with the  $\chi_1$  direction (within  $36^\circ$ ). The AMS axes are moderately to poorly clustered, in which the  $\chi_3$  axes plot near the dike pole, while  $\chi_1$  and  $\chi_2$  axes plot in the dike foliation plane (category 1). The mean total susceptibility anisotropy is low ( $H=0.74$ ). The inferred magma flow direction is  $292^\circ$  and up at an oblique angle of  $-46^\circ$  to the northwest.

Dike KD53 is 140 cm wide, and strikes  $310^\circ$  and has a vertical dip. It is highly weathered to a rust-brown color, and contains abundant, large (2–5 mm diameter), irregular to elongated zeolite-filled amygdales along the dike center. This dike has one of the lowest bulk densities ( $2.63 \text{ g cm}^{-3}$ ). The  $\chi_1$  are very well clustered in the dike foliation plane, while  $\chi_2$  and  $\chi_3$  axes poorly distributed along a shallow dipping girdle normal to the dike foliation plane (category 3). The magnetic fabric is slightly lineated and prolate shaped. The mean total susceptibility anisotropy is low ( $H=0.43$ ). The inferred magma flow direction is  $316^\circ$  and up at a steep angle,  $-72^\circ$  to the northwest.

Dike KD54 is 64 cm wide, and strikes  $295^\circ$  and has a vertical dip. It is moderately weathered and contains abundant, large zeolite-filled amygdales (2–3 mm diameter), as well as pipe vesicles along its margin. The pipe vesicles are elongated and slightly imbricated in an upward direction. The MSL plunge  $40^\circ$ SE and agree well with the  $\chi_1$  direction (within  $18^\circ$ ). The AMS axes are well clustered, in which the  $\chi_2$  axes plot near the dike pole, while  $\chi_1$  and  $\chi_3$  axes plot near the dike foliation plane (category 1?; however, the intermediate and minimum axes are transposed). Like the KD53, the mean total susceptibility anisotropy is low ( $H=0.45$ ), and the magnetic fabric is slightly lineated and prolate shaped. The AMS fabric is in good agreement with both the MSL plunge direction and the elongation direction (imbrication) of the pipe vesicles along each margin of the

dike, therefore the inferred magma flow direction is 272° and up at an oblique angle, -42° to the northwest.

Dike KD55 is 167 cm wide, and strikes 130° with a dip of 85°NE. It is moderately weathered to a light brownish gray and both margins are cut by a younger dikes. This dike contains two amygdaloidal zones, each 20 wide and offset 18 cm from the dike axis. Individual pipe vesicles are ≥1–2 cm in length. The mean bulk density is very low (2.68 g cm<sup>-3</sup>). The  $\chi_3$  (AMS) axes are well clustered near the dike pole, while both  $\chi_1$  and  $\chi_2$  axes are poorly clustered in the dike foliation plane. The magnetic fabric is foliated and oblate shaped. The mean total susceptibility anisotropy is 1.15%. Shown on the equal-area plot are two samples (labeled "C", in Appendix A) that were collected from the dike center between the two amygdaloidal zones. These two samples tend to have much lower plunge directions of the  $\chi_1$  axes by comparison to the samples collected from the dike margins. For consistency, these samples have been included in the mean AMS calculations. The inferred magma flow direction is 330° and nearly vertical upward at -74° to the northeast. *In summary*, the magnetic fabric of these five dikes (KD51-55) show a steeply inclined magma flow azimuth (up -54° toward the northwest). This steep flow azimuth is consistent with the highly vesicular nature of these dikes, generally containing large zeolite-filled amygdales. Furthermore, the lower than average bulk susceptibility of these dikes (2.79 g cm<sup>-3</sup>; only dike KD52 had an anomalously high density), suggests that these dikes were intruded under positive buoyancy forces. These dikes were intruded at relatively shallow depths and their inferred source lay to the southeast below the Kailua center.

#### **Dikes KD49, 50 and 59; Wailea Point, Lanikai: elevation 50–60 m**

Dike KD49 strikes 275° and is vertical. It is 100 cm wide and weathered to a rust-brown color along its margins. Its margins are irregular and flow-banded, and contain MSL that plunge nearly horizontal at 8° to the southeast. The AMS axes are poorly

clustered (category 6), and the mean total susceptibility anisotropy is low (0.52%). No interpretation of the magma flow direction is given.

Dike KD50 is 140 cm wide and strikes 285° and dips 80°E. It is moderately weathered to a brownish gray color, and has irregular margins that lack surface lineations. The AMS axes are moderately to poorly clustered, in which the  $\chi_3$  axes plot approximately near the dike plot, while the  $\chi_2$  axes plot in the dike foliation plane (category 1). However, the  $\chi_1$  axes are shifted considerably from the dike foliation plane. The mean total susceptibility anisotropy is 1.17%. The inferred magma flow direction is 157° and up at -44° to the southeast.

Dike KD59 is 102 cm wide, and has a variable strike of 290–305° and dips vertically. It is weathered to a dark brownish-gray color. It is aphyric, and contains nonglassy chilled margins that are highly fractured and jointed. The MSL plunge is 35°NW and agrees extremely well with the mean  $\chi_1$  direction (within 2°). The mean total susceptibility anisotropy is 1.54%. The AMS axes are very well clustered, in which the  $\chi_3$  axes plot near the dike pole, while  $\chi_1$  and  $\chi_2$  axes plot in the dike foliation plane. The  $\chi_1$  axes have a bimodal distribution (category 2), hence the absolute flow direction is 111° and up at -38° to the southeast away from the Kailua Caldera. *In summary*, magnetic fabrics for two of the dikes of this subset suggest moderate oblique magma flow directions that were up at -38 to -44° to the southeast.

#### **Dike KD56; Haipu, near Molii Pond (Kamahamaha Hwy)**

Dike KD56 is the only dike sampled at Haipuu, across from Molii Pond, northern Kaneohe Bay. It is a very wide dike (305 cm) that strikes 105° and has a vertical dip. It is moderately weathered to a light gray color, and plagioclase phyrlic. This dike intrudes aa lava flows, it has irregular margins, and contains three brecciated zones in its center (20, 30 and 48 cm wide) that are separated 78 cm and 55 cm apart. Thin vesicle segregation zones (20 cm wide) occur near each margin, while the dike center is more massively-grained.

Within individual vesicle-trains, the vesicles are very irregular and elongated parallel to the dike margins. This dike has the lowest mean bulk density ( $2.54 \text{ g cm}^{-3}$ ) of all the dikes sampled. It is also, one of only two dikes that has a normally magnetized NRM direction (refer to the section on "Natural Remanent Magnetization...", Chapter 1). The mean total susceptibility anisotropy is 1.02%. The AMS axes are moderately clustered, in which the  $\chi_3$  axes (well clustered) plot near the dike pole, while  $\chi_1$  and  $\chi_2$  axes plot in the dike foliation plane. The  $\chi_1$  axes have a bimodal distribution (category 2), hence the absolute flow direction is  $307^\circ$  and down at  $54^\circ$  to the northwest away from the Kaneohe center. The magnetic fabric is slightly foliated and oblate shaped. This dike is unusual, in that whilst the magnetic imbrication suggests downward flow vesicle segregation zones occur along the dike margins, thus is contrary to *Oliver's* [1962] hypothesis (refer to section on "Magma Flow Differentiation...", Chapter 4). The vesiculated nature of the dike also suggests that it probably was intruded at a very shallow level. It is not known whether the brecciated zones are related to magma drainback, however it is noted that the inferred absolute magma flow direction does support a steep downward plunging flow azimuth

#### **Dikes KD57, 60, and 61; Mokolii Island (Chinaman's Hat), N Kaneohe Bay**

All three dikes were sampled at an elevation of 0–2 m above sea level. Dikes 57 and 60 have reversely magnetized NRM directions, while KD61 is the only other dike besides KD56 to be normally magnetized. These dikes represents two distinct polarity intervals and thus indicate two separate intrusive events separated by at the least  $10^5$  yr (i.e. the minimum time period for a complete paleomagnetic magnetic reversal, *Oriel et al.*, 1976). Dike KD57 is 70 cm wide. Its strike is  $130^\circ$  and it has a vertical dip. It is only slightly weathered to a dark gray color, and has cooling joints normal to the nonglassy chilled margins. It is massive, aphyric, lacks vesicles, and has a higher than average bulk density ( $2.97 \text{ g cm}^{-3}$ ). The AMS axes are well clustered, in which the  $\chi_3$  axes (moderately

clustered) plot near the dike pole, while  $\chi_1$  and  $\chi_2$  axes plot in the dike foliation plane (category 1). The mean total susceptibility anisotropy is 1.88%. The magnetic fabric is slightly foliated and prolate shaped. The inferred magma flow direction is  $173^\circ$  and up at  $-65^\circ$  to the southeast from a source below northern Kaneohe Bay.

Dike KD60 is 82 cm wide, and strikes  $110^\circ$  with a vertical dip. It is slightly weathered to a medium-dark gray color and contains abundant large cooling joints (25–45 cm wide) perpendicular to its margins. This dike is massive, aphyric with glassy– semi-glassy chilled margins, and contains a vesicle concentration zone 55 cm wide along its center. It has a highest mean bulk density of all the dikes sampled ( $3.17 \text{ g cm}^{-3}$ ). The MSL plunge direction is  $30\text{--}40^\circ\text{NW}$  and varies  $42^\circ$  from the  $\chi_1$  direction. The AMS axes are well-moderately clustered, in which the  $\chi_3$  axes plot near the dike pole, while  $\chi_1$  and  $\chi_2$  axes plot in the dike foliation plane. The  $\chi_1$  axes have a slight bimodality (category 3). The inferred absolute magma flow direction is  $145^\circ$  and up at  $-79^\circ$  (representing the steepest magma flow direction).

Dike KD61 is 222 cm wide, and is weathered to a rust gray color. It strikes  $140^\circ$  and has a vertical dip. This dike is extremely vesicular in its center, most of the vesicles are spherical-shaped (maximum diameter is 5 mm), and the margins contain occasional pipe-vesicles. The mean bulk density is very low ( $2.66 \text{ g cm}^{-3}$ ). There are two brecciated zones within its interior, similar to those observed in dike KD56. The  $\chi_3$  axes are very well clustered near the dike pole, while  $\chi_1$  and  $\chi_2$  axes plot in the dike foliation plane (category 1). The magnetic fabric is slightly foliated and oblate shaped. The inferred magma flow direction is  $180^\circ$  and up at a fairly steep angle  $-62^\circ$ . *In summary*, based on the different remanent magnetization directions, this dike-set represents at least two separate intrusive events. Dike KD61 as well as KD56 are normally magnetized and since radiometric age dating [Doell and Dalrymple, 1973] indicates that the subaerial lava flows of the Koolau were erupted during the Matuyama reverse polarity chron at about 2.6–1.6 Ma, the only possible period for the a normal NRM paleomagnetic direction would be during the Gauss

normal polarity chron (e.g. >2.41 Ma). Therefore dikes KD61 and KD56 probably both represent the earliest intrusive events in the formation of the Koolau shield volcano.

**Dike KD58; Pali Lookout, near the old Pali Highway: elevation 330 m**

Dike KD58 is a moderately wide dike 136 cm located near the Pali Lookout, . It strikes of  $125^{\circ}$  and dips shallowly  $65^{\circ}$ SW, and is only slightly weathered to a medium-dark gray color. It has glassy chilled margins, contains cooling joints perpendicular to the margins, and the center has a vesicle concentration zone (55 cm wide). The dike center is slightly olivine porphyritic, and the whole rock bulk density is average ( $2.86 \text{ g cm}^{-3}$ ). The AMS axes are well clustered, in which the  $\chi_2$  axes plot near the pole of the dike and the  $\chi_1$  and  $\chi_3$  axes plot in the dike foliation plane (category 1?; with the  $\chi_2$  and  $\chi_3$  axes transposed). The mean total susceptibility anisotropy is 1.29%. The magnetic fabric is slightly lineated and prolate shaped. The inferred magma flow direction is  $4^{\circ}$  and steeply upward at  $-66^{\circ}$  to the north.

**Dikes KD62-63; Kaipapau Gulch: elevation 50 m**

Dike KD62 is a wide dike (372 cm), and strikes  $325^{\circ}$  and has a vertical dip. It is massive fine-grained to plagioclase porphyritic in the center, its margins are irregular, and small (1 mm diameter) vesicles occur infrequently near the center. The mean bulk density is above average at  $2.95 \text{ g cm}^{-3}$ . The AMS fabric is very well clustered, with the  $\chi_3$  axes plotting near the dike pole, while  $\chi_1$  and  $\chi_2$  axes plot in the dike foliation plane (category 1). The magnetic fabric is foliated and oblate shaped. The total susceptibility anisotropy is 2.33%. The inferred magma flow direction is  $297^{\circ}$  and near vertical, down at  $74^{\circ}$  to the northeast.

Dike KD63 is 241 cm wide, and strikes  $305^{\circ}$  and dips  $80^{\circ}$ NE. It is slightly weathered to a medium-dark gray, and is cross jointed perpendicular to the glassy chilled margins. It is massive, aphyric with a very high bulk density of  $3.05 \text{ g cm}^{-3}$ . The AMS axes are moderately/poorly clustered (category 6). The total susceptibility anisotropy is 1.71%.

The magnetic fabric is strongly foliated and oblate, therefore no interpretation of the magma flow direction is given.

#### **Dikes KD64-66; Maakua Gulch: elevation 30 m**

Dike KD64 is 160 cm wide, it is olivine tholeiitic, and intrudes aa lava flows of similar lithology. This dike strikes  $315^\circ$  and dips vertically. The margins are flow banded containing narrow (4 mm wide) vesicle segregation zones and fewer olivine phenocrysts (5 mm diameter), while the center is extremely vesicular and olivine-rich (up to 30%). The mean bulk density is low ( $2.75 \text{ g cm}^{-3}$ ). The AMS axes are poorly clustered (category 6), and the total susceptibility anisotropy is very low ( $H= 0.33\%$ ). The random distribution of the AMS axes suggests turbulent magma flow conditions.

Dike KD65 is 110 cm wide, and strikes  $320^\circ$  and is vertical. The non-glassy chilled margins are weathered to a rust brown color, the rest of the dike is a medium gray color. This dike is mostly aphyric with few olivine phenocrysts present. The mean bulk density is high ( $3.05 \text{ g cm}^{-3}$ ). The AMS axes are well clustered, in which the  $\chi_3$  axes plot near the dike pole, while  $\chi_1$  and  $\chi_2$  axes plot in the dike foliation plane. The  $\chi_1$  axes have a slight bimodality (category 3). The total susceptibility anisotropy is high ( $H= 3.44\%$ ). The magnetic fabric is strongly foliated and slightly oblate shaped. The inferred absolute magma flow direction is  $312^\circ$  and down at  $26^\circ$  to the northwest.

Dike KD66 is very wide 305 cm and strikes  $290^\circ$  and dips  $75^\circ\text{NE}$ . It is weathered to a medium light-gray color, and is massively-grained, slightly porphyritic, contains minor amounts of small plagioclase phenocrysts. The mean bulk density is also very high ( $3.07 \text{ g cm}^{-3}$ ). The AMS axes are very well clustered, in which the  $\chi_3$  axes plot near the dike pole, while  $\chi_1$  and  $\chi_2$  axes plot in the dike foliation plane (category 1). The total susceptibility anisotropy is  $2.07 \text{ g cm}^{-3}$ . The magnetic fabric is foliated and slightly oblate shaped. The inferred magma flow direction is  $300^\circ$  and nearly horizontal, up at  $-9^\circ$ . *In summary*, two of the dike of this set have well clustered AMS fabrics that suggest that the magma flow

direction plunged shallowly to the northwest between 26° and -9° away from the Kailua and Kaneohe centers.

#### **Dikes KD69-71; Koloa Gulch: elevation 50–60 m**

This dike-set is 22 km from the Kailua center and represents the farthest dikes sampled from its presumed source. All three dikes have a similar strike of 325° and vertical dip. They also have very similar bulk densities, averaging 2.81 g cm<sup>-3</sup>. Dike KD69 is offset 90 cm to southwest of KD70. It is 145 cm wide and has slightly irregular, nonglassy chilled margins. It is weathered to a medium-dark gray color, and contains abundant small ( $\leq 1$  mm) vesicles along its margins. It is massive aphyric, with fewer vesicles in the center. The AMS axes are very well clustered, in which the  $\chi_3$  axes plot at the dike pole, while  $\chi_1$  and  $\chi_2$  axes plot in the dike foliation plane. The  $\chi_1$  axes have a bimodality (category 3). The mean total susceptibility anisotropy is low ( $H = 0.74\%$ ). The magnetic fabric is slightly foliated and oblate shaped. The inferred absolute magma flow direction is 323° and down at 17° to the northwest.

Dike KD70 is very wide (365 cm), and has nonglassy chilled margins. The margins are flow banded and contain abundant narrow vesicle segregation zones (14 individual stringers, 7 along each margin, representing a total width of 70 cm in from the margins). The maximum vesicle diameter is 7.5 mm, and elongate irregular vesicles tend to occur parallel to the dike walls. The dike center is olivine and plagioclase porphyritic, with the elongate plagioclase platelets lacking any preferred lineation direction. The AMS axes are randomly distributed (category 6), with a very low mean total susceptibility anisotropy ( $H = 0.26\%$ ). No interpretation of the magma flow direction is possible. This very wide dike may have been emplaced under a turbulent flow conditions.

Dike KD71 represents the widest dike sampled at 408 cm, and is weathered to a rust-brown gray color. The margins are irregular, and flow banded. Abundant large vesicles are concentrated in segregation zones along each margin (totaling 100 cm distance inside

the margin). Pipe vesicles 1–2 cm in length occur subparallel to the margins. The AMS axes are moderately clustered, in which the  $\chi_3$  axes plot near the dike pole, while  $\chi_1$  and  $\chi_2$  axes plot in the dike foliation plane. The  $\chi_1$  axes have a strong bimodality (category 3). The mean total susceptibility anisotropy is low ( $H= 0.61\%$ ). The magnetic fabric is slightly foliated and oblate shaped. The inferred absolute magma flow direction is  $322^\circ$  and down at  $18^\circ$  to the northwest, very similar to dike KD69. *In summary*, the inferred absolute flow direction based on magnetic imbrication is virtually identical for dikes KD69 and 70, in which the magma flowed down at a very shallow angle towards the northwest at  $17\text{--}18^\circ$ . Note that the magnetic imbrication angle is greater for the widest dike (KD71). It is also interesting to note that like the Makapuu Point dike-set, these dikes indicate that the magma flow direction was mostly downward away from the Kailua center. The vesicle concentration zones sampled along the margins of KD69 and 70 are also in disagreement with *Oliver's* [1962] model, in which the less dense material should migrate axially during downward flow. Furthermore at these distal localities the dike intensity is much lower  $\leq 15\%$ , and the individual dikes tend to be much wider (2–4 m).

#### **Dikes KD74-77;N Mokolua Island, off of Lanikai: elevation 1–2 m**

This locality represents one of the highest dike intensities ( $>65\%$ ). The mean dike density for this dike-set is low ( $2.72 \text{ g cm}^{-3}$ ). Dike KD74 is 55 cm wide and strikes  $300^\circ$  and dips  $80^\circ\text{NE}$ . It is highly altered (chloritized) to a light-greenish gray color, contains zeolite-filled pipe vesicles along the margins (refer to Figure 1.10), and a zeolite-filled amygdale segregation zone occurs at the dike center (15 cm wide, with individual amygdales 3 mm in diameter). The long axis of the pipe vesicles is aligned parallel to the dike margins and plunge  $38^\circ$  towards the northwest. The AMS axes are moderately-poorly clustered, in which the  $\chi_3$  axes plot near the dike pole, while  $\chi_1$  and  $\chi_2$  axes plot in the dike foliation plane. The  $\chi_1$  axes have a strong bimodality (category 3). The mean total susceptibility anisotropy is low ( $H= 0.28\%$ ). The magnetic fabric is slightly lineated and

prolate shaped. The inferred absolute magma flow direction is  $129^\circ$  and horizontal (up  $-2^\circ$ ) to the southeast away from the Kailua center.

Dike KD75 is 60 cm wide, and strikes  $310^\circ$  and dips  $75^\circ$ NE. It intruded along the northeast margin of dike KD74, is less altered, and has nonglassy chilled margins weathered to a reddish-brown color. Dike KD75 contains abundant zeolite-filled amygdales (2 mm diameter) along the margins. The MSL plunge is shallow at  $20^\circ$ NW. The  $\chi_3$  AMS axes are very well clustered, while the  $\chi_1$  and  $\chi_2$  axes are randomly distributed along a girdle in the dike foliation plane (category 5). The total susceptibility anisotropy is low ( $H=0.52\%$ ), and the magnetic fabric is slightly lineated and prolate shaped. No interpretation of the magma flow directions is given.

Dike KD76 is 65 cm wide, and strikes  $315^\circ$  and dips  $80^\circ$ NE. It is weathered to a rust-gray color, and contains abundant zeolite-filled amygdales nearest the dike margin. The MSL plunge  $44^\circ$ NW toward the Kailua center and agree well with the mean  $\chi_1$  direction. The  $\chi_1$  axes are well clustered in the dike foliation plane, while the  $\chi_2$  and  $\chi_3$  axes are randomly distributed along a girdle normal to the dike strike. The total susceptibility anisotropy is low ( $H=0.73\%$ ), and the magnetic fabric is foliated and oblate shaped. The inferred magma flow direction is  $119^\circ$  and steeply up at  $-75^\circ$  away from the Kailua center.

Dike KD77 is 84 cm wide, and strikes  $315^\circ$  with a vertical dip. It is moderately weathered to a dark gray color, contains zeolite-filled amygdales (2 mm diameter) and pipe-vesicles are aligned parallel to the margins. The AMS axes are extremely-very well clustered, in which the  $\chi_3$  axes plot near the dike pole, while  $\chi_1$  and  $\chi_2$  axes plot in the dike foliation plane. The  $\chi_1$  axes have a strong bimodality (category 3). The mean total susceptibility anisotropy is 1.92%. The inferred absolute magma flow direction is  $133^\circ$  and up at  $-34^\circ$  to the southeast. *In summary*, the magnetic fabrics for three of the dikes (KD74, 76–77) suggest that the magma flow azimuth was away from the Kailua center, and was from nearly horizontal (up at  $2^\circ$ ) to nearly vertical (up at  $75^\circ$ ). The vesicularity

and low bulk densities of these dikes suggests that they were intruded at shallow depths under conditions of positive buoyancy.

### **Lava flows CV67, SW68, CV73 and ML78; Kilauea and Mauna Loa Volcanoes**

The magnetic fabric of four lava flows three from the Kilauea Volcano and one from Mauna Loa Volcano were studied in order to see if the AMS directions can be used to predict lava flow directions. Only two of the flows, CV67 (pahoehoe flow) and ML78 (aa flow) had high enough total susceptibility anisotropy that their magnetic fabrics could be successfully evaluated with the present AMS instrument. I sampled a pahoehoe lava flow (CV67) from the northeast rift zone of Kilauea Volcano. It is located near the active lava lake and had a flow direction of about  $120^\circ$  and dip a  $5^\circ$  to the southwest. The AMS axes are moderately-poorly clustered, with the  $\chi_3$  axes plot  $24^\circ$  from the vertical (i.e. the presumed magnetic imbrication angle), while  $\chi_1$  and  $\chi_2$  axes plot in the foliation plane of the lava flow. The  $\chi_1$  axes plunge shallowly in nearly the opposite direction from the presumed flow direction, and are therefore thought to represent a magnetic imbrication. The mean total susceptibility anisotropy is low ( $H= 0.14\%$ ). The magnetic fabric is slightly foliated and oblate shaped. The inferred magma flow direction is  $101^\circ$  towards the southeast.

The only other lava flow that showed good to moderate clustering of the AMS axes and has a relatively high mean total susceptibility anisotropy ( $H= 1.35\%$ ), is an olivine-rich aa lava flow (ML78) sampled from Humuhumu Point, along Southwest Rift Zone of the Mauna Loa Volcano. Only the massive interior of the aa flow was sampled in order to eliminate The  $\chi_3$  axes are fairly well clustered, while the  $\chi_1$  and  $\chi_2$  axes are only moderately clustered and plot along a steeply inclined foliation plane. The presumed magma flow direction is  $220^\circ$  and down  $5^\circ$  and agrees well with the trend of the mean  $\chi_1$  direction of  $215^\circ$ , however, the mean plunge direction is much steeper ( $36^\circ$ ).

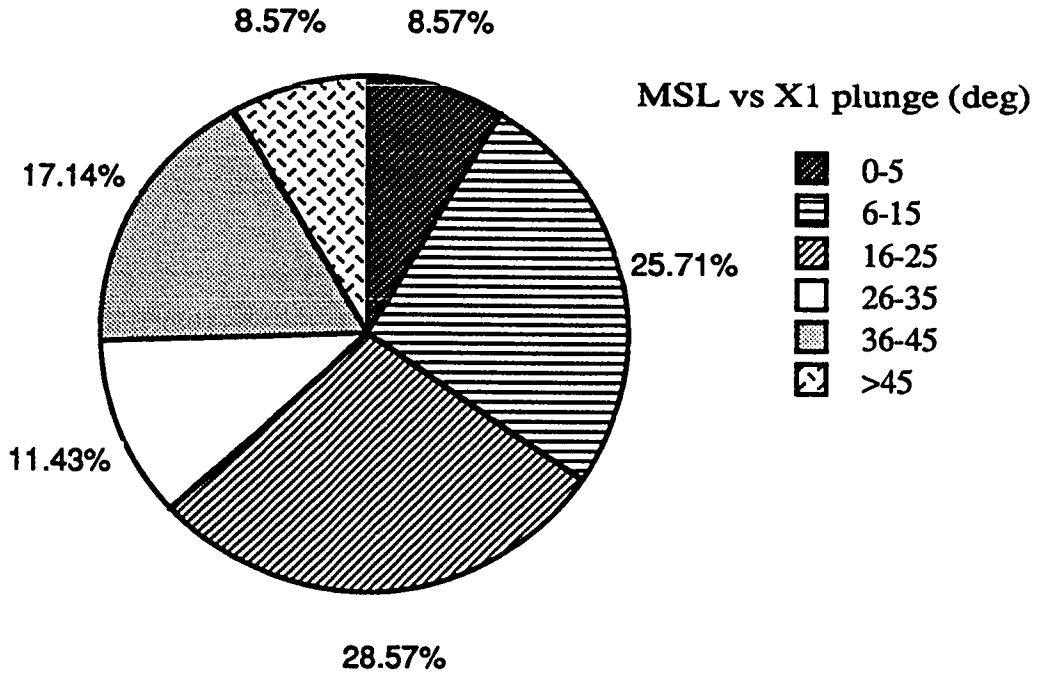
## SUMMARY AND INTERPRETATION OF THE AMS DATA

Magma flow in a dike is a dynamic process constantly changing along the dike in the direction of the flow. The problem of origin and emplacement direction of intrusive bodies in large shield volcanoes may be approached in a number of ways. Here I have explored the magnetofabric relationships employing the AMS method, which seems to provide a rapid and accurate evaluation of the orientation petrofabrics. A valid interpretation of the AMS fabric as a primary igneous feature may be related to the factors operating during emplacement as well as those operating after the magma flow has stopped (i.e., postemplacement history), and of particular interest is whether or not secondary (thermal or chemical) alteration has played a significant role in its development. The relatively pristine nature of the intrusive rocks of the Koolau volcano makes them ideal for this type of magnetic fabric study. The data shows that the AMS magnetic fabric of most of the dikes (88%) is nonrandom, has statistically significant  $\chi_1$  (AMS) clusters, and that their orientations compare well with the attitudes of the macroscopic flow lineations. Therefore I conclude that the dike emplacement directions can be determined from significant clustering of the  $\chi_1$  AMS axes parallel to the flow direction. Of the 35 dikes that had macroscopic surface lineations, 22 (63%) show a strong correlation ( $<25^\circ$  difference) between their plunge angle and the plunge of the  $\chi_1$  axes (Figure 3.5 a). It is noted that 17 (24%) of the dikes exhibit a bimodal distribution of the  $\chi_1$  axes. The cluster of  $\chi_1$  axes given by samples from the left-hand side of the dike is offset by  $10\text{--}60^\circ$  from the cluster given by samples from the right-hand side. I interpreted this type of bimodal clustering of the  $\chi_1$  axes to represent a magnetic imbrication along each dike margin, in which the ellipsoidal grains during laminar flow are piled up like roof tiles at low angles ( $5\text{--}30^\circ$ ) to the flow plane, dipping back toward the source of magma flow. I suggest that this sense of obliquity or magnetofabric imbrication relative to each dike wall is in response to velocity gradients of the magma within the dike, and the sense of imbrication relative to each dike wall provides a unique determination of the absolute flow azimuth. There is a general trend for the offset

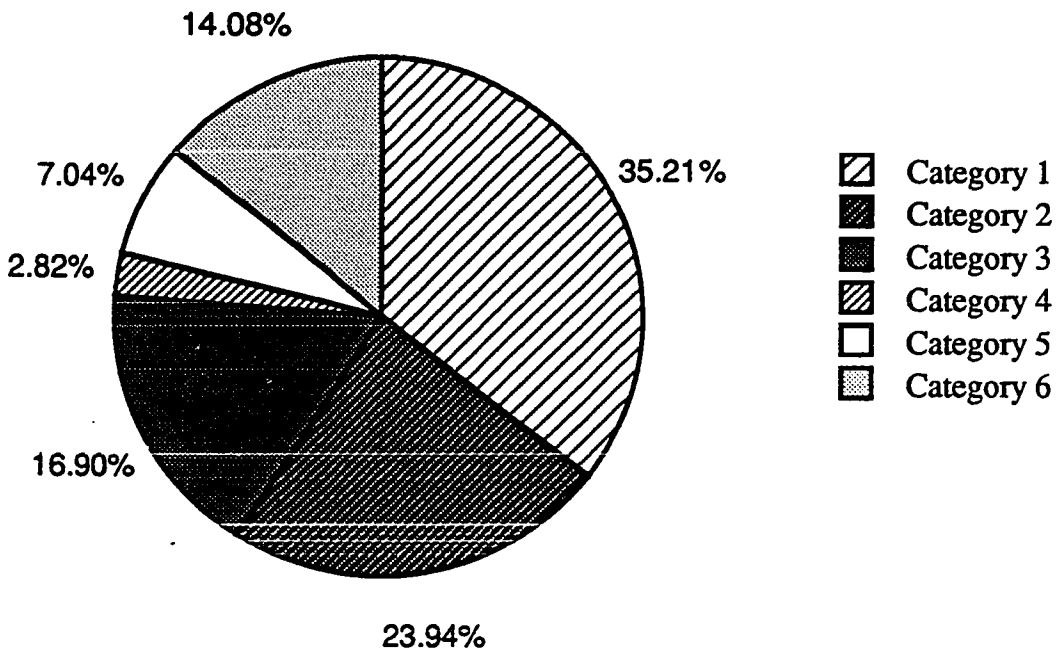
Figure 3.5 (a) Pie diagram of the agreement between the plunge direction of the macroscopic surface lineations (MSL) and  $\chi_1$  AMS plunge direction for 35 Koolau dikes. Six categories have arbitrarily been chosen, in which the MSL in three (8.6%) agree to within  $5^\circ$ , in 11 (25.7%) to within  $15^\circ$ , and to within  $25^\circ$  in 22 (63%) dikes show a strong correlation between their plunge angle and the plunge of the  $\chi_1$  axes.

(b) Pie diagram showing the percentage of Koolau dikes which fall within the six major categories of the AMS axial distributions. Note that 48 (69%) dikes fall within the first four, and it is these dikes in which the AMS directions have been used to infer the magma flow directions. 17 (24%) dikes fall within category 2 and exhibit a bimodal distribution of the  $\chi_1$  axes, and for these dikes the absolute magma flow azimuth is inferred.

### Agreement between MSL and X1 Plunge Direction



### AMS Axial Distribution Categories



angle between the bimodal clusters to increase as the width of the dike increases, suggesting that it is related to the magma flow velocity. In a majority of the widest dikes, the AMS axes are random, suggesting the onset of turbulence in dikes greater than 3.5 m wide (though the widest dike sampled KD71 has a well grouped bimodal cluster of the  $\chi_1$  axes).

It is also noted that the AMS axial distributions, their magnitudes and axial ratios, give important additional information about the relative magnitudes and orientation of the stresses operating during dike injection prior to solidification (extensional versus compressional or passive versus active dike injection). I interpret "category 3" to represent a possible realignment of the intermediate and minimum susceptibilities in a nonuniform stress field across the dike width (e.g., if the vertical gravitational stress field is greater than the horizontal compressional stress field of the fluid, then the intermediate and minimum axes will be able to rotate to the flow plane; if the vertical stress field is less than the horizontal stress, then the minimum axis will be near the pole). Naturally, the mechanics and hydrodynamics of magma flow during dike injection are in a constant state of flux between the (external) lithostatic load in the source region and (internal) hydrostatic magma pressure at the propagating dike tip. *Ryan* suggested that the balance between the internal and external stresses produces horizons of neutral buoyancy and magma stabilization. Therefore dike propagation must also be related to complex interactions between contractancy (the anelastic decrease in volume under lithostatic loading) and dilatancy of the country rock (the anelastic increase in volume under applied differential stresses), both processes are a function of depth. Thus the AMS axial distributions may give additional information about the relative magnitudes of the *in situ* stresses operating during dike injection prior to solidification and may aid in differentiating between forceful versus passive dike injection.

At the distal flanks of the Koolau volcano the AMS fabrics indicate that downward flow azimuths are most common, and therefore suggest passive dike injection. These downward directed magma flow azimuths may be related to the infilling of open fissures

and cracks or gravity faults along the lower flanks of the Koolau volcano [Dieterich, 1988], or due to gravity slumps initiated at the base of shallow rift intrusions that dip with the slope of the volcano flank [Moore and Krivoy, 1964].

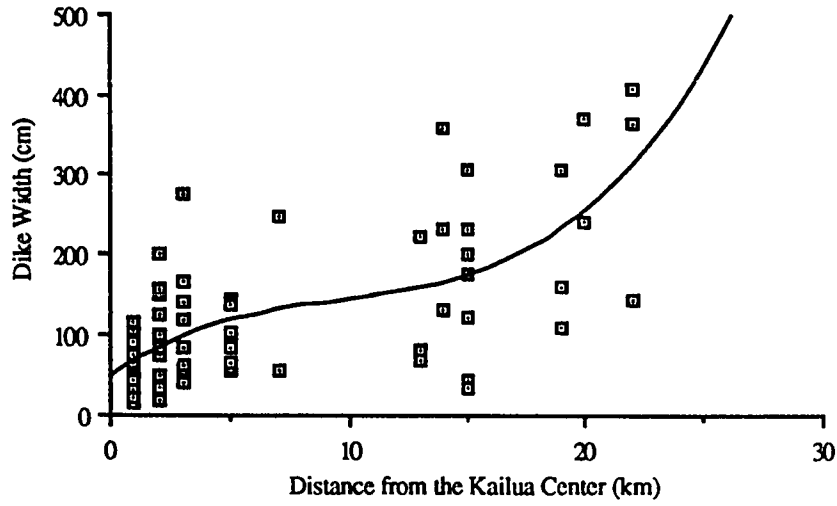
It is noted that the dikes closest to the presumed source reservoir tend to be narrower and have higher total susceptibility anisotropy (e.g.  $H \geq 1-8\%$ ), while dikes farthest from the presumed source are wider and have generally lower  $H$  values less than 4% (Figures 3.6a and b). Note that in Figure 3.6b there are at least two and possibly three peaks where the  $H$  values reach  $\geq 3.5\%$ . This relative increase in total anisotropy at distances of 15 and 19 km from the Kailua source could be a result of sample locality bias, or more likely these dike-sets may represent intrusive events from separate discrete source reservoirs. Hence, if one or two additional magma reservoirs were nearer these distal dikes (e.g. NW of the Kailua caldera) this might explain the observed relative increase in total susceptibility anisotropy. This interpretation would also support Walker's [1987] and Knight and Walker's [1988] suggestion for two or possibly three discrete magma bodies associated with the evolution of the Koolau shield volcano based on the plunge of MSL and  $\chi_1$  AMS directions. Figure 3.7 shows a summary of the inferred magma flow directions based on the mean  $\chi_1$  plunge direction. Note that a majority of the dikes (58%) are classified as having shallow ( $11-25^\circ$ ), oblique ( $26-45^\circ$ ) or steep ( $46-65^\circ$ ) magma flow directions, 28% are interpreted to have nearly vertical or nearly horizontal magma flow directions, and only 14% of the dikes gave random  $\chi_1$  directions (suggesting turbulent magma flow).

In conclusion, 25 (35%) dikes fall into category 1, 17 (24%) dikes and one filled lava tube fall into category 2, 12 (17%) dikes falls into category 3, two dikes fall into category 4, five dikes fall into category 5, and 10 dikes and one filled lava tube fall into category 6 (Figure 3.5b). The interpretations of the AMS data given in Appendix A, are summarized in Plate II. Plate II is a Summary Map of all the AMS data that show excellent to moderate grouping of the mean maximum  $\chi_1$  directions (the angle of plunge is positive down). It is evident from the diagrams shown in Plate II that the mean  $\chi_1$  AMS data at some localities

Figure 3.6 (a) A plot of distance (in kilometers) from the Kailua volcanic center (defined by the +310 mgal Bouguer gravity anomaly) versus dike width for the 71 Koolau dikes measured for AMS. Though this data set is relatively small by comparison to the much larger set of 2554 dikes plotted by *Walker* [1987], there is still a general increase in dike width with distance from the Kailua center. The line drawn through the data points represents a third order polynomial, with  $R = 0.68$ .

(b) A plot of distance (in kilometers) from the Kailua center versus total susceptibility anisotropy  $H$  in percent. Note that the highest  $H$  values are nearest the Kailua center and that there are at least two and possibly three peaks where the  $H$  values reach  $\geq 3.5\%$ . One at 15 km and another at 19 km from the presumed Kailua source. These two additional peaks where the total susceptibility increases to 4% or more may represent dikes that are associated with discrete intrusive events from separate source reservoirs northwest of the Kailua center.

(a). Distance from the Kailua Center vs Dike Width



(b). Distance from Source vs. Total Anisotropy (H)

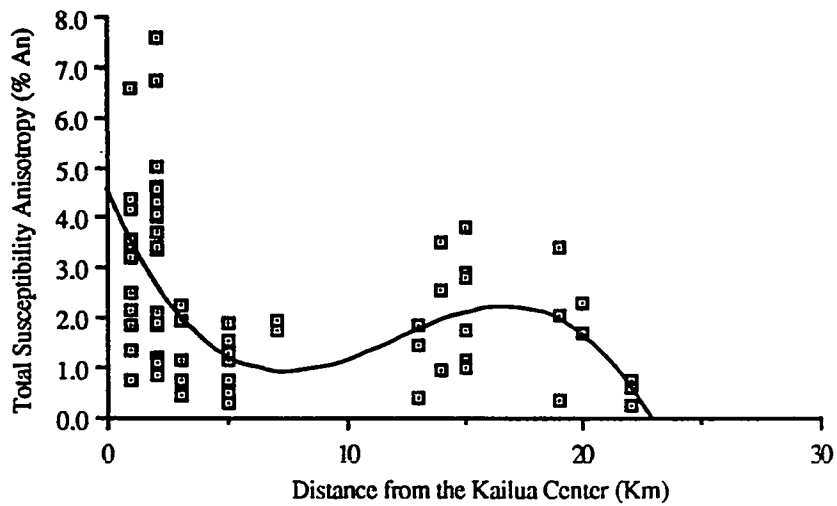
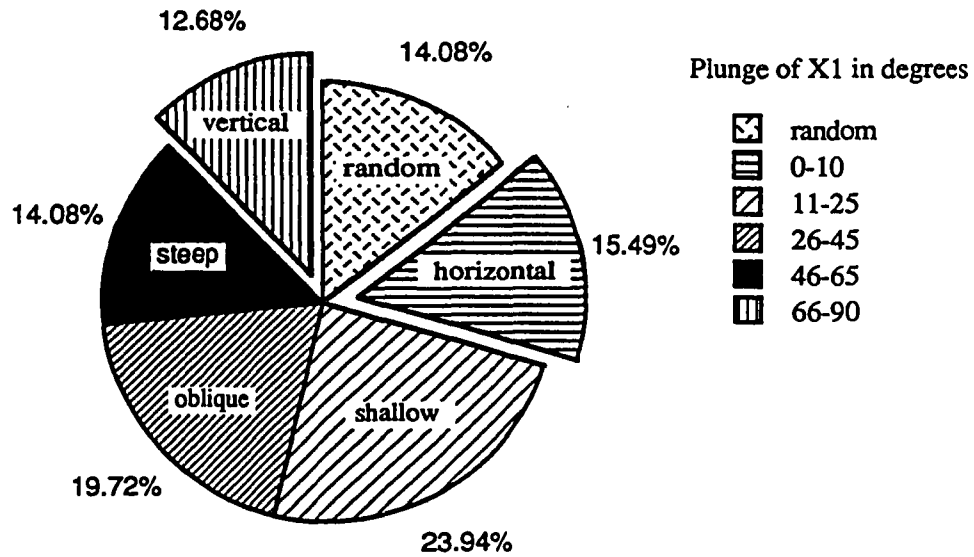


Figure 3.7 Pie diagram summarizing the AMS magma flow directions in 71 Koolau dikes. Based on inferred AMS flow directions, the magma in 31 (44%) dikes flowed at shallow to oblique angles of 11–45°, in 11 it flowed horizontally, in 9 it flowed vertically, and in 10 the AMS data is random suggesting either turbulent flow conditions occurred during dike emplacement or that the magnetic fabric is not a primary feature.

## Summary of AMS Magma Flow Directions in 71 Koolau Dikes



plunge in opposite directions, as is also true for the plunge directions of the surface lineations (e.g. the sites at Kapaa Quarry, northern H3 Highway cut near Puu Papaa, and the Kawainui Swamp). At these localities at least two separate stages of dike intrusion can be inferred from the plunge direction of the surface lineations, dike morphology, and crosscutting features. Hence an interpretation of opposing magma flow directions (shown as large open arrows) at these localities is not in conflict with the interpretation of several magma source bodies contributing to the evolution of the Koolau Volcano based on the AMS magnetic fabric.

The nature of the older dikes, with their irregular morphology and abundance of vesicles or amygdales, indicates that they were intruded at a shallow depth; possibly 100 m or less, at an early stage of shield growth [Walker, 1987]. In most cases the older vesicular dikes are associated with steep plunge directions (between  $50^{\circ}$  and  $85^{\circ}$ ) of the  $\chi_1$  AMS axes (e.g., KD53, KD56-58, KD60, and KD61), which gives support to the notion that near-vertical magma flow may be related to a higher buoyancy of the magma during dike intrusion.

Vesicle segregation zones found along the dike axes generally occur in dikes in which the AMS fabric indicates upward magma flow direction. While, vesicle segregation zones that occur along the dike margins can have magnetic fabrics that indicate either upward or downward flow azimuths. *Oliver* [1962] proposed that the lower density material (e.g. gas bubbles) will migrate towards the dike margins and that the denser crystals will concentrate along its axis. Contrary to *Oliver's* [1962] model, I find that for a majority of the vesiculated dikes in which the AMS fabric indicates upward directed magma flow, the vesicles are not only larger along the dike axis, but also are more abundant and occur in segregation zones 10–40 cm wide. On the other hand, the younger, massive, and generally less vesicular dikes (e.g., KD4–6) tend to have much shallower  $\chi_1$  AMS plunge directions ( $<35^{\circ}$ ) and thus could have been intruded at much greater depths in the Koolau edifice. Their generally higher bulk densities also supports this interpretation and is in agreement

with Ryan's [1987] *neutral buoyancy* model. It is also noted however that the shallow  $\chi_1$  plunge directions are not always restricted to the nonvesicular dikes (e.g., KD2, KD19, KD42; Table 3.2). It is suggested (Cross-section A–A', Plate II; a longitudinal section drawn parallel to the main rift axis of the Koolau complex) that, based on the intersection of the apparent plunge directions of the mean  $\chi_1$  axes there were at least three high-level (shallow) magma reservoirs between 1 and 2 km below the present erosional surface that fed the dikes and related lava flows of the shield. The oldest center was below the northwest end of Kaneohe Bay in which the AMS flow directions plunge very steeply (it is the only known area to have normally magnetized dikes and they tend to be highly vesicular), the next oldest center is 12 km to the southeast below the southern end of Kaneohe Bay, and the youngest center is below the Kawainui Swamp (6 km farther southeast). A hot-spot trace in this instance is thus marked by a progression of eruptive centers within a single volcano as well as a progression of volcanoes.

## CHAPTER 4

### MAGMA FLOW DIFFERENTIATION IN DIKES

#### INTRODUCTION

Early workers in fluid mechanics [Starkey, 1955, 1956; Scott-Blair, 1958] initially predicted that suspended solid particles undergoing horizontal viscous flow would migrate towards the axis of the conduit, however, it was not until *Bhattacharji and Smith's* [1964] dike modeling experiments that *flow differentiation* was acknowledged as a possible petrological process that caused the denser olivine crystals suspended in less dense basic magma to migrate towards the dike axis (i.e. during upward flow). Other experimental work [Oliver, 1962] predicted that during downward viscous flow the *denser particles* tended to *migrate towards the conduit walls* while those less dense than the fluid would migrate towards the axis of the conduit. *Jeffrey and Pearson* [1965] concluded that the opposite effect would apply to both neutrally buoyant particles as well as to particles denser than the fluid during upward flow. Further support is given by *Saffman* [1965], who calculated that during upward viscous flow, *denser solid particles* would *migrate axially* and those less dense than the fluid would migrate towards the walls of the conduit. Thus, the correct interpretation for apparent upward or downward magma flow directions can be inferred from observing the phenocryst and/or vesicle distribution patterns in near vertical dikes, and offers some explanation for the wide spectrum of crystal and vesicle distribution patterns observed throughout the Koolau dike complex (refer to Chapter 3 dike descriptions, e.g. dikes KD39, 42–43, 45, 53–55, 64, 69–71, 74–75, 77–78).

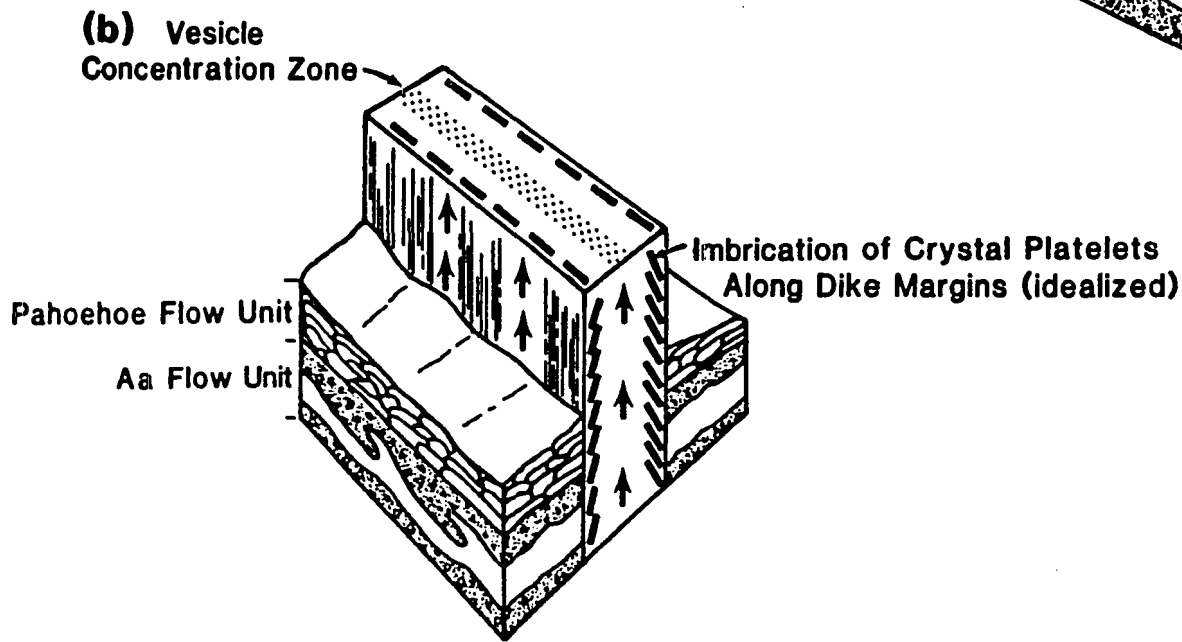
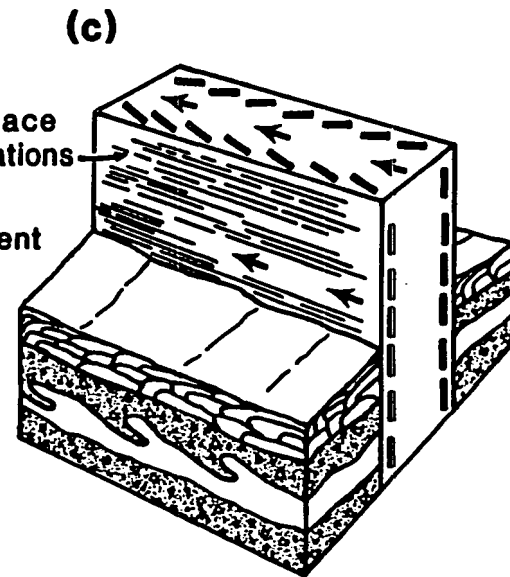
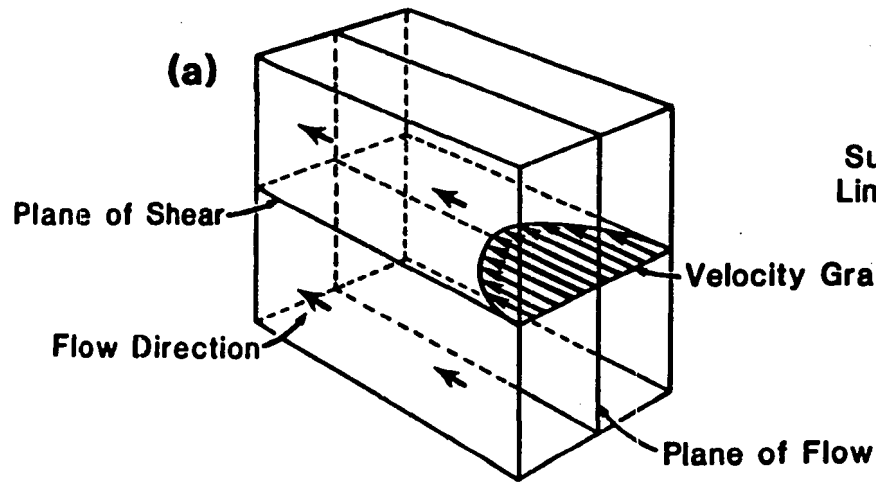
At low velocities and Reynolds numbers ( $<10^3$ ), well below the turbulent flow regime, two types of flow can occur, namely *plug flow* and *laminar flow*. Both flow types show laminar flow, but because plug flow characterizes plastics that possess a yield strength, internal shearing takes place only at the sides where frictional forces are great

enough to overcome the yield strength. *Gibb* [1968] indicates that in a highly viscous fluid undergoing plug flow (i.e. plug interior) that there should be no movement of the suspended particles relative to each other, nor should there be a concentration of the particles along the dike axis besides the initial development of a particle-free layer directly adjacent to the conduit or dike walls. However, during laminar flow conditions there may be both a continuous movement of the suspended crystals relative to each other as well as increased concentration of the crystals along the dike axis. During laminar flow of a viscous fluid in a conduit, *Starkey* [1962] and *Bhattacharji and Smith* [1964] suggest that axial particle migration is due to the *velocity profile* being *parabolic* and becoming zero at the conduit walls where the highest velocity gradient occurs (Figure 4.1a). Flow differentiation experiments by *Goldsmith and Mason* [1967] predict that as the particle concentration reaches a maximum at about 38% the velocity profile becomes blunted and is no longer perfectly parabolic, and thus the tendency towards plug flow at the center of the dike will result in limiting the maximum attainable concentration of olivine crystals. Field evidence, however, suggests that occasionally a few of the Koolau dikes have attained olivine concentrations as high as 60% (e.g. dike KD39), therefore it seems evident that other key factors are responsible for effectively increasing this critical concentration value. Sample EM1 collected from East Molokai is a narrow dike offshoot that is highly porphyritic along its axis with plagioclase crystal concentrations reaching >55% along a narrow zone 4 cm wide. One possible explanation for the anomalously high crystal concentration zones within some of the widest Koolau dikes (>3 m) that does not involve flow differentiation, is that multiple dike injections took place of increasingly more evolved and differentiated magma batches (possibly tapping the orthomagmatic differentiation stage of a deeper magma body that was equilibrating over extended periods of time) which will preferentially inject fluid containing high concentrations of crystals along the already thermally weakened dike flow axis. Another possible explanation for the observed high

Figure 4.1 (a) The velocity profile of a Newtonian or quasi-Newtonian fluid under horizontal laminar flow in a dike. The velocity gradient varies (parabolically) within the plane of shear, is a maximum along the center of the dike and a minimum along the walls where frictional forces are greatest. Also shown is the plane of flow.

(b) Cartoon of vertical magma flow in a dike, showing imbrication of idealized crystal platelets (plagioclase phenocrysts) along the margins and a vesicle segregation zone along the center of the dike.

(c) Cartoon of horizontal magma flow in a dike, showing imbrication of idealized crystal platelets (plagioclase phenocrysts) along the margins and horizontal surface lineations along the outer dike surface.



crystal concentrations in some of the narrower dikes (e.g. dike EM1) could be related to the piling up of the larger crystals near irregularities in the dike walls near offshoots.

Laminar flow in tholeiitic magmas causes early formed crystals of anisotropic habit such as olivine, plagioclase, orthopyroxene and clinopyroxene to orient themselves in the most stable orientation, that is, the direction of least resistance to the shearing forces during laminar flow. *Den Tex* [1969] and *Blanchard et al.* [1979] have experimentally modeled the angular relations of minerals under shear in basic magmas near the walls and the injection axis in dikes, and suggest that non-equant, anisotropic minerals will result in an *imbrication fabric* along the margins of the dikes. For example during laminar flow of the suspending magma the idealized {010} orthorhombic tablets of olivine, the {100} tablets of ortho- and clinopyroxene, or the {010} platelets of plagioclase will orient themselves in such a manner as to offer the least resistance to the shearing forces parallel to the *magmatic flow lines* (Figures 4.1*b* and *c*).

*Jeffery* [1922] first derived the equations of rotational motion for rigid non-spherical (ellipsoidal) grains suspended in a fluid under laminar shear in the absence of particle interaction. His experiments demonstrate that the ellipsoidal grains in addition to being transported in the direction of flow, will also be rotated orbits about their centers, with their long axes returning after time to their original orientation. In the simplest case when the long axis of a prolate-shaped grain is initially in the *plane of shear*, the long axis rotates so as to remain in this plane. Since the angular velocity has a maximum when the long axis of the grain is perpendicular to the plane of shear and a minimum when it is parallel to it, an elongate grain will spend more time with its long axis parallel or nearly parallel to the direction of flow [*Jeffery*, 1922]. Based on experimental evidence, *Mason and Manley* [1956] were only able to confirm *Jeffery's* theoretical predictions of motions of ellipsoidal grain when particle interactions occurred. They concluded that grain orientation distributions change with time until a steady state is attained at a certain particle density concentration, that the preferred orientation is in the direction of flow, and that there is a

finite period of time after the flow has stopped after which convection currents tend to redistribute the grains in the vertical direction. In the case of very wide intrusions (>100 m) *Barriere* [1976] gives supportive evidence of *Mason and Manley's* [1956] experimental observations, suggesting that *gravity controlled crystal settling, natural convection*, and *differentiated injection* can operate after the flow has ceased. These results may have a profound effect on the AMS fabric of those dikes in which gravity and convection can operate after intrusion, and could explain the anomalous AMS directions and slightly higher anisotropy observed in samples collected from the centers of the widest dikes (inferred to have the longest cooling history) in which the maximum elongation direction is more steeply inclined in the vertical direction. Based on all the AMS data for the Koolau dikes there is only a modest variation in the average plunge of the maximum susceptibility direction for samples collected from the centers ( $\chi_1 \text{ center} > 40^\circ$ ) compared to an average  $\chi_1$  plunge directions of all the dike specimens ( $\chi_1 = 34^\circ$ ) (refer to Appendix A; AMS samples labeled "C" represent specimens collected from the dike's center).

From a crystallographic perspective, large crystal faces show a marked preference for parallel to subparallel orientation in respect to the boundary surfaces between the igneous body and its wall-rocks (Figure 4.1b-c), while pronounced zone-axes tend to become aligned in the direction of the magmatic flow lines, or at right angles to them, depending on the measure of turbulence in the mechanism of flow [*Den Tex*, 1969]. Figure 4.1a shows the presumed *velocity profile* of a *Newtonian* or *quasi-Newtonian fluid* under steady, laminar flow in a parallel-walled dike. The velocity gradient for this special case is that of a *paraboloidal surface*, while the *plane of flow* describes a plane including the average direction of motion of particles moving downflow (in vertical dikes this is commonly assumed to be in the horizontal or vertical direction) in which the mean relative motion between particles is zero. The *plane of shear* contains the direction of mean motion and is normal to the plane of flow, and includes the direction of mean *velocity gradient* in the analogous case of a fluid in *simple shear*.

## FLOW DIFFERENTIATION AND CRYSTAL CONTENT ACROSS THE DIKE

The increase in concentration and average size of phenocrysts toward the center of dikes or sills is generally attributed to flow differentiation [*Bhattacharji and Smith*, 1964; *Bhattacharji*, 1967; *Simkin*, 1965, 1967; *Gibb*, 1966, 1968, 1972; *Komar*, 1972a, 1972b, 1976; *Barriere*, 1976]. Before discussing specific examples of inferred flow differentiation and its effectiveness for grain orientation in the Koolau dikes, sills, and filled lava tubes, it is appropriate first to summarize briefly the relationships between the intrusive flow models favored in the past and those processes presently accepted as the most valid.

Field evidence and petrographic studies indicate that the central parts of Hawaiian porphyritic dikes and sills contain higher concentration of increasingly larger phenocrysts of olivine, plagioclase, orthopyroxene, clinopyroxene, and opaques; the offshoots are hyalophitic when injected as thin dikelets (up to 2–5 cm wide) and generally glassy aphyric (hyalocrystalline) passing inward into a dolerite in larger bodies; and that there is considerable local variations within individual dikes. Early explanations for such variations in grain size distributions in intrusive bodies were based on multiple intrusions to form composite dikes or gravity settling of the earlier formed phenocrysts within the fluid magma. Presently, it is thought that such mineral distributions and crystal size variations occurring in dikes are analogous to those expected to arise during laminar flow in vertical conduits, and that flow differentiation is responsible for the observed grain fabrics, and that multiple dike injection is less common (e.g. possibly occurring locally in a few dikes found at the Kapaa Quarry). Generally the most significant variation is in the amount of olivine and/or vesicle content across the dike. Obviously the olivine variation is dependent on the modal mineral assemblage since some of the dikes are dominantly plagioclase phytic. As suggested by *Bowen* [1928] and later quantified by *Gibb's* [1968], ultrabasic dikes from Skye, Scotland, indicate that there are distinct types of variation in olivine concentration (percentage) across the dike width, and that narrower dikes generally contain less olivine

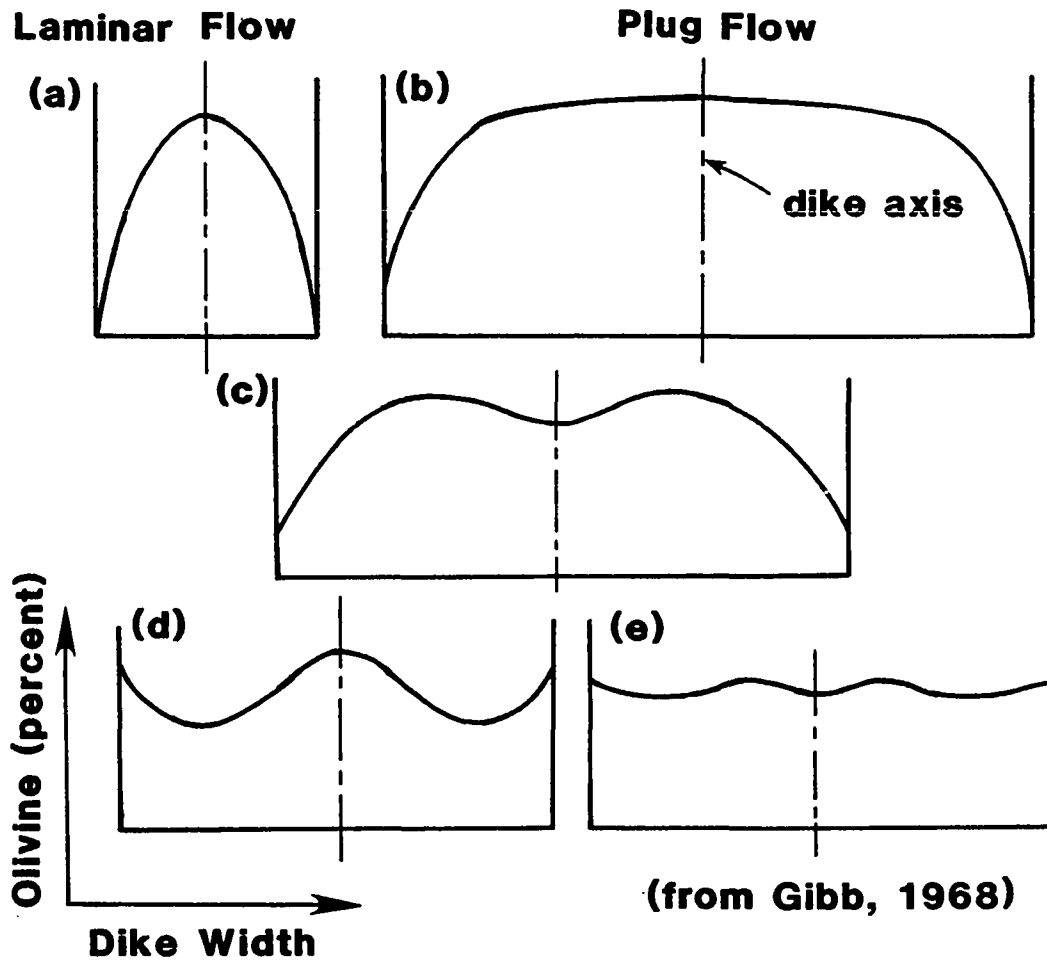
than wider ones. Figure 4.2 summarizes *Gibb's* [1968] investigation showing his five types of olivine concentration across these ultramafic dikes.

- (a) A single parabolic distribution of olivine reaching a maximum at the center of some dikes.
- (b) Basically similar to "a" but with a relatively flat profile in the central part of the dike, suggestive of plug-like flow of a non-Newtonian fluid.
- (c, d and e) Various kinds of bimodal peak distributions of olivine phenocrysts across the dike width.

The porphyritic Koolau dikes sampled for AMS studies, generally all show distribution patterns similar to that described by *Gibb* [1968]. Type (a), was the most common type observed in the widest dikes found at the distal ends of the dike complex far from their presumed source caldera (e.g. at the northern and southern ends of the NW-SE rift axis in the Koloa Gulch site KD70 and at Makapuu Head KD39). In these very wide dikes (both are over 350 cm wide) the olivine concentrations become nearly 30% in KD70 and exceeds 65% in KD39 (forming a coarse-grained massive picritic core at its center). I observed similar variations in phenocryst abundance and size variation across the dike width for the rare plagioclase phyric dikes, with the widest ones having very high concentrations at their centers. Occasional porphyritic dikes contain plagioclase phenocrysts that appear to lack any observable variation in abundance except right along the glassy selvages (Figures 4.3a–c, a narrow tholeiitic dike offshoot sampled from the East Molokai shield).

In a recent study of the olivine distribution pattern in various Hawaiian lava flows (particularly in the highly fluid lavas), *Rowland and Walker* [1988] demonstrated that *gravitational induced crystal settling* accumulated the olivine phenocrysts in a *lower concentration zone* and extracted them from an *upper depletion zone*. Similar relationships were observed in the picritic sills of NW Isle of Skye, in which *Simkin* [1966] indicates that hydrodynamic-gravity effected flow differentiation can be

Figure 4.2 Variation in olivine crystal content across the dike width (from Gibb, 1968).



**VARIATION IN OLIVINE CRYSTAL CONTENT  
ACROSS THE DIKE WIDTH**

attributed as the possible mechanism for the observed concentration zones. Though gravity effects can be quite dramatic in slow moving sub-horizontal lava flows and possibly to a lesser extent in sills, this gravitative accumulation of olivine crystals *in situ* in vertical porphyritic dikes may effectively be discounted and can not be responsible for the lateral differentiation observed.

Often the glassy selvages of the dikes have a trachytic texture in which the plagioclase microcrysts are tiny acicular to platy crystals highly aligned in the flow direction (during initial dike injection) near the contact and grade to elongate lath shaped phenocrysts in the center of the dike (e.g. dike KD60). In the coarser-grained examples the lath shaped plagioclase phenocrysts tend to be imbricated along the margins (Figures 4.3a -c). Along the dike center where crystal concentrations reach a maximum (up to 55%) there seems to be no preferential crystal alignment .

In many of the Koolau dikes there is a gradual change in texture from the margins to the centers, but some dikes show an abrupt variation in both phenocryst and vesicle concentration across the dike width. The narrow dike offshoots (locally occurring along preexisting joint fractures within the country rock) tend to have crystallized very quickly evident by their very fine-grained often glassy nature.

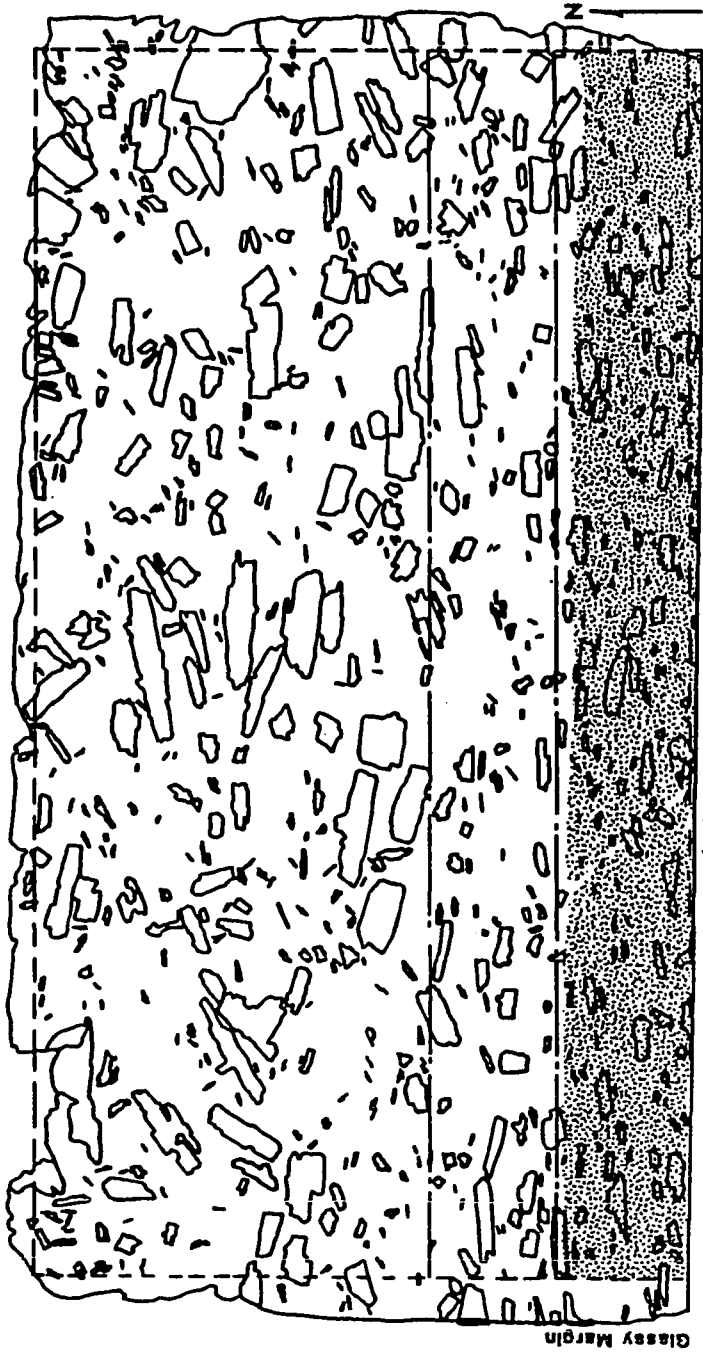
For upward directed magma flow in a non-vertical dike, *Gibb* [1968] offers a explanation for the *asymmetric distribution of phenocrysts*, in which the *force due to gravity* ( $G$ ) is not exactly opposite to the *viscous drag* acting along the dike ( $F$ ), and must be resolved into a component acting parallel to the walls of the dike ( $g_1$ ) and another acting perpendicular to the walls ( $g_2$ ) (Figure 4.4a). According to *Gibb* [1968], the component  $g_2$  acts in the same sense whatever the position of the particle relative to the dike walls, but the force which produces *axial migration* ( $f$ ) acts in opposite sense on opposite sides of the dike axis. Thus, the net result is to increase the force producing a more efficient axial migration of the particles adjacent to the hanging wall and decrease it in the area adjacent to the foot wall (Figure 4.4a). Such a model has great potential in

Figure 4.3 (a) Shows the outline and orientation of 565 grains measured for imbrication study, in thin section EM1-1 from an East Molokai dike, the stippled area represents the glassy chilled dike margin which is several millimeters wide. The rose diagram (below) indicates that the imbrication angle is dipping between  $5^{\circ}$  and  $10^{\circ}$ , the bar scale represents 15 grains.

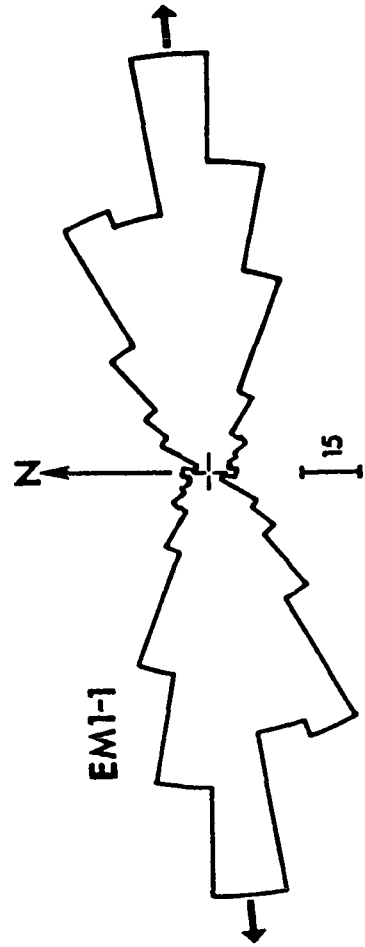
Figure 4.3 (b) Shows the outline and orientation of 607 grains measured for imbrication study, in thin section EM1-2 from an East Molokai dike, the stippled area represents the glassy chilled dike margin (north) which is several millimeters wide. The rose diagram (below) indicates that the imbrication angle is dipping between  $5^{\circ}$  and  $10^{\circ}$  in the opposite direction to that of Figure 4.3 (a), the bar scale represents 15 grains.

Figure 4.3 (c) Shows the outline and orientation of 553 grains measured for imbrication study, in thin section EM1-3 from an East Molokai dike, the stippled area represents the glassy chilled dike margin (south) which is several millimeters wide. The rose diagram (below) indicates that the imbrication angle is dipping between  $5^{\circ}$  and  $10^{\circ}$  in the opposite direction to that of Figure 4.3 (b), the bar scale represents 15 grains.

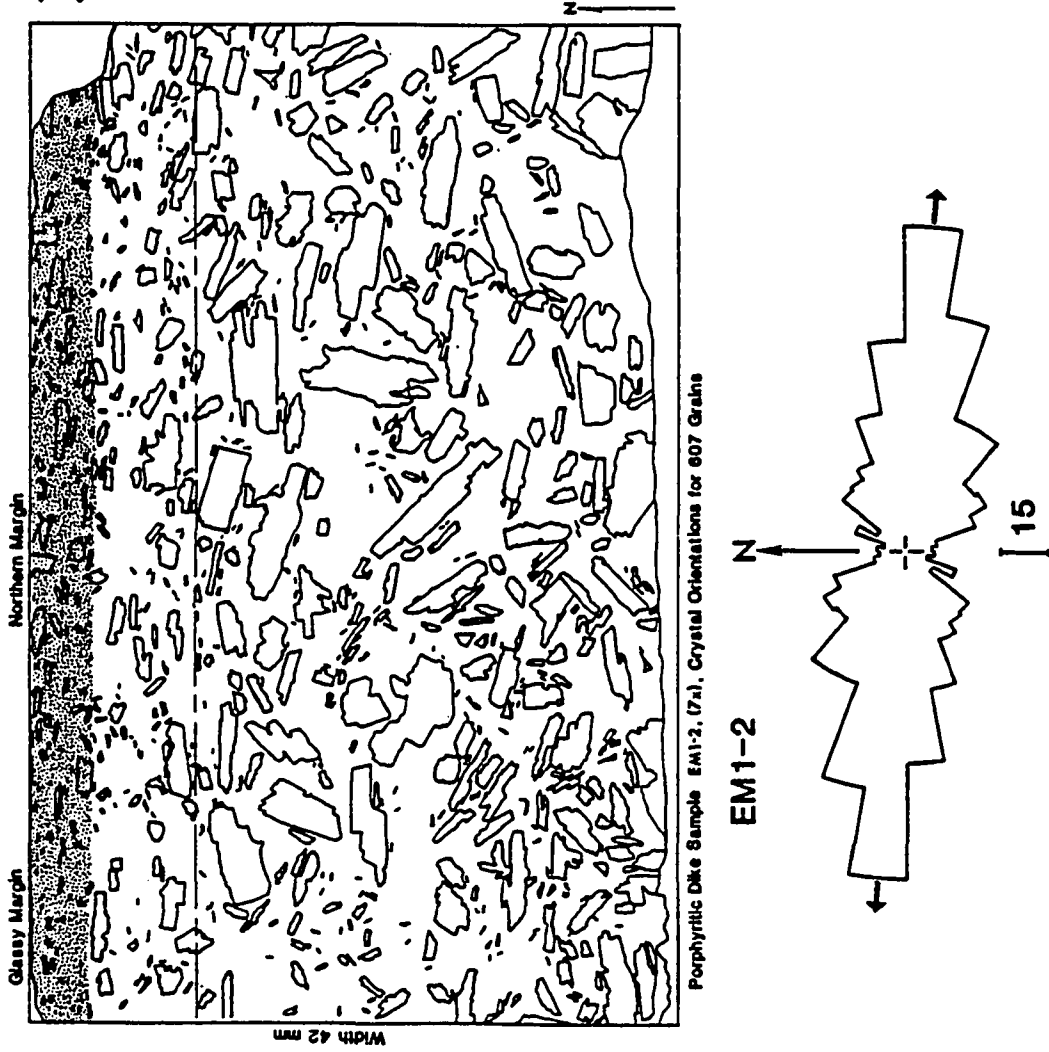
(a)



Porphyritic Dike Sample EM1-1, (7x), Crystal Orientations for 566 Grains



(b)



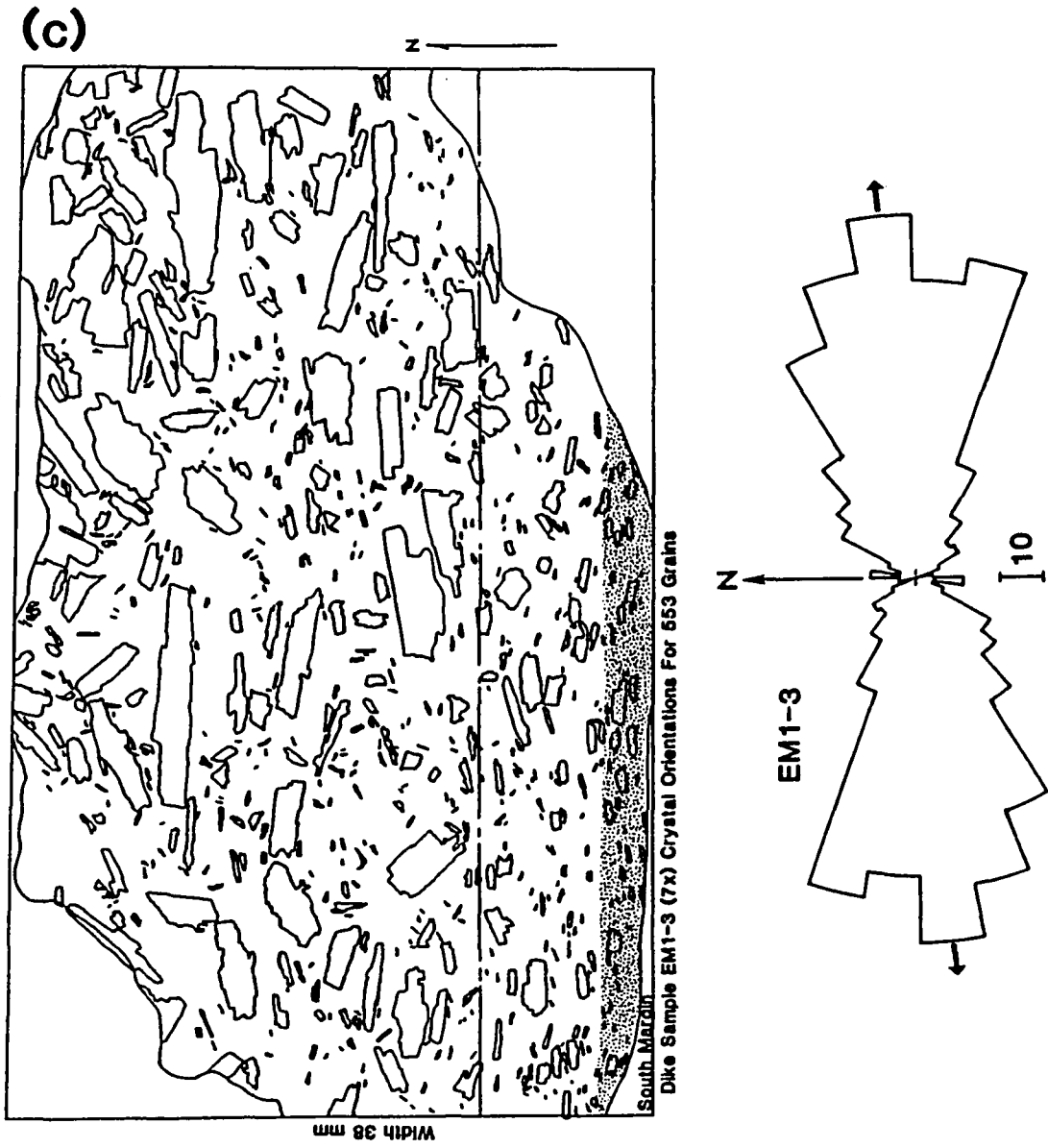


Figure 4.4 (a) Shows the forces acting on a spherical particle during upward, viscous, laminar flow in a non-vertical dike (after, *Gibb*, 1968). *Gibb* [1968] predicted that the component of gravity acting perpendicular to the dike walls ( $g_2$ ) acts in the same sense whatever the position of the particle relative to the dike walls, but the force which produces *axial migration* ( $f$ ) acts in opposite sense on opposite sides of the dike axis. Thus, the net result is to increase the force producing a more efficient axial migration of the particles adjacent to the hanging wall and decrease it in the area adjacent to the foot wall (dike margins are depicted by cross-hatches).

(b) Shows the forces acting on a spherical particle during downward, viscous, laminar flow in a non-vertical dike. In this example, during prolonged magma flow, the denser grains will be concentrated toward the foot wall of the dike.

(c) Equal area (lower hemisphere) plot of the AMS axial distributions for dike KD58. Note that for this relatively low angle dike that there is an asymmetric distribution of the maximum  $\chi_1$  axes along the foot wall. The presumed magma flow direction is downward, plunging steeply at  $64^\circ$  to the southeast. The nearly  $50^\circ$  discrepancy between the dike trend and inferred magma flow direction could be related to flow differentiation, similar to the mechanism shown in Figure 4b.

**(a) Forces Acting On A Spherical Particle  
During Upward Flow In A Non-Vertical Dike**

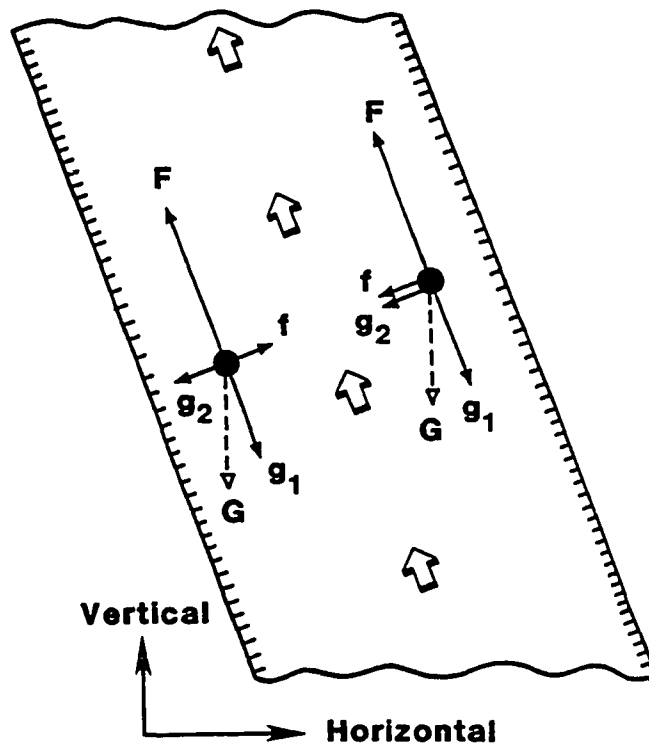
**G** force due to gravity

**F** force due to viscous drag acting along dike walls

**f** force which produces axial migration

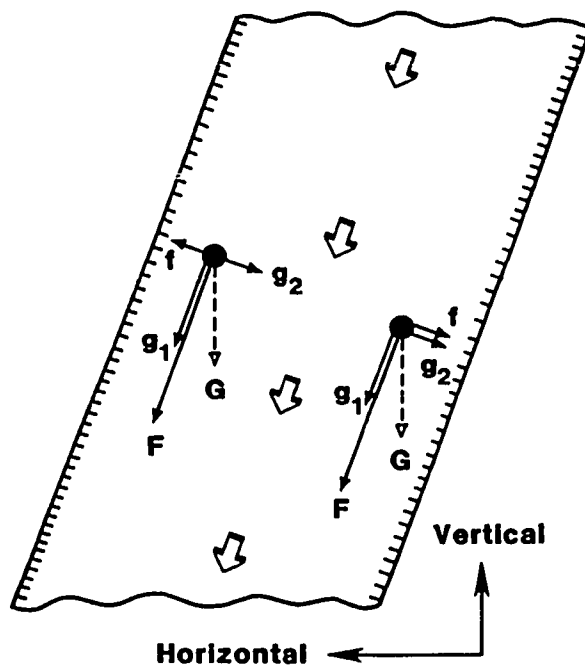
**$g_1$**  component of gravity acting parallel to dike walls

**$g_2$**  component of gravity acting perpendicular to dike walls

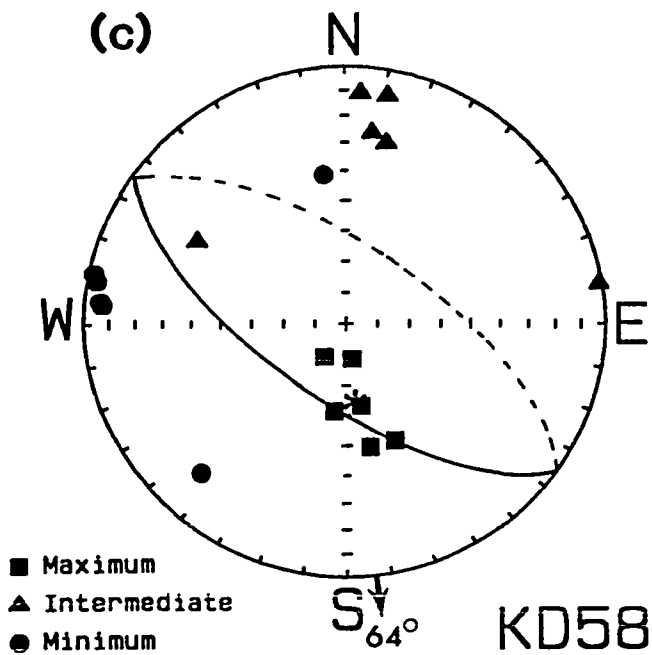


**(after Gibb, 1968)**

**(b) Forces Acting On A Particle During Downward Flow**



**(c)**



explaining some of the apparent discrepancies between the maximum AMS axial distributions shown on equal-area plots and the dike strike, particularly in those dikes with the lowest dip angles (e.g. KD20-22, KD33). Therefore, the suspended particles will be subjected to velocity gradients that cause rotation and axial migration during upward flow, while in the case of downward directed magma flow *Oliver* [1962] found that the higher density particles will migrate towards the dike walls and those less dense than the fluid migrated axially. Figure 4.4*b* shows the forces acting during downward flow in a dipping dike, in which the migration of particles is greater toward the foot wall. A similar mechanism is envisioned to explain the anomalous trend of the maximum AMS axes for dike KD58 (Figure 4.4*c*).

Another common fabric of the Koolau dikes is *igneous flow banding* (or mafic-segregation layers in the filled lava tube KT38), recognized in the field as lineated corrugations on weathered dolerite surfaces and in thin-section as subtle variations in mineralogy along segregation zones (e.g. abundance in incompatible minerals such as Na-enriched plagioclase, apatite, Fe-Ti oxides, and other mafic minerals), oriented in planes paralleling inferred isotherms. *Simkin* [1966] indicates that band spacing commonly decreases toward contacts, deuteric activity is asymmetric within bands, and essential mineralogy and texture are unchanged across them. His interpretation is that these features preclude standard layering mechanisms and suggest a rhythmic, Liesegang-like banding, build-up and precipitation of late-stage constituents in a largely crystalline rock.

As summarized by *Ross* [1986], at least three forces are involved in flow differentiation: The "*Bagnold effect*" [*Bagnold*, 1954], the "*Magnus effect*", and the "*wall effect*" [*Bhattacharji*, 1967; *Pao*, 1961]. The Bagnold effect produces a grain dispersive pressure (referred to as the Bagnold dispersive stress) when phenocrysts or vesicles are sheared past one another in a flowing magma (i.e. one that behaves in bulk as a quasi- or non-Newtonian fluid). This is thought to be the most important component of flow differentiation [*Komar*, 1972*a*; *Barriere*, 1976], and the resulting grain-dispersive

stress is directed inward normal to flow and proportional to the rate of shear. It requires a phenocryst concentration in flowing magma greater than about 5% (the grains need not actually collide to produce a grain dispersive pressure [Komar, 1972a]). Because of the increased viscosity and velocity gradient near dike walls phenocryst concentration must decrease toward the walls, which could explain the observed rapid gradation from phenocryst-poor margins to phenocryst-rich centers. Bagnold [1954] indicates that if phenocryst concentration is sufficiently large (>8%), then the grain dispersive pressure would depend on the size of the phenocrysts, and this dependence would cause the larger phenocrysts to migrate preferentially toward the dike center and the smaller grains toward the walls, thus giving the observed size gradient as well as concentration gradient across the dike half-width.

In classical fluid mechanics the *lift force* (or other single particle forces) or *Magnus effect* arises from rotation induced on individual grains by the motion of the surrounding fluid, in which a resultant transverse force produces an inward translation of the crystal. Within a one-meter wide dike Komar [1972a] considers the Magnus effect to be quite small in magnitude (one-hundredth the Bagnold effect).

The *wall effect* is thought to occur very near the dike margins, within several grain diameters of the wall (or in from the outer few centimeters of the phenocryst-free glassy salvage) and involves an "inward repulsion" arising from mechanical interaction between the conduit wall (frictional effects related to wall roughness and general morphology) and adjacent crystals [Barriere, 1976].

## RELATION OF AMS TO IMBRICATION FABRIC

Khan [1962], using both the AMS technique and microscopic analyses, has shown that the physical orientations of long, intermediate, and short axes of magnetite grains correspond very closely to the principal AMS ellipsoid axes. Owens [1969, 1974]

indicates that a mixture of prolate and oblate grains will develop a preferred orientation of long axes ( $\chi_1$ ) in the direction of flow and short axes ( $\chi_3$ ) normal to it in the plane of shear.

For the case in which elliptical particles are uniformly dispersed through a non-compressible viscous fluid, collisions will occur continually between particles of adjacent layers. By assuming elastic collisions, the force acting in each will be orthogonal to the tangent plane common to the two colliding particles. According to *Rees* [1968, 1979], this force will exert a couple on each particle, which tends to rotate the particles into the most stable state; for ellipsoidal grains rotation occurs when collisions take place near the symmetry axes. Hence the most stable condition for anisotropic grains occurs when the principal axes are tilted in the form of a flow imbrication.

In the three-dimensional case, an assemblage of ellipsoidal grains under shear will develop a preferred orientation that minimizes angular-momentum transfer and makes collisions as glancing as possible. This will occur when the maximum elongation direction ( $\chi_1$ ) is near the flow direction and the minimum ( $\chi_3$ ) is near the direction of the velocity gradient, since a particle in this orientation presents a section of maximum radius of curvature to the collision [*Rees*, 1968]. *Rees* indicates that the angle of particle rotation (imbrication angle) under inertial depositional conditions would be about  $18^\circ$  to ensure that the resultant forces of collision act parallel to the principal axes.

*Den Tex* [1969], *Blanchard et al.* [1979], and *Shelley* [1985] suggest that the *oblique fabrics (imbrication fabrics)* which develop across the dike width are in agreement with the velocity gradient models presented by others [*Bagnold*, 1954; *Khan*, 1962; *Bhattacharji and Smith*, 1964], and that laminar flow causes the early formed anisotropic grains (e.g., tablet-shaped phenocrysts of olivine, plagioclase, and pyroxene and/or needle-shaped microcrysts of magnetite) to orient themselves in such a manner as to offer least resistance to the forces of fluid movement. This results in the large crystal faces generally showing a marked preference for parallel orientation with respect to the boundary surfaces between the igneous fluid and dike walls, and hence their most stable orientation is an

imbricated one due to their piling up like roof tiles at low angles (10-30°) to the flow plane and dipping toward the source of the flow (Figures 4.5a– c). It is this same style of imbrication that we infer from our AMS measurements (i.e., symmetrically disposed paired clusters of  $\chi_1$  axes on either side of the plane of the dike) which has enabled us to interpret the absolute magma flow direction.

### ROLE OF TURBULENCE

Because no one has reportedly observed Hawaiian or any other basaltic lava flows flowing turbulently, most volcanologists conclude that most basaltic flows and, by implication, most dike intrusions are laminar. The accurate prediction of the absolute velocities, viscosities, and Reynolds number (*Re*) of magmatic fluids flowing within dikes are a difficult but important task. Based on fluid dynamic principles, *Shaw and Swanson* [1971] were among the first to analyse quantitatively the ascent of basaltic magmas through the crust. Their conclusion, based on the voluminous nature, areal extent, and great thickness of the Columbia River Plateau flood basalts, was that the lava would have flowed turbulently with Reynolds numbers greatly exceeding  $10^3$ . Based on the presumed high discharge rate and low viscosities, and morphology of the flow channel, *Hulme* [1973] argues that lunar sinuous rilles are a consequence of turbulent lava flows which eroded the underlying ground by assimilation. *Huppert and Sparks* [1985a] developed a model for thermal erosion in turbulently erupted komatite lavas, indicating that typical erosion rates of several meters/day occurred in the lava channels. The velocity of a fluid in turbulent flow differs fundamentally from one in laminar flow and the nature of the flow in a dike can be predicted from the Reynolds number. For an ascending magma driven upwards by positive buoyancy forces, this is given by

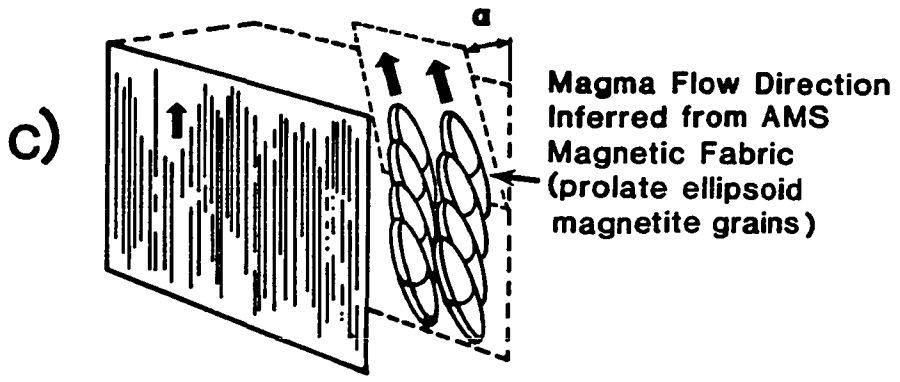
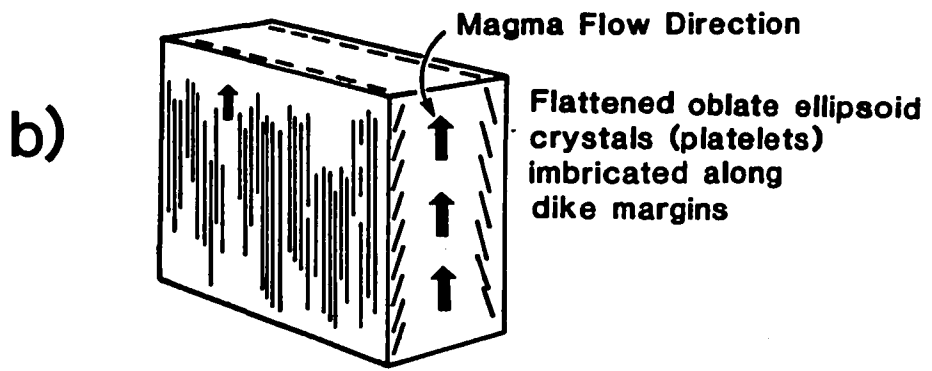
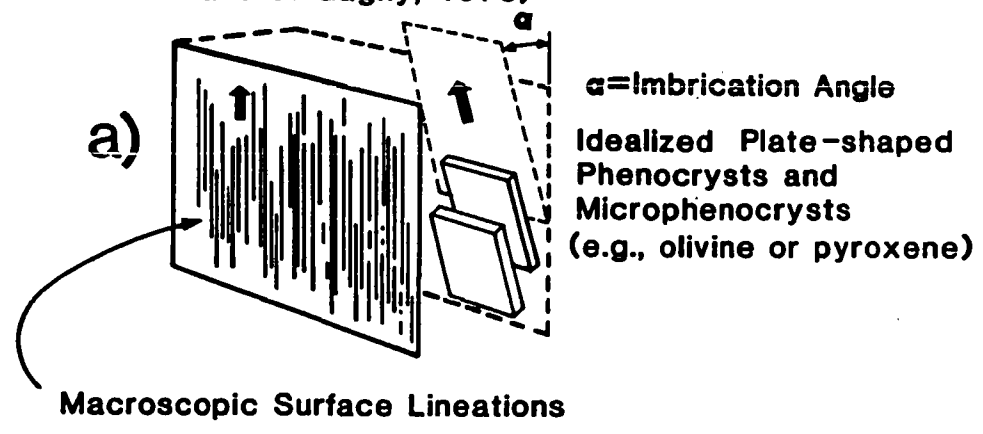
$$\text{Re} = \left[ \frac{g \Delta \rho}{k \rho_m} \right]^{1/2} d^{3/2} \nu^{-1} \quad (1)$$

Figure 4.5 (a) Idealized drawing showing imbrication of anisotropic tablet-shaped phenocrysts and microphenocrysts (olivine and pyroxene) along the dike walls during vertical upward laminar flow. In near-vertical dikes the imbrication angle ( $\alpha$ ) should be identical along both margins.

(b) Shows oblate ellipsoidal shaped crystals imbricated along both margins.

(c) Cartoon of prolate ellipsoidal shaped magnetite grains imbricated along the dike margin. Petrographic studies indicate that though magnetite is isotropic with a cubic crystal habit that commonly the grains exhibit irregular to elongate shapes. These prolate ellipsoid magnetite grains can then be imbricated along the dike margins during viscous laminar flow.

(Revised after Den Tex, 1969, and Blanchard, Boyer, and et Gagny, 1979)



where  $g = 980 \text{ cm s}^{-2}$ , is the acceleration due to gravity,  $\rho_m(30 \text{ km}) = 2800 \text{ kg m}^{-3}$ , is density of basaltic magma in the lower crust, and  $\rho_m(0 \text{ km}) = 2650 \text{ kg m}^{-3}$  is the density near the surface [Takada, 1989],  $k = 10^{-2} \text{ cm}^2 \text{ s}^{-1}$ , is the coefficient of friction (dependent on surface roughness of the dike wall rock) [Wilson and Head, 1981],  $d$  is the width of the dike,  $\nu$  is the kinematic viscosity and for the Koolau dikes, ranges between  $10^1$  and  $10^3 \text{ cm}^2 \text{ s}^{-1}$  (or a Newtonian viscosity between  $10^1$ – $10^2$  poise,  $\approx 350$  poise), and  $\Delta\rho$  is the average density difference averaged over the whole dike length [Campbell, 1985]. Huppert and Sparks [1985b] indicate that magma ascent in a dike driven by an excess hydrostatic pressure gradient  $g\Delta\rho$  is the result of the difference in density  $\Delta\rho$  between the magma of density  $\rho_m$  and the mean density of the column of rock overlying the magma source. Furthermore, this turbulent flow is resisted by frictional forces at the dike walls, and the balanced of these effects leads to the following relationship between flow rate,  $Q$ , and dike width  $D$  [Huppert and Sparks; 1985b]:

$$Q = (g \Delta\rho / f \rho_m)^{1/2} D^{3/2} \quad (2)$$

where  $f$  is a friction factor. Depending on the roughness of the conduit and the magnitude of the  $Re$  the value of  $f$  could range between about 0.01 and 0.06 [Huppert and Sparks [1985b]]. Note that the most important factor for turbulent flow in Equation 4.2 is the dike width. According to Huppert and Sparks [1985a,b], when primitive magma ascends turbulently through the crust, heat transfer can be rapid and the wall rocks of the conduit can melt and be assimilated into the magma. They indicate that the erosion rate of the conduit walls and amount of contamination are greatest for primitive magmas with high flow rates at Reynolds numbers around 2000, and least for cool, fractionated, slow moving intrusive flows. Thus, in the thinner dikes when the flow is entirely laminar, some of the ascending magma is quenched along the dike walls, preventing contamination of the remainder of the flow within the dike. If these assumptions are correct for the Koolau dike complex then a flow is turbulent if  $Re$  exceeds a critical value which is approximately 2000

[Goldstein, 1938; Wilson and Head, 1981; Campbell, 1985; Huppert and Sparks; 1985a,b]. It is clear from these equations that the critical factor controlling the *Re* and flow rate is  $d^{3/2}$ , the dike width. According to Campbell's [1985] calculations flow of basic magma in dikes wider than 3 meters will be fully turbulent, while Spera [1977] indicates that the inception of turbulence for a primitive melt with a viscosity of 300 poise occurs for dikes greater than 5 meters wide. The only Koolau dikes which meet this criteria (dike widths >3 m) and also exhibit random clustering of the AMS axes on equal-area plots are dikes KD39 (358 cm wide) and KD70 (365 cm wide). There are however, a few wide dikes (> 300 cm) that are interpreted to have laminar flow morphology, based on the occurrence of crystal segregation layers, multiple vesicle concentration zones along the margins, and flow banding, and furthermore their AMS fabrics display moderate to good clustering, as well as bimodal clustering (e.g. KD66, 305 cm wide and KD71, 408 cm wide). Therefore dikes KD66 and 71 agree better with Spera's [1977] criteria, in which a dike must be wider than 5 m for turbulent flow.

The unequivocal demonstration that a given magma body, based solely on the condition of its magnetic or petrologic fabric, was in a turbulent regime is difficult to prove, partly because *flow regimes* are markedly time dependent. In other words, turbulent flow should eventually transgress the threshold into the laminar flow regime during the final waning stages of dike intrusion, thus damping out accordingly, all indications of turbulence, such as a random distribution of early crystallized minerals. Therefore, the present condition of the petrologic fabric may not record the significant role that turbulence may have played during a prolonged intrusion history but only record the final condition prior to solidification. Two such examples that seem to fit this second criterion are: (1) an infilled lava tube KT38 that is suggested by Coombs and Walker (in review) to have undergone thermal erosion of the aa lavas that it cuts down through and therefore is likely to have been in a state of turbulence prior to solidification (thermal erosion is strongly favored by turbulence); and (2) a very wide dike (KD71) that also has a well clustered

magnetic fabric and shows bimodality of the distribution of the maximum AMS axes. Hence, other factors should produce recognizable clues to ascent of basaltic magmas within dikes under turbulent flow conditions, such as the occurrence of *wall rock assimilation*, *brecciation*, and *marginal (zonal) discontinuities* in the isotope geochemistry of phenocrysts and groundmass due to convective mixing, melting, and stopping of the adjacent country rock.

In this study turbulent flow was not inferred for the narrower dikes (<2.0 m wide; e.g. dikes KD8, 12, 48, and 64) that showed random AMS fabrics since there are a number of post-emplacment mechanisms that could easily have resulted in the observed (random) AMS fabric. The following is a list of some of these mechanisms: (1) post-emplacment crystallization; (2) very low modal magnetite, << 1.0% or its oxidation to a magnetic carrier that has a strong magnetocrystalline anisotropy (such as hematite); (3) low total susceptibility anisotropy due to secondary alteration, resulting in observed susceptibilities within the noise level of the balanced bridge; (3) realignment of the petrologic fabric across the dike width due to variations in the local stress field; (4) gravitational realignment of the distribution of earlier crystallized minerals; (5) effects of mineralogical variations (e.g. weathering, chemical, or hydrothermal alteration) on magnetic minerals responsible for the primary AMS signature; and (6) experimental problems encountered during sampling, such as the breaking of dike specimens along multiple fractures and small-scale jointing planes, or that too few samples have been collected at a particular dike outcrop for significant statistical representation of the AMS tensor.

## VESICLE ORIENTATIONS DURING MAGMA FLOW

### VESICLE MORPHOLOGY

Vesicles within the dikes, sills and filled lava tubes vary in size, shape, and modal abundance along discrete segregation zones from the walls inward. Here the term "*vesicle*" is restricted to predominantly *megascopic spheroidal voids* to distinguish

them from the minute, irregular, and pervasive intercrystalline voids that *McMillan et al.* [1987] refers to as microvesicles and that *Dickinson* [1965] referred to as diktitaxitic voids. In the vesiculated dikes the vesicles have diameters less than 1–2 mm, but occasionally they reach up to 2–14 cm along their maximum dimension (e.g. elongate tube vesicles, or pipe amygdales when they are infilled with secondary minerals). Their idealized shape depends mainly on the effective yield strength ( $\tau_y$ ) of the melt and may grade from spherical, through elliptical or ovate (teardrop shaped), to ellipsoidal-capped, elongate tube-shaped, and irregular (Table 4.1).

In lava flows the vesicular zones represent accumulations of upward-migrating bubbles sequentially frozen-in by the downward passage of the upper solidification front [*McMillan et al.*, 1987]. In the Koolau dikes narrow, multiple vesicle/amygdale concentration zones commonly occur only along the margins, with or without a wide massive central zone (i.e. paired, narrow vesicle segregation layers 1-10 cm wide, while the central zone can vary from <10 cm to >50 cm wide in the widest dikes) are common only in the shallowest intrusives and their origin and occurrence must be related to factors other than buoyancy alone. *Vesicle segregation layers* referred to here as *vesicle trains*, commonly occur as paired doublets, triplets or quintuplets, each being 1–3 cm wide and separated 2–5 cm apart and starting several centimeters inside the glassy selvage of the chilled margins (e.g. dikes KD53–55, 69 and 74). Individual vesicles within a single train are quite uniform in size, shape, and distribution, showing an abrupt, successive, gradational increase in their size and concentration inward toward the center of the dike. Their distribution and occurrence is very similar to the distribution of phenocryst and groundmass segregation zones observed in many porphyritic dikes and sills [*Bhattacharji and Smith*, 1964; *Simkin*, 1966; *Komar*, 1972]. *Bhattacharji and Smith* [1964] have proposed a type of flow differentiation model for the origin of the picritic interior of the Muskox feeder dike, and support their interpretation with convincing experimental work. Since vesicles and phenocrysts have been shown experimentally to behave similarly under

**TABLE 4.1** Vesicle Shape Classification Scheme, depending upon the orientation of the section and the portion of the vesicle which has been cut.

<b>Outline</b>	<b>Whole Bubble Morphology</b>
<b>Circular:</b>	Spherical, ellipsoidal, spheroidal, dimpled, spherical- / ellipsoidal-cap, irregular
<b>Elongate:</b>	(a) Elliptical: Ellipsoidal, spheroidal, dimpled, spherical-/ellipsoidal-cap, irregular (b) Ovate: Tear drop, dimpled, spherical-/ellipsoidal-cap, irregular (c) Tube: Ellipsoidal, spheroidal, straight parallel rod-like, irregular
<b>U-shaped:</b>	Dimpled, spherical-/ellipsoidal-cap, irregular
<b>Annular:</b>	Dimpled, spherical-/ellipsoidal-cap, irregular
<b>Irregular:</b>	Irregular

(After Kilburn, 1984)

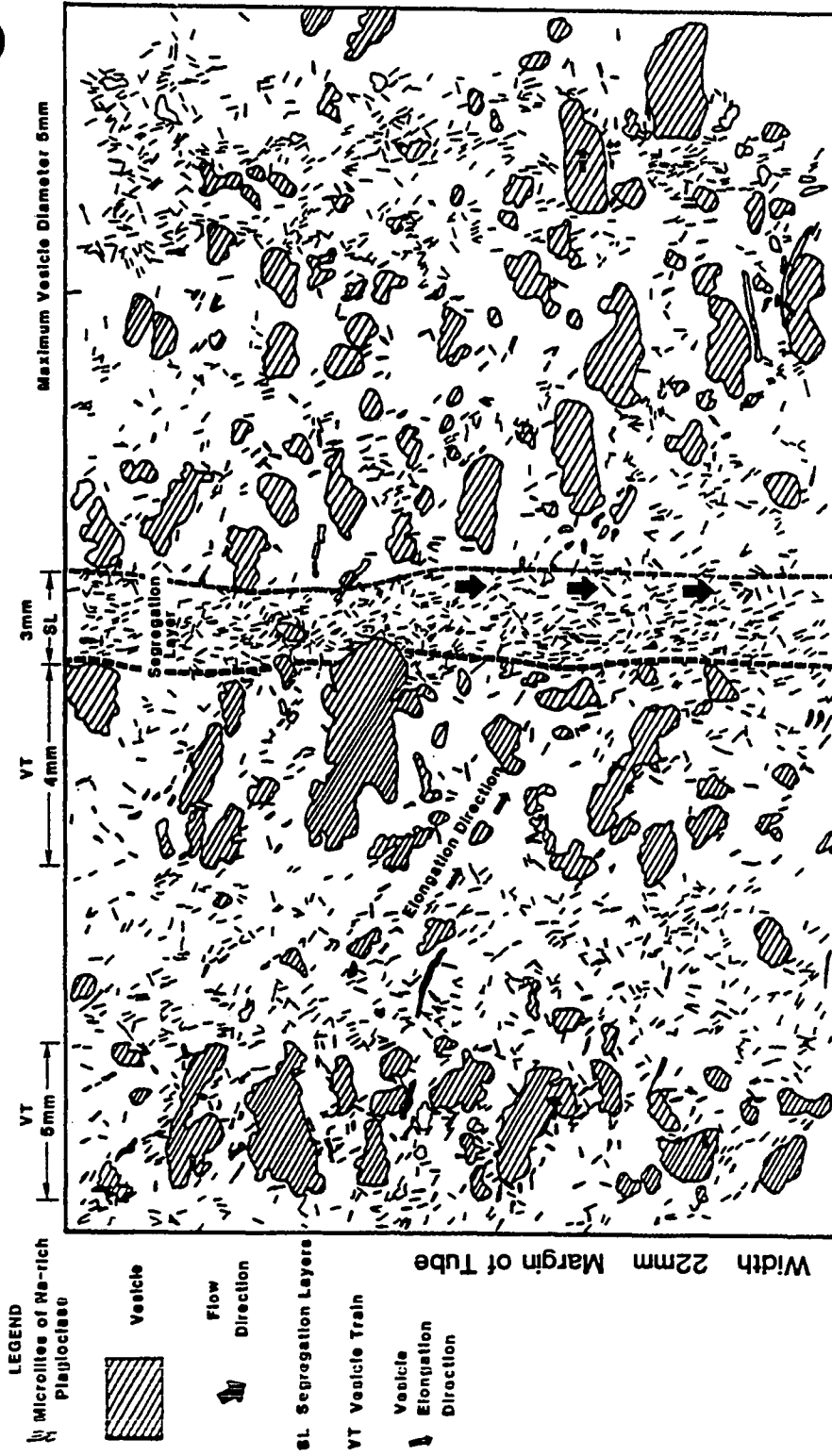
similar fluid dynamic conditions [*Bhattacharji and Smith, 1964; Bhattacharji, 1966; Blachard et al., 1979; Kilburn, 1984; Shelley, 1985*] thus, the hydrodynamic forces responsible for the migration of phenocrysts away from the margins must also be responsible for the abrupt variation in vesicle trains within the dikes. Flow differentiation during dike emplacement must also play an important part in the observed vesicle distributions (refer to the section on the "AMS data of the Koolau dikes", Chapter 3)

In the Koolau dikes, sills, and filled lava tubes the maximum observed axial ratio ( $m$ ) of elongated vesicles, ranges from 4:1 to more than 10:1, the later being observed in the special case of pipe vesicles/ amygdales that are common in the Kapaa Quarry and Mokolua Island dike swarms. Elongate vesicles within segregation layers show a moderately well defined preferred orientation along the principal flow azimuth. Their preferred orientation (elongation direction) is commonly inclined at angles between 30–45° to the dike walls, similar to observed imbricated crystals with their major axes dipping upflow. Less commonly the elongate vesicles and crystals are arranged normal to the margins.

In thin section, the vesicles appear to have either sharp or feathery outlines. The latter is a more common feature of the irregular vesicles (or microvesicles) associated with the mafic segregation zones of the filled lava tubes sampled at Makapuu Head (Figure 4.6a), in which the irregular microvesicles within interstitial mesostasis (last formed interstitial material) represent vesiculation in melt within the crystal framework of the rock [*Peck, 1978; Anderson et al., 1984; McMillan et al., 1987*]. According to *Kilburn's* [1984] study of the morphology and rheology of Etnean lavas, the vesicles with sharp boundaries are diagnostic of vesiculation from a liquid medium. The preservation of smooth bubble interfaces are usually bordered by microlites at low angles of contact or tangent to the bubble surface (Figure 4.6b). In the filled lava tube, a small proportion of the vesicles seem to have been utilized as substrates for crystal nucleation evidenced by a mantling of a narrow rim of radially disposed microlites (Figure 4.6c). Very fine groundmass particles, notably the opaques phases (e.g. subhedral- titanomagnetite grains), have also

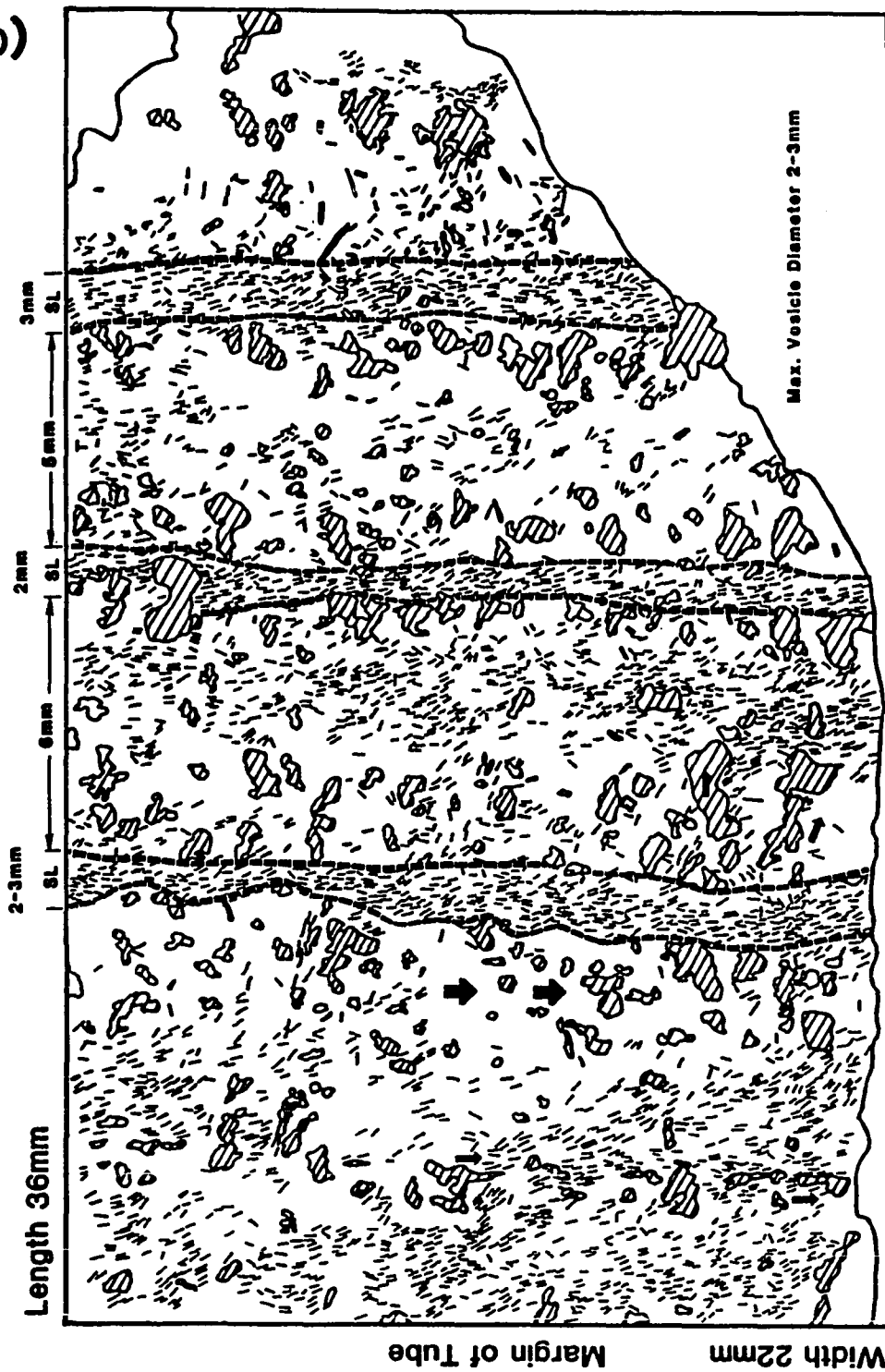
Figure 4.6 (a-c) Show the outline and orientation of vesicles, microvesicles, and microphenocrysts (microlites of Na-rich plagioclase) along the margins of a infilled lava tube (KT38), at Makapuu Point. Note that there is a preferred vesicle elongation direction within vesicle segregation zones, herein referred to as vesicle trains (VT). Small arrows indicate the elongation direction which are in agreement with the magnetic imbrication direction and inferred magma flow direction. Also shown are narrow zones of crystal segregation in which there is a preferred elongation direction of the microphenocrysts, the large arrows show the inferred magma flow direction.

(a)



Oriented Thin Section of Sample 4A, Left Margin of Filled Lava Tube Length 31mm

(b)

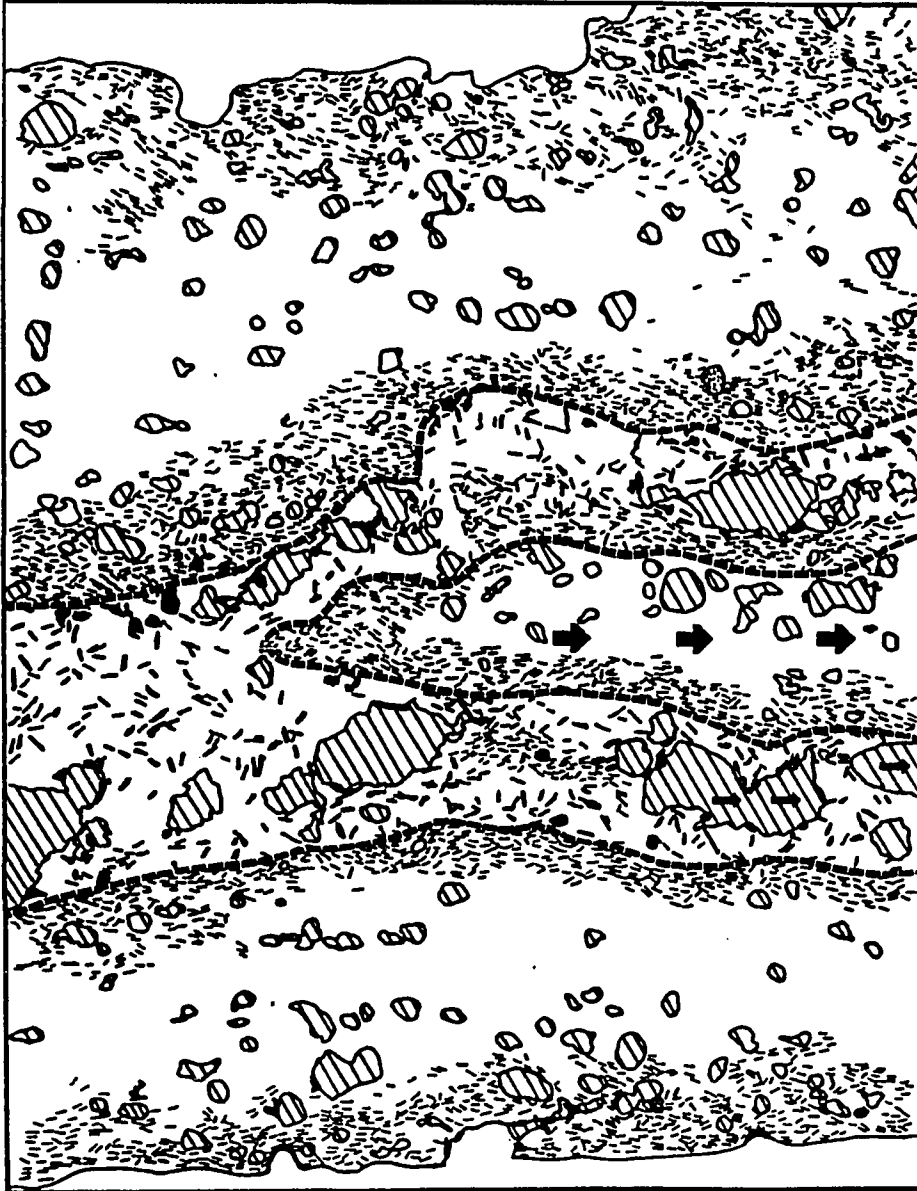


Oriented Thin Section, Sample 4B, Left Margin of Filled Lava Tube

(c)

Width 22 mm

Margin of Tube



Oriented Thin Section 10A, Right Margin of Filled Lava Tube

7.5 x Linear Scale

preferentially collected around some of the larger vesicle surfaces. As suggested by *Kilburn* [1984], this may be the result of local flocculation or of crystallization having been induced by the development of volatile rich haloes outside some vesicles.

The vesicles that exhibit feathery margins are generally smaller, less abundant and typically with subcircular to irregular cross-section. Microscopically these surfaces typically appear subangular to blocky, and irregular, owing to the projection of the enclosing microlites into the cavities resulting in a diktytaxitic texture. It is suggested [*Dickinson*, 1965; *Kilburn*, 1984] that basalts which exhibit this type of texture must have developed during late stages of crystallization, when insufficient liquid was available to produce a smooth bounded interface.

#### **BUBBLE DYNAMICS AND RHEOLOGY DURING INTRUSION**

The rheological and dynamical evolution of bubbles in steady simple shear, or in extensional or compressional strain motion is a highly complex problem integrating the external stresses (ambient flow plus other sources) to the surface stresses (surface tension of the bubble) plus the internal stresses (e.g. Poiseuille flow plus an unknown pressure at the bubble center which in turn is controlled by volume conservation requirements). Though the numerical techniques involved in solving the complex rheological problems of three-dimensional, or for that matter, even two-dimensional bubble flow are beyond the scope of this study, it is appropriate to briefly review some of the most relevant findings applicable to our understanding of how magma flows through dikes.

Using dimensional analysis, *Rallison* [1984] has investigated the deformation of small viscous drops and bubbles in sheared flows. From a fluid dynamics approach, it has been proven that drops of one fluid or gas phase suspended in a second fluid that is undergoing shear, will cause the drops or bubbles to deform, and, if the local shear rate is high, will break into two or more fragments. Many theoretical and experimental studies of bubble morphology have been concerned with how much distortion a given flow produces, how

strong the flow must be to break the bubble, and the number and size of the droplets that result from a burst. The factors that influence bubble morphology in dikes may be listed as follows (after *Grace*, 1971; *Kilburn* 1984):

- (1) *Fluid density*, its homogeneity and rheological properties (viscosity and crystal content).
- (2) The *surface tension* acting over the bubble-magma interface.
- (3) The *size and percentage of bubbles* and their steady, *terminal velocity*.
- (4) Any *accelerations acting upon the bubbles*, for instance, those due to the bulk motion of the magma or sudden local changes in pressure (e.g. wall effects, Magnus effects).

*Rallison* [1984] suggests that if the bubbles of the discrete phase are sufficiently small, the *Re* of the fluid motion responsible for deforming the drop is also low. He also points out that under *plane hyperbolic flow* when the ratio of flow forces to surface tension is small, initially spherical bubbles will deform into ellipsoidal shapes whose principal axis is aligned in the flow direction. However, at higher rates of flow the shape remains rounded only for moderate and large ratios of the drop viscosity compared to the suspending fluid (*Rallison*'s  $\lambda$  value), but comparatively inviscid drops develop a characteristic "point-end" or dimpled cusp shape (Table 4.1, Figure 4.6). Once the flow rate increases above a critical value high- $\lambda$  drops extend into a long, thin thread that breaks into a large number of small droplets [*Rallison*, 1984]. A low viscosity (10–100 poises) vesiculated tholeiitic magma flowing in a shallow dike with a presumed volatiles phase, e.g. H<sub>2</sub>O vapor, would have very low  $\lambda$ -values, say in the order of 10<sup>-3</sup>. Therefore, the gas bubbles are capable of extending into thin stable ellipsoid shapes for much higher flow rates, but at sufficiently high rates they will break, either by extension into long, thin tubes (e.g. pipe vesicles formed along some dike margins) or, if, by ejecting small bubbles at the pointed ends (tip streaming) so as to reduce the bubble volume and establish a new equilibrium between the

elongate vesicle and the viscous flow field (Figure 4.6). Furthermore, if steady-state laminar flow through a dike is suddenly switched off (e.g. during closure, necking, or along dike offshoots) an already highly elongate unbroken bubble will break by a Rayleigh-Taylor instability into a chain of drops of uniform size [Figure ]. Rollison [1984] predicts that the largest stable sustainable bubble distortion has an aspect ratio of about 5:1 for large  $\lambda$ , while also noting that simple shear is less effective in breaking drops than hyperbolic flow, in that higher flow rates are needed. The occurrence of pipe vesicles with aspect ratios >10:1 support the idea that the Koolau dikes must have had low  $\lambda$ -values, and that the magma flowed by simple shear.

*Richardson* [1973], in a two-dimensional analysis of bubbles in slow viscous flows, indicates that when surface tension effects are large, the cross-section of the bubble is nearly circular. When the surface tension is small, bubbles in a velocity profile will have a flatten (elliptical-cap) or dimpled (re-entrant cusps) shaped if they are at the center of the parabolic flow profile, and will be more irregular shaped if they are off-center (Figures a and b). Furthermore, *Richardson* determined that inviscid bubbles in either shear flow or pure straining motion will have an elliptical cross-section, in which the large bubbles moving under a pressure gradient through a circular tube develop a re-entrant cavity at their trailing-end and small bubbles tend to migrate towards the axis of flow. His two-dimensional solutions for bubble morphology show remarkable similarities with the observed three-dimensional examples seen in Koolau and Waianae vesiculated dikes, in which the vesicles along the center-line tend to be spheroidal while those nearest the margin have a much more varied shape (e.g. ellipsoidal, tear drop, ellipsoidal-cap or irregular; Table 4.1). *Goldsmith and Mason* 's [1962] experiments show that small bubbles introduced into a fluid flowing through a circular tube will migrate towards the axis even at very low  $Re$  in contrast to the behavior of solid neutrally buoyant spheres or anisotropic mineral grains, which show a migration across the streamlines only at higher  $Re$  [*Jeffery*, 1922; *Bhattacharji and Smith*, 1964; *Komar*, 1972a; *Richardson*, 1973; *Barriere*, 1976].

*Kilburn* [1984] and *Rollison* [1984] both derive the angle between the principal axis of the drop or bubble and the positive flow direction ( $\alpha$ ) for weak flows the deformation is elliptical and  $\alpha = 45^\circ$  and as the flow rate increases the equilibrium shape becomes more elongated, and for each fixed  $\lambda$ ,  $\alpha$  decreases towards  $0^\circ$  flow rate increases.

In conclusion, the orientation, distribution, and occurrence of elongate crystals and vesicles offers the opportunity to measure properties of magma flow rheology that may help distinguishing the absolute flow azimuths or sense of flow direction in dikes. The methods discussed above can then be used to compared with the AMS fabrics to infer the absolute (primary) magma flow directions

**CHAPTER 5**  
**VOLCANIC EVOLUTION AND MAGMA FLOW IN THE KOOLAU**  
**DIKE COMPLEX**

**DISCUSSION**

This study shows that the AMS technique has great potential for determining direction and mode of emplacement and flow azimuth (absolute magma flow direction based on a magnetic imbrication along each margin of the dike) reflecting the orientation of the internal stress field during magma injection. It also enables possible variation in magnetic grain distribution patterns across the dike width to be explored (e.g. the widest dikes tend to show an increase in the plunge angle of the maximum AMS direction in their central interior, only occasionally do they have random AMS directions) and may yield information on the flow regime. Mapping the three-dimensional internal structure, the dynamics and mechanics of magma transport within the dikes as they link together the calderas and major rift zones, and the kinematic evolution of the storage system(s) is extremely important in deciphering how large shield volcanoes grow.

Hotspot induced crack propagation and dike injection systems are presumed to be controlled by the stress field and production rate of magma-filled cracks in the mantle [Fedotov, 1978; Shaw, 1980; Takada, 1989]. Crack propagation systems are commonly indicated to propagate in the vertical plane (the minimum principal stress is assumed to be horizontal [Anderson, 1951]). Experimental modelling of liquid-filled cracks in gelatin [Fiske and Jackson, 1972; Pollard, 1973] predicted that a magma-filled crack (dike) propagates in the direction of maximum principle stress. Rubin and Pollard [1987] suggested that a crack can neither ascend nor descend if the tensile strength of the host rock is greater than maximum principal stress, or the fracture toughness is greater than the stress intensity factor. For this special case a magma-filled crack will propagate laterally and the dike is said to be in a state of neutral buoyancy [Ryan, 1980]. Buoyancy forces are

greatest in the lower crust because of the higher density difference between magma and the host rock. This allows magma filled cracks to rise vertically and magma flow directions to be inclined steeply. As the buoyancy forces become smaller an initial crack stops propagating in the vertical direction and under large magma production rates it can only propagate along the horizontal direction coinciding with the depth of neutral buoyancy.

The AMS method, discussed herein, and used to define the magma flow direction in dikes offers a new approach to understanding and determining the internal stress fields during dike injection and shield growth. For the Koolau dikes the AMS representation ellipsoid (susceptibility tensor) is assumed to be due to the preferred alignment of the magnetic grains resulting from either emplacement of a partially crystallized magma (primary magnetic fabric), crystal growth during or following magma emplacement, or realignment in a stress field (convection or gravitational). Though the dike specimens are only slightly anisotropic (mean total percent anisotropy is 2.4%) the AMS data obtained from these dikes do exhibit significant axial clustering. Hence, a slight prolate component in the plane of foliation, is interpreted to indicate initial flowage of the magma during the early stages of dike injection.

Measurements of dike strike, dip, size (width), magnetic fabric, morphology, surface lineations, elongation of vesicles, distribution of phenocrysts, and remanent magnetization direction indicate that at least two and probably three magma storage reservoirs may have evolved within the single volcanic edifice of the Koolau shield. This model for the internal structure of the volcano is based on measurements of the absolute magma flow direction (inferred from the AMS magnetic fabric) from 71 dikes, the orientation of surface lineations on many other dikes [Walker, 1987], and dike morphology. It is suggested that three separate magma bodies were successively emplaced at shallow depths (2–3 km) during the shield building stage. The oldest center was located below the NW-end of Kaneohe Bay, the next oldest center was 12 km to the SE below the south-end of Kaneohe Bay, and the youngest was 8 km further SE below the Koolau caldera where the Bouguer anomaly

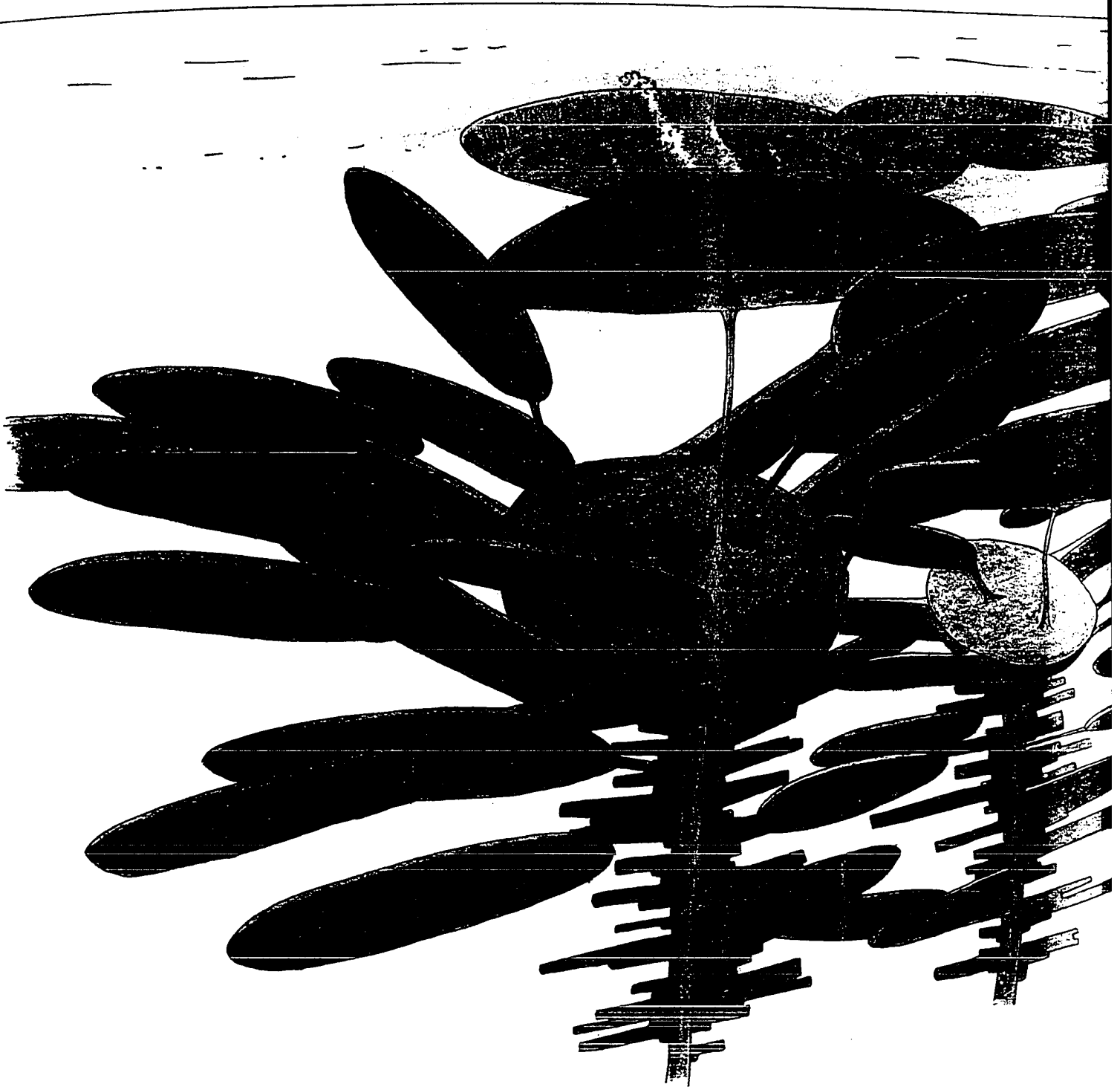
reaches its maximum value of +310 mgal. Based on a number of lines of evidence (e.g. dike stratigraphy, field relationships, and magma flow directions) it is inferred that any two adjacent reservoirs may have been contemporaneously active, feeding the nearly 50 km length of the NW rift system.

The Koolau Volcano must have evolved under the induced gravitational stress field of the pre-existing neighboring Waianae Volcano which mandated the initial dike injection direction perpendicular (tangential) to the minimum tensile stress. This present study suggests a revised model (after *Walker, 1987*) for the evolution of large shield volcanoes involving the evolution of three separate, shallow (<3 km deep) magma storage reservoirs within a single volcano in agreement with the Pacific plate motion theory over a fixed hotspot (Figure 5.1). Hence there is evidence for a progressive development of magma centers within a single volcano analogous with the progressive development of volcanoes in the Hawaiian chain. These ideas are in agreement with both the plate motion theory over a fixed Hawaiian hotspot and the induced gravitational stresses of a pre-existing neighboring buttressing edifice.

## CONCLUSION

The original structure of an eroded shield volcano has been reconstructed from dike-complex data [*Walker, 1987*] and from AMS magnetic fabric studies [*Knight and Walker, 1988*] for the Koolau dike complex, Oahu. Macroscopic surface lineations, elongation of vesicles, flow banding, and other magma flow structures show a strong correlation with detailed magnetic fabric analysis in many of the dikes. The plunge direction of the maximum  $\chi_1$  AMS axis shows excellent correlation (within  $\pm 35^\circ$ ) with the flow structures in 62% of the Koolau dikes. Only 9 (13%) of the 71 dikes studied for AMS have steeply plunging ( $\geq 66^\circ$ ) macroscopic flow lineations and/or magnetic fabric lineation directions. A majority of these dikes are concentrated in three areas. Two dikes located in northern Kaneohe Bay on the Mokolii Island (Chinaman's Hat) and a third dike located near Moli

Figure 5.1 Idealized drawing showing a few dike orientations, their possible emplacement directions (small arrows), and their relative ages. (The darker gray, purple, and blue colors represent the older or cooler dikes while the yellow and red colored dikes represent the younger or still active ones). Note that there is also an inferred progressive shallowing of the three magma reservoirs that may have occurred during the evolution of the Koolau shield volcano. The oldest and hence deepest center is shown by the dark, cool, colors and represents the reservoir below northeastern Kaneohe Bay, while the shallowest and youngest magma reservoir is shown by the light, hot, colors and represents the main center below Kailua.





Pond along Kamehameha Hwy. in this same general vicinity have steeply plunging magnetic lineation directions. A second group of dikes with similar near vertical plunge directions is located 14 kilometers to the southeast near the Kailua caldera, in the Kapaa Quarry, and at the northern H3 highway road cuts. It is also noted that most of the dikes in this region are hydrothermally altered or chloritized, and may represent a large thermal aureole of the central conduit associated with the Kailua caldera. It is also interesting to note that the good agreement between the MSL and  $\chi_1$  plunge directions for many of these hydrothermally altered dikes suggests that the magnetic carriers of the AMS signature have not been significantly altered.

It is noted that the dike morphology, e.g. strike of the dikes nearest the southern portion of the Kailua caldera in the vicinity of Keolu Hills show a significant change in trend that is more radial or normal to the major rift zone, pointing ENE to WSW. Dikes which outcrop along the northern rim of this caldera near the Castle Junction also show variable orientations, though they are commonly a low-angle type and less radial in occurrence. Such evidence suggests that the magma of these dikes was supplied from at least two separate conduit systems located close to the measured axis of the dike complex. Whether or not these dikes represent cone sheet intrusive events within the caldera walls is not known.

The occurrence of two normal polarity dikes near northern Kaneohe Bay further suggests that the oldest magma center was located in that general vicinity and would have been emplaced during the Gauss normal chron more than 2.4 Ma. These two dikes have not been radiometrically dated, but it is likely that they have similar ages to the oldest dated rocks of the Koolau, at 2.6 Ma [Doell and Dalrymple, 1973]. The remaining dikes show reverse or intermediate polarity directions and thus belong to the Matuyama reversed polarity chron (Refer to the section entitled "Natural Remanent Magnetization Directions of the Koolau Dikes"). Thus the entire period of dike intrusion covers a rather short time span (<0.8 m.y.) including a single polarity change. For the most part, these dikes also have

flow lineations that plunge much shallower, parallel to the NW- or SE-rift axis. These remaining dikes have flow lineations and magnetic fabrics which define two magma source regions only six kilometers apart, one near southern Kaneohe Bay and the other at the Kailua complex. Based on dike cross-cutting relationships the older magma reservoir must have been beneath southern Kaneohe Bay. Hence, the original volcanic construct must have formed from three nearby magmatic conduits, separated by no more than 15 km and aligned along a nearly linear NW-SE rift zone. Based on dike orientations, along with their corresponding AMS representation ellipsoid directions, indicates that the maximum horizontal compressive stress axis was oriented N50°W and S50°E, i.e. the trend of the main NW-SE rift axis.

Portions of the dike swarm might have been tilted by large submarine landslide events as envisioned by *Moore* [1963]. Specifically, those associated with the Mokulua Islands dike swarm, dip steeply 75°NE, in agreement with an E-NE oriented tilt-vector associated with listric or high angle normal faulting of the unbuttressed side of the Koolau shield during major slide events. The resultant amount of tilting would be small because the initial dike dips are presumed to be nearly vertical and the strikes of most dikes are normal to the minimum horizontal compressive stress axis. However, since most of the dikes in the Mokolua islands are associated with shallow dipping lava flows (15°NE), there is little evidence that this portion of the volcanic dome has undergone significant displacement, and therefore the dike structure could just as easily be interpreted as a primary feature of the off-axis dikes associated with this portion of the Koolau shield.

Flow lineation data were obtained from 38 dikes and magnetic fabric lineation data were obtained from 61 dikes and plotted parallel to the maximum horizontal compressive axis which strikes NW-SE and dip is vertical (Figures 4.1a and b). The results seem to be diverse, but three separate groups, here classified as groups I, II, and III are identified. Unlike the gradual variation in dike orientation with distance from the central conduit of a stratovolcano [*Knopf*, 1936; *Nakamura*, 1977], the linear dike swarms of the Koolau

shield, and probably similarly, the dike complexes of many of the other Hawaiian volcanoes are thought to develop tangentially to the flanks of pre-existing volcanoes resulting in nearly linear biaxial or triaxial rift systems [*Fiske and Jackson, 1972; Lipman, 1980*]. Similar to stratovolcanoes, the dike swarms near the central conduits of Hawaiian shield volcanoes commonly show a more radial distribution though this fact tends to be less dramatic for the Hawaiian type. The best examples being the radial swarms of the central Waianae Volcano and the main Kauai Volcano. Based on these and other findings, five general corollaries for the formation of intrusive magma flow lineations within shields and stratovolcanoes are suggested:

- (i) AMS fabrics agree well with the macroscopic surface lineation plunge direction, and are thought to represent a primary igneous flow fabric.
- (ii) Magma flow directions within central conduits tend to be at a high angle because of the greater hydraulic pressure of rising magma compared to the regional compressive stress field [*Ui et al., 1984; Chevallier and Verwoerd, 1988; Dieterich, 1988*] (e.g. dikes located in the Kapaa Quarry and northern H3 cuts).
- (iii) Due to increased radial hydraulic fracturing near the summit caldera dikes tend to be radially oriented, generally more vesiculated, and of low angle type [*Chevallier and Verwoerd, 1988*] (e.g. the dike swarms of Keolu Hills and Castle Junction cuts).
- (iv) Near the central conduit system intrusive magma flow lineations may be quite variable depending on degree of vesiculation, neutral buoyancy effects, and hydrodynamic forces.
- (v) Away from the central conduit dike orientations are dominated by the direction of the maximum horizontal compressive stress axis and will develop tangentially to the flanks of pre-existing volcanoes, and magma flow lineations tend to have shallow plunge directions (e.g. Koloa, Kalpapau, and Maakua Gulch dike-sets).
- (vi) Farthest from the central conduit intrusive magma flow directions have shallower injection angles, and even dip away from the presumed magma source (e.g. Koloa, Kalpapau, and Maakua Gulch dike-sets, and the Makapuu Head dikes).

(vii) Dike intensities are anomalously low within the source calderas of large shield volcanoes where they should reach a maximum. It is suggested that once the dike intensities reach 55-65% that further injection will occur down rift where dike intensities are lower and therefore can be more easily accommodated, and which has been referred to as the "density zonation model" by *Walker* [1987].

(viii) At the distal ends of large shield volcanoes the intrusive magma flow directions commonly dip away from the presumed magma source as a result of negative buoyancy conditions, where the higher density (e.g. >2.9–3.0) magma is injected above the zone of neutral buoyancy. In these regions (e.g. Koloa, Kalpapau, and Maakua Gulch dike-sets, and the Makapuu Point dikes) it is suggested that the neutral buoyancy zone also plunges shallowly away from the main reservoir. Hence, magma derived initially from the main reservoir (in a "happy" state of neutral buoyancy) finds that it must start to flow downward, away from its source to remain in balance with the gravitational forces acting on the edifice at its distal ends. This may occur either along preexisting fractures or be intimately related to zones of active faulting within the distal ends of the shield.

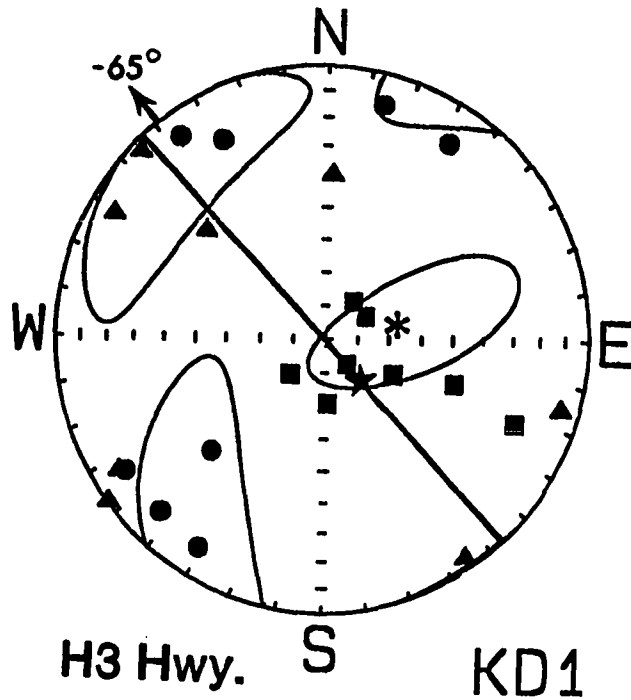
The pre-erosional structure of the Koolau shield is inferred to consist of three separate magmatic conduits clustered closely in space and time, and arranged NW–SE tangential to the minimum compressive stress field of the adjacent Waianae Volcano and uncoupled along its eastern shore-line. For the Koolau volcano the AMS method offers great promise in the determination of intrusive magma flow directions, even if the igneous bodies lack identifiable structures and no other means to determine the absolute magma flow direction.

## APPENDIX A

### Legend for AMS Equal-area Plots:

#### EXPLANATION

- ★ Macroscopic Lineation
  - R Sample from Right Side of Dike
  - L Sample from Left Side of Dike
  - \* Mean AMS Direction
  - 3° ← Magma Flow Direction and Plunge Angle
  - Maximum AMS Axis =  $X_1$
  - ▲ Intermediate AMS Axis =  $X_2$
  - Minimum AMS Axis =  $X_3$
  - Plane of Dike
- } lower hemisphere



	Mean X	H	Dmax	Imax	Dint	Iint	Dmin	Imin
KD1-1A	0.253E-02	1.5%	318.2	-7.3	224.8	-24.9	63.4	-63.8
KD1-1B	0.263E-02	1.0%	142.0	-7.1	52.7	-1.6	335.2	-82.8
KD1-2	0.234E-02	2.4%	45.3	-75.2	285.7	-7.4	194.0	-12.7
KD1-3A	0.297E-02	1.5%	33.1	-11.0	294.5	-37.6	136.7	-50.2
KD1-3B	0.309E-02	1.1%	316.8	-80.0	52.9	-0.6	143.1	-9.9
KD1-4	0.264E-02	1.2%	295.7	-66.1	57.1	-11.3	151.7	-19.8
KD1-5	0.224E-02	2.6%	217.6	-75.8	325.2	-4.4	56.2	-13.5
KD1-7A	0.208E-02	1.4%	292.8	-23.2	182.0	-39.6	45.1	-41.4
KD1-7B	0.207E-02	1.5%	287.7	-46.9	131.5	-40.6	30.9	-12.1
KD1-8	0.207E-02	1.7%	356.7	-70.9	119.7	-10.7	212.7	-15.7
KD1-6	0.183E-02	2.5%	240.9	-75.6	134.3	-4.2	43.3	-13.8

Site Statistics for KD1

Mean X = (2.408 +/- 0.382) x 1E-03

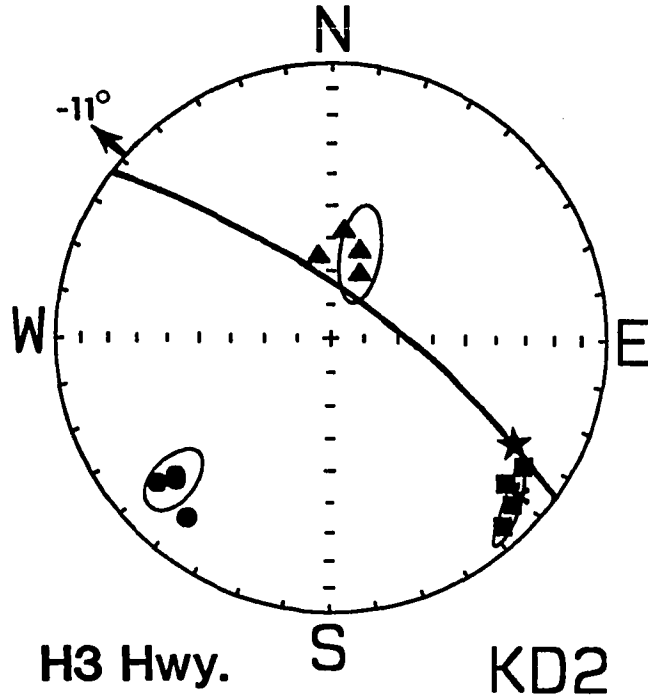
Xmax: Mean D = 320.7      Mean I = -64.9      a95 = 75:37  
 Xint: Mean D = 98.4      Mean I = -19.1      a95 = 74:36  
 Xmin: Mean D = 13.9      Mean I = 15.6      a95 = 56:37

Xmax/Xint = 1.003      Xint/Xmin = 1.005      Xmax/Xmin = 1.008

H = 0.75 +/- 0.45%

E = 1.002      Graham's V = 38.6

F = 0.6 +/- 0.5%      L = 0.3 +/- 0.4%



	Mean X	H	Dmax	Imax	Dint	Iint	Dmin	Imin
KD2-1	0.262E-02	2.9%	317.2	-8.4	204.3	-69.2	50.1	-18.9
KD2-2	0.230E-02	1.5%	312.1	-11.7	198.4	-62.7	47.5	-24.3
KD2-3A	0.265E-02	1.6%	309.3	-18.6	186.9	-57.8	48.4	-25.2
KD2-3B	0.266E-02	1.5%	303.3	-17.1	171.0	-65.4	38.7	-17.1

Site Statistics for KD2

Mean X = (2.557 +/- 0.151) x 1E-03

Xmax: Mean D = 312.7      Mean I = -11.4      a95 = 11: 3

Xint: Mean D = 199.0      Mean I = -63.4      a95 = 15: 6

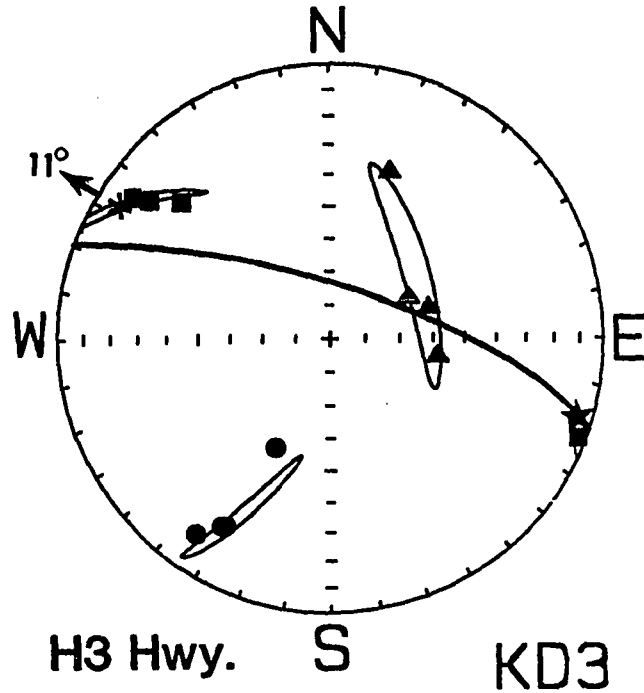
Xmin: Mean D = 47.8      Mean I = -23.7      a95 = 13: 5

Xmax/Xint = 1.013      Xint/Xmin = 1.005      Xmax/Xmin = 1.019

H = 1.86 +/- 0.33%

E = 0.992      Graham's V = 57.4

F = 1.2 +/- 0.3%      L = 1.3 +/- 0.3%



	Mean X	H	Dmax	Imax	Dint	Iint	Dmin	Imin
KD3-2	0.260E-02	2.8%	132.8	-27.5	279.9	-58.2	35.0	-14.7
KD3-5	0.272E-02	4.3%	125.5	-12.3	242.3	-64.3	30.4	-22.2
KD3-7	0.248E-02	5.8%	127.7	-18.3	252.6	-60.0	29.6	-22.9
KD3-8	0.249E-02	5.9%	292.0	-3.3	199.6	-36.2	26.6	-53.6

Site Statistics for KD3

Mean X = (2.572 +/- 0.109) x 1E-03

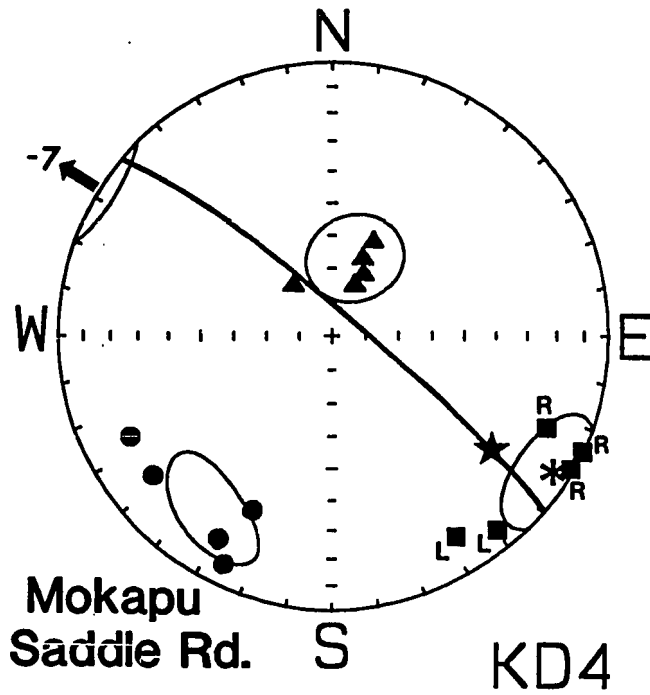
Xmax: Mean D = 303.3      Mean I = 11.1      a95 = 25: 1  
 Xint: Mean D = 231.6      Mean I = -58.0      a95 = 34: 4  
 Xmin: Mean D = 26.8      Mean I = -29.6      a95 = 26: 2

Xmax/Xint = 1.031      Xint/Xmin = 1.013      Xmax/Xmin = 1.045

H = 4.40 +/- 0.70%

E = 0.983      Graham's V = 57.1

F = 2.8 +/- 0.6%      L = 3.1 +/- 0.7%



	Mean X	H	Dmax	Imax	Dint	Iint	Dmin	Imin
KD4-2	0.316E-02	5.9%	299.3	-1.4	204.4	-73.6	29.7	-16.3
KD4-3	0.246E-02	4.5%	294.9	-0.4	204.1	-59.3	25.1	-30.7
KD4-4	0.309E-02	4.6%	293.3	-16.8	142.3	-70.9	25.9	-8.7
KD4-6	0.224E-02	2.2%	319.5	-7.9	207.4	-69.7	52.1	-18.5
KD4-7	0.243E-02	1.9%	328.2	-15.1	202.0	-65.4	63.5	-18.9

Site Statistics for KD4

Mean X = (2.675 +/- 0.378) x 1E-03

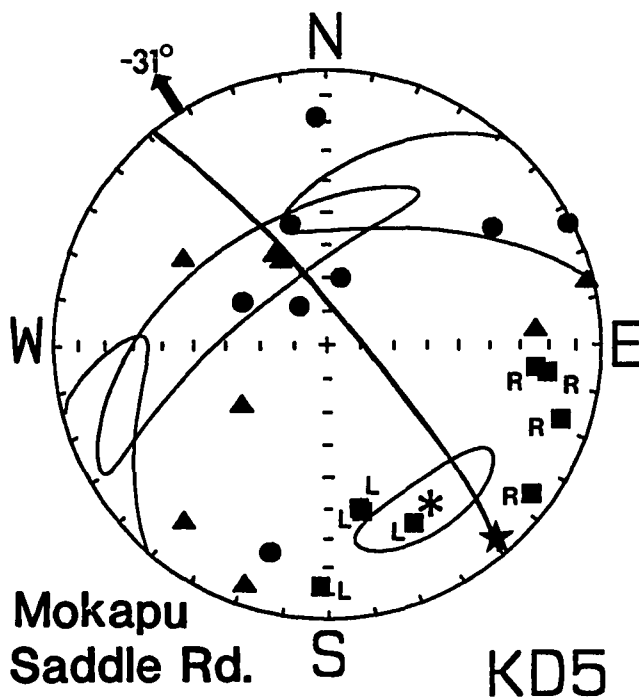
Xmax: Mean D = 302.3      Mean I = -6.9      a95 = 14:13  
 Xint: Mean D = 196.7      Mean I = -65.8      a95 = 15:13  
 Xmin: Mean D = 35.2      Mean I = -23.0      a95 = 17:10

Xmax/Xint = 1.024      Xint/Xmin = 1.011      Xmax/Xmin = 1.035

H = 3.46 +/- 0.87%

E = 0.988      Graham's V = 55.7

F = 2.3 +/- 0.7%      L = 2.4 +/- 0.6%



	Mean X	H	Dmax	Imax	Dint	Iint	Dmin	Imin
KD5-1	0.219E-02	1.4%	348.4	-37.9	256.3	-2.6	163.0	-52.0
KD5-2A	0.228E-02	0.9%	287.6	-11.6	19.3	-8.1	143.7	-75.8
KD5-2B	0.232E-02	0.6%	306.2	-8.8	39.2	-18.2	191.6	-69.6
KD5-3	0.198E-02	1.5%	276.1	-24.5	54.7	-58.7	177.5	-18.2
KD5-4	0.238E-02	1.9%	349.2	-39.3	120.9	-39.1	235.0	-26.6
KD5-5	0.224E-02	8.9%	334.3	-28.6	150.7	-61.3	243.4	-1.5
KD5-6	0.210E-02	1.5%	277.0	-20.3	149.5	-58.7	15.9	-22.7
KD5-7	0.250E-02	0.5%	2.0	-12.9	266.0	-24.6	117.2	-61.8

Site Statistics for KD5

Mean X = (2.249 +/- 0.156) x 1E-03

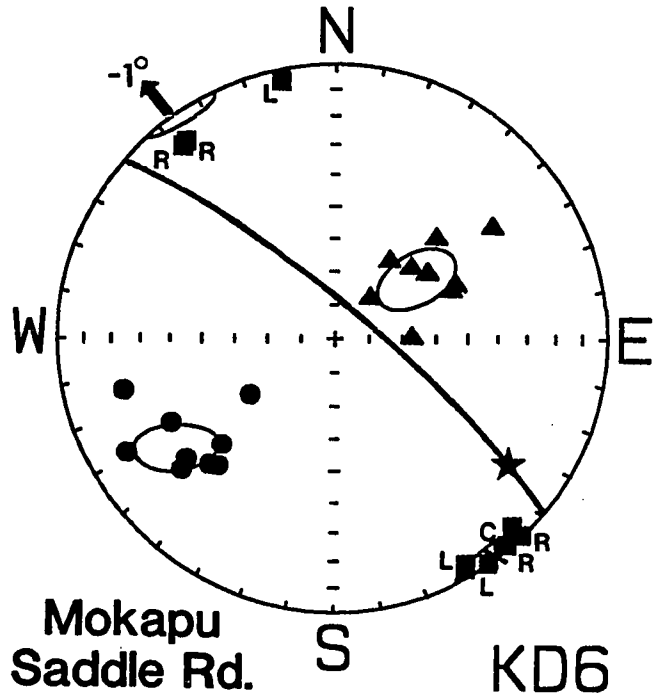
Xmax: Mean D = 327.6      Mean I = -31.1      a95 = 21: 9  
 Xint: Mean D = 115.3      Mean I = -54.5      a95 = 65:10  
 Xmin: Mean D = 48.0      Mean I = 15.4      a95 = 65:15

Xmax/Xint = 1.011      Xint/Xmin = 1.003      Xmax/Xmin = 1.014

H = 1.37 +/- 1.00%

E = 0.992      Graham's V = 64.0

F = 0.8 +/- 0.8%      L = 1.1 +/- 0.6%



	Mean X	H	Dmax	Imax	Dint	Iint	Dmin	Imin
KD6-1	0.276E-02	7.3%	316.1	-5.8	215.3	-61.6	49.2	-27.7
KD6-2	0.224E-02	4.9%	319.7	-1.7	227.0	-58.8	50.7	-31.2
KD6-3A	0.239E-02	2.6%	316.0	-0.7	225.3	-47.0	46.6	-43.0
KD6-3B	0.219E-02	2.6%	325.3	-0.6	235.0	-30.2	56.4	-59.8
KD6-4A	0.237E-02	3.2%	141.5	-11.7	245.9	-50.1	42.4	-37.5
KD6-4B	0.231E-02	2.9%	142.8	-11.1	247.3	-52.1	44.7	-35.7
KD6-5	0.229E-02	5.4%	330.1	-3.6	234.7	-56.1	62.5	-33.7
KD6-6	0.195E-02	2.7%	168.1	-4.6	269.0	-67.2	76.2	-22.3
KD6-7	0.249E-02	8.6%	329.6	-5.2	221.0	-74.0	61.0	-15.1

Site Statistics for KD6

Mean X = (2.331 +/- 0.213) x 1E-03

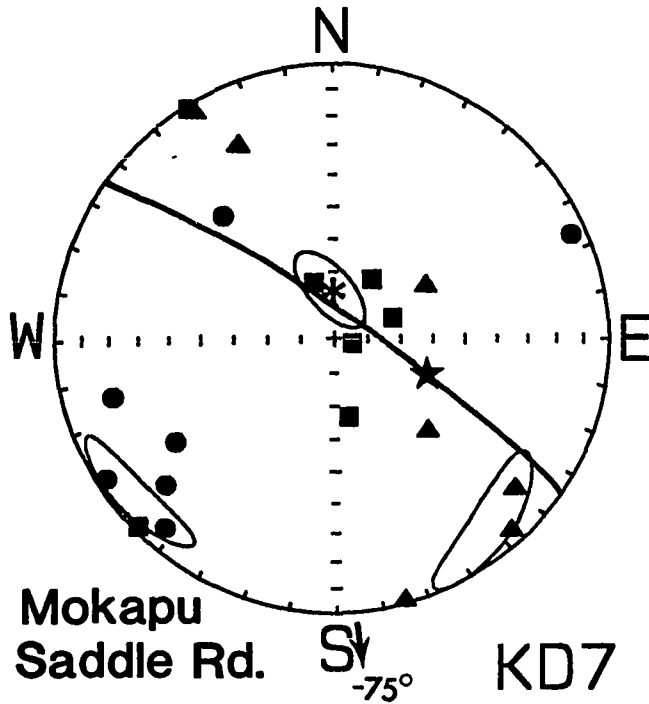
Xmax: Mean D = 324.8      Mean I = -0.6      a95 = 9: 6  
 Xint: Mean D = 233.8      Mean I = -59.7      a95 = 13: 7  
 Xmin: Mean D = 55.1      Mean I = -30.3      a95 = 14: 6

Xmax/Xint = 1.027      Xint/Xmin = 1.015      Xmax/Xmin = 1.042

H = 4.19 +/- 0.72%

E = 0.988      Graham's V = 54.1

F = 2.8 +/- 0.6%      L = 2.7 +/- 0.6%



	Mean X	H	Dmax	Imax	Dint	Iint	Dmin	Imin
KD7-1	0.267E-02	1.4%	46.6	-2.1	314.1	-50.1	138.4	-39.8
KD7-2	0.258E-02	0.7%	349.9	-66.4	154.0	-22.8	246.5	-5.8
KD7-3	0.278E-02	8.3%	283.5	-84.5	149.0	-3.9	58.7	-3.9
KD7-4	0.285E-02	0.7%	250.7	-71.2	345.0	-1.5	75.6	-18.7
KD7-5	0.304E-02	12.6%	160.6	-72.2	309.8	-15.5	42.2	-8.7
KD7-6	0.256E-02	1.7%	148.3	-1.5	240.7	-57.8	57.3	-32.1
KD7-7	0.358E-02	1.7%	213.0	-69.0	317.4	-5.5	49.4	-20.2

Site Statistics for KD7

Mean X = (2.865 +/- 0.338) x 1E-03

Xmax: Mean D = 355.8      Mean I = 75.2      a95 = 14: 6

Xint: Mean D = 140.1      Mean I = 12.1      a95 = 21: 7

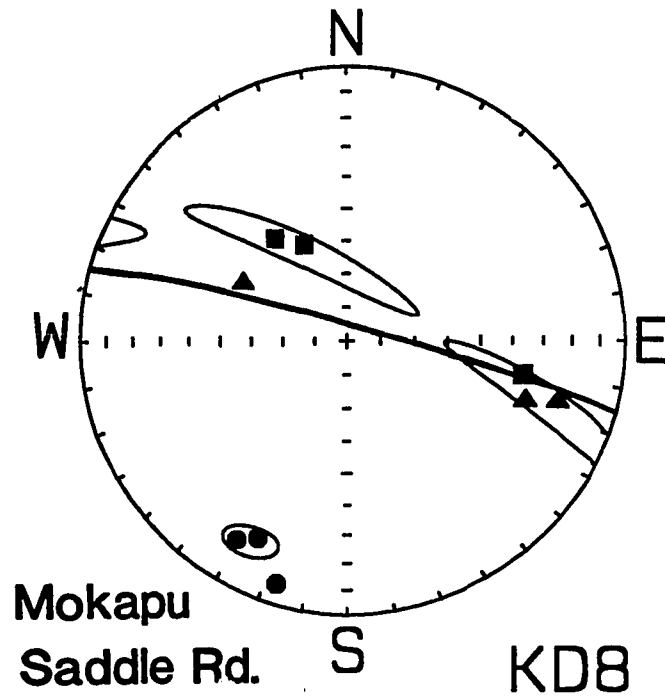
Xmin: Mean D = 51.9      Mean I = -8.4      a95 = 17: 6

Xmax/Xint = 1.008      Xint/Xmin = 1.025      Xmax/Xmin = 1.033

H = 3.24 +/- 1.93%

E = 1.018      Graham's V = 29.1

F = 2.9 +/- 1.7%      L = 0.8 +/- 1.2%



	Mean X	H	Dmax	Imax	Dint	Iint	Dmin	Imin
KD8-1	0.256E-02	1.0%	281.0	-35.6	118.4	-53.1	17.1	-8.4
KD8-2	0.219E-02	2.1%	155.5	-58.2	286.3	-22.1	25.6	-21.7
KD8-3	0.205E-02	2.2%	144.0	-51.8	288.8	-32.7	30.4	-17.4
KD8-4	0.425E-02	5.0%	221.6	-13.8	328.1	-49.3	120.8	-37.4

Site Statistics for KD8

Mean X = (2.760 +/- 0.879) x 1E-03

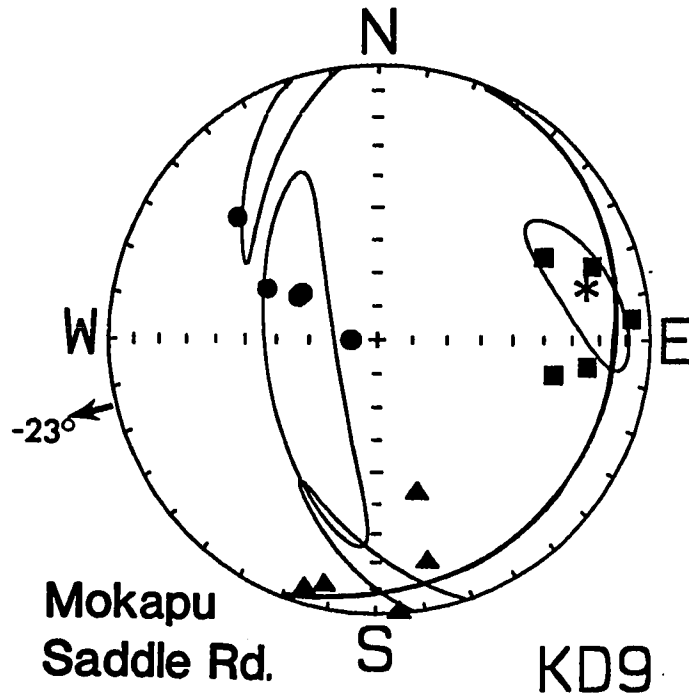
Xmax: Mean D = 54.6      Mean I = 45.8      a95 = 57:27  
 Xint: Mean D = 137.8      Mean I = -6.6      a95 = 81:27  
 Xmin: Mean D = 41.5      Mean I = -43.5      a95 = 81: 5

Xmax/Xint = 1.008      Xint/Xmin = 1.002      Xmax/Xmin = 1.010

H = 1.04 +/- 0.50%

E = 0.994      Graham's V = 62.8

F = 0.6 +/- 0.6%      L = 0.8 +/- 0.7%



	Mean X	H	Dmax	Imax	Dint	Iint	Dmin	Imin
KD9-1	0.381E-02	1.2%	281.4	-35.6	15.9	-6.4	114.6	-53.6
KD9-2	0.330E-02	3.4%	277.3	-24.0	11.7	-9.6	121.9	-63.9
KD9-3	0.340E-02	1.1%	251.1	-18.6	347.4	-18.3	118.7	-63.4
KD9-4	0.345E-02	2.0%	265.2	-7.4	355.3	-0.6	90.2	-82.5
KD9-5	0.427E-02	0.6%	243.3	-33.7	345.8	-42.0	130.6	-32.7

Site Statistics for KD9

Mean X = (3.645 +/- 0.359) x 1E-03

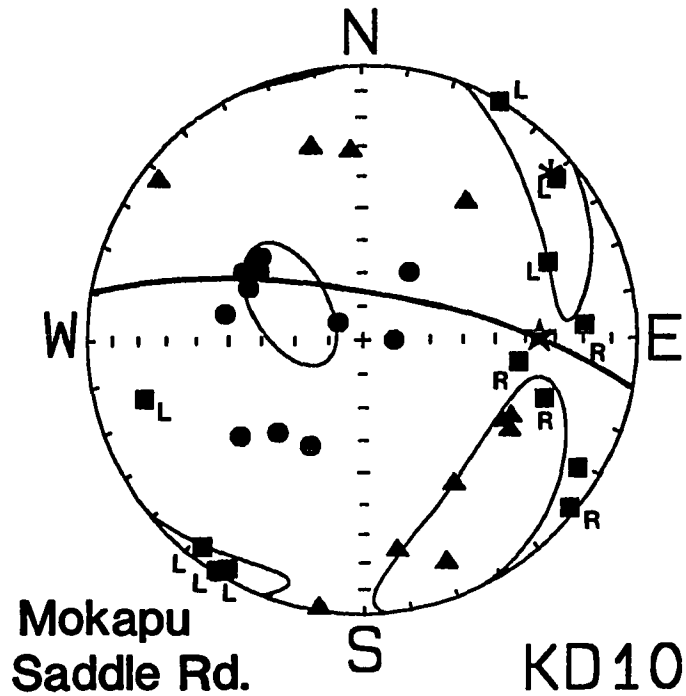
Xmax: Mean D = 76.0      Mean I = 23.3      a95 = 23: 9  
 Xint: Mean D = 165.2      Mean I = -1.9      a95 = 58: 5  
 Xmin: Mean D = 70.7      Mean I = -66.6      a95 = 58:11

Xmax/Xint = 1.014      Xint/Xmin = 1.007      Xmax/Xmin = 1.022

H = 2.14 +/- 0.82%

E = 0.993      Graham's V = 54.7

F = 1.4 +/- 1.2%      L = 1.4 +/- 1.2%



	Mean X	H	Dmax	Imax	Dint	Iint	Dmin	Imin
KD10-1	0.438E-02	2.0%	248.0	-27.4	350.9	-23.3	115.2	-52.7
KD10-2A	0.387E-02	2.4%	74.9	-19.3	339.8	-14.5	215.3	-65.5
KD10-2B	0.393E-02	3.2%	301.0	-8.9	31.1	-0.8	126.1	-81.0
KD10-3	0.438E-02	3.3%	37.8	-5.7	128.5	-7.3	270.3	-80.7
KD10-4	0.245E-02	1.9%	278.4	-41.8	9.6	-1.3	101.0	-48.2
KD10-5A	0.541E-02	3.4%	231.0	-8.9	328.0	-37.9	130.0	-50.7
KD10-5B	0.453E-02	3.6%	210.5	-0.2	300.6	-40.9	120.3	-49.1
KD10-6A	0.594E-02	5.5%	30.7	-3.9	297.6	-39.0	125.5	-50.8
KD10-6B	0.532E-02	5.4%	32.7	-1.2	301.8	-37.1	124.3	-52.9
KD10-7	0.519E-02	3.6%	266.5	-19.6	165.5	-28.2	26.5	-54.6
KD10-8	0.576E-02	3.3%	288.1	-30.7	176.7	-31.5	51.8	-43.1
KD10-9	0.198E-02	2.0%	309.3	-2.6	217.4	-37.4	42.7	-52.5

Site Statistics for KD10

Mean X = (4.428 +/- 1.189) x 1E-03

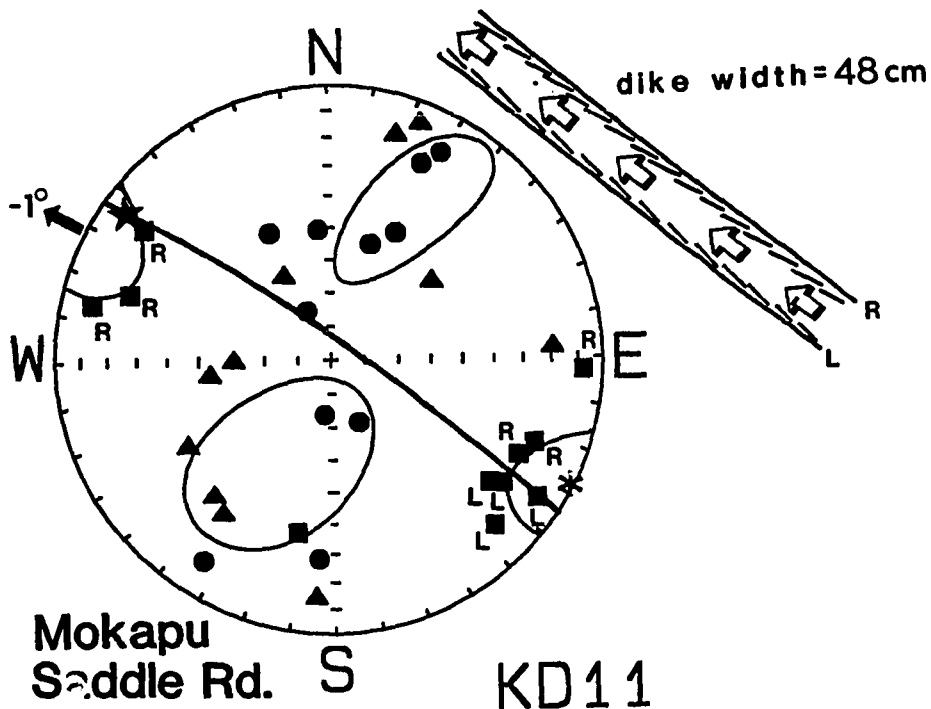
Xmax: Mean D = 49.5      Mean I = 9.9      a95 = 37: 9  
 Xint: Mean D = 143.5      Mean I = 21.8      a95 = 38:16  
 Xmin: Mean D = 296.8      Mean I = 65.8      a95 = 20:11

Xmax/Xint = 1.009      Xint/Xmin = 1.012      Xmax/Xmin = 1.022

H = 2.15 +/- 0.47%

E = 1.003      Graham's V = 41.5

F = 1.7 +/- 0.4%      L = 0.9 +/- 0.5%



	Mean X	H	Dmax	Imax	Dint	Iint	Dmin	Imin
KD11-1	0.655E-02	4.9%	315.9	-16.5	59.6	-38.7	207.7	-46.7
KD11-2	0.557E-02	2.3%	304.2	-10.4	41.5	-34.7	199.9	-53.3
KD11-4A	0.488E-02	2.7%	308.1	-27.9	83.1	-53.2	205.8	-22.0
KD11-4B	0.396E-02	2.7%	306.0	-24.1	89.6	-60.9	209.0	-15.3
KD11-5	0.554E-02	2.0%	12.1	-36.0	267.3	-19.4	154.7	-47.5
KD11-6	0.591E-02	5.6%	108.5	-24.4	233.0	-51.3	4.6	-28.0
KD11-7	0.561E-02	3.2%	272.6	-7.8	4.6	-14.0	154.3	-73.9
KD11-8	0.446E-02	2.2%	103.6	-12.4	197.1	-15.6	336.6	-69.9
KD11-9	0.596E-02	1.7%	125.4	-18.6	201.8	-8.5	7.6	-73.6
KD11-10A	0.641E-02	1.9%	292.6	-20.7	36.1	-31.8	175.2	-50.7
KD11-10B	0.473E-02	1.2%	297.2	-24.2	151.2	-61.5	33.6	-14.1

Site Statistics for KD11

Mean X = (5.416 +/- 0.783) x 1E-03

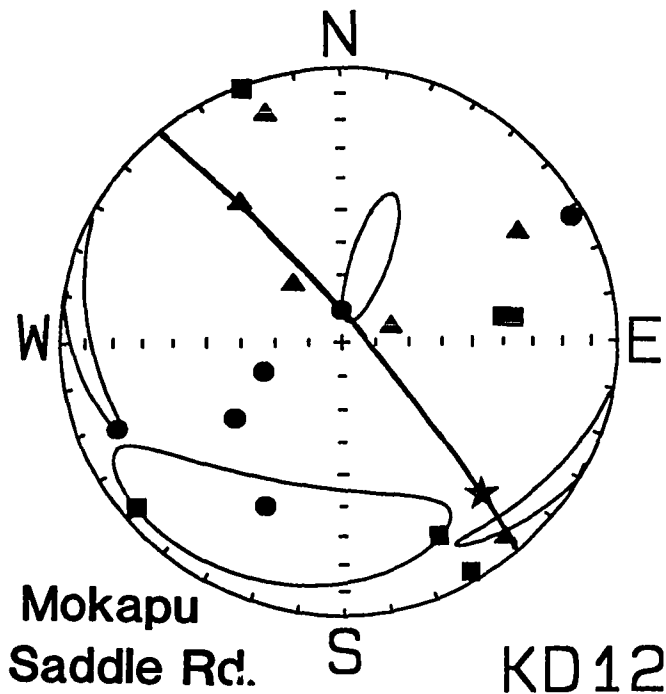
Xmax: Mean D = 298.3      Mean I = 0.8      a95 = 24:12  
 Xint: Mean D = 207.2      Mean I = 54.3      a95 = 33:21  
 Xmin: Mean D = 28.9      Mean I = 35.7      a95 = 33:12

Xmax/Xint = 1.020      Xint/Xmin = 1.005      Xmax/Xmin = 1.025

H = 2.53 +/- 0.79%

E = 0.966      Graham's V = 62.4

F = 1.5 +/- 1.0%      L = 2.0 +/- 0.9%



	Mean X	H	Dmax	Imax	Dint	Iint	Dmin	Imin
KD12-1A	0.433E-02	2.7%	333.7	-22.1	140.2	-67.4	241.7	-4.8
KD12-1B	0.438E-02	2.4%	159.0	-0.9	252.2	-74.7	68.7	-15.2
KD12-3A	0.507E-02	0.6%	261.4	-39.9	144.3	-37.5	25.6	-34.3
KD12-3B	0.422E-02	0.7%	262.2	-36.1	161.9	-13.5	54.8	-50.6
KD12-4	0.403E-02	1.5%	330.8	-4.2	238.8	-24.6	69.9	-65.0
KD12-6	0.457E-02	2.1%	50.9	-5.9	320.1	-7.5	178.9	-80.4

Site Statistics for KD12

Mean X = (4.436 +/- 0.331) x 1E-03

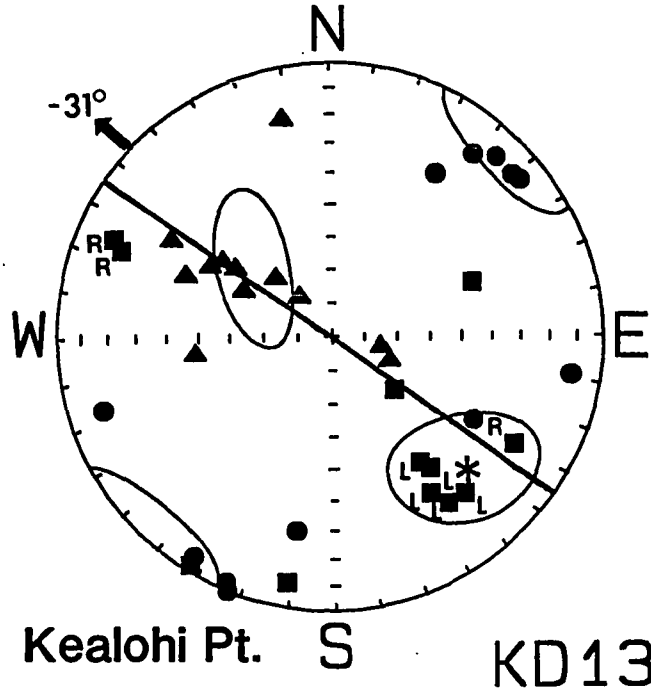
Xmax: Mean D = 19.2      Mean I = 63.1      a95 = 21: 5  
 Xint: Mean D = 198.9      Mean I = 26.9      a95 = 45:17  
 Xmin: Mean D = 289.0      Mean I = 0.1      a95 = 45: 4

Xmax/Xint = 1.019      Xint/Xmin = 1.017      Xmax/Xmin = 1.036

H = 3.56 +/- 3.83%

E = 0.999      Graham's V = 46.4

F = 2.6 +/- 2.9%      L = 1.9 +/- 2.2%



	Mean X	H	Dmax	Imax	Dint	Iint	Dmin	Imin
KD13-1	0.115E-02	2.3%	114.8	-14.7	281.1	-74.9	23.9	-3.4
KD13-2	0.218E-02	3.0%	113.0	-18.8	292.2	-71.2	22.9	-0.2
KD13-3	0.198E-02	5.4%	300.2	-23.0	137.2	-66.1	32.9	-6.3
KD13-4A	0.236E-02	2.4%	11.1	-10.0	141.5	-74.7	279.0	-11.4
KD13-5	0.254E-02	2.7%	32.6	-2.7	125.9	-50.4	300.4	-39.5
KD13-6	0.210E-02	2.9%	249.4	-43.5	121.9	-32.7	11.0	-29.0
KD13-7A	0.261E-02	2.7%	325.0	-43.3	113.6	-42.2	219.0	-16.3
KD13-7B	0.253E-03	2.7%	323.2	-39.8	121.0	-48.0	223.7	-11.2
KD13-8A	0.298E-02	3.4%	325.0	-26.8	118.8	-60.6	229.3	-11.2
KD13-8B	0.322E-02	3.8%	327.9	-33.0	126.5	-55.1	231.3	-10.1
KD13-9	0.264E-02	2.8%	310.0	-65.4	167.8	-19.9	72.7	-13.9
KD13-10	0.237E-02	3.4%	319.7	-25.8	83.0	-48.6	213.6	-29.9

Site Statistics for KD13

Mean X = (2.198 +/- 0.772) x 1E-03

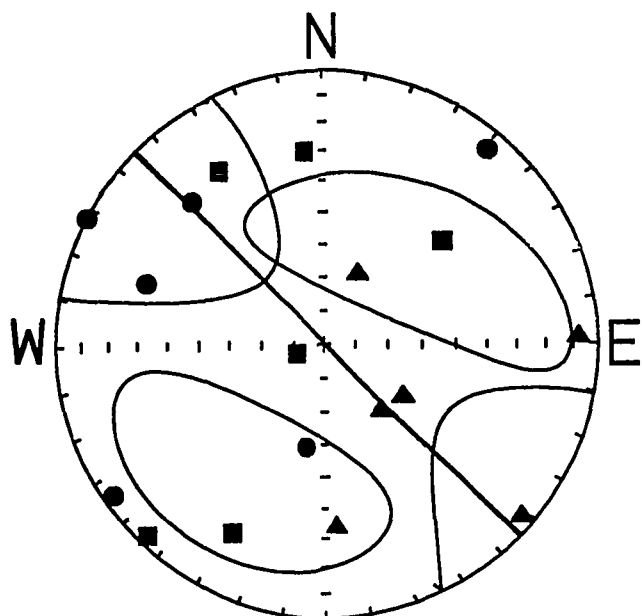
Xmax: Mean D = 314.7      Mean I = -31.3      a95 = 23:16  
 Xint: Mean D = 132.1      Mean I = -58.7      a95 = 24:10  
 Xmin: Mean D = 44.0      Mean I = 1.2      a95 = 19:16

Xmax/Xint = 1.007      Xint/Xmin = 1.011      Xmax/Xmin = 1.018

H = 1.78 +/- 0.57%

E = 1.004      Graham's V = 39.0

F = 1.4 +/- 0.5%      L = 0.7 +/- 0.4%



Kealohi Pt. S                      KD14

	Mean X	H	Dmax	Imax	Dint	Iint	Dmin	Imin
KD14-2	0.574E-02	4.8%	229.6	-41.8	356.2	-33.7	108.7	-29.9
KD14-4	0.661E-02	1.5%	174.0	-29.9	268.5	-7.8	11.6	-58.9
KD14-5	0.645E-02	2.8%	74.4	-80.9	311.2	-5.0	220.6	-7.6
KD14-6	0.651E-02	1.7%	27.9	-23.7	207.8	-66.3	297.9	0.0
KD14-7	0.674E-02	0.8%	44.5	-3.7	302.3	-61.0	136.1	-28.2
KD14-9	0.482E-02	4.3%	147.8	-26.2	317.7	-63.4	55.8	-4.0

Site Statistics for KD14

Mean X = (6.145 +/- 0.675) x 1E-03

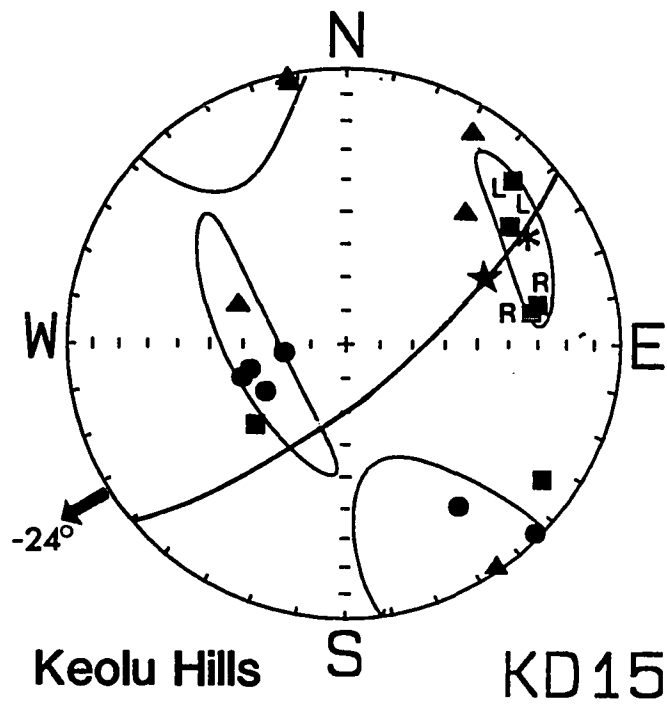
Xmax: Mean D = 47.7      Mean I = 49.4      a95 = 53:21  
 Xint: Mean D = 128.4      Mean I = -7.9      a95 = 56:27  
 Xmin: Mean D = 31.7      Mean I = -39.5      a95 = 43:25

Xmax/Xint = 1.010      Xint/Xmin = 1.010      Xmax/Xmin = 1.020

H = 1.98 +/- 1.07%

E = 1.000                      Graham's V = 45.3

F = 1.5 +/- 1.0%              L = 1.0 +/- 1.0%



	Mean X	H	Dmax	Imax	Dint	Iint	Dmin	Imin
KD15-1	0.205E-02	0.9%	258.6	-28.7	167.8	-1.6	74.9	-61.2
KD15-2	0.217E-02	0.6%	260.4	-31.5	168.1	-3.9	71.8	-58.2
KD15-3	0.232E-02	0.9%	47.7	-54.3	223.0	-35.5	314.5	-2.2
KD15-4	0.240E-02	0.7%	304.2	-13.5	211.4	-11.5	82.2	-72.1
KD15-5	0.202E-02	1.1%	234.6	-27.1	325.5	-1.7	58.8	-62.8
KD15-6	0.237E-02	0.7%	225.9	-15.8	110.3	-56.7	324.7	-28.4

Site Statistics for KD15

Mean X = (2.222 +/- 0.149) x 1E-03

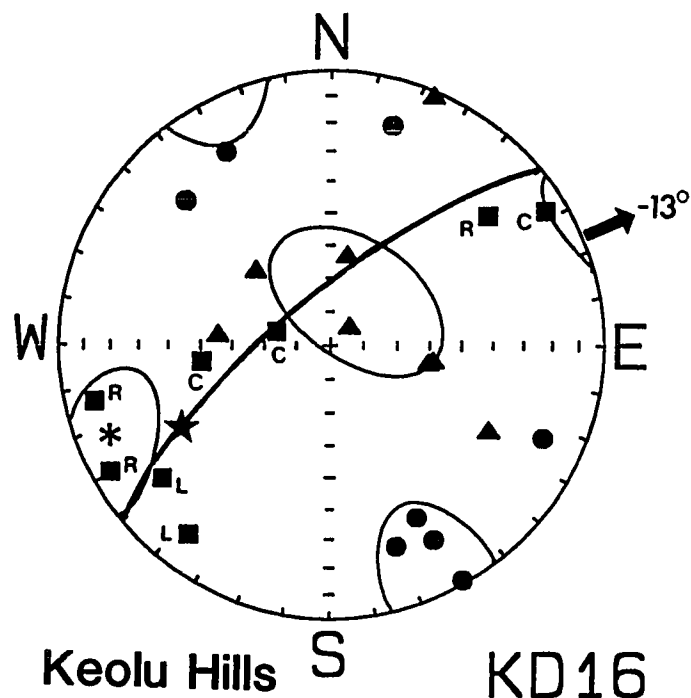
Xmax: Mean D = 58.7      Mean I = 24.5      a95 = 24: 8  
 Xint: Mean D = 153.7      Mean I = 10.8      a95 = 44:20  
 Xmin: Mean D = 85.6      Mean I = -62.9      a95 = 43: 8

Xmax/Xint = 1.004      Xint/Xmin = 1.001      Xmax/Xmin = 1.005

H = 0.50 +/- 0.16%

E = 0.998      Graham's V = 57.6

F = 0.3 +/- 0.2%      L = 0.4 +/- 0.2%



	Mean X	H	Dmax	Imax	Dint	Iint	Dmin	Imin
KD16-1	0.280E-02	1.5%	104.4	-73.4	202.8	-2.5	293.5	-16.4
KD16-2	0.258E-02	4.2%	238.0	-8.4	134.1	-58.3	332.9	-30.3
KD16-3	0.278E-02	4.5%	60.3	-7.5	227.8	-82.3	330.1	-1.6
KD16-4	0.265E-02	6.4%	76.7	-11.7	190.9	-63.2	341.5	-23.8
KD16-5	0.300E-02	0.5%	230.8	-26.4	94.7	-55.4	331.5	-20.6
KD16-6	0.285E-02	2.2%	83.0	-50.1	298.5	-34.1	195.8	-18.0
KD16-7	0.278E-02	1.9%	37.2	-14.5	280.8	-59.9	134.3	-25.8
KD16-8	0.249E-02	2.6%	51.9	-22.5	279.0	-58.6	150.9	-20.6

Site Statistics for KD16

Mean X = (2.741 +/- 0.156) x 1E-03

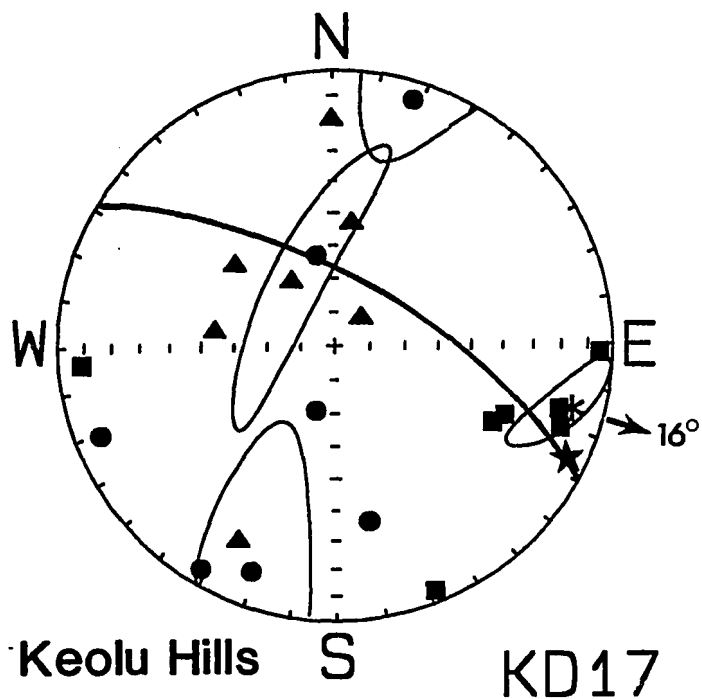
Xmax: Mean D = 66.7      Mean I = -13.0      a95 = 22:13  
 Xint: Mean D = 211.2      Mean I = -74.2      a95 = 29:18  
 Xmin: Mean D = 334.6      Mean I = -8.9      a95 = 27:13

Xmax/Xint = 1.011      Xint/Xmin = 1.012      Xmax/Xmin = 1.023

H = 2.26 +/- 0.74%

E = 1.001      Graham's V = 43.9

F = 1.7 +/- 0.6%      L = 1.1 +/- 0.5%



	Mean X	H	Dmax	Imax	Dint	Iint	Dmin	Imin
KD17-1	0.516E-02	2.7%	292.9	-35.1	97.5	-53.9	197.8	-7.4
KD17-2	0.223E-02	2.1%	271.7	-5.3	179.8	-19.0	16.7	-70.2
KD17-3	0.227E-02	2.6%	86.1	-9.0	188.2	-52.9	349.5	-35.6
KD17-4	0.271E-02	3.8%	286.2	-17.8	146.9	-67.0	20.8	-14.0
KD17-6	0.328E-02	4.3%	290.5	-15.1	26.9	-22.4	169.2	-62.5
KD17-7	0.219E-02	0.6%	338.6	-4.9	223.0	-78.7	69.5	-10.1
KD17-8	0.284E-02	1.8%	296.5	-37.7	129.6	-51.6	31.5	-6.4

Site Statistics for KD17

Mean X = (2.955 +/- 0.972) x 1E-03

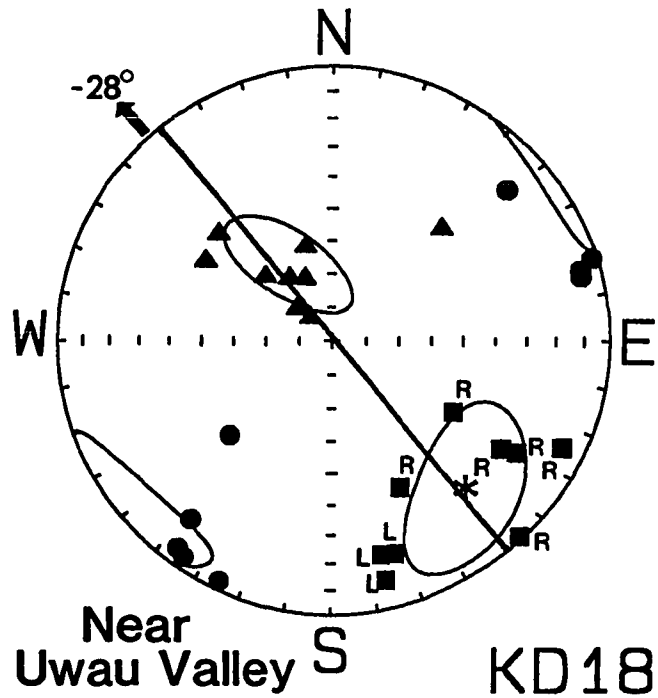
Xmax: Mean D = 285.7      Mean I = -16.2      a95 = 19: 6  
 Xint: Mean D = 152.7      Mean I = -67.0      a95 = 48: 8  
 Xmin: Mean D = 20.4      Mean I = -15.9      a95 = 48:13

Xmax/Xint = 1.017      Xint/Xmin = 1.002      Xmax/Xmin = 1.019

H = 1.94 +/- 0.50%

E = 0.986      Graham's V = 69.7

F = 1.1 +/- 0.4%      L = 1.7 +/- 0.5%



	Mean X	H	Dmax	Imax	Dint	Iint	Dmin	Imin
KD18.01	0.247E-02	2.4%	342.9	-20.2	156.3	-69.7	252.1	-2.2
KD18.02	0.241E-02	2.3%	346.7	-21.2	145.4	-67.4	253.8	-7.5
KD18.03	0.162E-02	1.7%	346.9	-11.7	131.7	-75.8	255.3	-8.0
KD18.06	0.348E-02	5.3%	299.9	-47.0	132.7	-42.2	36.8	-6.4
KD18.07	0.258E-02	2.0%	302.2	-27.4	133.7	-62.2	34.6	-4.8
KD18.08	0.153E-02	1.6%	316.0	-1.5	224.7	-42.2	47.6	-47.8
KD18.09	0.222E-02	2.1%	300.9	-22.3	164.1	-60.7	38.6	-18.1
KD18.10	0.202E-02	1.3%	334.6	-40.8	121.8	-44.2	229.2	-17.1
KD18.11	0.208E-02	1.6%	294.8	-8.9	137.0	-80.4	25.4	-3.6

Site Statistics for KD18

Mean X = (2.268 +/- 0.548) x 1E-03

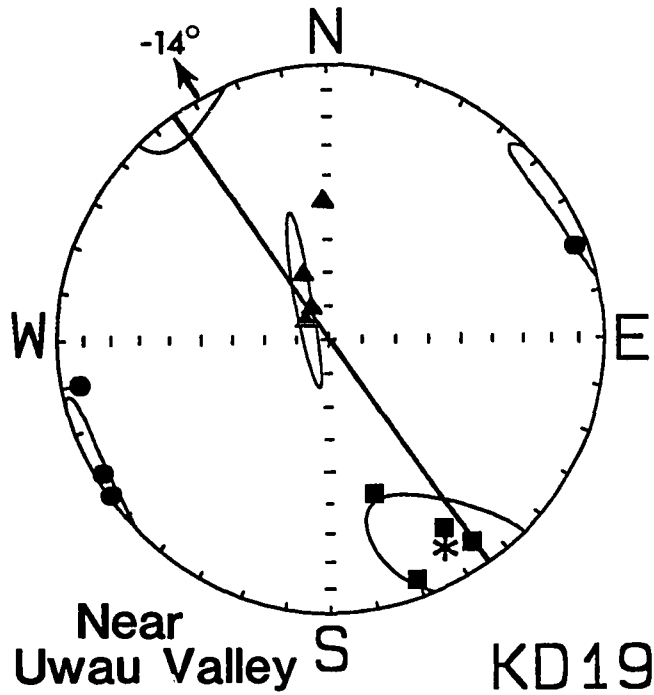
Xmax: Mean D = 317.2      Mean I = -28.3      a95 = 22:13  
 Xint: Mean D = 149.5      Mean I = -61.1      a95 = 18:11  
 Xmin: Mean D = 50.0      Mean I = -5.2      a95 = 20:10

Xmax/Xint = 1.009      Xint/Xmin = 1.009      Xmax/Xmin = 1.018

H = 1.77 +/- 0.35%

E = 0.999      Graham's V = 46.2

F = 1.3 +/- 0.3%      L = 0.9 +/- 0.2%



	Mean X	H	Dmax	Imax	Dint	Iint	Dmin	Imin
KD19.02	0.900E-03	1.4%	325.1	-10.7	151.5	-79.2	55.4	-1.2
KD19.03A	0.868E-03	1.8%	329.0	-20.5	158.6	-69.2	60.2	-3.2
KD19.03B	0.833E-03	0.9%	340.2	-7.6	128.1	-81.0	249.6	-4.7
KD19.05	0.946E-03	0.9%	343.8	-41.0	178.0	-48.1	80.0	-7.1

Site Statistics for KD19

Mean X = (8.868 +/- 0.422) x 1E-04

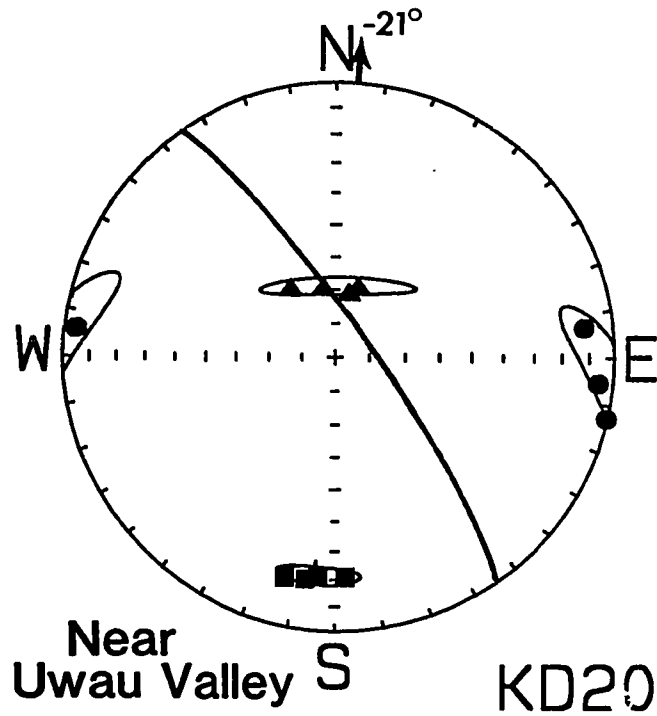
Xmax: Mean D = 331.1      Mean I = -14.2      a95 = 27:13  
 Xint: Mean D = 147.0      Mean I = -75.8      a95 = 27: 3  
 Xmin: Mean D = 60.8      Mean I = 1.0      a95 = 17: 6

Xmax/Xint = 1.005      Xint/Xmin = 1.007      Xmax/Xmin = 1.012

H = 1.16 +/- 0.26%

E = 1.002      Graham's V = 39.3

F = 0.9 +/- 0.2%      L = 0.5 +/- 0.2%



	Mean X	H	Dmax	Imax	Dint	Iint	Dmin	Imin
KD20.01	0.191E-02	3.1%	357.3	-20.9	145.8	-65.8	262.9	-11.5
KD20.02A	0.213E-02	2.5%	7.7	-19.7	169.5	-69.4	275.6	-6.0
KD20.02B	0.210E-02	3.0%	12.9	-19.0	191.7	-71.0	282.8	-0.4
KD20.03	0.202E-02	3.4%	4.4	-20.9	197.8	-68.6	96.1	-4.5

Site Statistics for KD20

Mean X = (2.038 +/- 0.088) x 1E-03

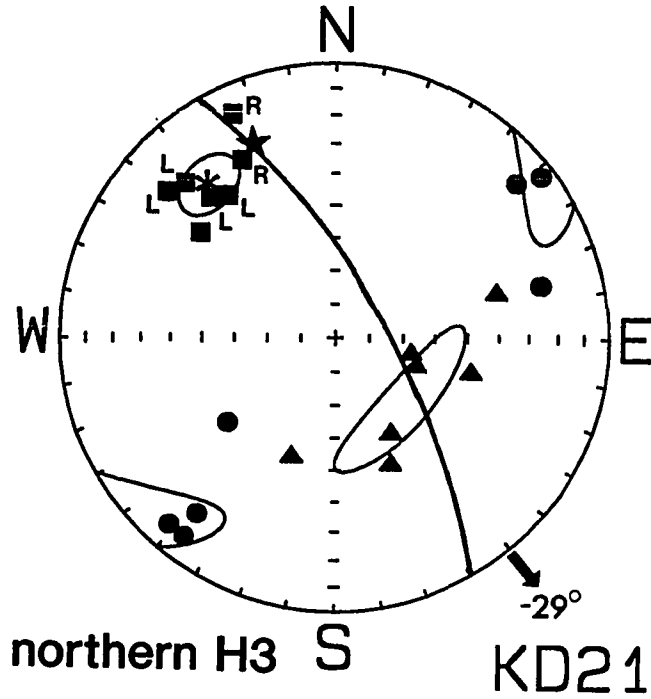
Xmax: Mean D = 4.3      Mean I = -21.2      a95 = 10: 3  
 Xint: Mean D = 179.9      Mean I = -68.8      a95 = 23: 3  
 Xmin: Mean D = 273.7      Mean I = -1.5      a95 = 24: 6

Xmax/Xint = 1.018      Xint/Xmin = 1.012      Xmax/Xmin = 1.030

H = 2.94 +/- 0.23%

E = 0.994      Graham's V = 50.9

F = 2.0 +/- 0.3%      L = 1.8 +/- 0.2%



	Mean X	H	Dmax	Imax	Dint	Iint	Dmin	Imin
KD21.02A	0.477E-02	3.4%	138.4	-32.6	329.9	-56.9	231.8	-5.3
KD21.02B	0.494E-02	3.8%	143.0	-35.7	284.6	-47.5	37.9	-19.9
KD21.03B	0.661E-02	5.6%	135.8	-22.9	289.1	-64.7	41.4	-10.2
KD21.04	0.581E-02	4.6%	130.9	-20.2	281.6	-67.1	37.0	-10.2
KD21.05	0.594E-02	5.6%	152.3	-27.9	19.6	-52.0	255.6	-23.6
KD21.06	0.442E-02	5.4%	128.0	-38.0	336.3	-48.4	229.5	-14.4
KD21.07	0.469E-02	1.8%	155.2	-11.6	254.7	-38.8	51.6	-48.9

Site Statistics for KD21

Mean X = (5.311 +/- 0.757) x 1E-03

Xmax: Mean D = 320.3      Mean I = 28.6      a95 = 9: 8

Xint: Mean D = 133.0      Mean I = 61.2      a95 = 28: 7

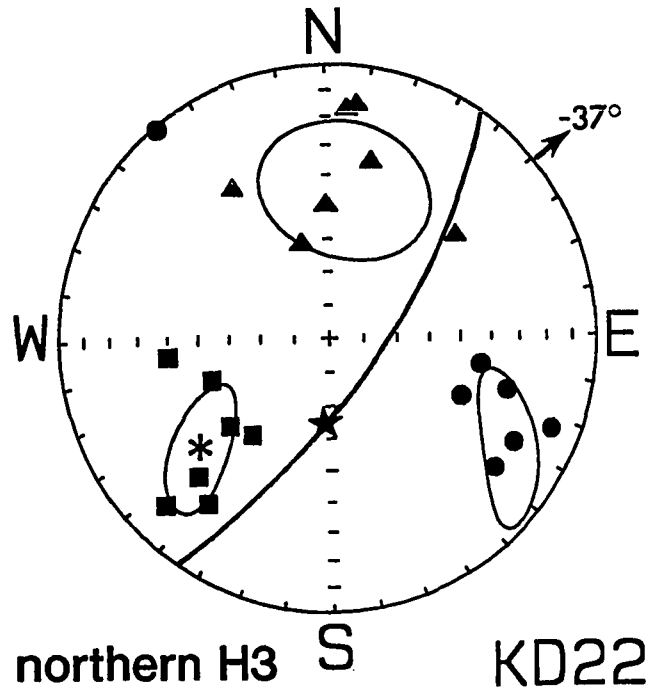
Xmin: Mean D = 48.6      Mean I = -3.1      a95 = 27: 9

Xmax/Xint = 1.032      Xint/Xmin = 1.008      Xmax/Xmin = 1.041

H = 4.02 +/- 0.49%

E = 0.977      Graham's V = 63.6

F = 2.4 +/- 0.4%      L = 3.2 +/- 0.4%



	Mean X	H	Dmax	Imax	Dint	Iint	Dmin	Imin
KD22.01	0.224E-02	0.8%	84.2	-39.8	187.5	-15.5	294.2	-46.1
KD22.02A	0.300E-02	1.9%	45.7	-15.4	165.3	-60.7	308.6	-24.2
KD22.03A	0.328E-02	1.3%	37.3	-26.0	148.0	-35.9	280.3	-42.9
KD22.03B	0.321E-02	1.2%	44.6	-30.9	179.5	-49.7	299.8	-23.2
KD22.04B	0.212E-02	1.8%	71.2	-52.3	185.2	-17.4	286.6	-32.2
KD22.05A	0.173E-02	2.0%	49.3	-49.8	232.1	-40.1	140.9	-1.4
KD22.05B	0.232E-02	0.8%	39.0	-53.0	194.2	-34.4	292.6	-12.1

Site Statistics for KD22

Mean X = (2.559 +/- 0.559) x 1E-03

Xmax: Mean D = 50.6      Mean I = -37.3      a95 = 22: 8

Xint: Mean D = 187.7      Mean I = -43.9      a95 = 24:22

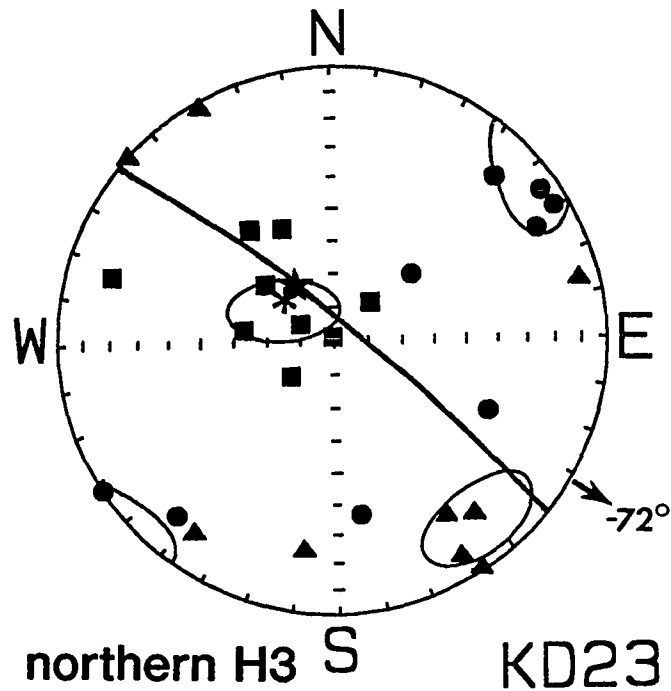
Xmin: Mean D = 301.7      Mean I = -23.0      a95 = 24: 8

Xmax/Xint = 1.005      Xint/Xmin = 1.007      Xmax/Xmin = 1.012

H = 1.20 +/- 0.19%

E = 1.002      Graham's V = 40.9

F = 0.9 +/- 0.2%      L = 0.5 +/- 0.2%



	Mean X	H	Dmax	Imax	Dint	Iint	Dmin	Imin
KD23.01	0.173E-02	1.5%	107.2	-17.5	9.2	-23.8	229.9	-59.8
KD23.02A	0.283E-02	1.2%	143.7	-47.9	37.0	-14.6	295.1	-38.4
KD23.02B	0.301E-02	1.1%	155.9	-52.8	256.6	-8.0	352.5	-36.0
KD23.03	0.408E-02	6.5%	117.1	-78.8	330.4	-9.4	239.4	-6.0
KD23.04	0.375E-02	2.4%	51.9	-73.4	151.0	-2.7	241.8	-16.3
KD23.05	0.484E-02	8.1%	97.6	-62.9	322.0	-20.1	225.4	-17.4
KD23.07	0.417E-02	5.5%	223.9	-74.5	132.9	-0.3	42.9	-15.5
KD23.08	0.422E-02	6.3%	161.7	-88.7	328.0	-1.3	58.0	-0.3
KD23.09	0.364E-02	3.6%	130.2	-63.5	328.3	-25.3	234.9	-7.2

Site Statistics for KD23

Mean X = (3.586 +/- 0.882) x 1E-03

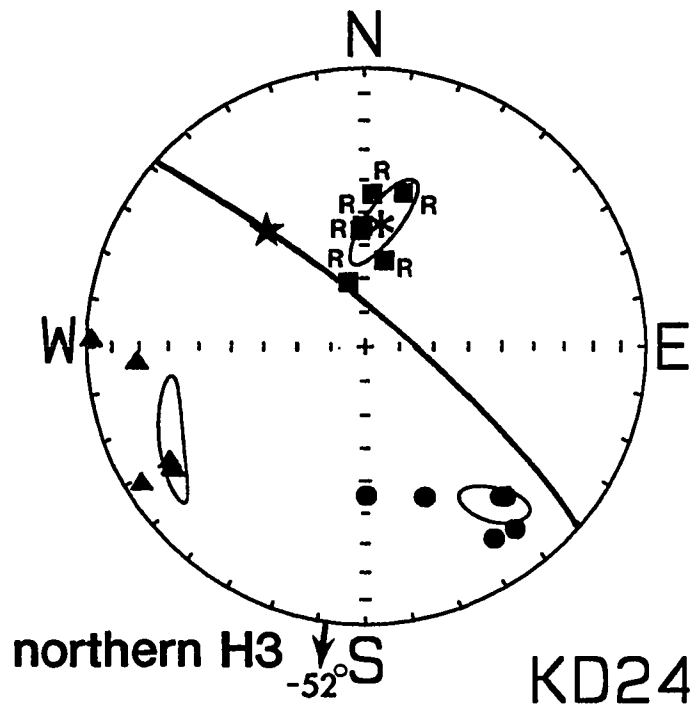
Xmax: Mean D = 302.2      Mean I = 72.4      a95 = 17: 9  
 Xint: Mean D = 142.4      Mean I = 16.5      a95 = 15:12  
 Xmin: Mean D = 50.7      Mean I = 5.7      a95 = 18:11

Xmax/Xint = 1.022      Xint/Xmin = 1.012      Xmax/Xmin = 1.034

H = 3.39 +/- 0.87%

E = 0.989      Graham's V = 54.5

F = 2.3 +/- 0.7%      L = 2.2 +/- 0.7%



	Mean X	H	Dmax	Imax	Dint	Iint	Dmin	Imin
KD24.01	0.520E-02	3.9%	179.1	-54.3	59.5	-19.5	318.4	-28.6
KD24.02	0.618E-02	3.5%	192.8	-64.1	57.1	-19.1	321.1	-16.7
KD24.03	0.615E-02	4.1%	166.4	-70.6	58.5	-6.2	326.5	-18.3
KD24.04	0.624E-02	5.5%	177.9	-55.6	57.7	-19.0	317.4	-27.5
KD24.06	0.593E-02	6.3%	194.3	-42.5	86.0	-18.9	338.4	-41.5
KD24.07	0.498E-02	2.4%	183.0	-44.4	91.3	-1.7	359.6	-45.5

Site Statistics for KD24

Mean X = (5.779 +/- 0.514) x 1E-03

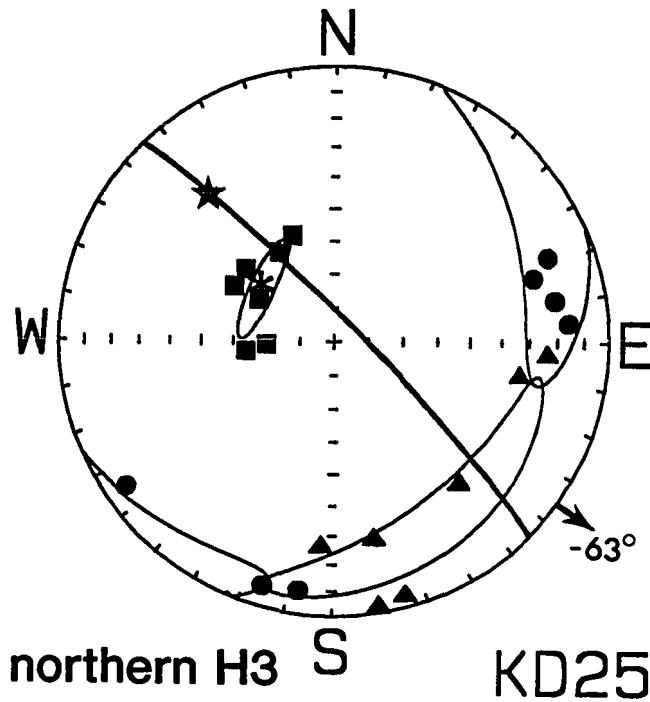
Xmax: Mean D = 8.5      Mean I = 52.3      a95 = 16: 5  
 Xint: Mean D = 244.3      Mean I = 23.5      a95 = 17: 4  
 Xmin: Mean D = 321.2      Mean I = -27.6      a95 = 11: 5

Xmax/Xint = 1.022      Xint/Xmin = 1.019      Xmax/Xmin = 1.041

H = 4.07 +/- 0.63%

E = 0.997      Graham's V = 47.1

F = 3.0 +/- 0.6%      L = 2.2 +/- 0.5%



	Mean X	H	Dmax	Imax	Dint	Iint	Dmin	Imin
KD25.02	0.581E-02	3.5%	158.2	-55.9	319.0	-32.6	54.8	-8.9
KD25.03	0.575E-02	3.4%	118.6	-55.9	280.5	-32.8	16.0	-8.4
KD25.04	0.447E-02	2.6%	118.6	-64.3	273.5	-23.5	7.7	-9.7
KD25.05	0.402E-02	1.7%	128.7	-55.9	348.3	-27.6	248.2	-18.4
KD25.06	0.535E-02	2.3%	147.6	-58.8	3.2	-26.2	265.3	-15.7
KD25.07	0.506E-02	2.1%	87.2	-69.9	350.1	-2.6	259.2	-19.9
KD25.08	0.509E-02	2.5%	83.7	-63.7	344.2	-4.7	252.0	-25.8

Site Statistics for KD25

Mean X = (5.080 +/- 0.606) x 1E-03

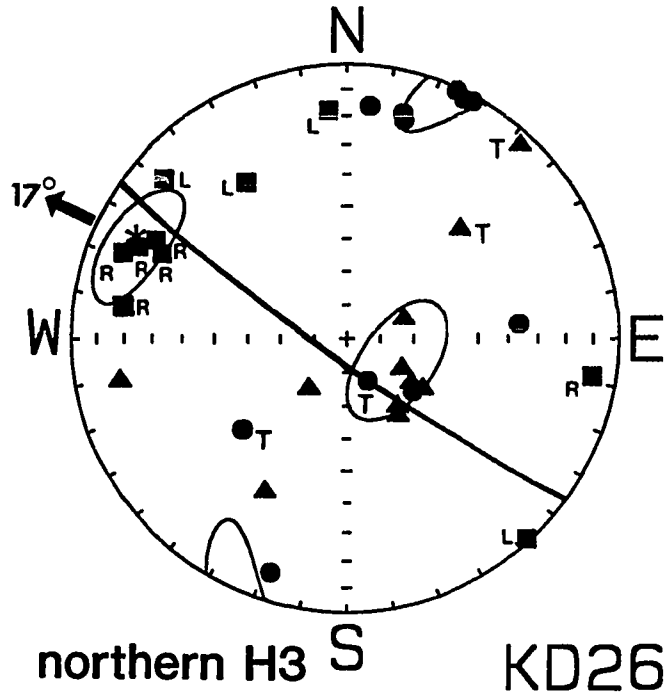
Xmax: Mean D = 306.2      Mean I = 63.2      a95 = 16: 4  
 Xint: Mean D = 150.8      Mean I = 24.6      a95 = 46: 9  
 Xmin: Mean D = 56.3      Mean I = 9.8      a95 = 46:13

Xmax/Xint = 1.015      Xint/Xmin = 1.007      Xmax/Xmin = 1.021

H = 2.13 +/- 0.24%

E = 0.992      Graham's V = 56.5

F = 1.4 +/- 0.2%      L = 1.5 +/- 0.3%



	Mean X	H	Dmax	Imax	Dint	Iint	Dmin	Imin
KD26.1	0.273E-02	5.5%	98.1	-19.3	325.8	-62.5	194.9	-18.8
KD26.2	0.209E-02	6.8%	113.8	-18.6	298.0	-71.4	204.2	-1.3
KD26.3A	0.303E-02	4.9%	117.3	-23.1	303.8	-66.8	208.3	-2.4
KD26.3B	0.301E-02	4.9%	114.8	-27.0	303.0	-62.8	206.5	-3.3
KD26.4	0.618E-02	8.1%	278.5	-9.3	37.7	-71.3	185.8	-16.0
KD26.6	0.485E-02	5.1%	111.1	-13.8	250.2	-72.0	18.3	-11.3
KD26.8A	0.390E-02	3.8%	175.3	-17.8	79.6	-17.2	308.4	-64.8
KD26.8B	0.373E-02	4.2%	131.2	-12.9	222.4	-5.1	333.4	-76.1
KD26.9	0.590E-02	4.4%	317.6	-1.4	226.4	-41.8	49.2	-48.2
KD26.10	0.410E-02	4.1%	147.1	-32.6	28.5	-36.9	265.1	-36.3

Site Statistics for KD26

Mean X = (3.841 +/- 1.273) x 1E-03

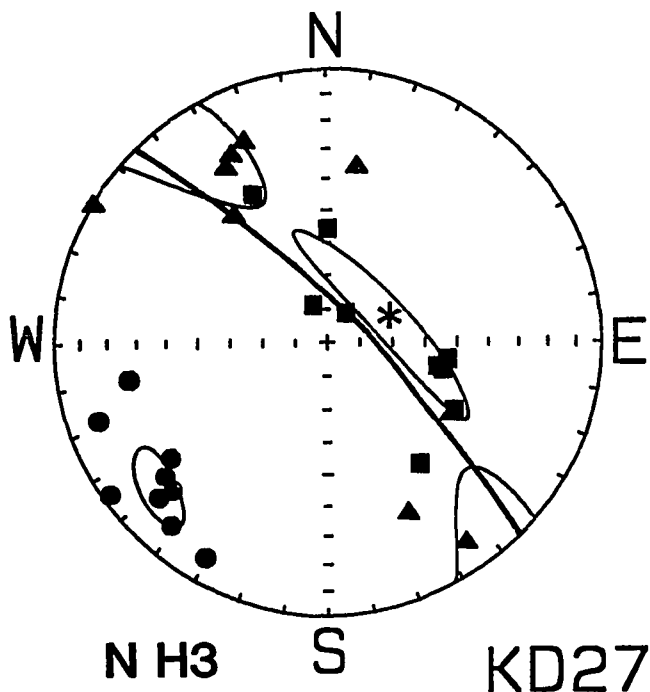
Xmax: Mean D = 294.2      Mean I = 16.8      a95 = 16:10  
 Xint: Mean D = 113.5      Mean I = 73.2      a95 = 20:11  
 Xmin: Mean D = 24.2      Mean I = -0.2      a95 = 24: 6

Xmax/Xint = 1.030      Xint/Xmin = 1.008      Xmax/Xmin = 1.038

H = 3.72 +/- 0.70%

E = 0.979      Graham's V = 63.0

F = 2.2 +/- 0.7%      L = 2.9 +/- 0.5%



	Mean X	H	Dmax	Imax	Dint	Iint	Dmin	Imin
KD27.1	0.213E-02	14.6%	282.1	-55.2	152.5	-23.9	51.3	-23.7
KD27.2	0.195E-02	12.3%	277.9	-52.7	157.0	-21.4	54.4	-29.0
KD27.3A	0.164E-02	5.5%	297.8	-45.6	143.0	-41.6	41.3	-12.9
KD27.3B	0.191E-02	10.8%	213.5	-79.6	120.6	-0.5	30.5	-10.4
KD27.5	0.178E-02	6.2%	283.0	-53.5	149.4	-27.0	47.2	-22.5
KD27.6	0.155E-02	2.1%	322.0	-43.2	190.3	-35.3	79.8	-26.4
KD27.7	0.186E-02	12.5%	152.7	-39.2	299.9	-45.8	48.2	-17.0
KD27.8	0.173E-02	4.9%	159.7	-78.0	325.0	-11.6	55.6	-3.0
KD27.9	0.210E-02	11.0%	180.4	-55.9	334.1	-31.3	71.7	-12.2

Site Statistics for KD27

Mean X = (1.852 +/- 0.203) x 1E-03

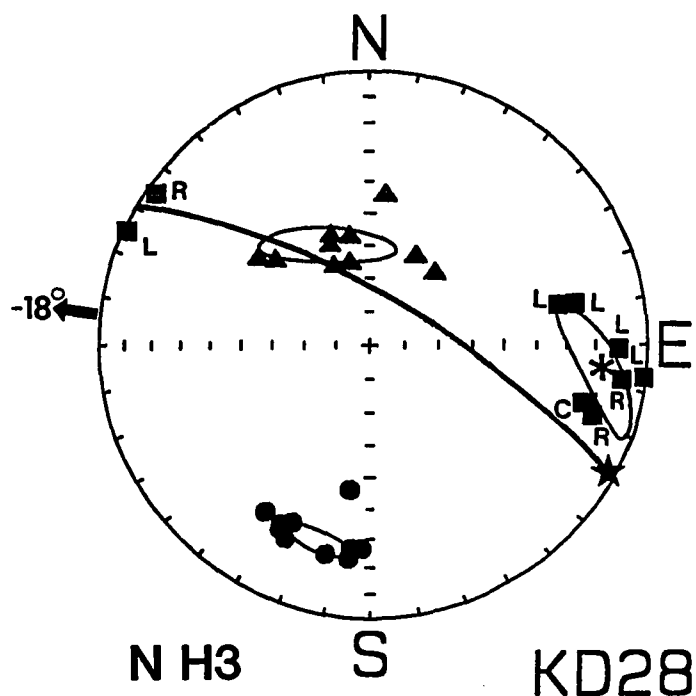
Xmax: Mean D = 69.4      Mean I = 70.0      a95 = 39: 6  
 Xint: Mean D = 142.4      Mean I = -6.1      a95 = 39:10  
 Xmin: Mean D = 50.3      Mean I = -19.0      a95 = 11: 6

Xmax/Xint = 1.016      Xint/Xmin = 1.064      Xmax/Xmin = 1.081

H = 7.61 +/- 1.20%

E = 1.047      Graham's V = 27.5

F = 6.9 +/- 1.2%      L = 1.6 +/- 0.9%



	Mean X	H	Dmax	Imax	Dint	Iint	Dmin	Imin
KD28.1	0.786E-02	4.9%	285.0	-20.5	158.5	-57.8	24.4	-23.7
KD28.2	0.776E-02	11.3%	270.9	-11.6	155.8	-64.2	5.8	-22.8
KD28.3A	0.700E-02	10.3%	258.5	-25.8	131.1	-51.5	2.4	-26.5
KD28.3B	0.674E-02	10.4%	257.9	-31.5	127.1	-46.9	5.4	-26.2
KD28.4	0.735E-02	3.4%	276.9	-1.0	186.0	-44.3	7.9	-45.7
KD28.5	0.902E-02	7.6%	114.8	-1.2	207.0	-60.3	24.2	-29.7
KD28.6	0.811E-02	8.1%	278.1	-9.8	166.6	-64.8	12.3	-23.0
KD28.7A	0.699E-02	6.3%	285.5	-22.0	160.3	-55.1	26.7	-25.7
KD28.7B	0.677E-02	6.2%	288.0	-17.2	169.6	-56.9	27.2	-27.3
KD28.8	0.632E-02	5.2%	124.8	-3.7	221.5	-61.3	32.8	-28.5

Site Statistics for KD28

Mean X = (7.393 +/- 0.801) x 1E-03

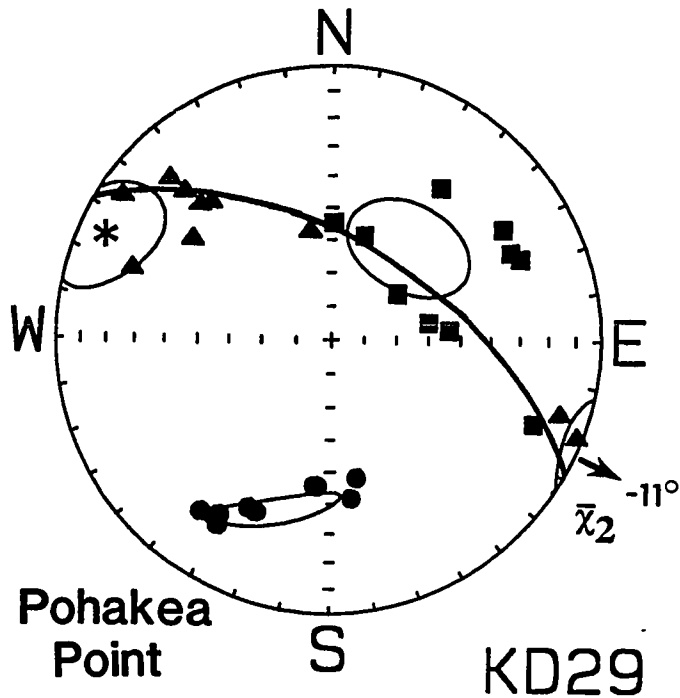
Xmax: Mean D = 275.9      Mean I = -17.8      a95 = 21: 6  
 Xint: Mean D = 156.3      Mean I = -57.0      a95 = 20: 5  
 Xmin: Mean D = 15.2      Mean I = -26.8      a95 = 9: 4

Xmax/Xint = 1.022      Xint/Xmin = 1.047      Xmax/Xmin = 1.071

H = 6.74 +/- 0.82%

E = 1.024      Graham's V = 35.2

F = 5.7 +/- 0.8%      L = 2.3 +/- 0.6%



	Mean X	H	Dmax	Imax	Dint	Iint	Dmin	Imin
KD29.1	0.337E-02	2.8%	291.8	-19.5	169.1	-56.8	31.7	-25.7
KD29.2	0.439E-02	7.1%	260.3	-59.5	134.8	-18.9	36.5	-23.0
KD29.3A	0.348E-02	8.4%	180.8	-54.8	287.6	-11.5	25.1	-32.7
KD29.3B	0.486E-02	10.0%	197.7	-57.4	291.1	-2.2	22.5	-32.5
KD29.4	0.445E-02	1.2%	265.4	-53.4	135.2	-25.7	32.7	-24.2
KD29.5	0.564E-02	8.0%	235.8	-65.6	124.6	-9.3	30.7	-22.3
KD29.6	0.476E-02	7.6%	216.4	-31.9	109.6	-25.0	349.1	-47.4
KD29.7	0.398E-02	3.6%	237.8	-25.4	125.9	-38.2	352.3	-41.3
KD29.8	0.474E-02	4.2%	247.2	-24.7	138.9	-34.3	5.1	-45.4
KD29.10	0.542E-02	3.4%	244.6	-26.8	135.9	-32.4	5.7	-45.6

Site Statistics for KD29

Mean X = (4.507 +/- 0.717) x 1E-03

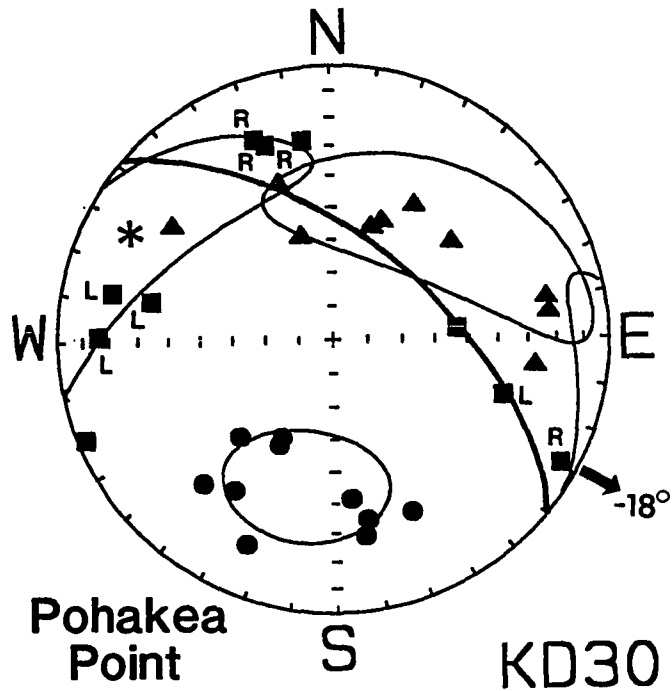
Xmax: Mean D = 40.3      Mean I = 53.2      a95 = 19:14  
 Xint: Mean D = 114.9      Mean I = -11.2      a95 = 19:13  
 Xmin: Mean D = 17.1      Mean I = -34.5      a95 = 18: 4

Xmax/Xint = 1.024      Xint/Xmin = 1.023      Xmax/Xmin = 1.048

H = 4.64 +/- 0.84%

E = 0.999      Graham's V = 45.7

F = 3.5 +/- 0.7%      L = 2.4 +/- 0.6%



	Mean X	H	Dmax	Imax	Dint	Iint	Dmin	Imin
KD30.1	0.579E-02	5.4%	288.6	-35.6	161.7	-40.0	42.9	-29.9
KD30.2	0.660E-02	5.6%	91.2	-15.9	202.5	-51.8	350.3	-33.7
KD30.3	0.686E-02	5.7%	102.4	-33.2	230.9	-43.6	351.8	-28.4
KD30.4	0.716E-02	5.9%	102.5	-19.5	211.4	-42.5	354.4	-41.1
KD30.5	0.540E-02	5.0%	299.2	-7.1	199.1	-54.5	34.1	-34.5
KD30.6	0.511E-02	6.7%	161.6	-26.2	263.1	-22.1	27.9	-54.5
KD30.7	0.393E-02	4.9%	172.1	-27.7	277.8	-27.2	44.5	-49.3
KD30.8	0.731E-02	6.4%	68.5	-3.2	163.6	-57.8	336.6	-32.0
KD30.9	0.517E-02	6.0%	159.3	-23.1	259.3	-22.3	28.4	-56.9
KD30.10	0.483E-02	4.6%	265.0	-53.0	125.8	-29.7	23.8	-20.0

Site Statistics for KD30

Mean X = (5.817 +/- 1.075) x 1E-03

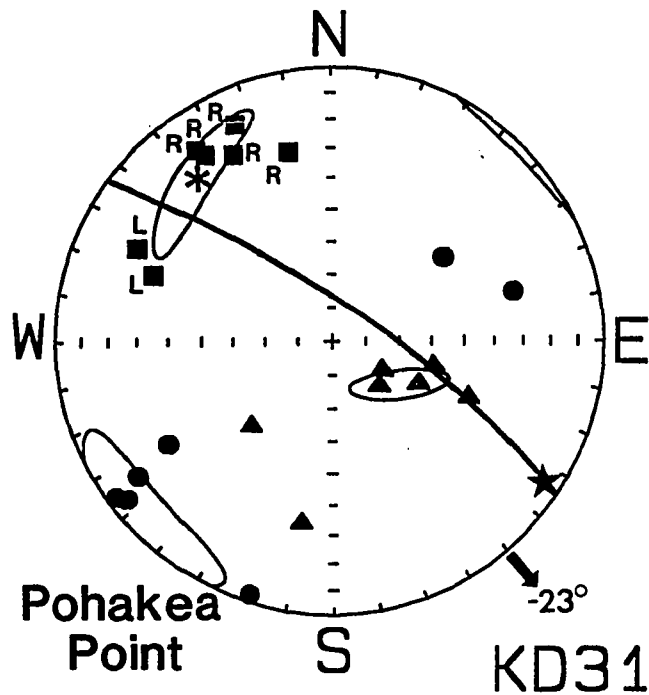
Xmax: Mean D = 299.4      Mean I = 17.5      a95 = 52:17  
 Xint: Mean D = 225.2      Mean I = -40.9      a95 = 51:19  
 Xmin: Mean D = 11.7      Mean I = -43.9      a95 = 23:18

Xmax/Xint = 1.007      Xint/Xmin = 1.028      Xmax/Xmin = 1.035

H = 3.44 +/- 0.38%

E = 1.021      Graham's V = 27.0

F = 3.1 +/- 0.3%      L = 0.7 +/- 0.4%



	Mean X	H	Dmax	Imax	Dint	Iint	Dmin	Imin
KD31.1	0.336E-02	2.6%	115.7	-22.9	9.6	-33.3	233.3	-47.8
KD31.2	0.496E-02	8.8%	110.5	-31.3	283.5	-58.6	18.6	-3.1
KD31.3	0.441E-02	7.2%	152.2	-24.1	296.1	-61.0	55.3	-15.1
KD31.4	0.413E-02	4.6%	156.0	-14.6	44.2	-54.8	255.1	-31.2
KD31.5	0.273E-02	1.8%	167.5	-29.7	292.4	-45.1	58.1	-30.2
KD31.6	0.378E-02	7.1%	144.4	-15.7	300.1	-72.9	52.5	-6.7
KD31.7	0.404E-02	7.1%	145.6	-18.9	313.7	-70.8	54.3	-3.7

Site Statistics for KD31

Mean X = (3.915 +/- 0.679) x 1E-03

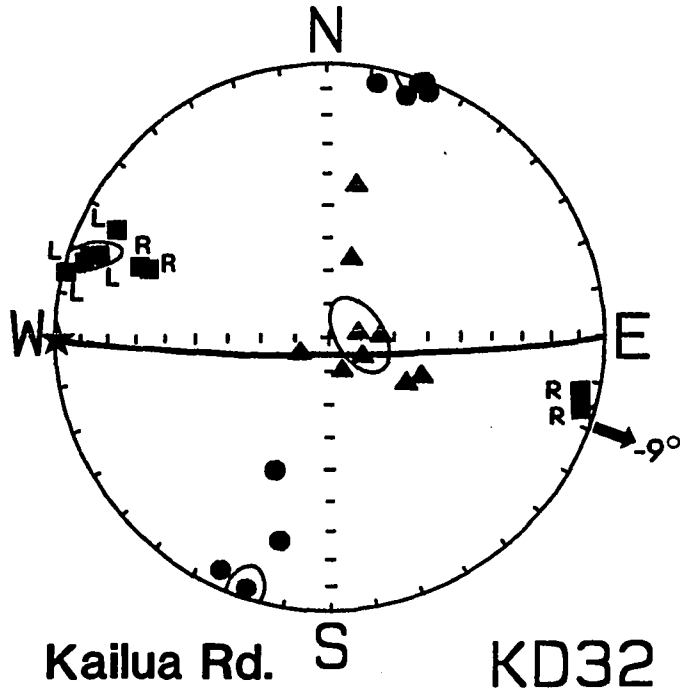
Xmax: Mean D = 320.0      Mean I = 23.1      a95 = 23: 6  
 Xint: Mean D = 123.0      Mean I = 65.9      a95 = 15: 4  
 Xmin: Mean D = 47.3      Mean I = -6.3      a95 = 23:10

Xmax/Xint = 1.026      Xint/Xmin = 1.020      Xmax/Xmin = 1.047

H = 4.57 +/- 0.99%

E = 0.994      Graham's V = 48.9

F = 3.3 +/- 0.9%      L = 2.6 +/- 0.7%



	Mean X	H	Dmax	Imax	Dint	Iint	Dmin	Imin
KD32.1A	0.451E-02	3.8%	111.1	-30.3	292.8	-59.6	201.5	-0.7
KD32.1B	0.432E-02	5.6%	110.8	-26.9	300.3	-62.7	202.8	-3.9
KD32.2	0.467E-02	5.7%	109.2	-8.2	262.2	-80.8	18.6	-4.1
KD32.3	0.400E-02	5.5%	282.4	-7.4	62.5	-80.4	191.6	-6.1
KD32.7A	0.467E-02	4.6%	286.4	-5.4	191.4	-42.8	22.2	-46.7
KD32.7B	0.470E-02	5.0%	104.4	-1.2	197.1	-65.3	13.9	-24.7
KD32.8	0.461E-02	5.1%	107.6	-6.9	337.2	-79.5	198.6	-7.9
KD32.10	0.418E-02	6.4%	117.1	-14.1	268.7	-74.1	25.2	-7.3
KD32.11	0.440E-02	6.1%	110.1	-11.7	298.5	-78.1	200.4	-1.7

Site Statistics for KD32

Mean X = (4.452 +/- 0.253) x 1E-03

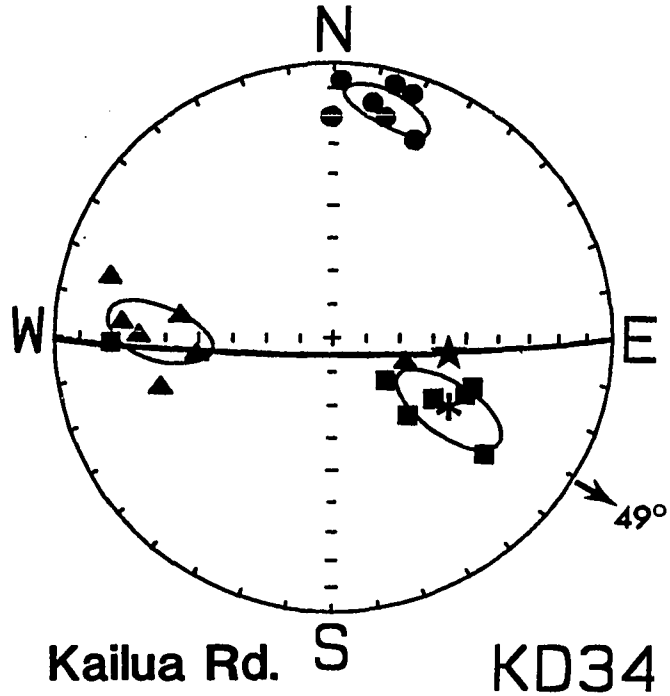
Xmax: Mean D = 289.2      Mean I = 8.8      a95 = 11: 3  
 Xint: Mean D = 266.1      Mean I = -80.5      a95 = 12: 7  
 Xmin: Mean D = 18.6      Mean I = -3.7      a95 = 10: 4

Xmax/Xint = 1.033      Xint/Xmin = 1.018      Xmax/Xmin = 1.051

H = 5.03 +/- 0.39%

E = 0.985      Graham's V = 54.2

F = 3.4 +/- 0.4%      L = 3.3 +/- 0.4%



	Mean X	H	Dmax	Imax	Dint	Iint	Dmin	Imin
KD34.1	0.385E-02	13.2%	307.5	-31.6	82.8	-49.1	202.2	-23.1
KD34.2	0.410E-02	11.0%	301.0	-54.8	90.5	-31.3	189.5	-14.5
KD34.4	0.472E-02	4.1%	293.0	-46.8	73.5	-36.0	179.4	-20.7
KD34.6	0.448E-02	5.2%	289.5	-45.4	98.1	-44.0	193.6	-5.8
KD34.7A	0.439E-02	6.4%	308.4	-69.8	105.3	-18.7	197.9	-7.4
KD34.7B	0.426E-02	6.0%	315.5	-57.7	94.0	-25.3	193.2	-18.7
KD34.9	0.375E-02	5.3%	88.8	-21.7	288.5	-67.1	181.6	-7.0

Site Statistics for KD34

Mean X = (4.222 +/- 0.348) x 1E-03

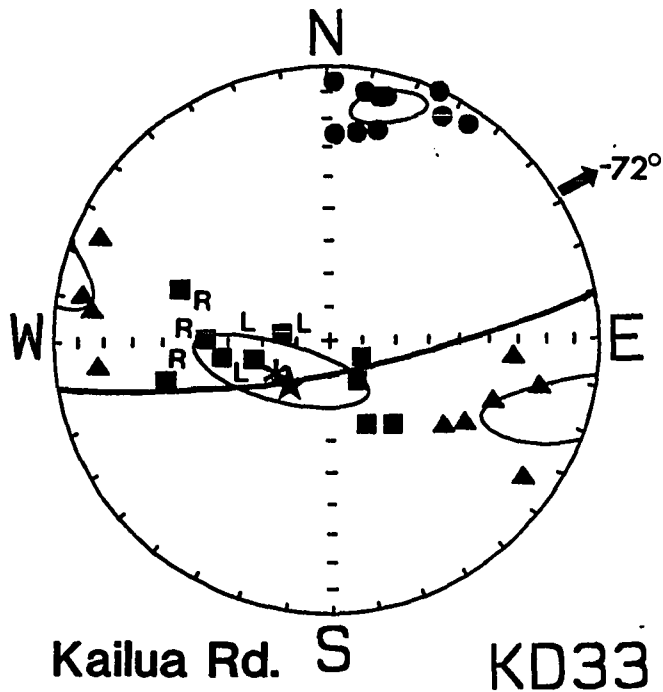
Xmax: Mean D = 301.4      Mean I = -48.7      a95 = 19: 7  
 Xint: Mean D = 91.4      Mean I = -37.3      a95 = 17: 7  
 Xmin: Mean D = 13.4      Mean I = 15.2      a95 = 12: 6

Xmax/Xint = 1.032      Xint/Xmin = 1.035      Xmax/Xmin = 1.068

H = 6.61 +/- 1.17%

E = 1.003      Graham's V = 44.2

F = 5.0 +/- 1.0%      L = 3.2 +/- 0.8%



	Mean X	H	Dmax	Imax	Dint	Iint	Dmin	Imin
KD33.1	0.226E-02	4.5%	91.1	-53.1	290.7	-35.3	193.9	-9.5
KD33.2	0.269E-02	5.6%	109.6	-42.3	307.2	-46.3	207.8	-8.9
KD33.3	0.231E-02	5.6%	76.6	-39.2	301.6	-40.9	188.3	-24.5
KD33.4	0.284E-02	6.3%	325.7	-75.4	100.6	-10.4	192.5	-10.1
KD33.5A	0.231E-02	4.3%	76.9	-66.8	282.7	-21.1	189.1	-9.2
KD33.5B	0.226E-02	4.0%	81.8	-57.6	275.4	-31.7	181.6	-6.1
KD33.6	0.344E-02	5.2%	323.3	-58.5	83.5	-17.1	182.0	-25.6
KD33.7	0.323E-02	4.9%	336.7	-62.7	97.5	-14.8	193.7	-22.4
KD33.8	0.239E-02	2.9%	99.0	-75.6	305.4	-13.0	214.0	-6.2
KD33.9	0.273E-02	5.2%	297.9	-79.3	114.7	-10.7	204.8	-0.6

Site Statistics for KD33

Mean X = (2.647 +/- 0.405) x 1E-03

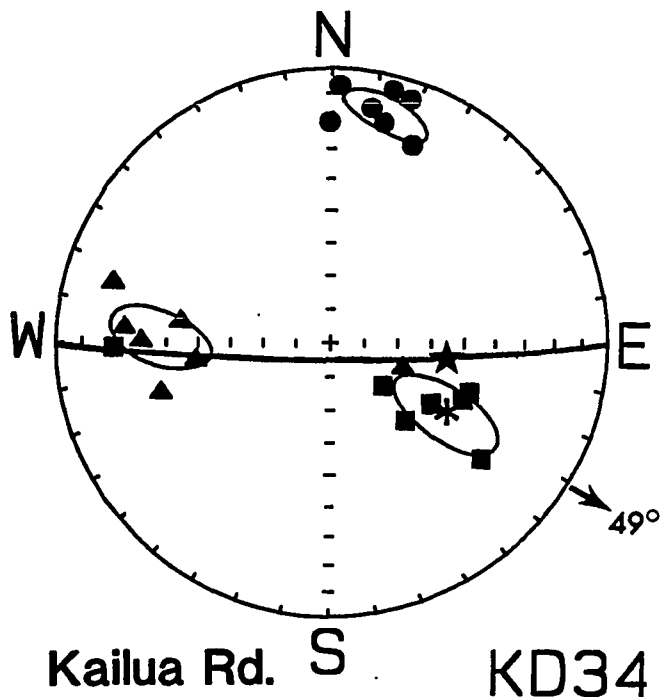
Xmax: Mean D = 57.7      Mean I = -72.5      a95 = 27: 9  
 Xint: Mean D = 107.6      Mean I = 11.5      a95 = 27: 8  
 Xmin: Mean D = 14.9      Mean I = 13.0      a95 = 10: 5

Xmax/Xint = 1.015      Xint/Xmin = 1.028      Xmax/Xmin = 1.043

H = 4.19 +/- 0.35%

E = 1.013      Graham's V = 36.5

F = 3.5 +/- 0.4%      L = 1.5 +/- 0.3%



	Mean X	H	Dmax	Imax	Dint	Iint	Dmin	Imin
KD34.1	0.385E-02	13.2%	307.5	-31.6	82.8	-49.1	202.2	-23.1
KD34.2	0.410E-02	11.0%	301.0	-54.8	90.5	-31.3	189.5	-14.5
KD34.4	0.472E-02	4.1%	293.0	-46.8	73.5	-36.0	179.4	-20.7
KD34.6	0.448E-02	5.2%	289.5	-45.4	98.1	-44.0	193.6	-5.8
KD34.7A	0.439E-02	6.4%	308.4	-69.8	105.3	-18.7	197.9	-7.4
KD34.7B	0.426E-02	6.0%	315.5	-57.7	94.0	-25.3	193.2	-18.7
KD34.9	0.375E-02	5.3%	88.8	-21.7	288.5	-67.1	181.6	-7.0

Site Statistics for KD34

Mean X = (4.222 +/- 0.348) x 1E-03

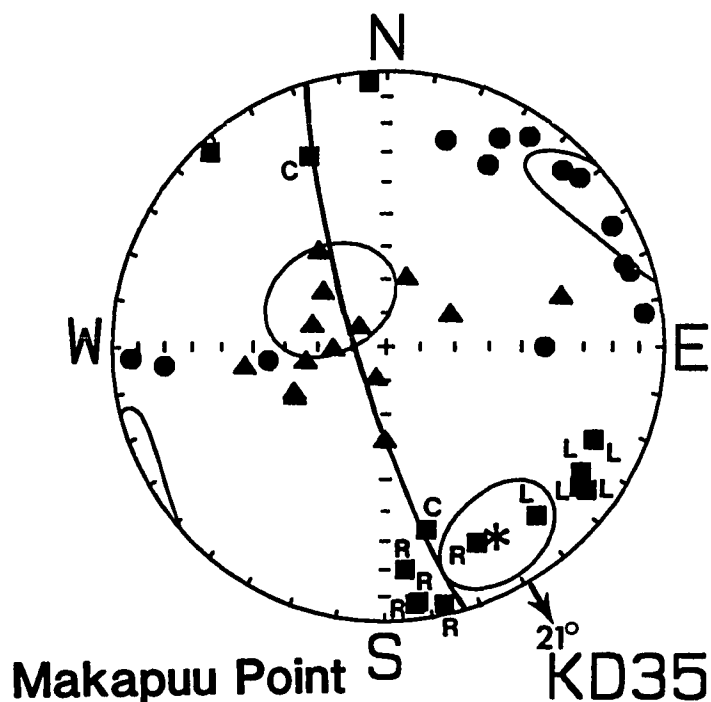
Xmax: Mean D = 301.4      Mean I = -48.7      a95 = 19: 7  
 Xint: Mean D = 91.4      Mean I = -37.3      a95 = 17: 7  
 Xmin: Mean D = 13.4      Mean I = 15.2      a95 = 12: 6

Xmax/Xint = 1.032      Xint/Xmin = 1.035      Xmax/Xmin = 1.068

H = 6.61 +/- 1.17%

E = 1.003      Graham's V = 44.2

F = 5.0 +/- 1.0%      L = 3.2 +/- 0.8%



	Mean X	H	Dmax	Imax	Dint	Iint	Dmin	Imin
KD35.1	0.140E-02	3.0%	176.2	-4.2	81.6	-46.9	270.1	-42.8
KD35.2	0.138E-02	4.6%	306.2	-14.8	62.9	-59.6	208.8	-25.9
KD35.4	0.128E-02	4.9%	347.1	-4.4	254.1	-35.1	83.3	-54.6
KD35.6	0.145E-02	3.8%	158.1	-26.4	0.4	-61.8	252.7	-9.2
KD35.7	0.138E-02	4.0%	305.9	-12.1	87.2	-74.6	213.9	-9.3
KD35.8	0.140E-02	2.9%	353.3	-6.5	125.5	-80.4	262.5	-7.0
KD35.9	0.877E-03	5.4%	137.6	-5.2	16.6	-80.1	228.4	-8.5
KD35.10	0.870E-03	5.7%	318.6	-19.2	105.9	-67.5	224.6	-11.2
KD35.11	0.964E-03	4.2%	352.5	-7.1	243.7	-69.0	85.1	-19.7
KD35.12	0.110E-02	4.4%	354.9	-19.7	196.5	-68.9	87.5	-7.2
KD35.13	0.984E-03	4.7%	347.5	-32.4	145.0	-55.5	250.7	-10.5
KD35.14	0.916E-03	4.2%	335.4	-22.4	131.4	-65.7	241.6	-8.9
KD35.3	0.161E-02	4.6%	303.1	-17.7	79.0	-66.0	208.0	-15.6
KD35.5	0.135E-02	3.2%	294.5	-19.3	60.3	-59.1	195.8	-23.2

Site Statistics for KD35

Mean X = (1.212 +/- 0.242) x 1E-03

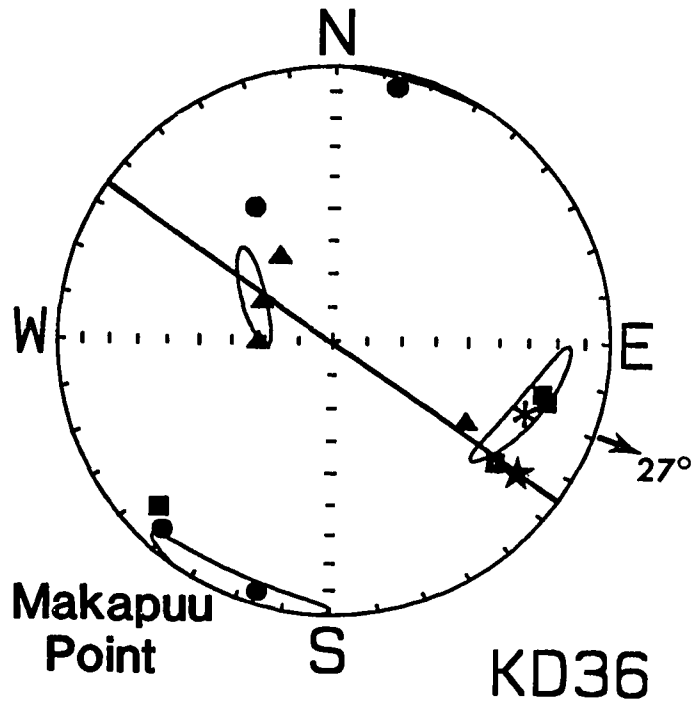
Xmax: Mean D = 329.5      Mean I = -20.7      a95 = 17:15  
 Xint: Mean D = 130.1      Mean I = -68.2      a95 = 20:16  
 Xmin: Mean D = 57.0      Mean I = 6.6      a95 = 23:10

Xmax/Xint = 1.010      Xint/Xmin = 1.018      Xmax/Xmin = 1.029

H = 2.84 +/- 0.42%

E = 1.008      Graham's V = 37.3

F = 2.3 +/- 0.5%      L = 1.0 +/- 0.3%



	Mean X	H	Dmax	Imax	Dint	Iint	Dmin	Imin
KD36.2	0.808E-03	9.7%	283.9	-23.2	118.3	-66.2	16.1	-5.3
KD36.3	0.811E-03	2.3%	285.5	-21.0	88.4	-68.1	193.2	-5.8
KD36.4	0.768E-03	4.3%	306.6	-27.9	147.6	-60.5	41.4	-9.0
KD36.5	0.178E-03	0.6%	45.6	-14.2	301.8	-43.3	149.4	-43.3

Site Statistics for KD36

Mean X = (6.412 +/- 2.684) x 1E-04

Xmax: Mean D = 289.1      Mean I = -26.7      a95 = 20: 4

Xint: Mean D = 118.5      Mean I = -63.0      a95 = 15: 4

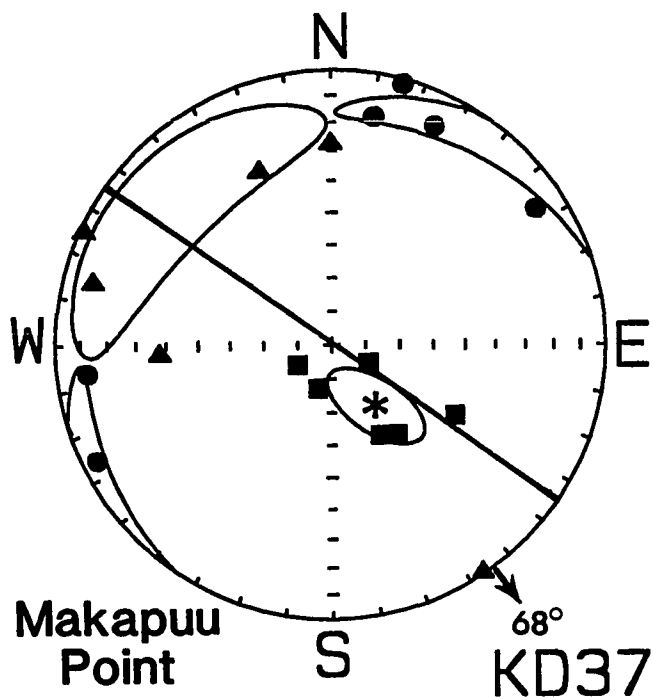
Xmin: Mean D = 21.1      Mean I = -3.8      a95 = 21: 6

Xmax/Xint = 1.013      Xint/Xmin = 1.026      Xmax/Xmin = 1.039

H = 3.82 +/- 2.07%

E = 1.013      Graham's V = 35.4

F = 3.2 +/- 2.0%      L = 1.3 +/- 1.3%



	Mean X	H	Dmax	Imax	Dint	Iint	Dmin	Imin
KD37.1	0.207E-03	1.1%	296.0	-78.1	104.9	-11.7	195.4	-2.2
KD37.2	0.260E-03	1.5%	332.1	-59.5	179.8	-27.6	83.4	-12.1
KD37.4	0.333E-03	0.7%	59.8	-78.4	326.6	-0.7	236.5	-11.6
KD37.5	0.314E-03	1.6%	17.5	-76.6	114.8	-1.7	205.2	-13.3
KD37.6	0.347E-03	1.2%	324.4	-57.0	157.6	-32.3	63.8	-6.0
KD37.9	0.533E-03	1.6%	299.9	-47.4	87.0	-37.7	190.6	-16.9

Site Statistics for KD37

Mean X = (3.324 +/- 1.015) x 1E-04

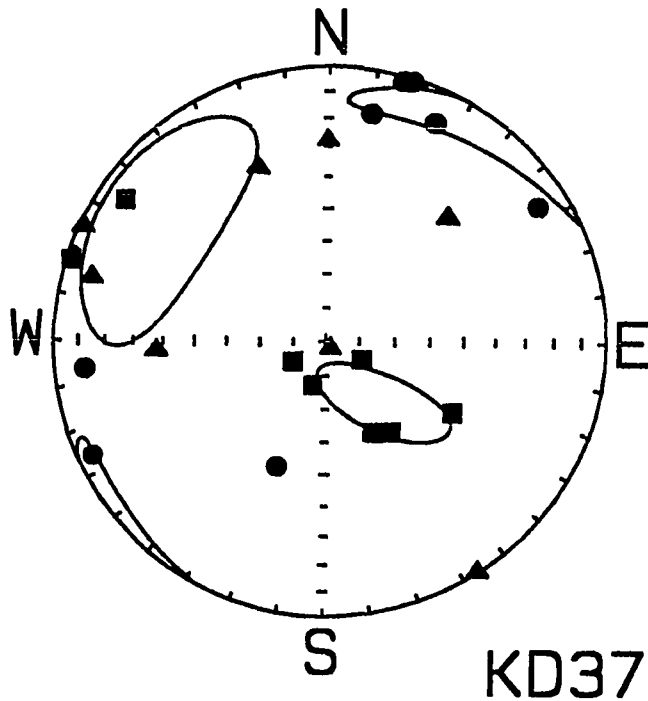
Xmax: Mean D = 324.8      Mean I = -67.5      a95 = 17: 8  
 Xint: Mean D = 132.0      Mean I = -22.0      a95 = 44:17  
 Xmin: Mean D = 43.8      Mean I = 4.5      a95 = 44: 8

Xmax/Xint = 1.006      Xint/Xmin = 1.004      Xmax/Xmin = 1.010

H = 1.04 +/- 0.12%

E = 0.998      Graham's V = 50.6

F = 0.7 +/- 0.1%      L = 0.6 +/- 0.1%



	Mean X	H	Dmax	Imax	Dint	Iint	Dmin	Imin
KD37.1	0.207E-03	1.1%	296.0	-78.1	104.9	-11.7	195.4	-2.2
KD37.2	0.260E-03	1.5%	332.1	-59.5	179.8	-27.6	83.4	-12.1
KD37.3	0.613E-03	0.6%	124.4	-10.8	223.1	-38.2	21.4	-49.8
KD37.4	0.333E-03	0.7%	59.8	-78.4	326.6	-0.7	236.5	-11.6
KD37.5	0.314E-03	1.6%	17.5	-76.6	114.8	-1.7	205.2	-13.3
KD37.6	0.347E-03	1.2%	324.4	-57.0	157.6	-32.3	63.8	-6.0
KD37.8	0.277E-03	1.0%	107.3	-1.9	322.5	-87.7	197.3	-1.3
KD37.9	0.533E-03	1.6%	299.9	-47.4	87.0	-37.7	190.6	-16.9

Site Statistics for KD37

Mean X = (3.605 +/- 1.310) x 1E-04

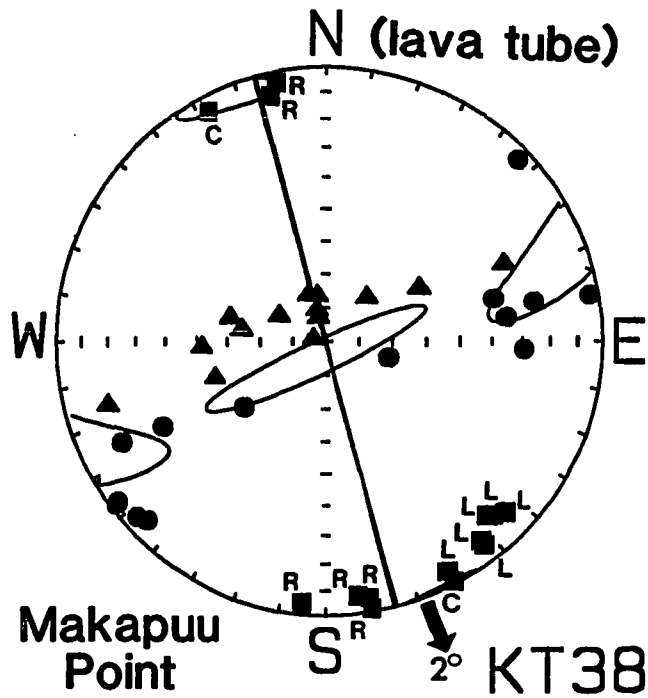
Xmax: Mean D = 317.5      Mean I = -65.2      a95 = 21: 8  
 Xint: Mean D = 124.6      Mean I = -24.2      a95 = 33:21  
 Xmin: Mean D = 36.8      Mean I = 4.9      a95 = 33: 8

Xmax/Xint = 1.004      Xint/Xmin = 1.005      Xmax/Xmin = 1.008

H = 0.83 +/- 0.17%

E = 1.001      Graham's V = 42.3

F = 0.6 +/- 0.2%      L = 0.4 +/- 0.2%



	Mean X	H	Dmax	Imax	Dint	Iint	Dmin	Imin
KT38.1	0.144E-03	8.0%	29.7	-11.7	299.2	-2.6	197.0	-78.0
KT38.2	0.478E-03	3.1%	317.6	-15.2	118.5	-74.0	226.2	-5.0
KT38.3	0.131E-02	8.9%	332.2	-6.0	223.5	-71.8	64.1	-17.1
KT38.4	0.121E-02	8.0%	152.4	-6.3	246.2	-30.8	52.0	-58.4
KT38.5	0.130E-02	7.5%	167.0	-9.0	74.2	-17.1	283.6	-70.6
KT38.6	0.116E-02	8.5%	168.9	-4.6	72.4	-54.5	262.2	-35.1
KT38.7	0.960E-03	4.0%	349.9	-1.6	103.8	-86.1	259.8	-3.5
KT38.8	0.147E-02	9.4%	5.2	-5.0	103.9	-60.0	272.3	-29.5
KT38.9A	0.842E-03	4.3%	350.1	-5.9	87.7	-51.7	255.6	-37.7
KT38.9B	0.925E-03	3.6%	352.5	-7.4	98.1	-64.1	259.1	-24.6
KT38.10	0.128E-02	9.3%	63.0	-0.9	153.0	-0.1	248.8	-89.1
KT38.11A	0.572E-03	1.6%	314.0	-11.4	169.3	-76.1	45.6	-7.8
KT38.12A	0.655E-03	2.1%	316.3	-13.7	160.0	-75.2	47.7	-5.7
KT38.13	0.359E-03	8.9%	322.4	-7.1	162.6	-82.5	52.7	-2.6
KT38.14	0.329E-03	3.5%	322.4	-9.2	164.0	-80.2	53.0	-3.5
KT38.15A	0.103E-02	8.0%	332.1	-1.3	240.0	-57.6	62.9	-32.4

Site Statistics for KT38

Mean X = (8.765 +/- 3.972) x 1E-04

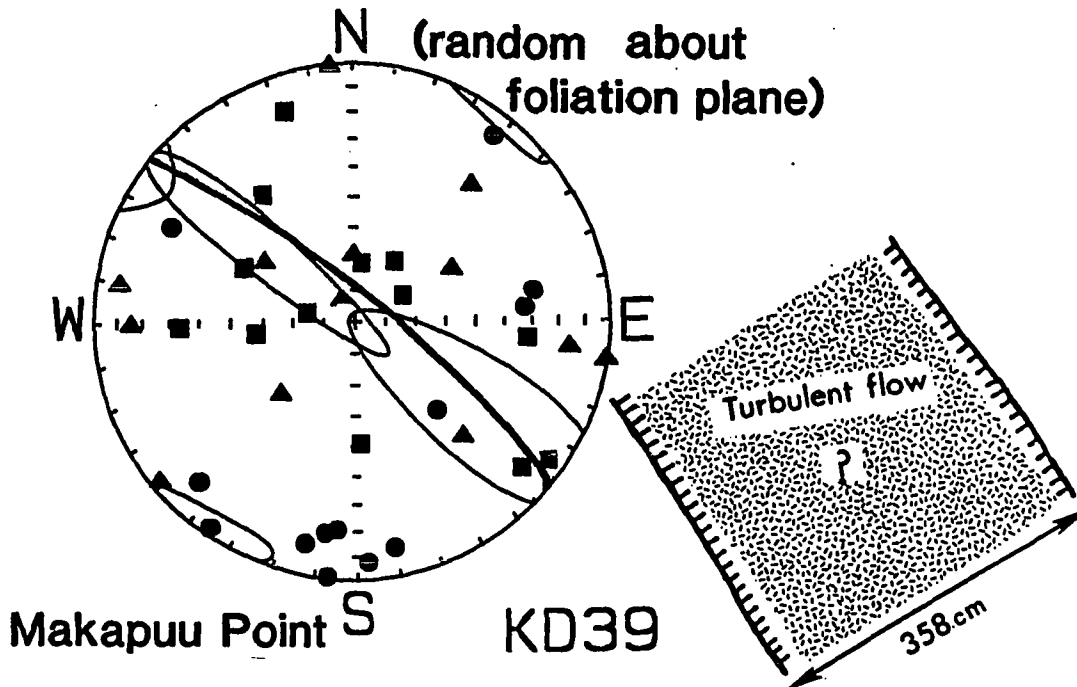
Xmax: Mean D = 339.8      Mean I = 1.5      a95 = 14: 6  
 Xint: Mean D = 246.9      Mean I = 61.8      a95 = 70: 8  
 Xmin: Mean D = 70.6      Mean I = 28.1      a95 = 70:10

Xmax/Xint = 1.032      Xint/Xmin = 1.005      Xmax/Xmin = 1.036

H = 3.63 +/- 0.65%

E = 0.974      Graham's V = 69.0

F = 2.0 +/- 0.6%      L = 3.1 +/- 0.6%



	Mean X	H	Dmax	Imax	Dint	Iint	Dmin	Imin
KD39.1	0.963E-03	7.9%	305.3	-7.4	150.4	-81.8	35.8	-3.4
KD39.2	0.227E-02	2.3%	161.8	-15.5	46.8	-56.9	260.5	-28.5
KD39.3	0.172E-02	0.9%	275.2	-31.6	123.6	-55.0	13.7	-13.4
KD39.4	0.113E-02	0.4%	241.9	-72.3	89.6	-15.7	357.4	-7.8
KD39.5	0.760E-03	0.5%	187.4	-71.3	278.8	-0.4	8.9	-18.7
KD39.6	0.699E-03	0.5%	88.7	-33.5	242.7	-53.7	350.2	-12.5
KD39.7	0.865E-03	0.5%	214.4	-66.9	99.5	-10.1	5.7	-20.5
KD39.8	0.744E-03	0.3%	144.1	-38.9	51.0	-3.9	316.3	-50.9
KD39.9	0.893E-03	0.7%	83.9	-57.6	175.0	-0.7	265.4	-32.4
KD39.10	0.236E-02	1.1%	310.7	-14.1	179.9	-68.9	44.7	-15.3
KD39.12	0.343E-04	2.9%	101.5	-74.5	276.7	-15.4	7.0	-1.2
KD39.13	0.538E-04	1.3%	116.3	-50.1	316.1	-38.2	218.3	-9.8
KD39.14	0.979E-03	0.4%	357.7	-51.1	222.0	-30.0	118.3	-22.3

Site Statistics for KD39

Mean X = (1.036 +/- 0.681) x 1E-03

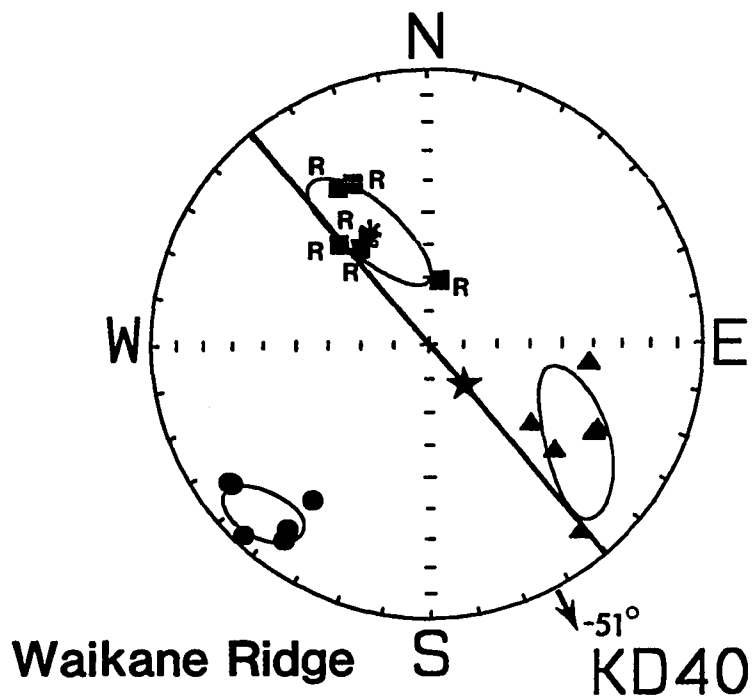
Xmax: Mean D = 308.7      Mean I = 51.3      a95 = 53: 8  
 Xint: Mean D = 124.8      Mean I = 38.7      a95 = 53:15  
 Xmin: Mean D = 36.3      Mean I = -1.9      a95 = 16: 8

Xmax/Xint = 1.002      Xint/Xmin = 1.007      Xmax/Xmin = 1.010

H = 0.97 +/- 0.50%

E = 1.005      Graham's V = 29.7

F = 0.9 +/- 0.5%      L = 0.2 +/- 0.4%



	Mean X	H	Dmax	Imax	Dint	Iint	Dmin	Imin
KD40.1B	0.748E-04	3.1%	150.5	-34.6	277.2	-40.9	37.1	-29.9
KD40.1A	0.591E-03	2.9%	151.3	-53.4	297.3	-31.6	37.8	-16.5
KD40.2	0.512E-03	2.5%	155.4	-35.7	308.6	-51.1	55.6	-13.3
KD40.3	0.587E-03	2.6%	145.3	-54.8	298.9	-32.3	36.9	-12.5
KD40.4	0.536E-03	2.6%	189.6	-70.8	321.5	-13.1	54.7	-13.8
KD40.5	0.563E-03	2.7%	138.8	-49.8	311.0	-40.0	44.3	-3.9

Site Statistics for KD40

Mean X = (4.774 +/- 1.822) x 1E-04

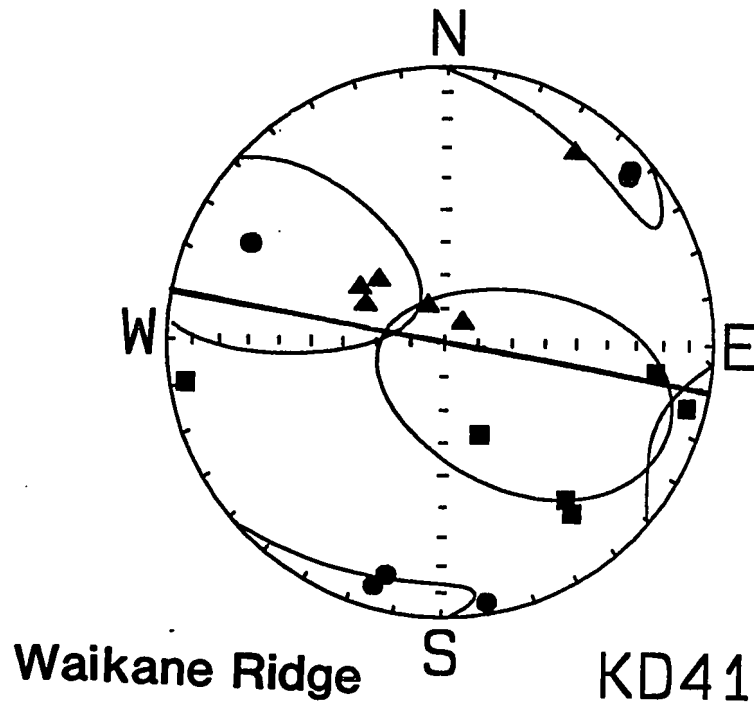
Xmax: Mean D = 333.3      Mean I = 50.9      a95 = 24: 8  
Xint: Mean D = 123.8      Mean I = 35.2      a95 = 24: 9  
Xmin: Mean D = 44.5      Mean I = -14.7      a95 = 11: 8

Xmax/Xint = 1.008      Xint/Xmin = 1.018      Xmax/Xmin = 1.026

H = 2.57 +/- 0.11%

E = 1.011      Graham's V = 32.9

F = 2.2 +/- 0.1%      L = 0.8 +/- 0.1%



	Mean X	H	Dmax	Imax	Dint	Iint	Dmin	Imin
KD41.1	0.655E-03	5.2%	80.5	-6.3	222.2	-82.0	350.0	-4.9
KD41.2	0.706E-03	6.1%	277.3	-22.2	133.4	-63.2	13.3	-14.2
KD41.3	0.737E-03	4.4%	284.2	-7.8	154.5	-77.9	15.5	-9.2
KD41.4	0.713E-03	3.1%	338.4	-60.6	214.1	-17.6	116.5	-22.7
KD41.5	0.799E-03	6.9%	321.5	-28.4	122.7	-60.3	227.1	-8.1
KD41.6	0.782E-03	6.5%	322.4	-23.4	115.5	-64.2	227.8	-10.4

Site Statistics for KD41

Mean X = (7.320 +/- 0.515) x 1E-04

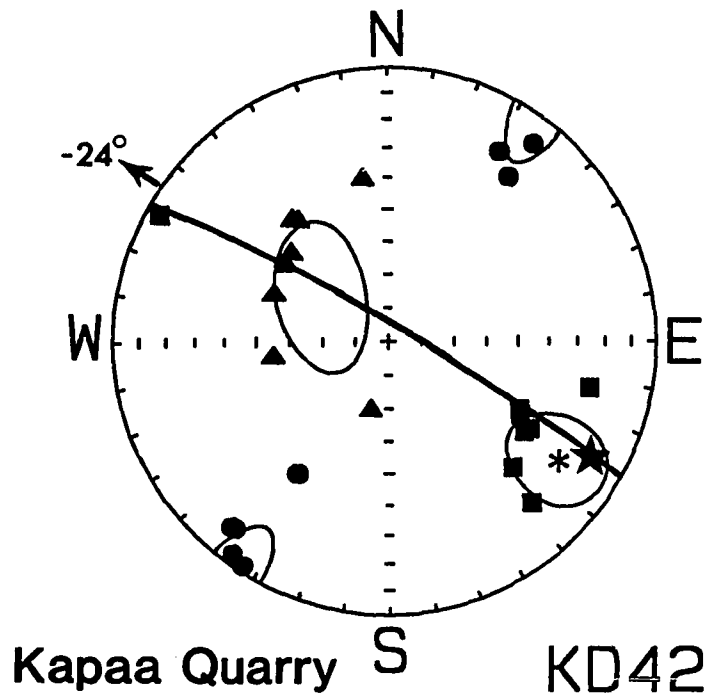
Xmax: Mean D = 299.9      Mean I = -59.3      a95 = 48:29  
 Xint: Mean D = 115.3      Mean I = -30.7      a95 = 48:25  
 Xmin: Mean D = 26.5      Mean I = 2.0      a95 = 36:11

Xmax/Xint = 1.004      Xint/Xmin = 1.032      Xmax/Xmin = 1.036

H = 3.51 +/- 0.72%

E = 1.028      Graham's V = 19.1

F = 3.3 +/- 0.8%      L = 0.4 +/- 0.6%



	Mean X	H	Dmax	Imax	Dint	Iint	Dmin	Imin
KD42.2	0.494E-02	2.3%	282.7	-23.9	171.0	-39.8	35.2	-40.8
KD42.3	0.443E-02	2.3%	119.2	-5.4	14.9	-68.9	211.2	-20.3
KD42.4A	0.396E-02	1.7%	298.8	-43.4	142.9	-44.0	40.7	-12.3
KD42.4B	0.441E-02	1.8%	297.0	-44.5	141.6	-42.8	39.6	-12.6
KD42.5A	0.482E-02	2.0%	301.3	-38.4	126.7	-51.5	33.4	-2.6
KD42.5B	0.389E-02	1.6%	303.3	-39.6	131.9	-50.1	36.8	-4.2
KD42.6	0.519E-02	2.4%	315.0	-35.1	112.5	-52.7	217.2	-10.9
KD42.7	0.510E-01	3.0%	318.0	-21.6	82.6	-55.1	216.9	-26.0

Site Statistics for KD42

Mean X = ( $\pm 10.325$  +/-  $\pm 15.364$ ) x 1E-03

Xmax: Mean D = 304.5      Mean I = -24.3      a95 = 19:11

Xint: Mean D = 123.4      Mean I = -65.7      a95 = 23:13

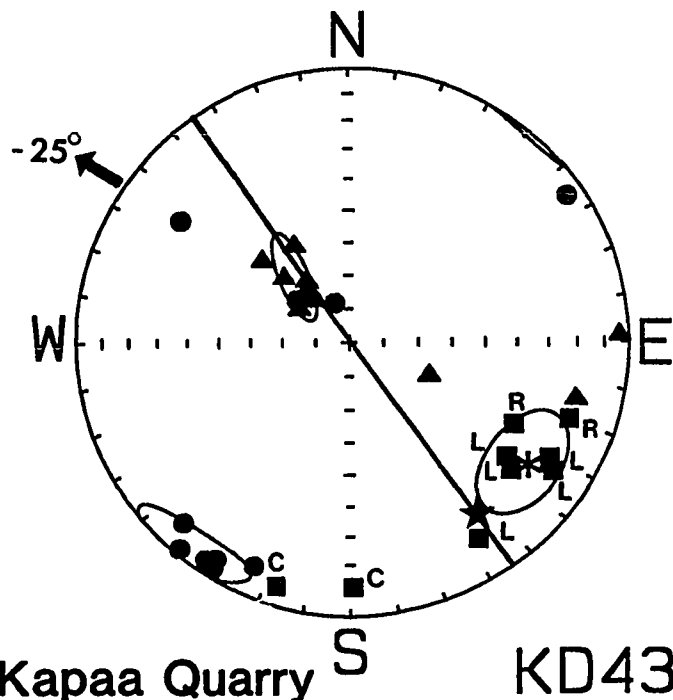
Xmin: Mean D = 34.3      Mean I = 0.4      a95 = 20: 6

Xmax/Xint = 1.009      Xint/Xmin = 1.009      Xmax/Xmin = 1.019

H = 1.87 +/- 0.17%

E = 1.000      Graham's V = 45.4

F = 1.4 +/- 0.2%      L = 0.9 +/- 0.2%



	Mean X	H	Dmax	Imax	Dint	Iint	Dmin	Imin
KD43.1	0.537E-02	4.1%	33.4	-4.8	293.1	-64.7	125.6	-24.8
KD43.2	0.539E-02	2.6%	296.9	-34.7	133.0	-54.2	32.3	-7.7
KD43.3	0.601E-02	4.0%	289.6	-18.2	145.7	-67.9	23.7	-12.1
KD43.4A	0.275E-02	0.5%	17.1	-8.0	284.4	-18.1	129.9	-70.1
KD43.4B	0.305E-02	0.6%	359.3	-11.8	268.4	-3.9	160.6	-77.6
KD43.5	0.514E-02	4.4%	300.5	-18.7	133.9	-70.9	31.9	-4.1
KD43.6A	0.505E-02	2.8%	301.9	-17.6	140.0	-71.5	33.6	-5.4
KD43.6B	0.483E-02	3.1%	303.0	-15.1	142.1	-74.1	34.3	-5.0
KD43.7A	0.489E-02	2.5%	308.8	-27.1	135.0	-62.8	40.1	-2.5
KD43.7B	0.464E-02	2.4%	306.5	-30.9	150.7	-56.8	43.3	-11.1
KD43.8	0.504E-02	4.4%	327.4	-16.2	124.5	-72.4	235.5	-6.5

Site Statistics for KD43

Mean X = (4.741 +/- 0.939) x 1E-03

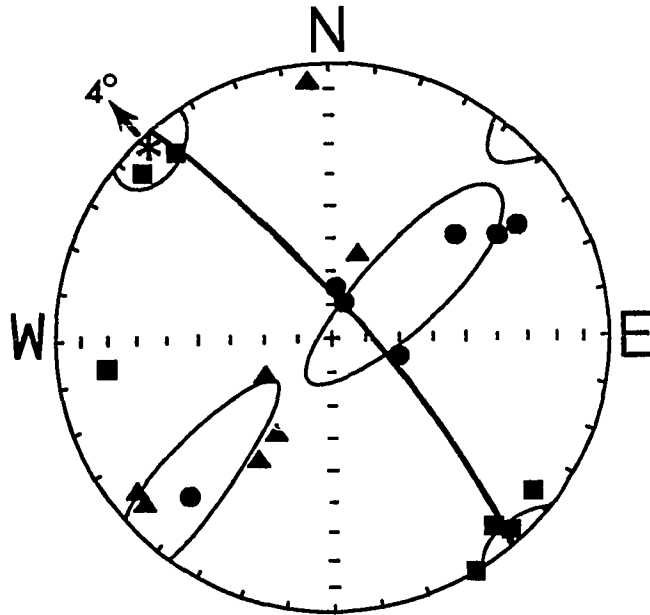
Xmax: Mean D = 305.5      Mean I = -24.8      a95 = 15:13  
 Xint: Mean D = 140.2      Mean I = -64.5      a95 = 14: 4  
 Xmin: Mean D = 38.1      Mean I = -5.7      a95 = 15: 7

Xmax/Xint = 1.013      Xint/Xmin = 1.006      Xmax/Xmin = 1.019

H = 1.90 +/- 0.63%

E = 0.993      Graham's V = 55.9

F = 1.2 +/- 0.5%      L = 1.3 +/- 0.4%



Kapaa Quarry S KD44

	Mean X	H	Dmax	Imax	Dint	Iint	Dmin	Imin
KD44.1	0.213E-02	1.4%	317.9	-5.4	48.9	-9.8	199.6	-78.8
KD44.2	0.163E-02	1.6%	82.8	-19.0	175.3	-7.3	285.4	-69.5
KD44.3	0.114E-02	0.6%	320.1	-10.8	52.1	-10.6	185.5	-74.8
KD44.4	0.166E-02	1.5%	140.9	-13.0	30.2	-56.7	238.6	-30.0
KD44.5	0.184E-02	1.5%	329.2	-0.4	60.2	-67.4	239.1	-22.6
KD44.6	0.193E-02	1.5%	131.9	-9.8	31.2	-47.0	230.6	-41.4
KD44.7	0.240E-02	1.4%	308.2	-9.5	198.0	-64.2	42.4	-23.8

Site Statistics for KD44

Mean X = (1.818 +/- 0.374) x 1E-03

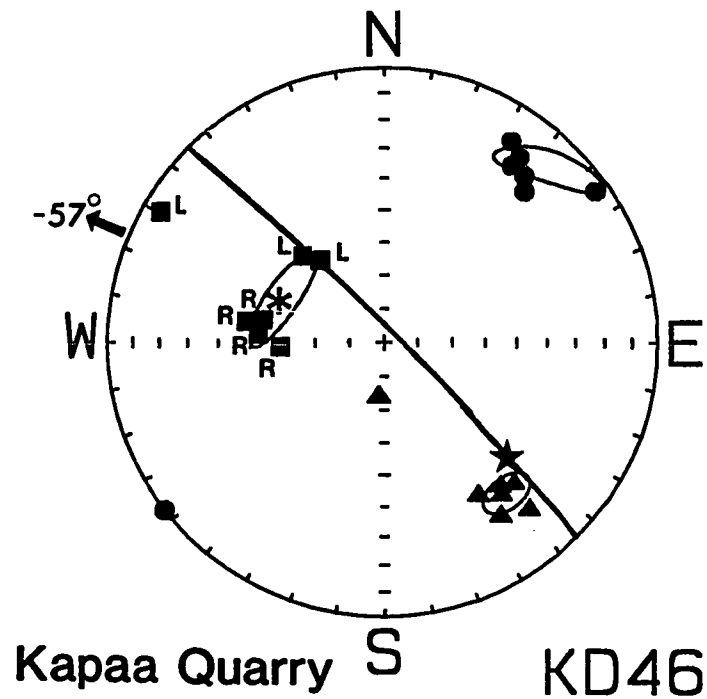
Xmax: Mean D = 317.3      Mean I = 4.4      a95 = 13:10  
 Xint: Mean D = 225.0      Mean I = 27.8      a95 = 42:9  
 Xmin: Mean D = 55.6      Mean I = 61.8      a95 = 42:12

Xmax/Xint = 1.008      Xint/Xmin = 1.003      Xmax/Xmin = 1.011

H = 1.10 +/- 0.14%

E = 0.994      Graham's V = 60.6

F = 0.7 +/- 0.2%      L = 0.8 +/- 0.2%



	Mean X	H	Dmax	Imax	Dint	Iint	Dmin	Imin
KD46.1	0.584E-02	1.8%	93.8	-52.4	326.2	-25.1	223.0	-25.9
KD46.2	0.578E-02	3.2%	87.8	-59.3	318.9	-20.5	220.2	-21.9
KD46.3	0.586E-02	5.0%	100.8	-53.3	317.3	-31.0	216.2	-17.7
KD46.4	0.572E-02	5.7%	98.9	-48.4	321.1	-33.3	215.8	-21.9
KD46.6	0.532E-02	7.7%	137.1	-54.6	328.5	-34.9	234.7	-5.4
KD46.7	0.535E-02	6.3%	142.5	-59.1	322.5	-30.9	232.5	0.0
KD46.5	0.591E-02	3.7%	120.5	-7.0	5.4	-73.8	212.3	-14.5

Site Statistics for KD46

Mean X = (5.683 +/- 0.258) x 1E-03

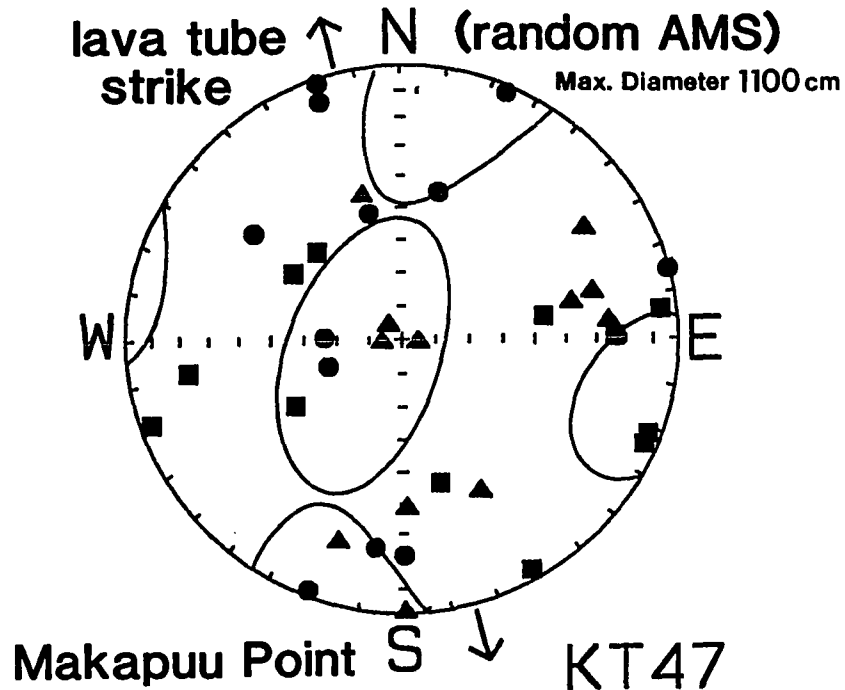
Xmax: Mean D = 293.3      Mean I = 56.9      a95 = 16: 5  
 Xint: Mean D = 141.0      Mean I = 30.0      a95 = 7: 5  
 Xmin: Mean D = 43.5      Mean I = 12.7      a95 = 16: 5

Xmax/Xint = 1.015      Xint/Xmin = 1.029      Xmax/Xmin = 1.045

H = 4.34 +/- 0.67%

E = 1.014      Graham's V = 36.2

F = 3.6 +/- 0.6%      L = 1.5 +/- 0.5%



	Mean X	H	Dmax	Imax	Dint	Iint	Dmin	Imin
KT47.2	0.109E-02	0.3%	263.5	-6.4	358.7	-38.6	165.6	-50.7
KT47.3	0.115E-02	0.3%	71.5	-4.3	278.3	-85.2	161.6	-2.2
KT47.4	0.122E-02	0.4%	59.0	-51.6	257.9	-36.9	160.8	-9.3
KT47.5	0.127E-02	0.3%	331.0	-4.4	239.1	-23.4	71.0	-66.1
KT47.6A	0.117E-02	0.8%	293.8	-5.1	84.0	-84.1	203.5	-2.9
KT47.6B	0.109E-02	0.7%	291.4	-5.3	137.2	-84.2	21.6	-2.5
KT47.7	0.124E-02	0.3%	345.7	-45.2	164.9	-44.8	255.3	-0.4
KT47.8A	0.130E-02	0.4%	135.5	-53.1	265.2	-25.6	7.9	-24.6
KT47.8B	0.134E-02	0.2%	121.1	-51.5	256.3	-29.5	359.8	-22.4
KT47.9	0.109E-02	0.2%	261.1	-46.5	18.5	-23.6	125.6	-34.1
KT47.10	0.138E-02	0.7%	269.3	-23.7	359.7	-0.9	91.7	-66.3
KT47.11A	0.127E-02	0.2%	81.4	-22.0	333.1	-37.9	194.4	-44.0

Site Statistics for KT47

Mean X = (1.217 +/- 0.097) x 1E-03

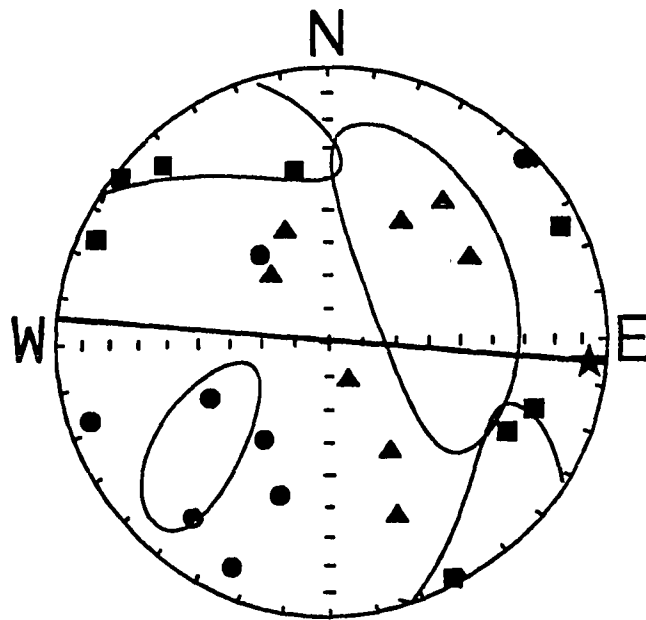
Xmax: Mean D = 284.5      Mean I = -10.8      a95 = 24:19  
 Xint: Mean D = 249.6      Mean I = 76.9      a95 = 43:23  
 Xmin: Mean D = 13.1      Mean I = 7.3      a95 = 43:19

Xmax/Xint = 1.001      Xint/Xmin = 1.001      Xmax/Xmin = 1.002

H = 0.18 +/- 0.08%

E = 0.999      Graham's V = 54.3

F = 0.1 +/- 0.1%      L = 0.1 +/- 0.1%



Wailea Point S KD49

	Mean X	H	Dmax	Imax	Dint	Iint	Dmin	Imin
KD49.1	0.414E-02	1.5%	169.0	-36.6	331.1	-52.1	72.5	-8.7
KD49.2	0.803E-02	1.7%	332.4	-2.8	240.1	-39.8	65.8	-50.1
KD49.3	0.474E-02	0.5%	243.9	-7.7	338.8	-32.3	142.0	-56.6
KD49.4	0.485E-02	0.3%	128.2	-2.7	220.0	-34.8	34.3	-55.1
KD49.5	0.310E-02	0.5%	297.3	-28.3	159.1	-54.2	38.7	-20.1
KD49.6	0.287E-02	0.3%	288.9	-23.0	139.7	-63.7	24.1	-12.0
KD49.7	0.436E-02	1.1%	136.6	-12.0	333.6	-77.4	227.3	-3.6
KD49.8	0.397E-02	0.3%	114.1	-6.8	211.7	-47.9	18.0	-41.3

Site Statistics for KD49

Mean X = (4.508 +/- 1.485) x 1E-03

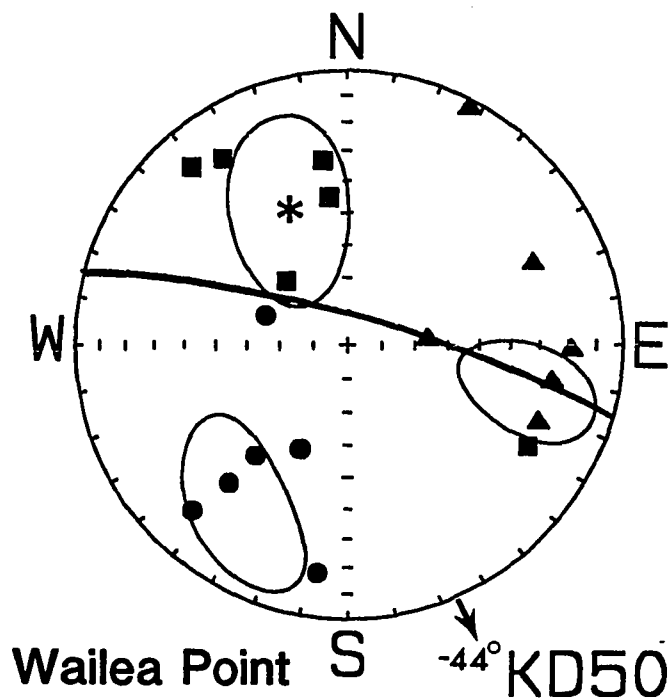
Xmax: Mean D = 325.4      Mean I = 3.6      a95 = 49:16  
 Xint: Mean D = 239.9      Mean I = -51.4      a95 = 50:22  
 Xmin: Mean D = 52.5      Mean I = -38.4      a95 = 30:12

Xmax/Xint = 1.002      Xint/Xmin = 1.003      Xmax/Xmin = 1.005

H = 0.52 +/- 0.18%

E = 1.001      Graham's V = 38.5

F = 0.4 +/- 0.2%      L = 0.2 +/- 0.1%



	Mean X	H	Dmax	Imax	Dint	Iint	Dmin	Imin
KD50.1	0.350E-02	3.0%	136.9	-63.7	271.4	-19.1	7.6	-17.4
KD50.2	0.268E-02	1.7%	173.3	-44.9	291.9	-25.6	40.8	-34.1
KD50.3	0.272E-02	1.9%	172.8	-32.7	280.1	-24.9	39.7	-46.7
KD50.4	0.206E-02	0.9%	146.1	-19.7	246.5	-26.6	24.2	-55.9
KD50.5	0.245E-02	1.3%	138.4	-15.0	265.7	-66.1	43.4	-18.1
KD50.6	0.228E-02	0.4%	299.3	-25.4	207.6	-3.5	110.4	-64.3

Site Statistics for KD50

Mean X = (2.616 +/- 0.456) x 1E-03

Xmax: Mean D = 336.9      Mean I = 44.5      a95 = 31:17

Xint: Mean D = 103.9      Mean I = 31.5      a95 = 25:12

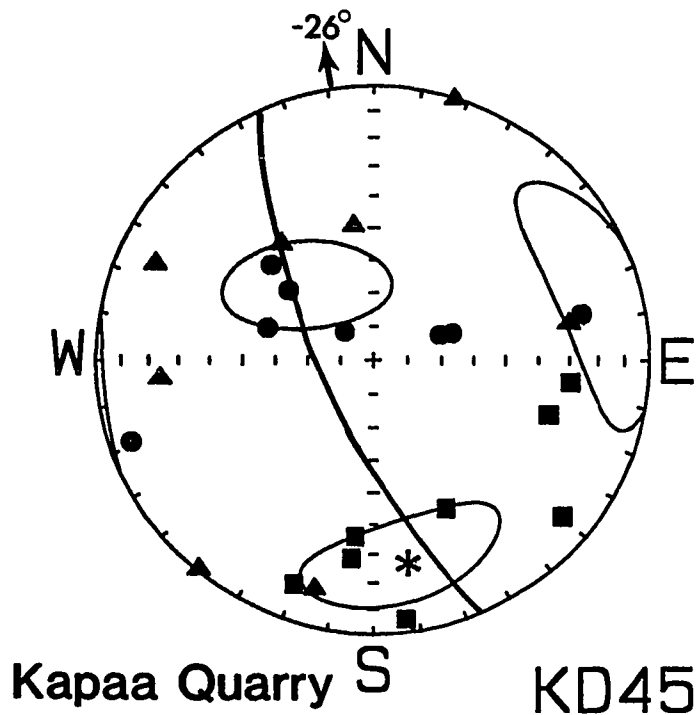
Xmin: Mean D = 33.8      Mean I = -29.1      a95 = 27:15

Xmax/Xint = 1.007      Xint/Xmin = 1.005      Xmax/Xmin = 1.012

H = 1.17 +/- 0.33%

E = 0.998      Graham's V = 50.9

F = 0.8 +/- 0.3%      L = 0.7 +/- 0.3%



	Mean X	H	Dmax	I <sub>max</sub>	D <sub>int</sub>	I <sub>int</sub>	D <sub>min</sub>	I <sub>min</sub>
KD45.1	0.376E-02	1.2%	287.3	-34.0	197.1	-0.3	106.6	-56.0
KD45.2	0.333E-02	1.5%	6.5	-28.3	259.0	-29.1	132.1	-47.2
KD45.3	0.401E-02	1.2%	20.1	-14.2	114.0	-14.9	248.5	-69.2
KD45.4	0.398E-02	1.1%	352.8	-5.5	85.2	-23.8	250.6	-65.5
KD45.5	0.351E-02	0.8%	309.8	-12.3	40.0	-0.9	133.9	-77.7
KD45.6	0.369E-02	0.8%	276.3	-29.2	14.8	-14.9	128.6	-56.5
KD45.7	0.415E-02	1.4%	333.9	-39.8	171.3	-48.9	71.2	-8.7
KD45.8	0.473E-02	1.7%	6.1	-35.5	140.7	-44.5	257.2	-24.4

Site Statistics for KD45

Mean X = (3.896 +/- 0.406) x 1E-03

X<sub>max</sub>: Mean D = 351.3      Mean I = -26.3      a<sub>95</sub> = 27:14

X<sub>int</sub>: Mean D = 253.9      Mean I = -14.7      a<sub>95</sub> = 32:16

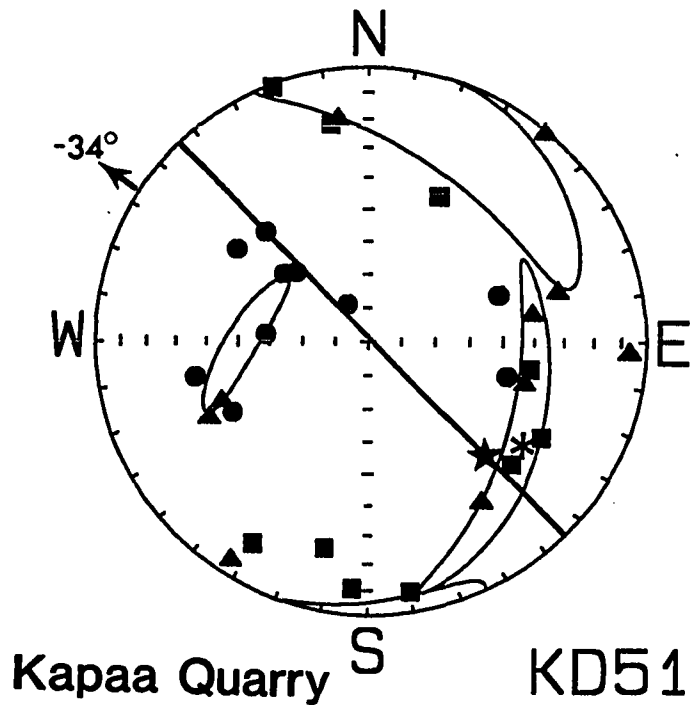
X<sub>min</sub>: Mean D = 317.7      Mean I = 59.4      a<sub>95</sub> = 25:13

X<sub>max</sub>/X<sub>int</sub> = 1.006      X<sub>int</sub>/X<sub>min</sub> = 1.003      X<sub>max</sub>/X<sub>min</sub> = 1.008

H = 0.84 +/- 0.17%

E = 0.997      Graham's V = 54.5

F = 0.6 +/- 0.2%      L = 0.6 +/- 0.2%



	Mean X	H	Dmax	Imax	Dint	Iint	Dmin	Imin
KD51.1	0.186E-02	0.3%	12.1	-23.9	260.4	-39.8	124.6	-40.7
KD51.2	0.179E-02	0.2%	30.0	-16.1	285.2	-41.4	136.4	-44.2
KD51.3A	0.169E-02	0.3%	158.9	-1.1	67.9	-41.3	250.1	-48.7
KD51.3B	0.172E-02	0.2%	170.0	-20.7	64.5	-35.4	284.2	-47.3
KD51.4A	0.540E-02	0.9%	310.7	-32.5	220.0	-1.1	128.3	-57.5
KD51.4B	0.552E-02	1.0%	299.1	-29.3	32.5	-6.1	133.1	-60.0
KD51.5	0.166E-02	0.4%	3.7	-10.6	272.4	-6.7	150.8	-77.4
KD51.6	0.506E-02	2.2%	279.6	-40.7	172.0	-19.4	62.8	-43.0
KD51.7	0.206E-02	0.8%	350.0	-8.4	255.1	-29.9	94.0	-58.8
KD51.8	0.539E-02	1.0%	206.0	-40.8	325.0	-29.3	78.4	-35.3

Site Statistics for KD51

Mean X = (3.216 +/- 1.745) x 1E-03

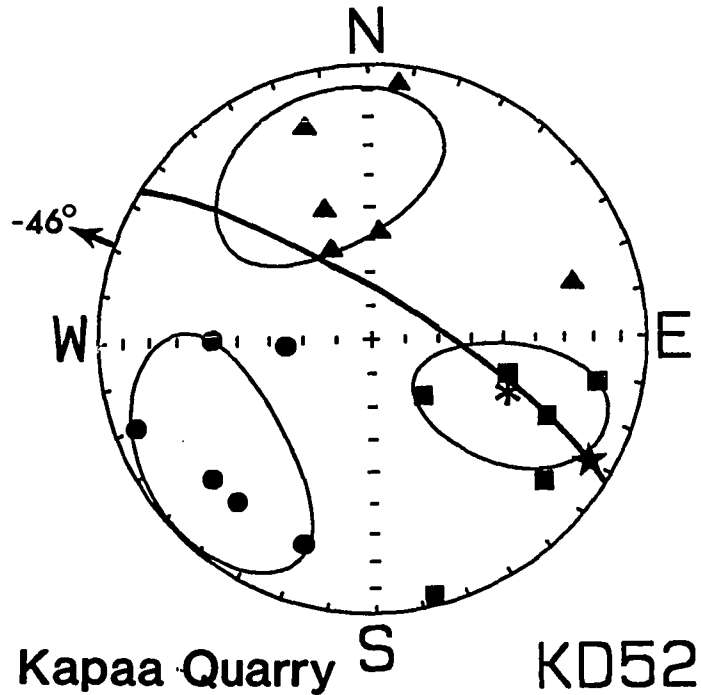
Xmax: Mean D = 303.0      Mean I = -33.9      a95 = 49: 5  
 Xint: Mean D = 201.4      Mean I = -16.7      a95 = 50:15  
 Xmin: Mean D = 89.5      Mean I = -51.2      a95 = 23: 5

Xmax/Xint = 1.002      Xint/Xmin = 1.003      Xmax/Xmin = 1.005

H = 0.45 +/- 0.12%

E = 1.001      Graham's V = 35.8

F = 0.4 +/- 0.1%      L = 0.2 +/- 0.1%



	Mean X	H	Dmax	Imax	Dint	Iint	Dmin	Imin
KD52.1	0.359E-02	1.0%	294.3	-30.8	161.5	-48.7	40.2	-24.6
KD52.2	0.387E-02	0.6%	310.1	-19.9	184.9	-57.9	49.4	-24.1
KD52.3	0.308E-02	1.1%	281.3	-17.2	157.3	-61.0	18.8	-22.6
KD52.5	0.265E-02	0.9%	285.1	-47.4	187.0	-7.3	90.4	-41.7
KD52.6	0.481E-02	1.3%	318.1	-67.1	163.7	-20.8	70.2	-9.0

Site Statistics for KD52

Mean X = (3.601 +/- 0.739) x 1E-03

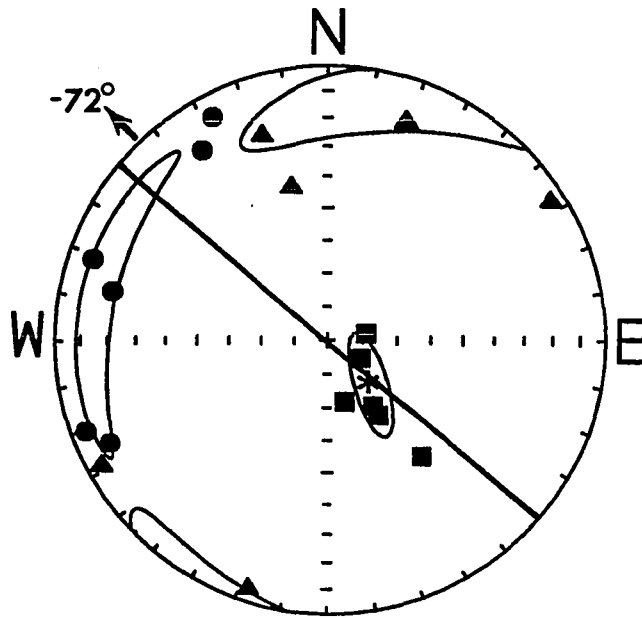
Xmax: Mean D = 291.9      Mean I = -45.8      a95 = 34:10  
 Xint: Mean D = 157.2      Mean I = -34.4      a95 = 34:22  
 Xmin: Mean D = 49.4      Mean I = -24.1      a95 = 35:24

Xmax/Xint = 1.003      Xint/Xmin = 1.004      Xmax/Xmin = 1.007

H = 0.74 +/- 0.10%

E = 1.001      Graham's V = 42.0

F = 0.6 +/- 0.1%      L = 0.3 +/- 0.1%



Kapaa Quarry S KD53

	Mean X	H	Dmax	Imax	Dint	Iint	Dmin	Imin
KD53.1	0.313E-02	0.7%	259.6	-78.8	18.0	-5.4	108.9	-9.8
KD53.3	0.322E-02	0.4%	299.1	-79.1	61.2	-5.9	152.2	-9.2
KD53.4	0.378E-02	0.4%	344.5	-71.1	237.8	-5.6	146.0	-18.0
KD53.7	0.320E-02	0.4%	326.4	-63.3	199.1	-17.0	102.7	-20.0
KD53.8	0.268E-02	0.4%	321.9	-45.2	166.6	-42.1	64.9	-12.6
KD53.9	0.388E-02	0.6%	326.0	-66.5	161.9	-22.7	69.5	-5.8

Site Statistics for KD53

Mean X = (3.313 +/- 0.407) x 1E-03

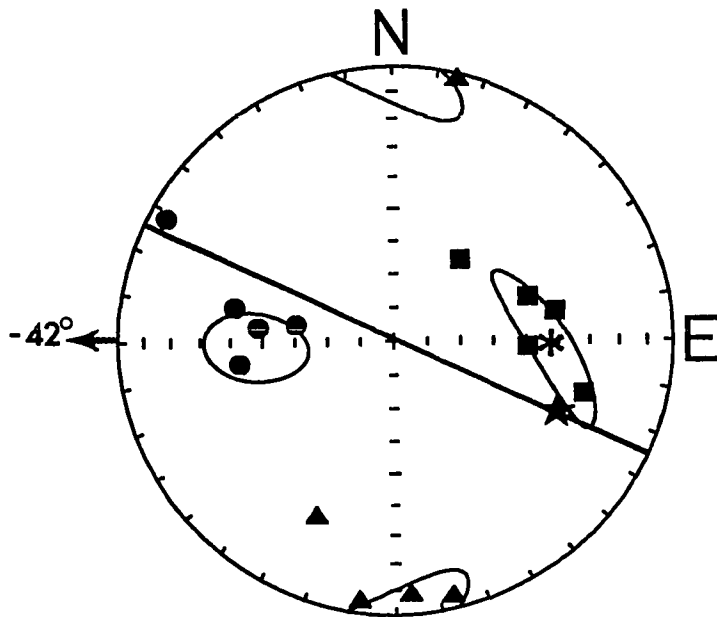
Xmax: Mean D = 316.3      Mean I = -71.7      a95 = 16: 5  
 Xint: Mean D = 193.9      Mean I = -10.1      a95 = 39:12  
 Xmin: Mean D = 281.2      Mean I = 15.2      a95 = 39: 6

Xmax/Xint = 1.003      Xint/Xmin = 1.001      Xmax/Xmin = 1.004

H = 0.43 +/- 0.07%

E = 0.998 -      Graham's V = 58.4

F = 0.3 +/- 0.1%      L = 0.3 +/- 0.1%



Kapaa Quarry S KD54

	Mean X	H	Dmax	Imax	Dint	Iint	Dmin	Imin
KD54.2	0.392E-02	0.4%	251.9	-47.3	347.2	-4.9	81.8	-42.3
KD54.5	0.312E-02	0.5%	259.6	-40.3	356.6	-8.2	96.0	-48.6
KD54.6	0.358E-02	0.9%	285.7	-29.9	194.2	-2.6	99.7	-60.0
KD54.7	0.405E-02	0.5%	272.4	-49.4	8.0	-4.8	102.1	-40.2
KD54.8	0.260E-02	0.2%	219.7	-58.6	24.5	-30.5	118.6	-6.8

Site Statistics for KD54

Mean X = (3.453 +/- 0.535) x 1E-03

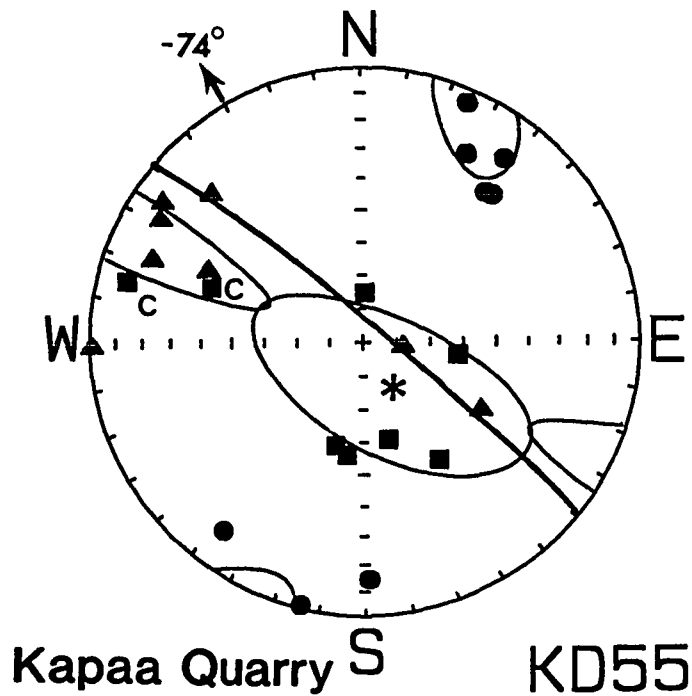
Xmax: Mean D = 271.9      Mean I = -42.3      a95 = 26: 6  
 Xint: Mean D = 180.0      Mean I = -2.0      a95 = 22: 9  
 Xmin: Mean D = 87.8      Mean I = -47.6      a95 = 17: 9

Xmax/Xint = 1.003    Xint/Xmin = 1.002    Xmax/Xmin = 1.004

H = 0.45 +/- 0.07%

E = 0.999      Graham's V = 53.4

F = 0.3 +/- 0.1%    L = 0.3 +/- 0.1%



	Mean X	H	Dmax	Imax	Dint	Iint	Dmin	Imin
KD55.1	0.217E-02	1.6%	346.0	-60.0	111.5	-18.5	209.5	-22.7
KD55.2	0.200E-02	1.6%	327.5	-47.6	114.7	-37.5	218.2	-16.9
KD55.3	0.445E-02	1.1%	182.7	-75.3	89.3	-0.9	359.0	-14.7
KD55.4	0.520E-02	1.9%	104.7	-11.8	276.1	-78.1	14.3	-1.7
KD55.5	0.357E-02	1.4%	8.6	-55.9	121.3	-14.6	220.0	-30.1
KD55.6	0.316E-02	0.8%	15.4	-57.9	125.0	-11.9	221.8	-29.4
KD55.7	0.493E-02	2.5%	109.8	-40.5	300.3	-49.0	204.3	-5.3
KD55.8	0.212E-02	2.3%	277.6	-61.3	134.3	-23.7	37.4	-15.2

Site Statistics for KD55

Mean X = (3.450 +/- 1.217) x 1E-03

Xmax: Mean D = 330.0      Mean I = -74.0      a95 = 46:20

Xint: Mean D = 115.6      Mean I = -13.3      a95 = 46: 8

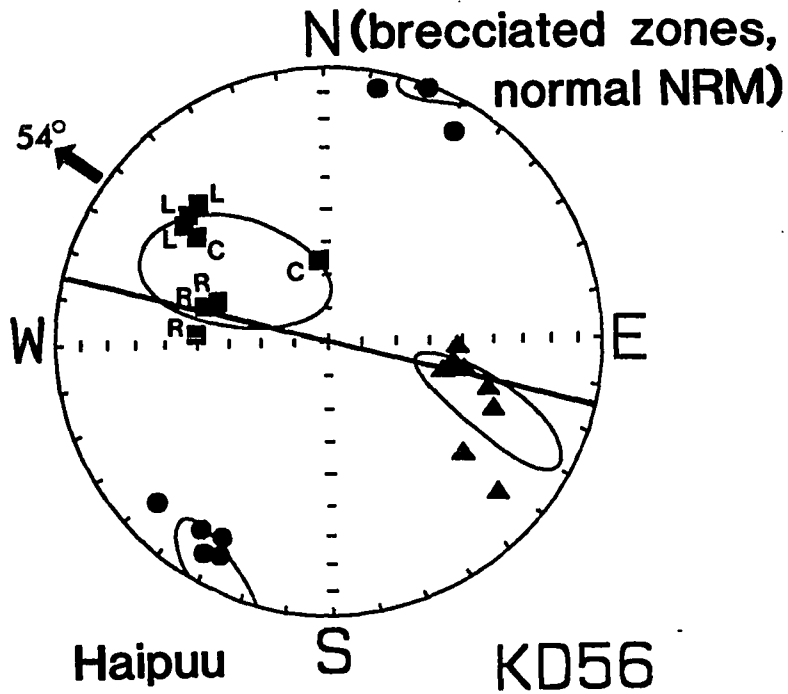
Xmin: Mean D = 27.7      Mean I = 8.7      a95 = 20:10

Xmax/Xint = 1.003      Xint/Xmin = 1.009      Xmax/Xmin = 1.012

H = 1.15 +/- 0.19%

E = 1.006      Graham's V = 28.1

F = 1.0 +/- 0.2%      L = 0.3 +/- 0.2%



	Mean X	H	Dmax	Imax	Dint	Iint	Dmin	Imin
KD56.1A	0.190E-02	0.7%	137.2	-31.4	280.2	-52.6	35.6	-18.2
KD56.1B	0.186E-02	0.7%	129.4	-32.8	285.4	-54.9	32.0	-11.3
KD56.2	0.154E-02	1.6%	174.6	-65.5	312.8	-18.7	48.1	-15.2
KD56.3	0.119E-02	1.6%	94.1	-49.6	287.6	-39.6	192.0	-6.7
KD56.5	0.147E-02	1.2%	129.1	-38.3	282.8	-48.6	28.3	-13.3
KD56.6	0.127E-02	1.5%	110.7	-54.3	293.3	-35.7	202.4	-1.2
KD56.7	0.132E-02	1.1%	106.6	-50.8	311.0	-36.7	211.8	-12.1
KD56.8	0.181E-02	1.2%	132.6	-31.7	273.3	-51.5	29.9	-19.6

Site Statistics for KD56

Mean X = (1.545 +/- 0.264) x 1E-03

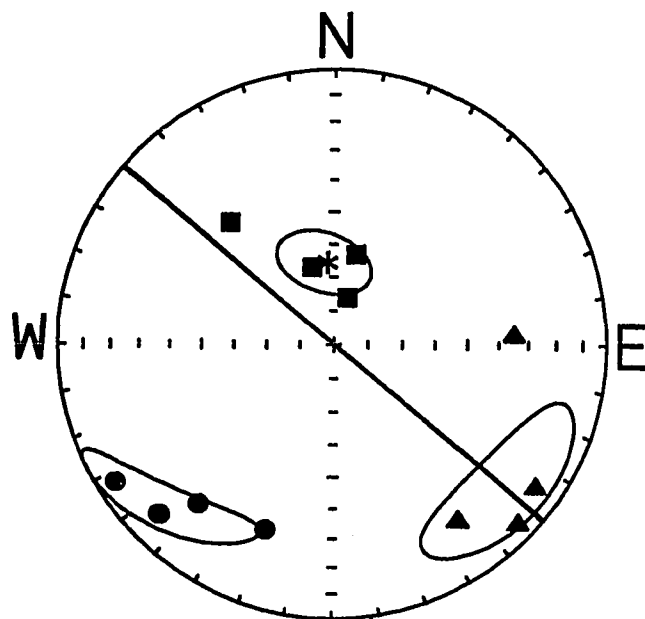
Xmax: Mean D = 307.3      Mean I = 54.2      a95 = 30:16  
 Xint: Mean D = 113.6      Mean I = 35.0      a95 = 30: 7  
 Xmin: Mean D = 28.2      Mean I = -6.5      a95 = 16: 7

Xmax/Xint = 1.002      Xint/Xmin = 1.009      Xmax/Xmin = 1.010

H = 1.02 +/- 0.11%

E = 1.007      Graham's V = 24.0

F = 0.9 +/- 0.1%      L = 0.2 +/- 0.1%



Mokolii Island S  $-65^\circ$  KD57

	Mean X	H	Dmax	Imax	Dint	Iint	Dmin	Imin
KD57.1	0.489E-03	1.7%	196.3	-75.6	314.0	-6.8	45.5	-12.6
KD57.2	0.539E-03	2.1%	194.1	-62.5	305.2	-10.6	40.2	-25.1
KD57.3	0.736E-03	3.2%	164.5	-66.2	324.6	-22.5	57.6	-7.3
KD57.4	0.566E-03	1.0%	139.5	-41.4	267.2	-34.8	20.0	-29.1

Site Statistics for KD57

Mean X = (5.825 +/- 0.928) x 1E-04

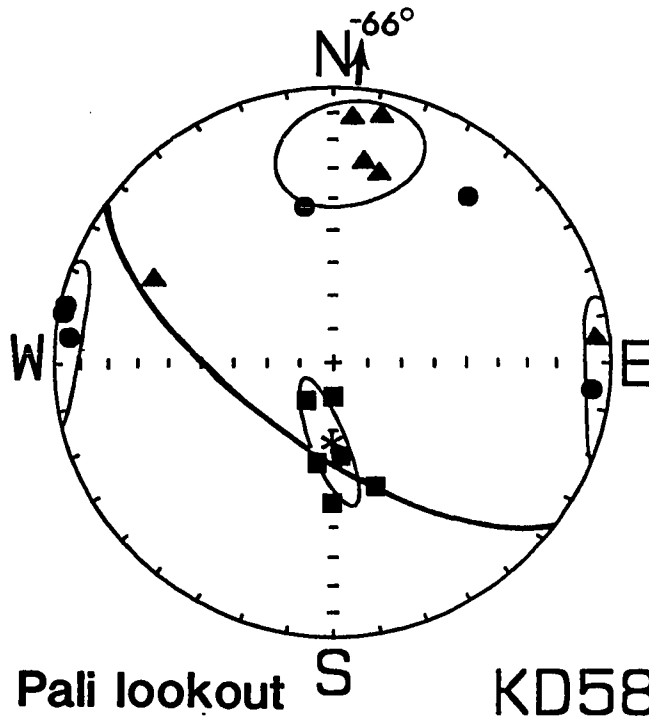
Xmax: Mean D = 353.3    Mean I = 65.3    a95 = 14: 9  
 Xint: Mean D = 129.8    Mean I = 18.5    a95 = 25:13  
 Xmin: Mean D = 45.2    Mean I = -15.8    a95 = 26: 7

Xmax/Xint = 1.011    Xint/Xmin = 1.007    Xmax/Xmin = 1.019

H = 1.88 +/- 0.50%

E = 0.996    Graham's V = 51.2

F = 1.3 +/- 0.4%    L = 1.1 +/- 0.4%



	Mean X	H	Dmax	Imax	Dint	Iint	Dmin	Imin
KD58.1	0.559E-03	0.9%	9.0	-59.7	193.7	-30.2	102.5	-2.1
KD58.2	0.642E-03	1.2%	355.4	-62.2	188.7	-27.2	95.8	-5.5
KD58.3	0.683E-03	1.5%	341.5	-50.8	115.0	-29.3	219.2	-23.5
KD58.5	0.803E-03	1.7%	0.4	-80.0	191.1	-9.8	100.8	-1.8
KD58.6	0.651E-03	2.6%	35.7	-76.4	184.5	-11.7	275.9	-6.8
KD58.7	0.310E-03	0.9%	0.5	-47.6	264.6	-5.4	169.7	-41.9

Site Statistics for KD58

Mean X = (6.079 +/-1.517) x 1E-04

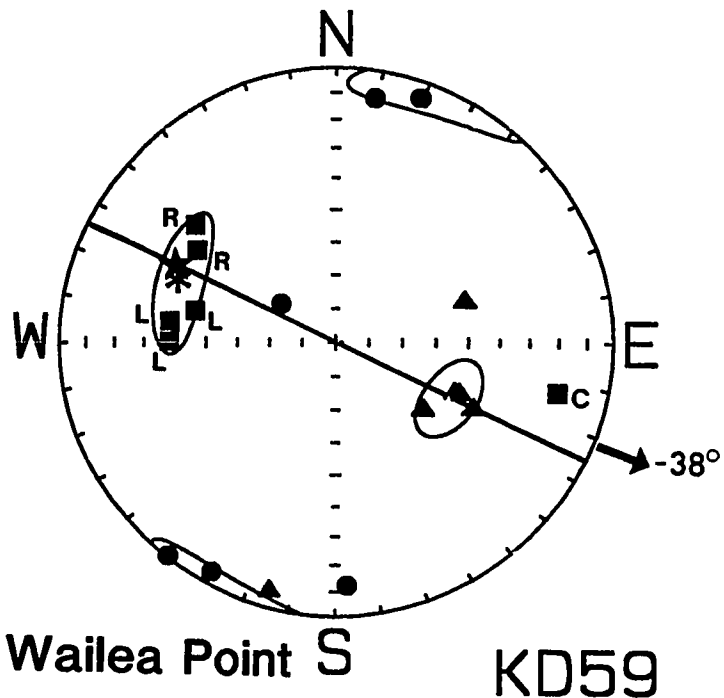
Xmax: Mean D = 3.5      Mean I = -66.0      a95 = 21: 5  
 Xint: Mean D = 184.2      Mean I = -24.0      a95 = 20:17  
 Xmin: Mean D = 274.1      Mean I = 0.3      a95 = 19: 9

Xmax/Xint = 1.009      Xint/Xmin = 1.004      Xmax/Xmin = 1.013

H = 1.29 +/- 0.30%

E = 0.996      Graham's V = 55.1

F = 0.9 +/- 0.3%      L = 0.9 +/- 0.2%



	Mean X	H	Dmax	Imax	Dint	Iint	Dmin	Imin
KD59.1	0.280E-02	1.5%	102.4	-45.5	295.7	-43.7	199.3	-6.7
KD59.3	0.338E-02	2.1%	90.4	-38.3	292.4	-49.6	189.2	-11.0
KD59.5	0.274E-02	1.7%	97.1	-38.1	252.4	-49.2	357.2	-12.4
KD59.6	0.391E-02	2.3%	123.0	-38.5	292.7	-51.0	29.0	-5.1
KD59.7	0.539E-02	2.7%	129.2	-33.1	307.2	-56.9	38.6	-0.9
KD59.8	0.226E-02	0.4%	282.7	-18.6	15.1	-7.0	124.9	-70.0

Site Statistics for KD59

Mean X = (3.415 +/- 1.026) x 1E-03

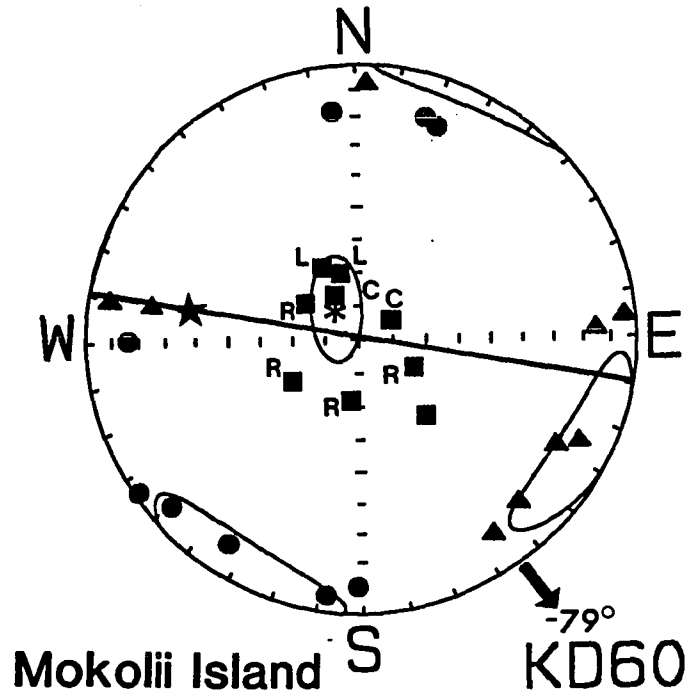
Xmax: Mean D = 290.8      Mean I = 38.2      a95 = 19: 8  
 Xint: Mean D = 116.1      Mean I = 51.7      a95 = 12: 8  
 Xmin: Mean D = 22.8      Mean I = 2.6      a95 = 21: 9

Xmax/Xint = 1.009      Xint/Xmin = 1.006      Xmax/Xmin = 1.015

H = 1.54 +/- 0.32%

E = 0.997      Graham's V = 50.1

F = 1.1 +/- 0.3%      L = 0.9 +/- 0.2%



	Mean X	H	Dmax	Imax	Dint	Iint	Dmin	Imin
KD60.1	0.467E-03	1.2%	152.7	-75.0	326.0	-14.9	56.4	-1.7
KD60.2	0.772E-03	1.8%	124.9	-70.8	268.0	-15.5	1.1	-11.0
KD60.3	0.589E-03	1.7%	59.5	-66.6	295.8	-13.5	201.1	-18.7
KD60.6	0.367E-03	1.4%	238.9	-79.0	99.3	-8.4	8.3	-7.0
KD60.7	0.781E-03	3.7%	153.8	-66.0	299.2	-20.2	33.9	-12.5
KD60.9A	0.434E-03	1.2%	8.6	-71.8	265.4	-4.3	174.1	-17.6
KD60.9B	0.231E-03	0.5%	296.9	-72.0	182.6	-7.6	90.4	-16.2
KD60.10	0.186E-03	0.4%	319.3	-59.8	99.7	-24.2	197.6	-17.0
KD60.11	0.626E-03	3.8%	165.1	-69.5	316.3	-18.2	49.4	-9.2

Site Statistics for KD60

Mean X = (4.947 +/-2.030) x 1E-04

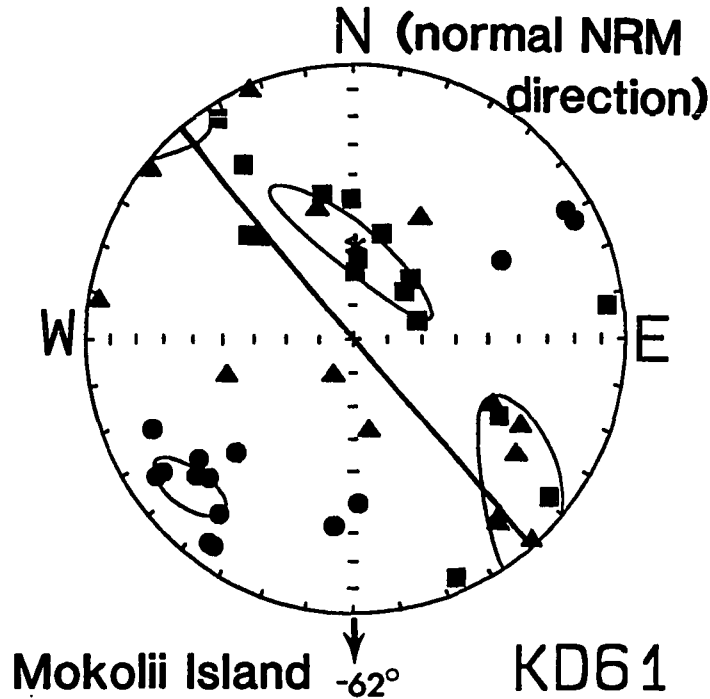
Xmax: Mean D = 324.9      Mean I = 78.6      a95 = 16: 8  
 Xint: Mean D = 117.6      Mean I = 10.2      a95 = 24:10  
 Xmin: Mean D = 28.5      Mean I = -5.1      a95 = 25:12

Xmax/Xint = 1.010      Xint/Xmin = 1.005      Xmax/Xmin = 1.015

H = 1.46 +/- 0.41%

E = 0.995      Graham's V = 54.4

F = 1.0 +/- 0.3%      L = 1.0 +/- 0.3%



	Mean X	H	Dmax	Imax	Dint	Iint	Dmin	Imin
KD61.1	0.592E-03	0.3%	308.8	-8.9	208.6	-48.5	46.4	-40.1
KD61.2	0.119E-02	0.2%	298.1	-40.1	136.5	-48.4	36.0	-9.2
KD61.3A	0.153E-02	0.5%	134.2	-44.9	295.5	-43.6	34.6	-9.4
KD61.4	0.980E-03	1.0%	253.6	-70.6	157.1	-2.3	66.4	-19.2
KD61.5A	0.124E-02	0.6%	226.8	-69.3	129.1	-2.9	38.0	-20.5
KD61.6A	0.159E-02	0.7%	183.5	-66.2	320.8	-17.9	55.8	-15.1
KD61.7A	0.746E-03	0.3%	147.4	-25.8	350.3	-62.3	242.0	-9.4
KD61.7B	0.666E-03	0.4%	147.9	-6.0	28.5	-77.9	239.1	-10.5
KD61.8	0.929E-03	0.2%	337.0	-6.2	74.3	-49.9	241.9	-39.4
KD61.9A	0.148E-02	0.5%	179.2	-47.6	305.6	-28.5	52.8	-28.5
KD61.9B	0.142E-02	0.6%	168.1	-45.2	297.7	-32.3	46.7	-27.3
KD61.10	0.113E-02	0.9%	223.2	-65.5	318.6	-2.4	49.7	-24.3
KD61.11	0.102E-02	0.3%	195.1	-57.4	98.4	-4.3	5.7	-32.2
KD61.12	0.126E-02	0.3%	262.5	-6.6	164.8	-49.4	358.1	-39.8
KD61.6B	0.158E-02	0.7%	181.7	-69.9	322.2	-15.8	55.7	-12.2

Site Statistics for KD61

Mean X = (1.158 +/- 0.320) x 1E-03

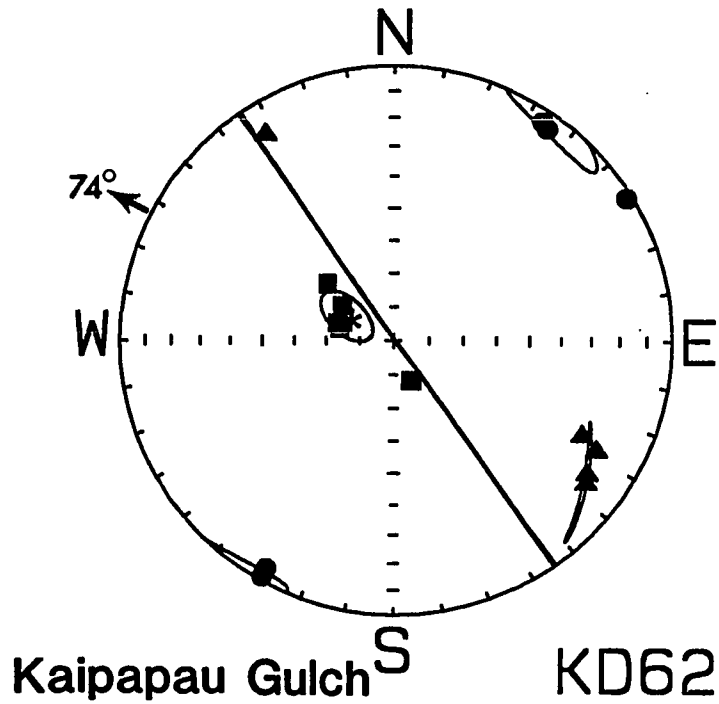
Xmax: Mean D = 0.2      Mean I = 62.3      a95 = 30: 7  
 Xint: Mean D = 131.5      Mean I = 19.1      a95 = 30:11  
 Xmin: Mean D = 48.4      Mean I = -19.3      a95 = 11: 7

Xmax/Xint = 1.001      Xint/Xmin = 1.003      Xmax/Xmin = 1.004

H = 0.38 +/- 0.07%

E = 1.002      Graham's V = 25.1

F = 0.3 +/- 0.1%      L = 0.1 +/- 0.0%



	Mean X	H	Dmax	Imax	Dint	Iint	Dmin	Imin
KD62.3	0.132E-02	2.7%	107.6	-72.4	304.9	-16.8	213.4	-4.9
KD62.6	0.154E-02	1.6%	337.3	-77.2	147.6	-12.6	238.0	-2.1
KD62.7	0.121E-02	3.4%	124.4	-71.6	298.8	-18.3	29.4	-1.7
KD62.8	0.880E-03	1.7%	130.5	-64.0	297.0	-25.4	29.5	-5.3

Site Statistics for KD62

Mean X = (1.256 +/- 0.216) x 1E-03

Xmax: Mean D = 297.4      Mean I = 74.3      a95 = 10: 5

Xint: Mean D = 126.9      Mean I = 15.5      a95 = 16: 1

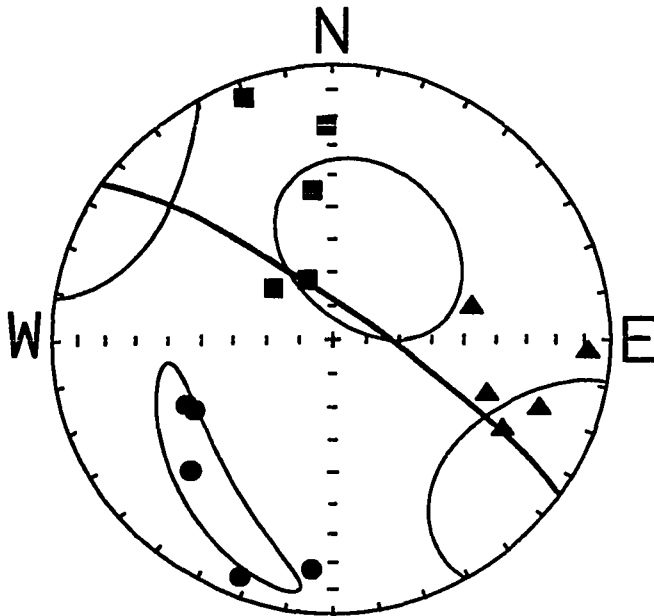
Xmin: Mean D = 36.2      Mean I = 2.5      a95 = 14: 5

Xmax/Xint = 1.011      Xint/Xmin = 1.013      Xmax/Xmin = 1.024

H = 2.33 +/- 0.36%

E = 1.002      Graham's V = 42.9

F = 1.8 +/- 0.3%      L = 1.1 +/- 0.3%



**Kaipapau Gulch<sup>S</sup>      KD63**

	Mean X	H	Dmax	Imax	Dint	Iint	Dmin	Imin
KD63.1	0.184E-02	3.0%	172.4	-44.4	297.7	-30.5	47.7	-30.2
KD63.2	0.178E-02	2.3%	159.8	-6.9	257.1	-46.3	63.3	-42.8
KD63.4	0.167E-02	1.6%	178.4	-23.2	289.3	-39.8	66.4	-41.3
KD63.6	0.125E-02	2.6%	157.2	-70.8	272.7	-8.6	5.4	-17.1
KD63.9	0.106E-02	1.9%	131.2	-66.6	288.4	-21.7	21.7	-8.2

Site Statistics for KD63

Mean X = (1.517 +/- 0.309) x 1E-03

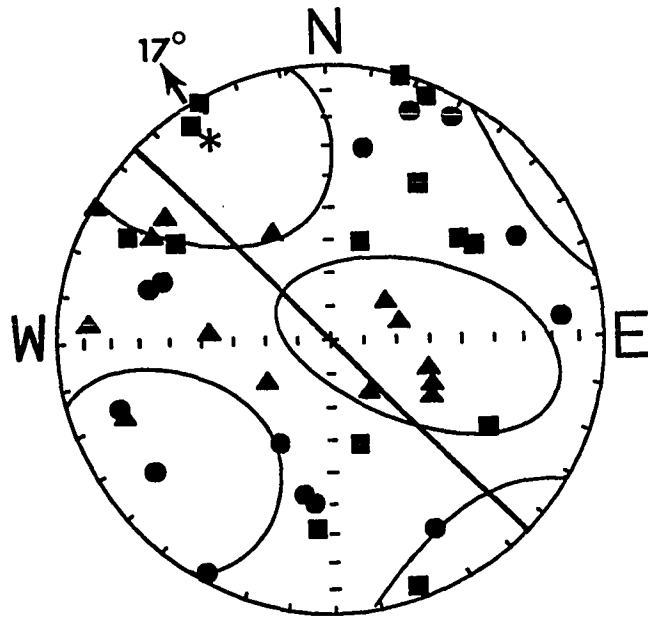
Xmax: Mean D = 22.9	Mean I = 59.6	a95 = 30:24
Xint: Mean D = 125.6	Mean I = 7.4	a95 = 34:26
Xmin: Mean D = 39.8	Mean I = -29.3	a95 = 36: 8

Xmax/Xint = 1.003    Xint/Xmin = 1.014    Xmax/Xmin = 1.017

H = 1.71 +/- 0.33%

E = 1.011                      Graham's V = 26.2

F = 1.5 +/- 0.3%              L = 0.3 +/- 0.3%



Maakua Gulch S KD64

	Mean X	H	Dmax	Imax	Dint	Iint	Dmin	Imin
KD64.1A	0.686E-03	0.8%	196.2	-0.3	286.7	-59.2	106.1	-30.8
KD64.1B	0.753E-03	0.7%	202.8	-4.9	299.8	-55.1	109.4	-34.4
KD64.2A	0.688E-03	0.8%	210.7	-34.7	119.7	-1.4	27.7	-55.3
KD64.2B	0.772E-03	0.8%	237.5	-36.9	126.5	-25.5	10.7	-42.3
KD64.3A	0.500E-03	0.6%	197.9	-59.3	70.4	-19.9	331.8	-22.4
KD64.3B	0.501E-03	0.8%	233.0	-39.5	120.1	-25.3	6.7	-40.0
KD64.4	0.679E-03	1.5%	122.1	-33.2	294.1	-56.5	29.7	-3.7
KD64.5	0.648E-03	1.6%	151.3	-1.7	57.4	-66.7	242.0	-23.3
KD64.6	0.865E-03	1.7%	147.2	-7.4	256.5	-68.4	54.5	-20.2
KD64.7	0.112E-02	0.5%	5.1	-31.5	151.7	-53.7	264.9	-16.2
KD64.8	0.729E-03	0.3%	117.4	-17.5	323.3	-70.6	209.9	-7.9
KD64.9A	0.640E-03	0.7%	345.1	-57.6	94.1	-11.7	190.9	-29.7
KD64.9B	0.932E-03	0.7%	299.5	-34.7	93.6	-52.4	200.5	-12.7
KD64.11	0.982E-03	0.5%	341.1	-5.3	236.3	-69.8	73.0	-19.2

Site Statistics for KD64

Mean X = (7.494 +/- 1.680) x 1E-04

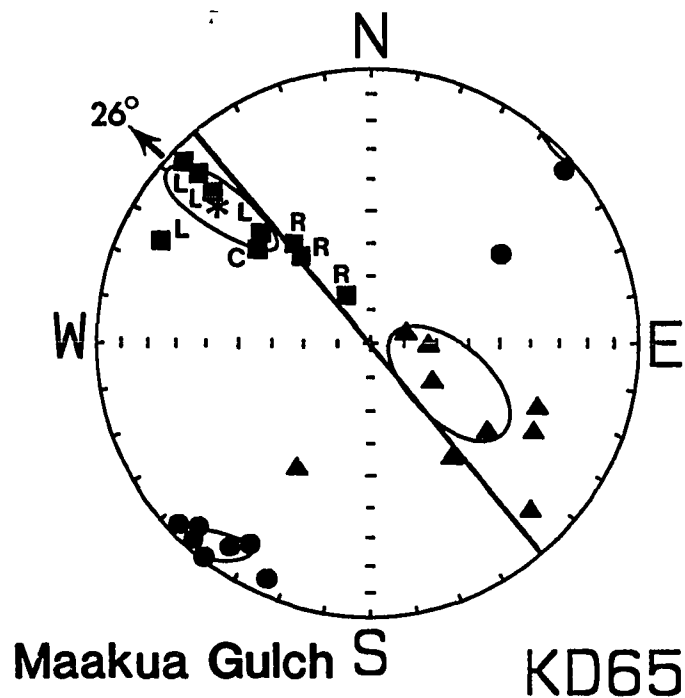
Xmax: Mean D = 329.2      Mean I = 16.6      a95 = 40:28  
 Xint: Mean D = 92.7      Mean I = 61.7      a95 = 46:23  
 Xmin: Mean D = 52.2      Mean I = -22.3      a95 = 36:28

Xmax/Xint = 1.001      Xint/Xmin = 1.002      Xmax/Xmin = 1.003

H = 0.33 +/- 0.15%

E = 1.001      Graham's V = 38.7

F = 0.3 +/- 0.1%      L = 0.1 +/- 0.1%



	Mean X	H	Dmax	Imax	Dint	Iint	Dmin	Imin
KD65.1	0.686E-03	6.0%	134.6	-13.1	30.7	-46.0	236.3	-41.1
KD65.2	0.691E-03	5.3%	134.7	-42.5	324.0	-47.1	229.0	-4.6
KD65.3	0.651E-03	2.9%	133.7	-21.5	301.5	-68.0	42.1	-4.2
KD65.4	0.649E-03	4.5%	134.0	-5.6	254.6	-79.1	43.1	-9.3
KD65.5	0.621E-03	3.8%	116.0	-16.1	272.2	-72.5	24.0	-6.7
KD65.6	0.886E-03	4.3%	141.3	-56.4	298.0	-31.4	34.7	-10.8
KD65.7	0.671E-03	2.1%	129.3	-45.1	306.4	-44.9	37.9	-1.5
KD65.8	0.727E-03	4.1%	142.1	-52.1	290.6	-33.6	31.2	-15.5
KD65.9	0.265E-03	0.9%	152.0	-73.9	315.4	-15.5	46.6	-4.4

Site Statistics for KD65

Mean X = (6.495 +/- 1.547) x 1E-04

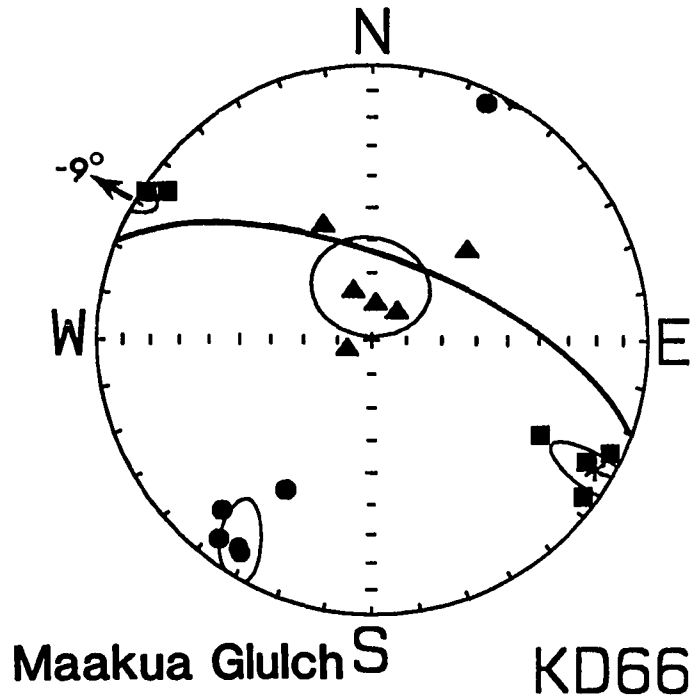
Xmax: Mean D = 312.0      Mean I = 26.3      a95 = 23: 6  
 Xint: Mean D = 116.0      Mean I = 62.8      a95 = 23:11  
 Xmin: Mean D = 38.8      Mean I = -6.5      a95 = 12: 5

Xmax/Xint = 1.014      Xint/Xmin = 1.020      Xmax/Xmin = 1.035

H = 3.44 +/- 0.52%

E = 1.006      Graham's V = 40.3

F = 2.7 +/- 0.5%      L = 1.4 +/- 0.5%



	Mean X	H	Dmax	Imax	Dint	Iint	Dmin	Imin
KD66.1	0.209E-02	1.4%	306.7	-5.6	185.5	-79.2	37.6	-9.2
KD66.2	0.171E-02	2.5%	299.7	-12.0	159.4	-74.5	31.7	-9.6
KD66.3	0.222E-02	2.8%	123.0	-1.6	221.4	-79.0	32.7	-10.8
KD66.5	0.162E-02	2.2%	295.5	-5.4	69.8	-82.4	205.0	-5.4
KD66.6	0.142E-02	1.8%	125.5	-8.1	225.8	-51.7	29.4	-37.2
KD66.9	0.192E-02	2.5%	299.8	-31.3	157.1	-52.7	41.4	-18.3

Site Statistics for KD66

Mean X = (1.832 +/- 0.277) x 1E-03

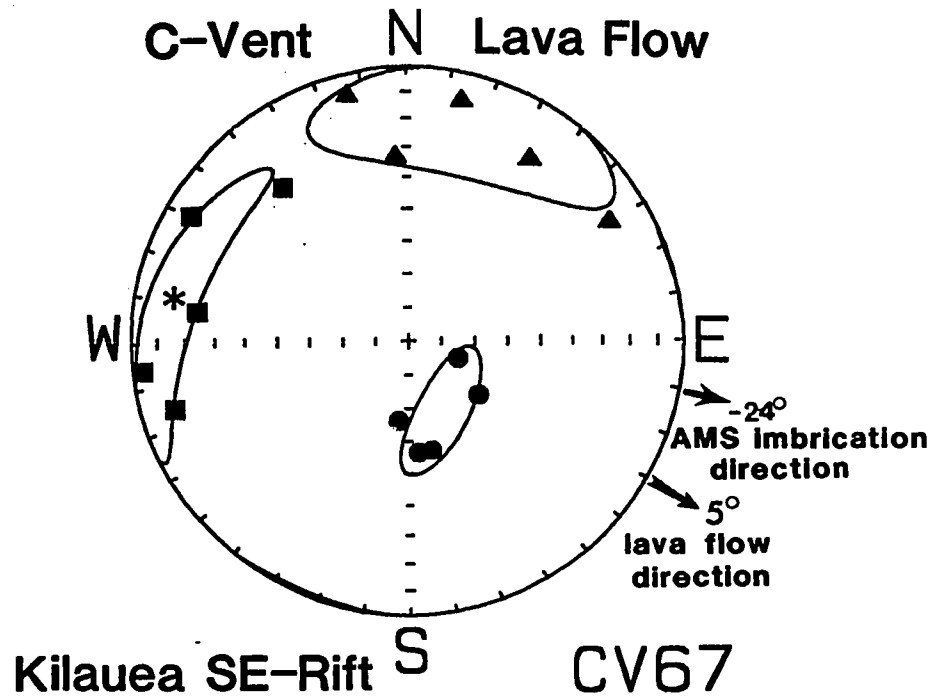
Xmax: Mean D = 300.9      Mean I = -9.0      a95 = 17: 4  
 Xint: Mean D = 177.4      Mean I = -74.0      a95 = 17:15  
 Xmin: Mean D = 33.0      Mean I = -13.1      a95 = 15: 5

Xmax/Xint = 1.007      Xint/Xmin = 1.013      Xmax/Xmin = 1.021

H = 2.07 +/- 0.23%

E = 1.006      Graham's V = 36.9

F = 1.7 +/- 0.2%      L = 0.7 +/- 0.2%



	Mean X	H	Dmax	Imax	Dint	Iint	Dmin	Imin
CV67.1	0.567E-03	0.1%	98.3	-23.7	193.4	-11.3	307.0	-63.4
CV67.2	0.780E-03	0.2%	74.2	-13.1	166.2	-8.6	288.5	-74.2
CV67.3	0.362E-03	0.2%	83.9	-4.0	176.5	-33.3	347.8	-56.5
CV67.4	0.515E-03	0.1%	120.5	-9.9	214.5	-21.5	7.3	-66.1
CV67.6	0.191E-02	0.1%	140.8	-28.6	239.7	-15.8	355.0	-56.6

Site Statistics for CV67

Mean X = (8.262 +/- 5.567) x 1E-04

Xmax: Mean D = 281.1      Mean I = 14.6      a95 = 39: 9

Xint: Mean D = 196.0      Mean I = -18.1      a95 = 39:19

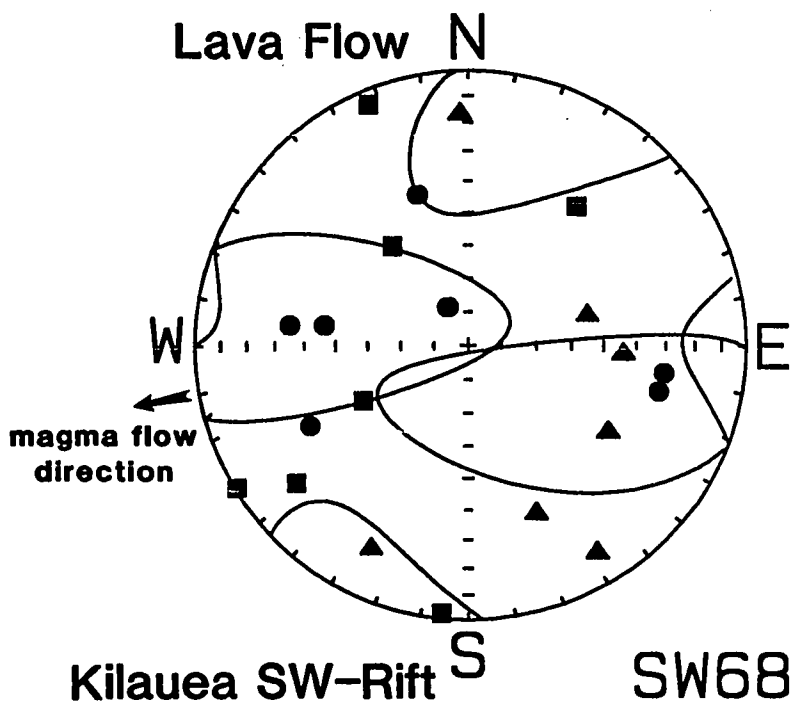
Xmin: Mean D = 334.4      Mean I = -66.4      a95 = 21: 8

Xmax/Xint = 1.000      Xint/Xmin = 1.001      Xmax/Xmin = 1.001

H = 0.14 +/- 0.02%

E = 1.001      Graham's V = 27.6

F = 0.1 +/- 0.0%      L = 0.0 +/- 0.0%



	Mean X	H	Dmax	I <sub>max</sub>	D <sub>int</sub>	I <sub>int</sub>	D <sub>min</sub>	I <sub>min</sub>
SW68.1	0.428E-03	0.3%	217.4	-36.5	338.0	-34.6	96.6	-34.7
SW68.2	0.852E-03	0.2%	142.9	-52.6	25.6	-19.3	283.7	-30.6
SW68.3	0.312E-03	0.1%	157.5	-5.8	255.3	-53.8	63.3	-35.7
SW68.4	0.690E-03	0.2%	58.7	-0.9	328.5	-12.8	152.7	-77.2
SW68.5	0.535E-03	0.1%	51.5	-21.0	302.2	-40.7	161.6	-41.8
SW68.6	0.367E-03	0.1%	5.6	-2.5	273.0	-43.9	98.2	-46.1
SW68.8	0.248E-03	0.0%	62.4	-54.6	178.1	-16.9	278.1	-30.0

**Site Statistics for SW68**

Mean X = (4.904 +/- 2.008) x 1E-04

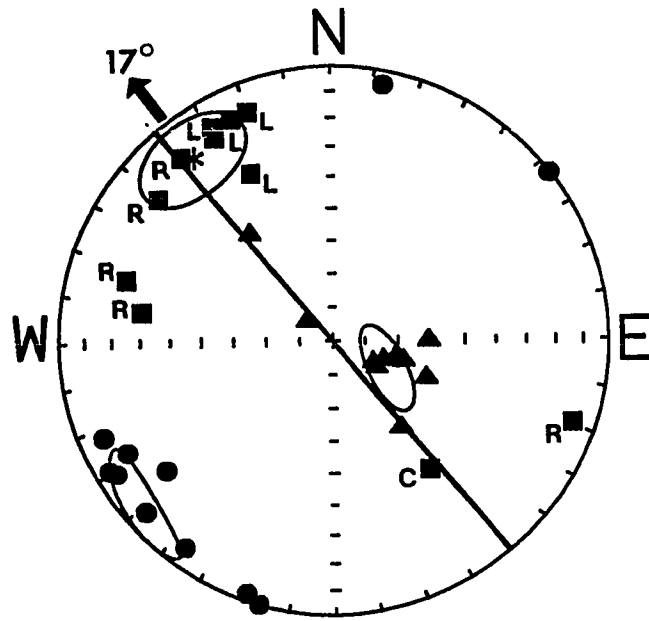
X<sub>max</sub>: Mean D = 17.3      Mean I = 12.1      a<sub>95</sub> = 44:24  
 X<sub>int</sub>: Mean D = 121.5      Mean I = 48.9      a<sub>95</sub> = 62:22  
 X<sub>min</sub>: Mean D = 277.5      Mean I = 38.6      a<sub>95</sub> = 63:24

X<sub>max</sub>/X<sub>int</sub> = 1.000      X<sub>int</sub>/X<sub>min</sub> = 1.000      X<sub>max</sub>/X<sub>min</sub> = 1.001

H = 0.05 +/- 0.03%

E = 1.000      Graham's V = 49.6

F = 0.0 +/- 0.0%      L = 0.0 +/- 0.0%



Koloa Gulch S KD69

	Mean X	H	Dmax	Imax	Dint	Iint	Dmin	Imin
KD69.1A	0.163E-02	0.7%	150.1	-15.5	270.2	-61.0	53.1	-23.8
KD69.1B	0.169E-02	0.6%	159.9	-12.1	300.1	-74.4	67.8	-9.7
KD69.2	0.187E-02	1.2%	154.3	-32.6	321.4	-56.7	60.5	-5.9
KD69.3	0.244E-02	1.3%	140.6	-14.4	289.9	-73.4	48.5	-8.1
KD69.4	0.145E-02	1.6%	155.7	-12.3	282.8	-70.1	62.2	-15.3
KD69.5	0.157E-02	1.6%	150.9	-11.6	296.7	-76.0	59.3	-7.7
KD69.6	0.137E-02	0.9%	323.0	-40.8	142.4	-49.2	232.7	-0.3
KD69.7	0.150E-02	0.3%	129.3	-19.1	285.2	-69.2	36.6	-7.9
KD69.8	0.128E-02	0.4%	106.8	-22.3	285.6	-67.7	16.6	-0.4
KD69.9	0.131E-02	0.9%	99.0	-29.8	291.8	-59.6	192.2	-5.6
KD69.11	0.741E-03	0.7%	289.3	-9.1	128.6	-80.3	19.8	-3.1

Site Statistics for KD69

Mean X = (1.532 +/- 0.399) x 1E-03

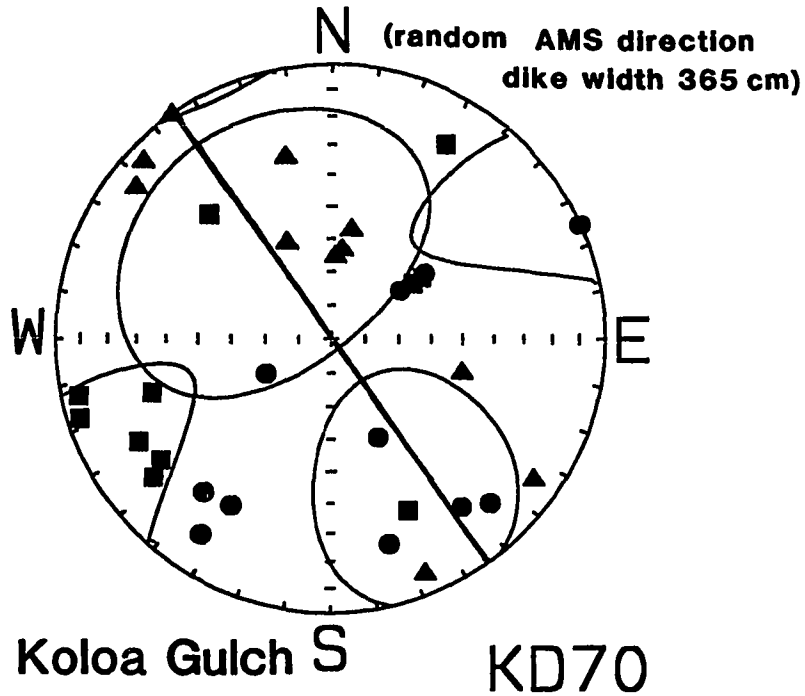
Xmax: Mean D = 322.7      Mean I = 16.7      a95 = 15:14  
 Xint: Mean D = 116.3      Mean I = 71.5      a95 = 14: 6  
 Xmin: Mean D = 50.4      Mean I = -7.8      a95 = 15: 6

Xmax/Xint = 1.002      Xint/Xmin = 1.006      Xmax/Xmin = 1.007

H = 0.74 +/- 0.16%

E = 1.004      Graham's V = 30.3

F = 0.6 +/- 0.1%      L = 0.2 +/- 0.1%



	Mean X	H	Dmax	Imax	Dint	Iint	Dmin	Imin
KD70.1	0.147E-02	0.2%	135.6	-36.7	284.4	-48.9	33.4	-15.8
KD70.2	0.810E-03	0.3%	335.6	-32.0	154.9	-58.1	245.4	-0.3
KD70.3A	0.116E-02	0.9%	236.0	-57.3	127.6	-11.4	30.9	-30.2
KD70.3B	0.123E-02	0.9%	235.9	-60.5	133.3	-7.0	39.4	-28.5
KD70.4	0.120E-02	0.8%	210.6	-19.2	304.4	-10.8	62.2	-67.8
KD70.5	0.112E-01	0.3%	77.1	-7.0	182.7	-65.4	344.0	-23.4
KD70.6	0.991E-03	0.4%	73.3	-32.7	337.8	-8.5	235.1	-55.9
KD70.7	0.934E-03	0.5%	61.7	-22.0	190.3	-57.0	321.7	-23.2
KD70.8	0.996E-03	1.0%	51.9	-19.6	186.9	-63.3	315.5	-17.4
KD70.9	0.100E-02	1.1%	72.3	-5.1	165.5	-32.2	334.3	-57.4
KD70.11	0.986E-03	0.8%	54.3	-25.1	144.4	-0.3	235.0	-64.9

Site Statistics for KD70

Mean X = (2.002 +/- 2.927) x 1E-03

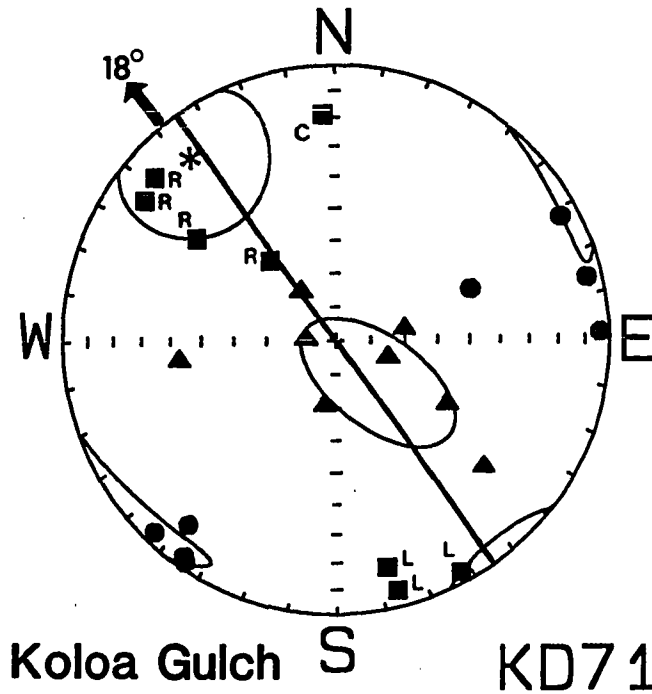
Xmax: Mean D = 59.1      Mean I = 2.9      a95 = 52:18  
 Xint: Mean D = 145.1      Mean I = -54.5      a95 = 50:39  
 Xmin: Mean D = 331.1      Mean I = -35.3      a95 = 40:28

Xmax/Xint = 1.001      Xint/Xmin = 1.001      Xmax/Xmin = 1.003

H = 0.26 +/- 0.11%

E = 1.000      Graham's V = 45.8

F = 0.2 +/- 0.1%      L = 0.1 +/- 0.1%



	Mean X	H	Dmax	Imax	Dint	Iint	Dmin	Imin
KD71.1	0.147E-02	1.1%	126.5	-15.2	288.5	-74.1	35.2	-4.7
KD71.2	0.107E-02	1.0%	141.6	-59.6	311.0	-29.9	43.7	-4.6
KD71.3	0.105E-02	0.7%	126.7	-38.0	300.4	-51.7	34.3	-3.1
KD71.4	0.126E-02	1.0%	132.3	-12.8	260.3	-69.8	38.7	-15.4
KD71.5	0.872E-03	0.9%	177.1	-18.9	9.4	-70.6	268.4	-3.8
KD71.6	0.805E-03	0.1%	346.7	-6.9	83.0	-42.5	249.4	-46.7
KD71.8	0.101E-02	0.3%	347.9	-16.3	146.5	-72.5	256.1	-6.1
KD71.9	0.829E-03	1.2%	332.2	-4.4	93.4	-81.6	241.6	-7.1

Site Statistics for KD71

Mean X = (1.046 +/- 0.213) x 1E-03

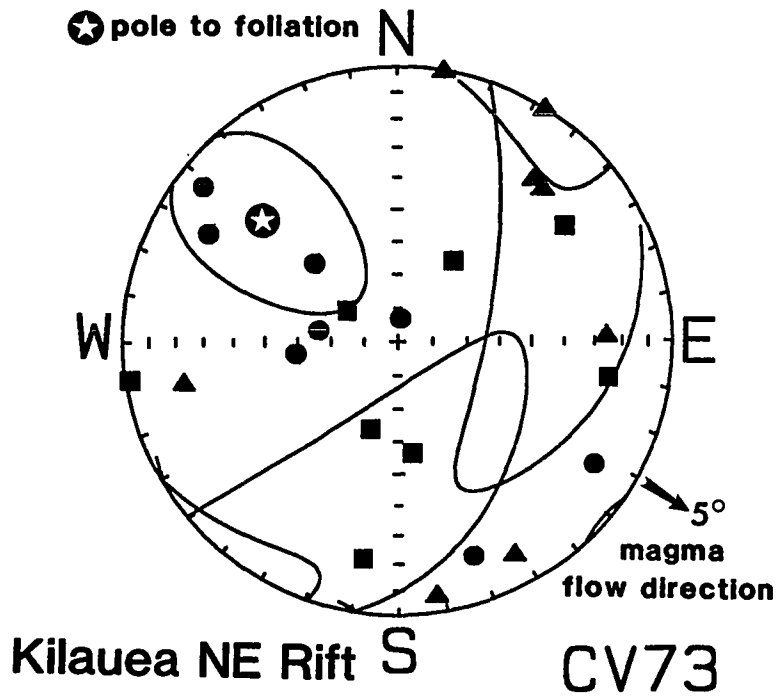
Xmax: Mean D = 322.0      Mean I = 18.0      a95 = 26:19  
 Xint: Mean D = 135.2      Mean I = 71.9      a95 = 27:13  
 Xmin: Mean D = 51.4      Mean I = -2.0      a95 = 23: 6

Xmax/Xint = 1.002      Xint/Xmin = 1.004      Xmax/Xmin = 1.006

H = 0.61 +/- 0.15%

E = 1.002      Graham's V = 33.0

F = 0.5 +/- 0.1%      L = 0.2 +/- 0.1%



	Mean X	H	Dmax	Imax	Dint	Iint	Dmin	Imin
CV73.1	0.772E-03	0.2%	81.9	-1.8	351.7	-6.7	186.5	-83.0
CV73.2	0.542E-03	0.3%	9.3	-20.9	268.7	-25.8	133.4	-55.8
CV73.3	0.442E-03	0.1%	279.9	-24.0	189.6	-0.5	98.4	-66.1
CV73.4	0.432E-03	0.1%	214.1	-61.0	78.8	-21.6	341.2	-18.5
CV73.5	0.550E-03	0.1%	121.4	-72.3	212.4	-0.3	302.5	-17.6
CV73.7A	0.342E-03	0.2%	235.0	-27.6	331.8	-12.4	83.4	-59.4
CV73.9A	0.293E-03	0.3%	352.9	-56.4	220.1	-24.3	119.7	-21.8
CV73.9B	0.290E-03	0.3%	17.4	-62.7	223.6	-24.8	128.6	-10.6

Site Statistics for CV73

Mean X = (4.580 +/- 1.516) x 1E-04

Xmax: Mean D = 10.1      Mean I = -37.0      a95 = 67:25

Xint: Mean D = 250.2      Mean I = -33.4      a95 = 67:23

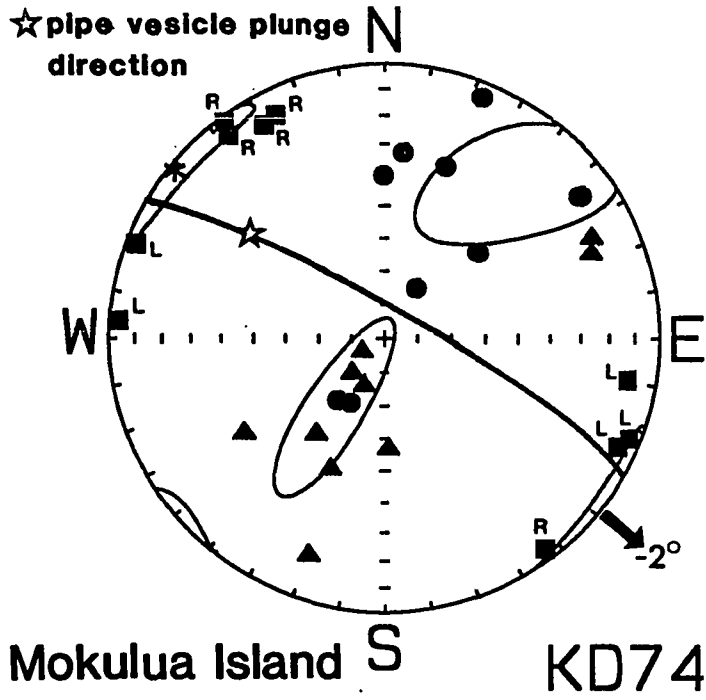
Xmin: Mean D = 312.4      Mean I = 35.3      a95 = 38:19

Xmax/Xint = 1.000      Xint/Xmin = 1.001      Xmax/Xmin = 1.001

H = 0.09 +/- 0.04%

E = 1.001      Graham's V = 24.4

F = 0.1 +/- 0.0%      L = 0.0 +/- 0.0%



	Mean X	H	Dmax	Imax	Dint	Iint	Dmin	Imin
KD74.1	0.114E-02	0.3%	279.9	-11.7	23.1	-47.2	179.8	-40.4
KD74.2	0.147E-02	0.2%	292.5	-4.8	61.2	-82.3	202.0	-6.0
KD74.3	0.314E-02	0.5%	110.8	-3.7	19.7	-17.2	212.4	-72.4
KD74.4B	0.280E-02	0.4%	93.8	-3.5	358.1	-57.1	186.0	-32.6
KD74.6	0.216E-02	0.5%	322.9	-4.4	56.3	-37.9	227.3	-51.9
KD74.7B	0.989E-03	0.2%	295.2	-7.8	36.3	-54.6	199.8	-34.1
KD74.8A	0.215E-02	0.4%	153.6	-10.4	247.5	-20.5	38.2	-66.8
KD74.8B	0.196E-02	0.3%	150.1	-11.7	243.9	-18.0	28.7	-68.4
KD74.10A	0.257E-02	0.6%	143.1	-2.2	44.2	-75.9	233.6	-13.9
KD74.10B	0.287E-02	0.6%	142.1	-7.3	24.2	-74.8	233.8	-13.3

Site Statistics for KD74

Mean X = (2.126 +/- 0.704) x 1E-03

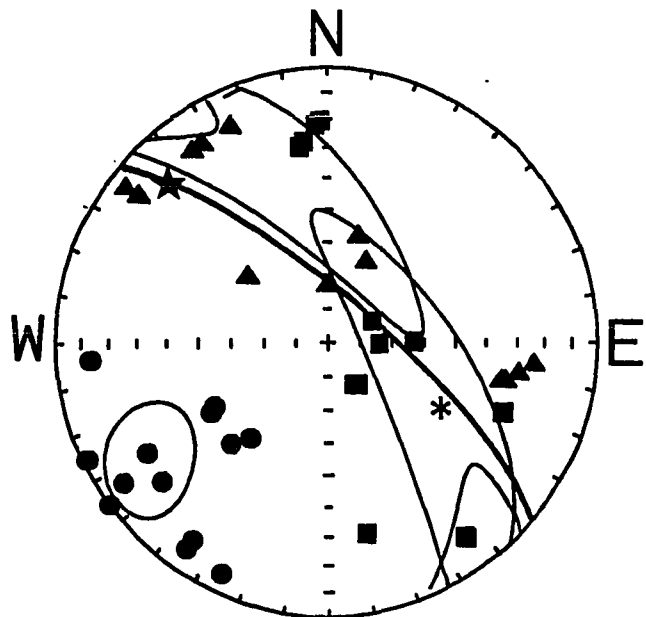
Xmax: Mean D = 309.4      Mean I = 1.5      a95 = 21: 6  
 Xint: Mean D = 216.2      Mean I = 63.7      a95 = 32: 9  
 Xmin: Mean D = 40.1      Mean I = 26.2      a95 = 34:15

Xmax/Xint = 1.002      Xint/Xmin = 1.001      Xmax/Xmin = 1.003

H = 0.28 +/- 0.05%

E = 0.999      Graham's V = 58.4

F = 0.2 +/- 0.1%      L = 0.2 +/- 0.0%



Mokulua Island<sup>S</sup> KD75

	Mean X	H	Dmax	Imax	Dint	Iint	Dmin	Imin
KD75.1	0.554E-02	0.8%	348.2	-29.8	197.1	-56.8	86.0	-13.3
KD75.2	0.449E-02	1.1%	323.7	-13.0	206.5	-63.2	59.3	-23.0
KD75.3	0.425E-02	0.8%	323.8	-13.8	179.9	-73.1	56.2	-9.6
KD75.4A	0.459E-02	1.6%	323.3	-74.6	144.2	-15.4	54.2	-0.2
KD75.4B	0.454E-02	1.5%	327.5	-75.4	155.0	-14.5	64.6	-1.8
KD75.5A	0.504E-02	1.4%	171.5	-28.9	279.0	-28.6	45.0	-47.2
KD75.5B	0.506E-02	1.4%	172.9	-27.3	275.9	-23.5	40.5	-52.6
KD75.6A	0.264E-02	1.5%	176.6	-21.9	282.2	-33.7	60.1	-48.1
KD75.6B	0.233E-02	1.4%	178.1	-20.5	282.0	-32.6	61.7	-50.0
KD75.7	0.462E-02	0.7%	291.1	-30.5	128.5	-58.3	25.7	-7.8
KD75.8A	0.458E-02	1.5%	271.0	-74.0	127.4	-13.0	35.3	-9.2
KD75.8B	0.431E-02	1.5%	244.9	-74.9	127.0	-7.2	35.3	-13.2
KD75.9	0.335E-02	1.2%	269.3	-63.1	147.0	-15.1	50.9	-21.6

Site Statistics for KD75

Mean X = (4.258 +/- 0.901) x 1E-03

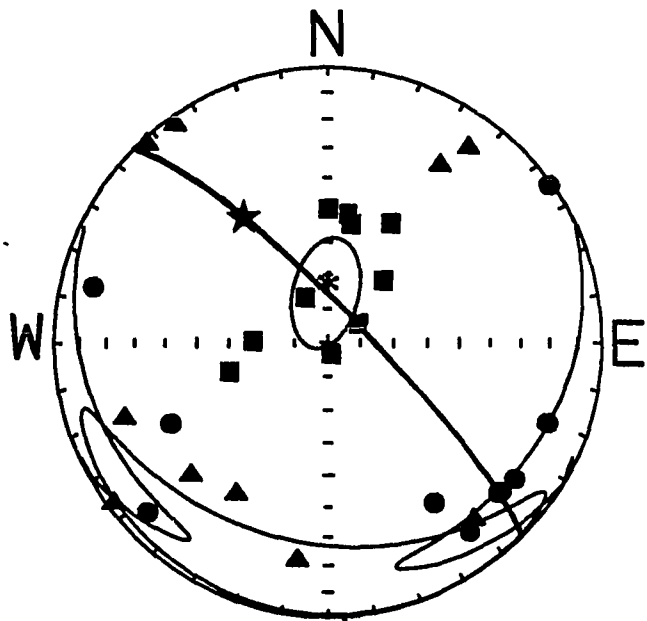
Xmax: Mean D = 298.8      Mean I = -49.9      a95 = 69:15  
 Xint: Mean D = 162.0      Mean I = -31.5      a95 = 69:14  
 Xmin: Mean D = 57.6      Mean I = -22.1      a95 = 19:12

Xmax/Xint = 1.001    Xint/Xmin = 1.007    Xmax/Xmin = 1.007

H = 0.73 +/- 0.13%

E = 1.006      Graham's V = 17.3

F = 0.7 +/- 0.1%      L = 0.1 +/- 0.2%



Mokulua Island  $S_{-75^\circ}$  KD76

	Mean X	H	Dmax	Imax	Dint	Iint	Dmin	Imin
KD76.1A	0.215E-02	0.7%	180.4	-49.9	31.8	-35.8	290.0	-15.8
KD76.1B	0.194E-02	0.6%	222.4	-64.9	8.3	-21.2	103.3	-12.8
KD76.2A	0.416E-02	1.3%	238.7	-79.1	137.5	-2.1	47.1	-10.6
KD76.2B	0.493E-02	1.7%	344.1	-86.6	144.7	-3.2	234.7	-1.1
KD76.3B	0.237E-02	0.3%	208.6	-49.1	320.0	-17.5	63.1	-35.5
KD76.6	0.324E-02	0.8%	153.3	-75.0	53.5	-2.6	322.8	-14.8
KD76.7A	0.330E-02	0.4%	191.7	-53.7	46.5	-31.1	306.0	-16.8
KD76.7B	0.335E-02	0.4%	189.3	-50.9	69.8	-21.8	326.1	-30.6
KD76.9A	0.305E-02	0.5%	74.0	-59.0	212.7	-24.3	311.1	-18.0
KD76.9B	0.478E-02	0.6%	91.5	-67.5	216.2	-13.2	310.5	-17.8

Site Statistics for KD76

Mean X = (3.328 +/- 0.984) x 1E-03

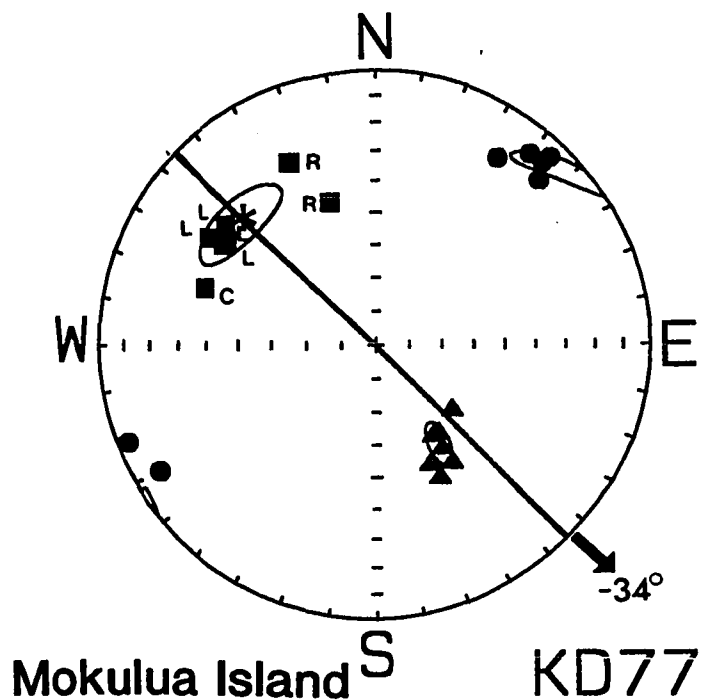
Xmax: Mean D = 358.0      Mean I = 75.2      a95 = 17:10  
 Xint: Mean D = 189.3      Mean I = 14.5      a95 = 65:13  
 Xmin: Mean D = 278.6      Mean I = -2.8      a95 = 64: 9

Xmax/Xint = 1.004      Xint/Xmin = 1.001      Xmax/Xmin = 1.005

H = 0.52 +/- 0.11%

E = 0.997      Graham's V = 65.5

F = 0.3 +/- 0.1%      L = 0.4 +/- 0.1%



	Mean X	H	Dmax	Imax	Dint	Iint	Dmin	Imin
KD77.1	0.460E-02	1.1%	109.0	-36.1	326.8	-47.3	214.0	-19.6
KD77.2	0.363E-02	2.1%	155.5	-28.1	310.5	-59.5	59.6	-10.9
KD77.3	0.397E-02	1.8%	162.7	-44.6	334.1	-45.1	68.4	-4.3
KD77.4A	0.523E-02	2.7%	129.6	-32.0	324.6	-57.1	223.9	-6.8
KD77.4B	0.475E-02	2.8%	126.3	-35.3	327.3	-52.8	223.5	-10.2
KD77.5A	0.490E-02	2.4%	123.6	-30.1	327.9	-57.6	220.0	-11.0
KD77.5B	0.445E-02	2.1%	124.3	-35.5	335.5	-50.2	225.8	-15.7

Site Statistics for KD77

Mean X = (4.502 +/- 0.511) x 1E-03

Xmax: Mean D = 312.7      Mean I = 34.5      a95 = 14: 7

Xint: Mean D = 147.6      Mean I = 54.6      a95 = 7: 3

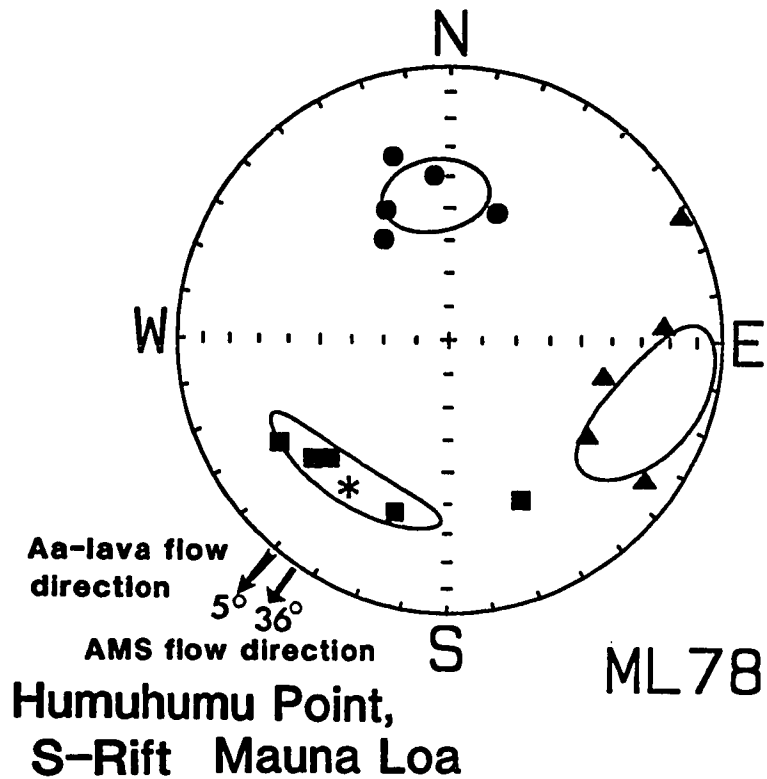
Xmin: Mean D = 47.6      Mean I = 7.0      a95 = 14: 3

Xmax/Xint = 1.010      Xint/Xmin = 1.010      Xmax/Xmin = 1.019

H = 1.92 +/- 0.25%

E = 1.000      Graham's V = 44.7

F = 1.4 +/- 0.2%      L = 1.0 +/- 0.2%



	Mean X	H	Dmax	Imax	Dint	Iint	Dmin	Imin
ML78.1	0.326E-03	1.4%	335.2	-36.1	242.0	-4.3	146.2	-53.6
ML78.2	0.719E-03	1.3%	49.1	-33.7	283.4	-41.2	162.3	-30.5
ML78.4	0.422E-03	2.6%	59.0	-27.6	304.6	-38.1	174.4	-39.4
ML78.5	0.814E-03	0.6%	17.4	-34.4	266.3	-22.0	153.3	-46.0
ML78.6	0.254E-03	1.5%	45.4	-38.2	305.3	-12.5	200.5	-49.0

Site Statistics for ML78

Mean X = (5.070 +/- 2.206) x 1E-04

Xmax: Mean D = 35.4      Mean I = -36.2      a95 = 27: 7  
 Xint: Mean D = 108.3      Mean I = 21.9      a95 = 26:14  
 Xmin: Mean D = 354.0      Mean I = 45.7      a95 = 15:12

Xmax/Xint = 1.004      Xint/Xmin = 1.009      Xmax/Xmin = 1.014

H = 1.35 +/- 0.34%

E = 1.005      Graham's V = 35.0

F = 1.1 +/- 0.4%      L = 0.4 +/- 0.3%

## APPENDIX B

	K <sub>11</sub>	K <sub>22</sub>	K <sub>33</sub>	K <sub>12</sub>	K <sub>23</sub>	K <sub>13</sub>	
I <sub>A</sub>	0.1667	0.1666	-0.3333	-0.6667	0.3333	0.3333	
I <sub>A'</sub>	0.1667	0.1667	-0.3333	0.6667	0.3333	-0.3333	
I <sub>B</sub>	0.1667	0.1667	-0.3333	-0.6667	-0.3333	-0.3333	
I <sub>B'</sub>	0.1667	0.1667	-0.3333	0.6667	-0.3333	0.3333	
I <sub>C</sub>	0.1667	0.1667	-0.3333	-0.6667	0.3333	0.3333	
I <sub>C'</sub>	0.1667	0.1667	-0.3333	0.6667	0.3333	-0.3333	
I <sub>D</sub>	0.1667	0.1667	-0.3333	-0.6667	-0.3333	-0.3333	
I <sub>D'</sub>	0.1667	0.1667	-0.3333	0.6667	-0.3333	0.3333	
Q <sub>A</sub>	0.2887	-0.2887	0.0000	0.0000	0.5773	-0.5773	= R
Q <sub>A'</sub>	-0.2887	0.2887	0.0000	0.0000	-0.5773	-0.5773	
Q <sub>B</sub>	0.2887	-0.2887	0.0000	-0.0000	-0.5773	0.5773	
Q <sub>B'</sub>	-0.2887	0.2887	0.0000	-0.0000	0.5773	0.5773	
Q <sub>C</sub>	-0.2887	0.2887	0.0000	-0.0000	-0.5773	0.5773	
Q <sub>C'</sub>	0.2887	-0.2887	0.0000	-0.0000	0.5773	0.5773	
Q <sub>D</sub>	-0.2887	0.2887	0.0000	0.0000	0.5773	-0.5773	
Q <sub>D'</sub>	0.2887	-0.2887	0.0000	0.0000	-0.5773	-0.5773	
BS	0.5000	0.5000	0.0000	1.0000	0.0000	0.0000	

	K <sub>11</sub>	K <sub>22</sub>	K <sub>33</sub>	K <sub>12</sub>	K <sub>23</sub>	K <sub>13</sub>	
I <sub>A</sub>	0.1875	0.1875	-0.1875	-0.1875	0.0938	0.0938	
I <sub>A'</sub>	-0.1875	-0.1875	-0.5625	0.1875	0.0938	-0.0938	
I <sub>B</sub>	0.1875	0.1875	-0.1875	-0.1875	-0.0938	-0.0938	
I <sub>B'</sub>	-0.1875	-0.1875	-0.5625	0.1875	-0.0938	0.0938	
I <sub>C</sub>	0.1875	0.1875	-0.1875	-0.1875	0.0938	0.0938	
I <sub>C'</sub>	-0.1875	-0.1875	-0.5625	0.1875	0.0938	-0.0938	
I <sub>D</sub>	0.1875	0.1875	-0.1875	-0.1875	-0.0938	-0.0938	
I <sub>D'</sub>	-0.1875	-0.1875	-0.5625	0.1875	-0.0938	0.0938	
Q <sub>A</sub>	0.2165	-0.2165	0.0000	0.0000	0.1624	-0.1624	= (R <sup>T</sup> R) <sup>-1</sup> R <sup>T</sup>
Q <sub>A'</sub>	-0.2165	0.2165	-0.0000	0.0000	-0.1624	-0.1624	
Q <sub>B</sub>	0.2165	-0.2165	0.0000	-0.0000	-0.1624	0.1624	
Q <sub>B'</sub>	-0.2165	0.2165	-0.0000	-0.0000	0.1624	0.1624	
Q <sub>C</sub>	-0.2165	0.2165	-0.0000	-0.0000	-0.1624	0.1624	
Q <sub>C'</sub>	0.2165	-0.2165	0.0000	-0.0000	0.1624	0.1624	
Q <sub>D</sub>	-0.2165	0.2165	-0.0000	0.0000	0.1624	-0.1624	
Q <sub>D'</sub>	0.2165	-0.2165	0.0000	0.0000	-0.1624	-0.1624	
BS	1.0000	1.0000	1.0000	0.0000	0.0000	0.0000	

Where R is a (17 x 6) matrix of coefficients calculated from the fixed set of angles representing the directions of each measured component (I is the in-phase component, Q is the out-of-phase component, and I' and Q's are the measured components rotated 180°

about the reference direction.  $\chi$  is then obtained from the second (17 x 6) matrix using the least squares inverse.

## REFERENCES

- Adams, W. M., and A. S. Furumoto, A seismic refraction study of the Koolau volcanic plug, *Pacific Sci.*, 17, 296-305, 1965.
- Anderson, A. T., G. W. Swihart, G. Artioli, and C. A. Geiger, Segregation vesicles, gas filter-pressing, and igneous differentiation, *J. Geology*, 92, 55-72, 1984.
- Baer, G. and Ze'ev Reches, Flow patterns of magma in dikes, Makhtest Ramon, Israel, *Geology*, 15, 569-572, 1987.
- Bagnold, R. A., Experiments on gravity-free dispersion of large spheres in a Newtonian fluid under shear, *Proc. R. Soc. London, Ser. A*, 225, 49-63, 1954.
- Balsley, J. R., and A. F. Buddington, Iron-titanium oxide minerals, rocks and aeromagnetic anomalies of the Adirondack area, New York, *Econ. Geol.*, 53, 777-805, 1958.
- Barriere, M., Flowage differentiation: Limitation of the "Bagnold effect" to the narrow intrusions, *Contrib. Mineral. Petrol.*, 55, 139-145, 1976.
- Bhattacharji, S., and C. H. Smith, Flow differentiation, *Science*, 145, 150-153, 1964.
- Bhattacharji, S., Mechanics of flow differentiation in ultramafic and mafic sills, *J. Geology*, 75, 101-112, 1966.
- Bhathal, R. S. and F. D. Stacey, Field-induced anisotropy of magnetic susceptibility in rocks, *Pure Appl. Geophys.*, 76, 123-129, 1969.
- Bhathal, R. S., Magnetic anisotropy in rocks, *Earth-Sci. Rev.*, 7, 227-253, 1971.
- Bigelow, G. E., Distribution and characteristics of dikes in the southeast part of the Koolau Range, M.S. thesis, submitted to Univ. Hawaii, pp. 27, 1968.
- Blanchard, J.-P., P. Boyer, and et C. Gagny, Un nouveau reitere de sens de en place dans une caisse filonienne: Le "pincement" des mineraux aux epointes, *Tectonophysics*, 53, 1-25, 1979.
- Bowen, N. L., *The evolution of the igneous rocks*, Princeton University Press, 1928.

- Campbell, I. H., The difference between oceanic and continental tholeiites: a fluid dynamic explanation, *Contr. Min. Petro.*, 91, 37–43, 1985.
- Chevallier L. and W. J. Verwoerd, A numerical model for the mechanical behavior of intraplate volcanoes, *J. Geophys. Res.*, 93, 4182–4198, 1988.
- Cogne, J. P., and H. Perroud, Anisotropy of magnetic susceptibility as a strain gauge in the Flamanville granit, NW France, *Physics Earth Planet. Int.*, 51, 264–270, 1988.
- Collinson, D. C., Methods in rock magnetism and paleomagnetism: Techniques and instrumentation, editor David Wright, Chapman and Hall, 503 pp., 1983.
- Coombs, C. and G. P. L. Walker, (in review).
- Crosson, R. S., and E. T. Endo, Focal mechanisms and locations of earthquakes in the vicinity of the 1975 Kalapana earthquake aftershock zone 1970–1979: implications for tectonics of the south flank of Kilauea Volcano, Island of Hawaii, *Tectonics*, 1, 495–542, 1982.
- Daly, R. A., Igneous Rocks and the Depths of the Earth, McGraw-Hill Book Co., New York, 1933.
- Delaney, P. T., and D. D. Pollard, Solification of basaltic magma during flow in a dike, *Amer. J. Sci.*, 282, 856–885, 1982.
- Den Tex, E., Origin of ultramafic rocks, their tectonic setting and history: A contribution to the discussion of the paper "The origin of ultramafic and ultrabasic rocks" by P. J. Wyllie, *Tectonophysics*, 7, 457–488, 1969.
- Dickinson, W. R., Geology of the Suplee-Izee area, Crook, Grant, and Harney counties, Oregon, *Oregon Dept. Geol. Min. Res. Bull.*, 66, 707–725, 1965.
- Dieterich, J. H., Growth and persistence of Hawaiian volcanic rift zones, *J. Geophys. Res.* 93, 4258–4270, 1988
- Diller, D. E., Contributions to the geology of West Maui Volcano, M.S. thesis, 237 pp., Univ. Hawaii, 1982.

- Doell, R. R. and G. B. Dalrymple, Potassium-argon ages and paleomagnetism of the Waianae and Koolau volcanic series, Oahu, Hawaii, *Geol. Soc. Am. Bull.*, 84, 1217–1242, 1973.
- Duffield, W. A., R. L. Christiansen, R. Y. Koyanagi, and D. W. Peterson, Storage, migration and eruption of magma at Kilauea volcano, Hawaii, 1971–1972, *J. Volcan. Geotherm. Res.*, 13, 273–307, 1982.
- Dvorak, J. J., and A. T. Okamura, A hydraulic model to explain variations in summit tilt rate at Kilauea and Mauna Loa volcanoes, in Volcanism in Hawaii, *U. S. Geol. Surv. Prof. Pap.*, 1350, 2, 1281–1296, 1987.
- Dzurisin, D. R., Y. Koyanagi, and T. T. English, Magma supply and storage at Kilauea Volcano, Hawaii, 1956–1983, *J. Volcanol. Geotherm. Res.*, 21, 177–206, 1984
- Easton, R. M., and J. P. Lockwood, "Surface-fed dikes" –the origin of some unusual dikes along the Hilina fault zone, Kilauea Volcano, Hawaii, *Bull. Volcanol.*, 46, 45–53, 1983.
- Ellsworth, W. L., and R. Y. Koyanagi, Three-dimensional crust and mantle structure of Kilauea volcano, Hawaii, *J. Geophys. Res.*, 82, 5379–5394, 1977.
- Ellwood, B. B., Analysis of emplacement mode in basalt from Deep Sea Drilling Project holes 319a and 321 using anisotropy of magnetic susceptibility, *J. Geophys. Res.*, 80, 4805–4808, 1975.
- Ellwood, B. B., Flow and emplacement direction determined for selected basaltic bodies using magnetic susceptibility anisotropy of magnetic susceptibility measurements, *Earth Planet. Sci. Lett.*, 41, 254–264, 1978.
- Ellwood, B. B., Estimates of flow direction for calc-alkaline welded tuffs and paleomagnetic data reliability from anisotropy of magnetic susceptibility measurements: Central San Juan Mountains, southwest Colorado, *Earth Planet. Sci. Lett.*, 59, 303–314, 1982.

- Ellwood, B. B., Magnetic Fabric in sediments: A discussion on factors controlling interpretation of geological processes, (abstract) *Eos Trans.*, 69, 1159, 1988.
- Ellwood, B. B. and M. R. Fisk, Anisotropy of magnetic susceptibility variations in a single Icelandic columnar basalt, *Earth Planet. Sci. Lett.*, 35, 116–122, 1977.
- Ellwood, B. B. and J. A. Wolff, Welded-tuff dykes: Possible implications for the mechanism of explosive-effusion transition during the closing stages of pyroclastic eruptions (abstract), *Eos Trans. AGU*, 66, 1151, 1985.
- Epp, D., R. W. Decker and A. T. Okamura, Relation of summit deformation to east rift zone eruptions on Kilauea volcano, Hawaii, *Geophys. Res. Lett.*, 10, 493–496, 1983.
- Fedotov, S. A., Ascent of Basic magmas in the crust and the mechanism of basaltic fissure eruptions, *Internat. Geol. Rev.*, 20, 33–48, 1978.
- Fisher, R. A., Dispersion on a sphere, *Proc. R. Soc. London*, 217, 295–305, 1953.
- Fiske, R. S. and E. D. Jackson, Orientation and growth of Hawaiian volcanic rifts: the effect of regional structure and gravitational stress, *Phil. Trans. Soc. London, Ser A*, 329, 299–326, 1972.
- Flinn, D., On folding during three-dimensional progressive deformation, *Geol. Soc. London Quart. J.*, 118, 385–433, 1962.
- Furumoto, A. S., and R. L. Kovach, The Kalapana earthquake of November 29, 1975: an intraplate earthquake and its relation to geothermal processes, *Phys. Earth Planet Interiors*, 18, 197–208, 1979.
- Gartner, A. and P. Delaney, Dominantly horizontal propagation directions of diabasic dikes, San Rafael Desert Region, Utah, *Eos Trans.*, 66, 1145, 1985.
- Gibb F. G. F., Flow differentiation in the xenolithic ultrabasic dykes of the Cuillins and the Strathaird Peninsula, Isle of Skye, Scotland, *J. Petrology*, 9, 411–443, 1968.
- Goldsmith, J. L., and S. G. Mason, The microrheology of dispersions, in Rheology, theory and application, editor F. R. Eirich, New York, Academic Press, Inc., v. 4, 85–250, 1967.

- Goldstein, S., Modern developments in fluid mechanics, Oxford: Clarendon Press, 1938.
- Grabopvsky, A. and S. Yu. Brodskaya, Normal magnetization and thermal magnetization of anisotropic rocks, *Bull. Acad. Sci. U.S.S.R., Geophys. Ser.*, 8, 560–566, 1958.
- Grace, H. P., Dispersion phenomena in high viscosity immiscible fluid systems and application of static mixers as dispersion devices in such systems, *Eng. Found., Res. Conf. Mixing, 3 rd, Andover, N. H.*, republished in: *Chem. Eng. Commun.* 14, 225–277 (1982), 1971.
- Graham, J. W., Changes of ferromagnetic minerals and their bearing on magnetic properties of rocks, *J. Geophys. Res.*, 58, 243–260, 1953.
- Graham, J. W., Significance of magnetic anisotropy in Appalachian sedimentary rocks, in The Earth Beneath the Continents, Geophys. Monogr. Ser., 10, edited by J. A. Steinhart and T. J. Smith, 627–648 pp., Washington, D. C., 1966.
- Granar, L., Magnetic measurements on Swedish varved sediments, *Arkiv. F. Geofysik*, 3, 1–40, 1958.
- Gudmundsson, A., Form and dimensions of dykes in eastern Iceland, *Tectonophysics*, 95, 295–307, 1983.
- Harker, A., Tertiary igneous rocks of Skye, *Memoir. of the Geol. Survey of Scotland*, 1904.
- Hoffman J. P., Pu'u O'o's plumbing system, Kilauea, Hawaii, M.S. thesis, pp., Univ. Hawaii, 1988.
- Holcomb, R. T., Kilauea Volcano, Hawaii: Chronology and morphology of the surficial lava flows, Palo Alto, Stanford University, Ph.D. thesis, 321 pp., 1980.
- Holcomb, R. T., Kilauea Volcano, Hawaii: Chronology and morphology of the surficial lava flows, Ph.D., Stanford University, 321 pp., 1980.
- Holcomb, R. T., Eruptive history and long-term behavior of Kilauea Volcano, in *Volcanism in Hawaii, 1, U.S. Geol. Surv. Prof. Pap.*, 1350, 261–350, 1987.

- Hill, D. P., Crustal structure of the island of Hawaii from seismic refraction measurements, *Bull. Seismol. Soc. Am.*, 59, 101–130, 1969.
- Hill, D. P., and J. J. Zucca, Geophysical constraints on the structure of Kilauea and Mauna Loa Volcanoes and some implications for seismomagmatic processes, in *Volcanism in Hawaii, 2, U.S. Geol. Surv. Prof. Pap., 1350*, 903–918, 1987.
- Hrouda, F., M. Chlupacova, and L. Rejl, The mimetic fabric of magnetite in some foliated granodiorites, as indicated by magnetic anisotropy, *Earth Planet. Sci. Letters*, 11, 381–384, 1971.
- Hulme, G., Turbulent lava flow and the formation of lunar sinuous rilles, *Mod. Geol.*, 4, 107–117, 1973.
- Huppert, H. E. and R. S. J. Sparks, Komatiites, I. Eruption and flow, *J. Petrol.*, 26, 1985a.
- Huppert, H. E. and R. S. J. Sparks, Cooling and contamination of mafic and ultramafic magmas during ascent through continental crust, *Earth and Planet. Sci. Let.*, 74, 371–386, 1985b.
- Incoronato, A., F. T. Addison, D. H. Tarling, G. Nardi, and T. Pescatore, Magnetic fabric investigation of some pyroclastic deposits from the Phlegrean Fields, southern Italy, *Nature*, 306, 461–463, 1983.
- Jackson, E. D., and T. L. Wright, Xenoliths in the Honolulu Volcanic Series, Hawaii, *J. Petrol.*, 11, 405–430, 1970.
- Jeffrey, G. H., The motion of ellipsoidal particles immersed in a viscous fluid, *Proc. R. Soc. London, Ser. A*, 102, 161–179, 1922.
- Jeffrey, R. C., and J. R. S. Pearson, Partical motion in laminar vertical tube flow, *J. Fluid. Mech.*, 22, 721–735, 1965.
- Jelinek, V., Statistical processing of anisotropy of magnetic susceptibility measured on groups of specimens, *Stud. Geophys. Geod.*, 22, 50–62, 1978.

- Jelinek, V., Characterization of magnetic fabric of rocks, *Tectonophysics*, 79, 563–567, 1980.
- Khan, M. A., The anisotropy of magnetic susceptibility of some igneous and metamorphic rocks, *J. Geophys. Res.*, 67, 2873–2885, 1962.
- Kilburn, C. R. J., A study of the morphological and rheological development of the basaltic aa lavas on Mt. Etna, Sicily, (Ph. D.), Univ. London Obser. Planet. Image Center, 1984.
- King, R. F., and A. I. Rees, The measurement of the anisotropy of magnetic susceptibility of rocks by the torque method, *J. Geophys. Res.*, 67, 1565–1572, 1962.
- Kinoshita, W. T., H. L. Krivoy, D. R. Mabey, and R. R. MacDonald, Gravity survey of the Island of Hawaii, *U.S. Geol. Survey Prof. Pap.*, 475–C, 114–116, 1963.
- Kligfield, R., W. Lowrie, and I. W. D. Dalziel, Magnetic susceptibility anisotropy as a strain indicator in the Sudbury Basin, Ontario, *Tectonophysics*, 40, 287–308, 1977.
- Klein, F. W., R. Y. Koyanagi, J. S. Nakata, and W. R. Tanigawa, The seismicity of Kilauea's magma system, in Volcanism in Hawaii, *U. S. Geol. Surv. Prof. Pap.*, 1350, 2, 1019–1186, 1987.
- Knight M. D., G. P. L. Walker, B. B. Ellwood, and J. F. Diehl, Stratigraphy, Paleomagnetic, and magnetic fabric of the Toba Tuffs: Constraints on the source and eruptive styles, *J. Geophys. Res.*, 91, 10,355–10,382, 1986.
- Knight M. D., and G. P. L. Walker, Magma flow directions in dikes of the Koolau Complex, Oahu, determined from magnetic fabric studies, *J. Geophys. Res.*, 93, 4301–4319, 1988.
- Knopf, A., Igneous geology of the Spanish Peaks region, Colorado, *Bull. Geol. Soc. Am.*, 47, 1727–1784, 1936.
- Komar, P. D., Mechanical interactions of Phenocrysts and flow differentiation of igneous dikes and sills, *Geol. Soc. Am. Bull.*, 83, 973–988, 1972.

- Larson, E. E., and D. W. Strangway, Magnetization of the Spanish Peak Dike Swarm, Colorado, and Shiprock Dike, New Mexico, *J. Geophys. Res.*, 74, 1505–1514, 1969
- Lienert, B. R., Calculation of AMS errors, (abstract) *Eos Trans.*, 69, 1159, 1988.
- Lipman, P. W., The southwest rift zone of Mauna Loa: Implications for structural evolution of Hawaiian volcanoes, *Am. Jour. Sci.*, 280, 752–776, 1980.
- Lipman, P. W., J. P. Lockwood, R. T. Okamura, D. S. Swanson, and K. M. Yamashita, Ground deformation associated with the 1975 Kalapana magnitude 7.2 earthquake and resulting changes of activity of Kilauea volcano, Hawaii, *U.S. Geol. Surv. Prof. Pap.*, 1276, 45 pp., 1985.
- Lockwood J. P., J. J. Dvorak, T. T. English, R. Y. Koyanagi, A. T. Okamura, M. L. Summers, and W. R. Tnigawa, Mauna Loa 1974–1984: A decade of intrusive and extrusive activity, in Volcanism in Hawaii, *U. S. Geol. Surv. Prof. Pap.*, 1350, 1, 537–570, 1987
- Macdonald, G. A., Pahoehoe, aa, and block lava, *Am. J. Sci.*, 251, 169–191, 1953.
- Macdonald, G. A., A. T. Abbott, and F. L. Peterson, Volcanoes in the sea, the geology of Hawaii, University of Hawaii press, Honolulu, 517 pp., 1983.
- Macdonald, W. D., and B. B. Ellwood, Magnetic fabric of peridotite with intersecting petrofabric surfaces, Tinaquillo, Venezuela, *Physics Earth Planet. Int.*, 51, 301–312, 1988.
- Mason, S. G. and R. St J. Manley, Particle motions in sheared suspensions: orientations and interactions of ridge rods, 117–131, 1956.
- McDougall I. and D. H. Tarling, Dating of polarity zones on the Hawaiian Islands, *Nature*, 200, 54–56, 1963.
- McMillan, K., R. W. Cross, and P. E. Long, Two-stage vesiculation in the Cohasset flow of the Grande Ronde Basalt, south-central Washington, *Geology*, 15, 809–812, 1987.
- Moore, J. G., Giant submarine landslides on the Hawaiian ridge, *U. S. Geol. Surv. Prof. Pap.*, 501-D, 95–98, 1964.

- Moore, J. G., and H. L. Krivoy, The 1962 flank eruption of Kilauea volcano and structure of the East Rift Zone, *J. Geophys. Res.*, 69, 2033–2045, 1964.
- Moore, J. G., and R. S. Fiske, Volcanic substructure inferred from dredge samples and ocean-bottom photographs, Hawaii: *Geol. Soc. Am. Bull.*, 80, 1191–1202, 1969.
- Morgan, W. J., Convection plumes in the lower mantle, *Nature*, 230, 42–43, 1971.
- Morgan, W. J., Plate Motions and deep mantle convection, in *Studies in Earth and Space Science*, edited by R. Shagam, R. B. Hargraves, W. J. Morgan, F. B. Van Houten, C. A. Burk, H. D. Halland, and L. C. Hollister, *Mem. Geol. Soc. Am.*, 132, 7–22, 1972.
- Nagata, T., Rock Magnetism, Maruzen, Tokyo, pp. 225, 1953.
- Nagata, T., Rock Magnetism, 2nd Ed., Maruzen, Tokyo, pp. 350, 1961.
- Nakamura, K., Volcanoes as possible indicators of tectonic stress orientation— principle and proposal, *J. Volcan. Geotherm. Res.*, 2, 1–16, 1977.
- Nye, J. R., *Physical Properties of Crystals*, Oxford University Press, New York, 322 pp., 1969.
- Oliver, D. R., Influence of particle rotation on radial migration in the Poiseuille flow of suspensions, *Nature*, 194, 1269–1271, 1962.
- Oriel, S. S., and others, Stratigraphic Commission Note 44— Application for addition to code concerning magnetostratigraphic units, *A.A.P.G. Bull.*, 60, 273–277.
- Owens, W. H., Theoretical aspects of the magnetic anisotropy of rocks, (Ph. D. thesis), Univ. Birmingham, 178 pp., 1969.
- Owens, W. H., Mathematical model studies on factors affecting the magnetic anisotropy of deformed rocks, *Tectonophysics*, 24, 115–131, 1974.
- Peck, D. L., Cooling and vesiculation of Alae lava lake, Hawaii, *U.S. Geol. Surv. Prof. Pap.*, 935-B, 59 pp., 1978.
- Philpotts, A. R., and C. L. Lewis, Pipe vesicles—An alternate model for their origin, *Geology*, 15, 971–974, 1987.

- Pollard, D. D., Derivation and evaluation of a mechanical model for sheet intrusions, *Tectonophysics*, 19, 233–269, 1973.
- Pollard, D. D., P. T. Delaney, W. A. Duffield, E. T. Endo, and A. T. Okamura, Surface deformation in volcanic rift zones, *Tectonophysics*, 94, 541–584, 1983.
- Pollard, D. D., O. H. Muller, and D. R. Dockstader, The form and growth of fingered sheet intrusions, *Geol. Soc. Am. Bull.*, 86, 351–363, 1975.
- Pollard, D. D., and O. H. Muller, The effect of gradients in regional stress and magma pressure on the form of sheet intrusions in cross section, *J. Geophys. Res.*, 81, 975–984, 1976.
- Rallison, J. M., The deformation of small viscous drops and bubbles in shear flows, *Ann. Rev. Fluid Mech.*, 16, 45–66, 1984.
- Rees, A. I., The uses of anisotropy of magnetic susceptibility in the estimation of sedimentary fabric, *Sedimentology*, 4, 257–271, 1965.
- Rees, A. I., The effect of depositional slopes on the anisotropy of magnetic susceptibility of laboratory deposited sands, *J. Geol.*, 74, 856–876, 1966.
- Rees, A. I., The production of preferred orientation in a concentrated dispersion of elongated and flattened grains, *J. Geol.*, 76, 457–465, 1968.
- Rees, A. I., The orientation of grains in a sheared dispersion, *Tectonophysics*, 55, 275–287, 1979.
- Richardson, S., Two-dimensional bubbles in slow viscous flows. Part 2, *J. Fluid Mech.*, 58, 115–127, 1973.
- Rowland, S. K., and G. P. L. Walker [in review].
- Rubin, A. M., and D. D. Pollard, Dike-induced faulting in rift zones of Iceland and Afar, *Geology*, 16, 413–417, 1988.
- Rubin, A. M., and D. D. Pollard, Origins of blade-like dikes in volcanic rift zones, in Volcanism in Hawaii, *U.S. Geol. Surv. Prof. Pap.*, 1350, 2, 1449–1470, 1987.

- Ryan, M. P., The elasticity and contractancy of Hawaiian olivine tholeiite and its role in the stability and structural evolution of subcaldera magma reservoirs and rift systems, *U.S. Geol. Surv. Prof. Pap., 1350*, vol. 2, 1395–1447, 1987a.
- Ryan, M. P., Neutral buoyancy and the mechanical evolution of magmatic systems, in *Magmatic Processes: Physiochemical Principles Spec. Publ. 1*, edited by B. O. Mysen, pp. 259–287, The Geochemical Society, University Park, Pa., 1987b.
- Ryan, M. P., The mechanics and three-dimensional internal structure of active magmatic systems: Kilauea Volcano, Hawaii, *J. Geophys. Res.*, 93, 4213–4248, 1988.
- Ryan, M. P., J. Y. K. Blevins, A. T. Okamura, and R. Y. Koyanagi, Magma reservoir subsidence mechanics: Theoretical summary and application to Kilauea volcano, Hawaii, *J. Geophys. Res.*, 88, 4147–4181, 1983.
- Saffman, P. D., The lift on a small sphere in a slow shear flow, *J. Fluid Mechanics*, 22, 385–400, 1965.
- Scott-Blair, G. W., The importance of the sigma phenomenon in the study of the flow of blood, *Rheol. Acta*, 1, 123–126, 1958.
- Sears, F. W., M. W. Zemansky, and H. D. Young, *University Physics*, Published by Addison-Wesley, 1982.
- Shaw, H. R., The fracture mechanisms of magma transport from the mantle to the surface, in *Physics of Magmatic Processes*, edited by R. B. Hargraves, pp. 201–264, Princeton University Press, Princeton, N. J., 1980.
- Shaw, H. R., and D. A. Swanson, Eruption and flow rates of flood basalts, *Proc. 2nd Columbia River Basalt Symposium*, 271–299, 1971.
- Shelley, D., Determining paleo-flow directions from groundmass fabrics in the Lyttelton radial dykes, New Zealand, *J. Volcanol. Geotherm. Res.*, 25, 69–79, 1985.
- Shive, P. N., Suggestions for the use of SI units in magnetism, *J. Geophys. Res., Eos Trans.*, Jan. 21, 1986.

- Simkin, T. E., The picritic sills of northwest Trotternish Isle of Skye, Scotland, (Ph.D. thesis), Princeton University, 139 pp., 1966.
- Spera, F. J., Aspects of the thermodynamic and transport behavior of basic magma, (Ph.D. thesis), Univ. Calif. at Berkley, 1977.
- Stacey, F. D., Magnetic anisotropy of igneous rocks, *J. Geophys. Res.*, *65*, 2429–2442, 1960a.
- Stacey, F. D., Magnetic anisotropy of dispersed powders, *Australian J. Phys.*, *13*, 196–201, 1960b.
- Stacey, F. D., J. F. Lovering, and L. G. Parry, Thermomagnetic properties, natural magnetic moments, and magnetic anisotropies of some chondritic meteorites, *J. Geophys. Res.*, *96*, 1523–1534, 1961.
- Starkey, T. V., The laminar flow of suspensions in tubes, *British J. Appl. Phys.*, *6*, 34–37, 1955.
- Stearns, H. T., Geological map and guide of the island of the island of Oahu, Hawaii, *Hawaii Div. Hydrography Bull*, *2*, 75 pp., 1939.
- Stoner, E. C., The demagnetizing factors for ellipsoids, *Phil. Mag.*, *36*, 803–821, 1945.
- Strange, W. E., L. F. Machesky, and G. P. Woollard, A gravity survey of the island of Oahu, Hawaii, *Pacific Sci.*, *19*, 350–353, 1965.
- Swanson, D. A., W. A. Duffield, and R. S. Fiske, Displacement of the south flank of Kilauea Volcano: Result of forceful intrusion of magma into the rift zones, *U.S. Geol. Survey Prof. Paper 963*, 39 pp, 1976.
- Taira, A., Contributions to sedimentology, (Ph.D. thesis), Dallas, Univ. Texas, pp. 320, 1976.
- Taira, A., and B. R. Lienert, The comparative reliability of magnetic, photometric and microscopic methods of determining the orientations of sedimentary grain, *J. Sediment. Petrol.*, *49(3)*, 759–772, 1979.

- Takada, A., Propagation system of magma-filled cracks; Model and experiment, Kagoshima International Conference on Volcanoes 1988, Proceedings, 99–101, 1989.
- Takasaki, K. J., G. T. Hirashima, and E. R. Lubke, Water resources of windward Oahu, Hawaii, *U.S. Geol. Survey Water-Supply Paper 1894*, pp. 119, 1969.
- Takasaki, K. J., and J. F. Mink, Water resources of southeastern Oahu, Hawaii, *U.S. Geol. Survey Water Resources Invest. 82-628*, 97 pp., 1982.
- Tarling, D. H., The paleomagnetism of some of the Hawaiian Islands, *Geophys. J.*, 10, 93–104, 1965.
- Turcotte, D. L., and G. Schubert, Geodynamics: Application of Continuum Physics to Geological Problems, 450 pp., John Wiley, New York, 1982.
- Ui, T., M. Kono, Y. Hamano, F. Monge, and Y. Aota, Reconstruction of a volcanic edifice using the dike swarm at Ocos, Peruvian Andies, *Bull. Volcanol. Soc. Japan*, 29, 285–296, 1984.
- Urrutis-Fucugauchi, J., On the relationship between the magnetic and strain fabric in slates and possible effects of consistent instrumental discrepancies, *Tectonophysics*, 69, 15–23, 1980a.
- Urrutis-Fucugauchi, J., Paleomagnetic studies of Mexican Rocks, (Ph.D. thesis), University of Newcastle upon Tyne, pp. 689, 1980b.
- Uyeda, S., M. D. Fuller, J. C. Belshe, and R. W. Girdler, Anisotropy of magnetic susceptibility in rocks and minerals, *J. Geophys. Res.* 68, 279–291, 1963.
- Walker, G. P. L., Three Hawaiian calderas: an origin through loading by shallow intrusions?, *J. Geophys. Res.*, 93, 14,773–14,784, 1989.
- Walker, G. P. L., The dike complex of Koolau volcano, Oahu: internal structure of a Hawaiian rift zone, in Volcanism in Hawaii, *U.S. Geol. Surv. Prof. Pap.*, 1350, 2, 961–993, 1987.

- Walker, G. P. L., Calderas of Hawaiian volcanoes: Subsidence at a hot spot, (abstract) *Hawaii Symposium on How Volcanoes Work, Diamond Jubilee, Hawaiian Volcano Observatory*, 262, 1987.
- Walker, G. P. L., Koolau Dike Complex, Oahu: Intensity and origin of a sheeted-dike complex high in a Hawaiian volcanic edifice, *Geology*, 14, 310–313, 1986.
- Walker, G. P. L. and G. P. Leedal, The Barnesmore granite complex, County Donegal, *Roy. Dublin Soc. Sci. Proc.*, 26, 207–243, 1956.
- Wentworth, C. K., Geology and groundwater resources of the Honolulu-Pearl Harbor area, Oahu, Hawaii, *Board Water Supply, Honolulu, Hawaii*, 111 pp., 1951.
- Wentworth, C. K. and A. E. Jones, Intrusive rocks of the leeward slope of the Koolau Range, Oahu, *J. Geol.*, 48, 975–1006, 1940.
- Wentworth, C. K. and G. A. Macdonald, Structures and forms of basaltic rocks in Hawaii, *U.S. Geol. Surv. Bull.*, 994, 1953.
- Wentworth, C. K. and H. Winchell, Koolau basalt Series, Oahu, Hawaii, *Bull. Geol. Soc. Am.*, 58, 49–78, 1947.
- Wilson, J. T., Evidence from islands on the spreading of ocean floors, *Nature*, 197, 536–538, 1963a.
- Wilson, J. T., A possible origin of the Hawaiian Islands, *Can. J. Physics*, 41, 863–870, 1963b.
- Wilson, L., and J. W. Head, Ascent and eruption of basaltic magma on the Earth and Moon, *J. Geophys. Res.*, 86, 2971–3001, 1981.
- Wilson, L., and J. W. Head, Nature of local magma storage zones and geometry of conduit systems below basaltic eruption sites: Pu'u 'O'o, Kilauea East Rift, Hawaii, example, *J. Geophys. Res.*, 93, 14,785–14,792, 1989.
- Winchell, H., The Honolulu series, Oahu, Hawaii, *Geol. Soc. Am. Bull.*, 58, 1–48, 1947.

Wright, T. L., Chemistry of Kilauea and Mauna Loa lava in space and time, *U.S. Geol. Survey Prof. Paper 735*, 1–40, 1971.

Zijderveld, J. D. A., A.f. demagnetization of rocks: Analysis of results, in Developments in Solid Earth Geophysics, vol. 3, Methods on Paleomagnetism, edited by D. W. Collinson, R. M. Creer, and S. K. Runcon, 254–286, Elsevier, New York, 1967.



**PLEASE NOTE:**

Oversize maps and charts are filmed in sections in the following manner:

**LEFT TO RIGHT, TOP TO BOTTOM, WITH SMALL OVERLAPS**

The following map or chart has been refilmed in its entirety at the end of this dissertation (not available on microfiche). A xerographic reproduction has been provided for paper copies and is inserted into the inside of the back cover.

Standard 35mm slides or 17" x 23" black and white photographic prints are available for an additional charge.

**U·M·I**

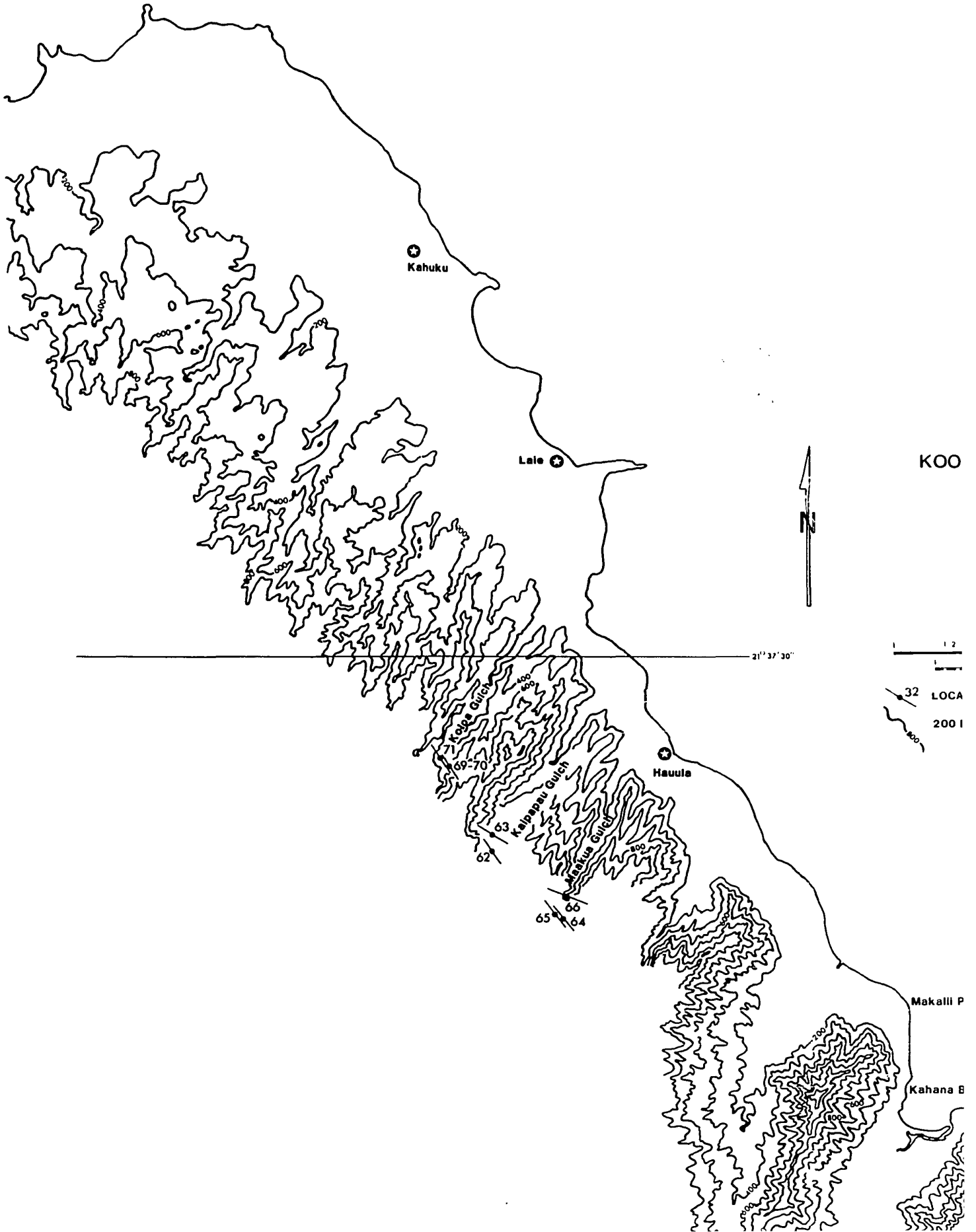
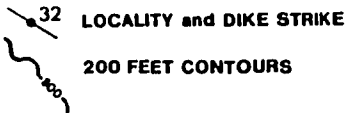
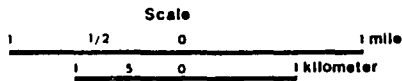


PLATE I

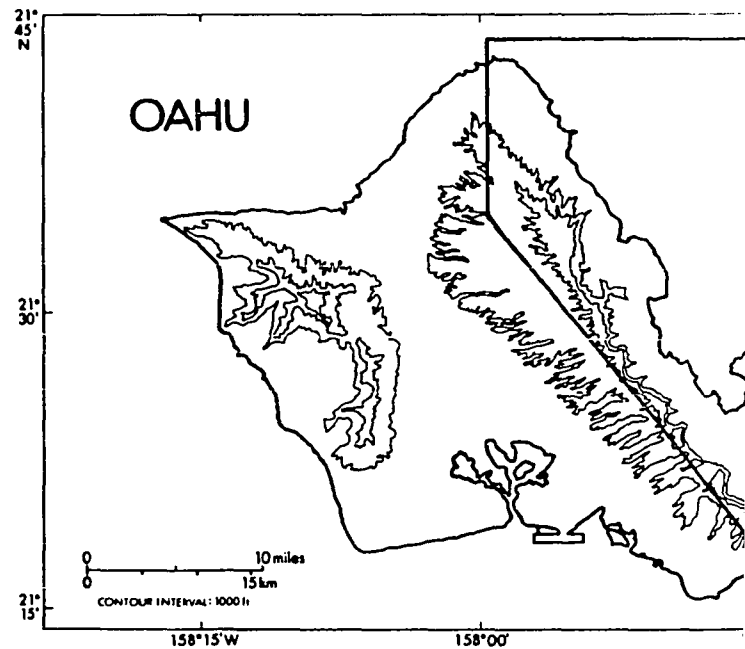
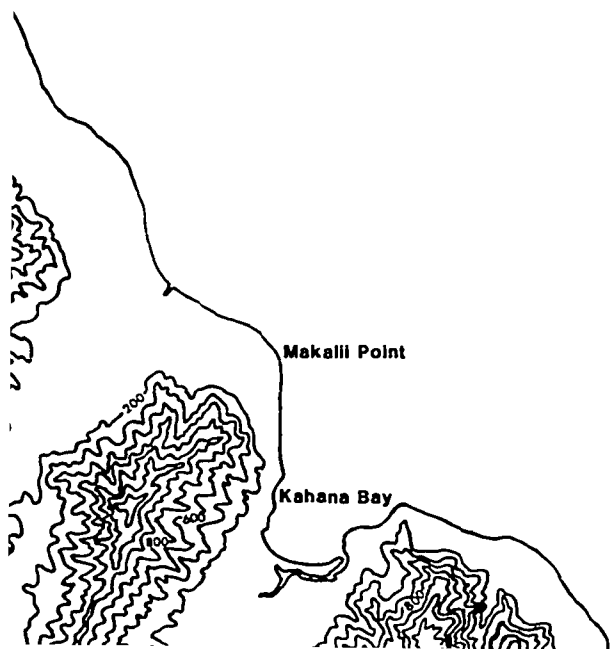
LOCALITY MAP  
KOOLAU DIKE COMPLEX  
OAHU, HAWAII



LEGEND

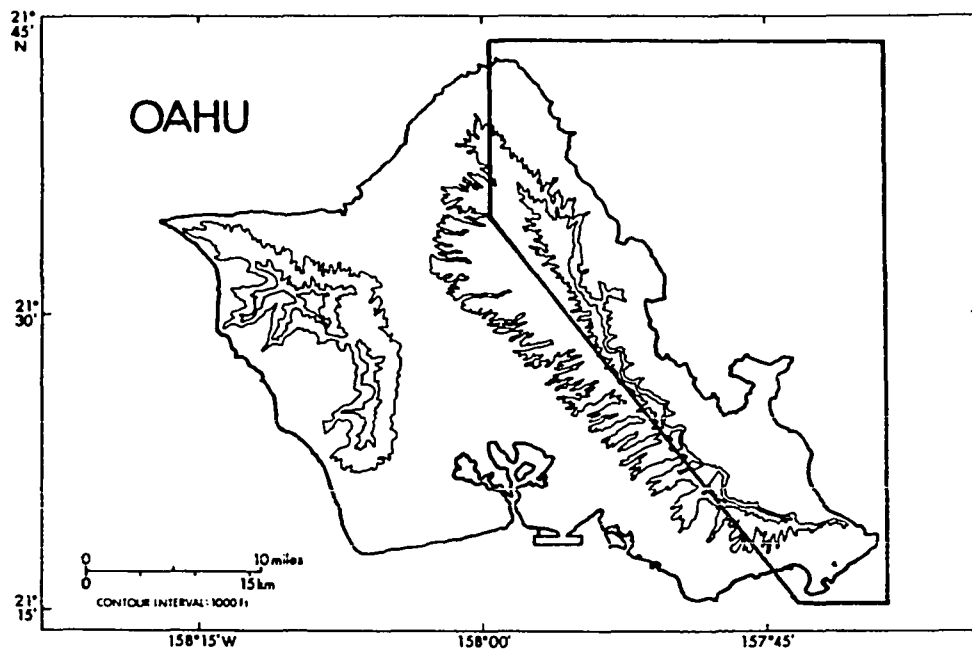


-21° 37' 30"



EX

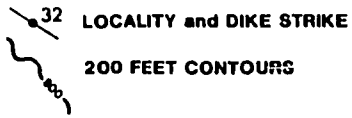
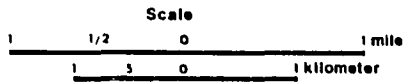
the



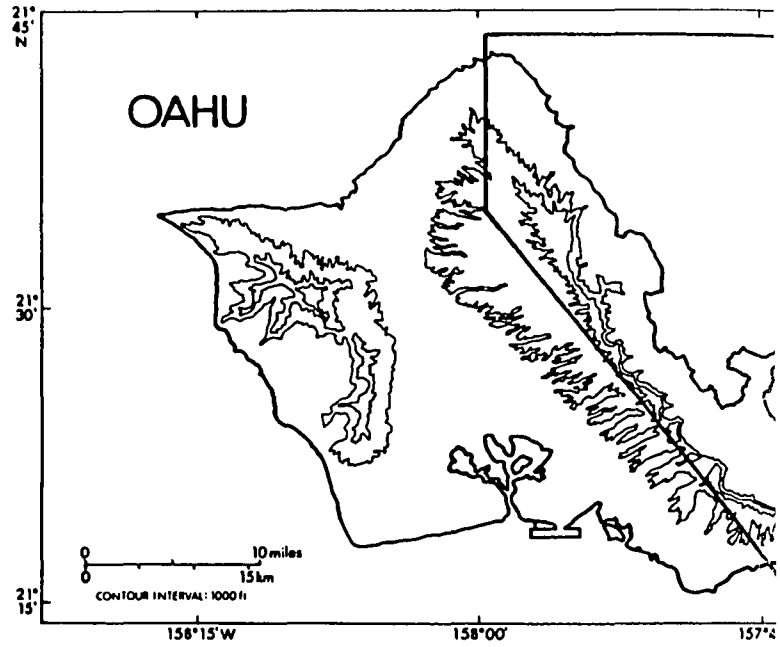


21° 37' 30"

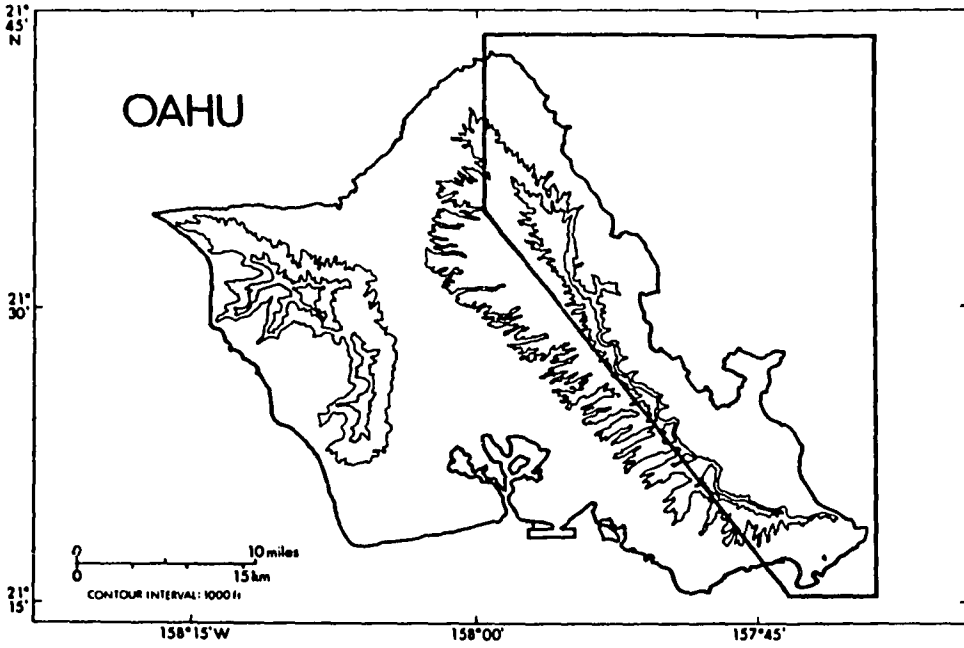
# LEGEND



57 60-61  
Mokolii Is.



Kaneohe Bay

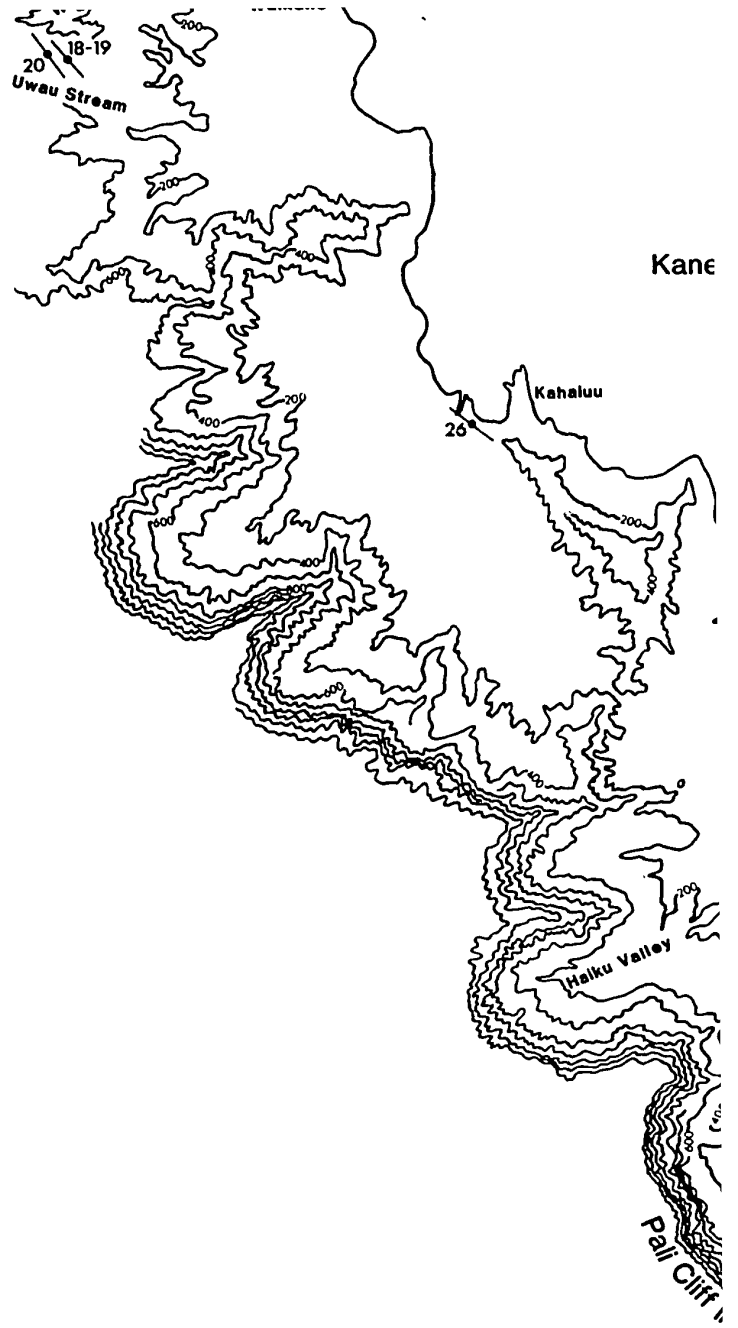


60-61  
koll la.

Kaneohe Bay

shaluu





18-19  
20  
Uwau Stream

# Kaneohe Bay

Kahaluu

26

13-14  
Kealahi Point

Kaneohe Marine Co  
Air Station

Nuupia Pond

Pohakea Point

29-31

Kaneohe

21-25

27-28

Moku Valley

1-7

8-9

10-12

Kailua

Kawainui  
Swamp

45-46

51-55

42-44

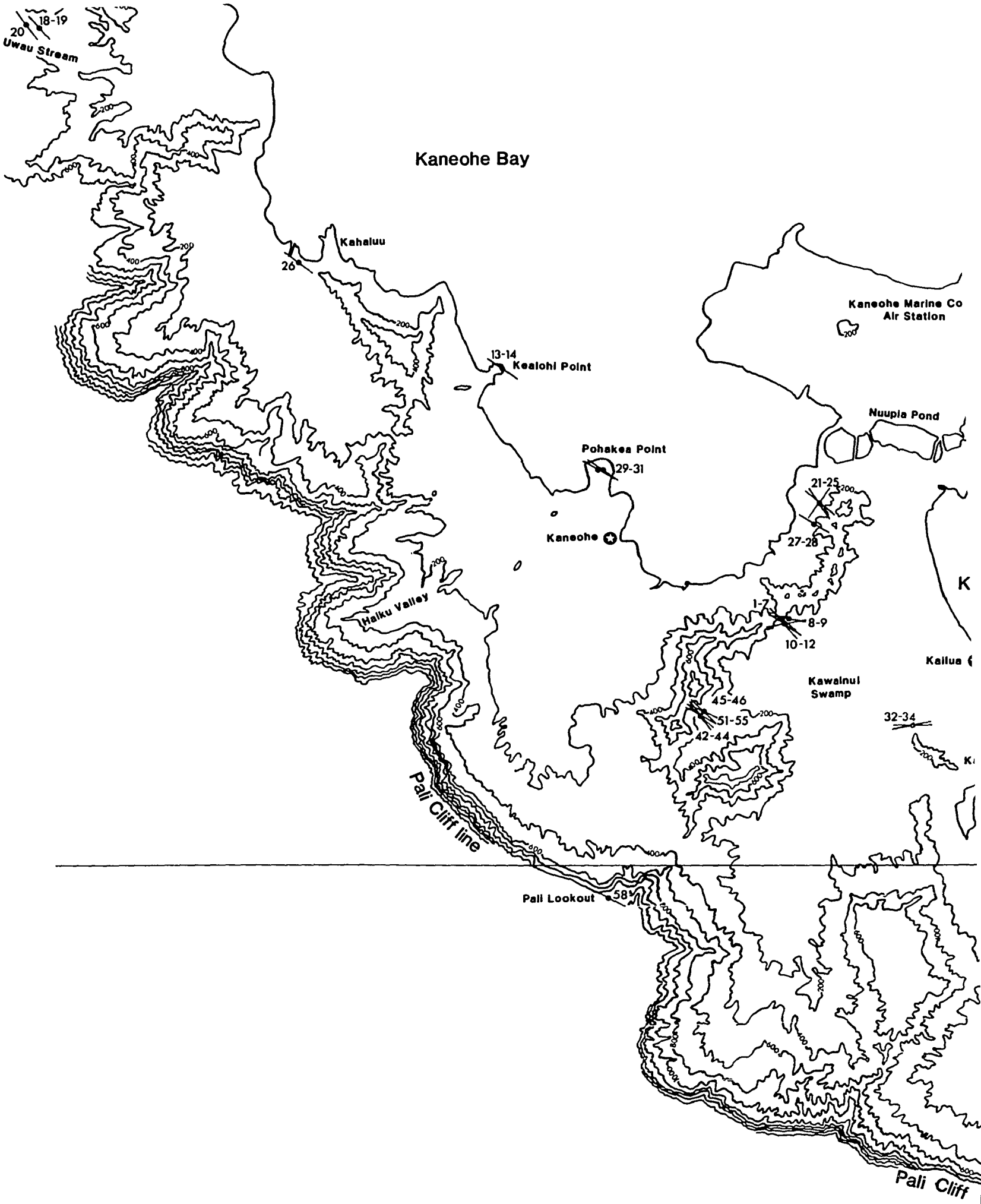
32-34

Pali Cliff line

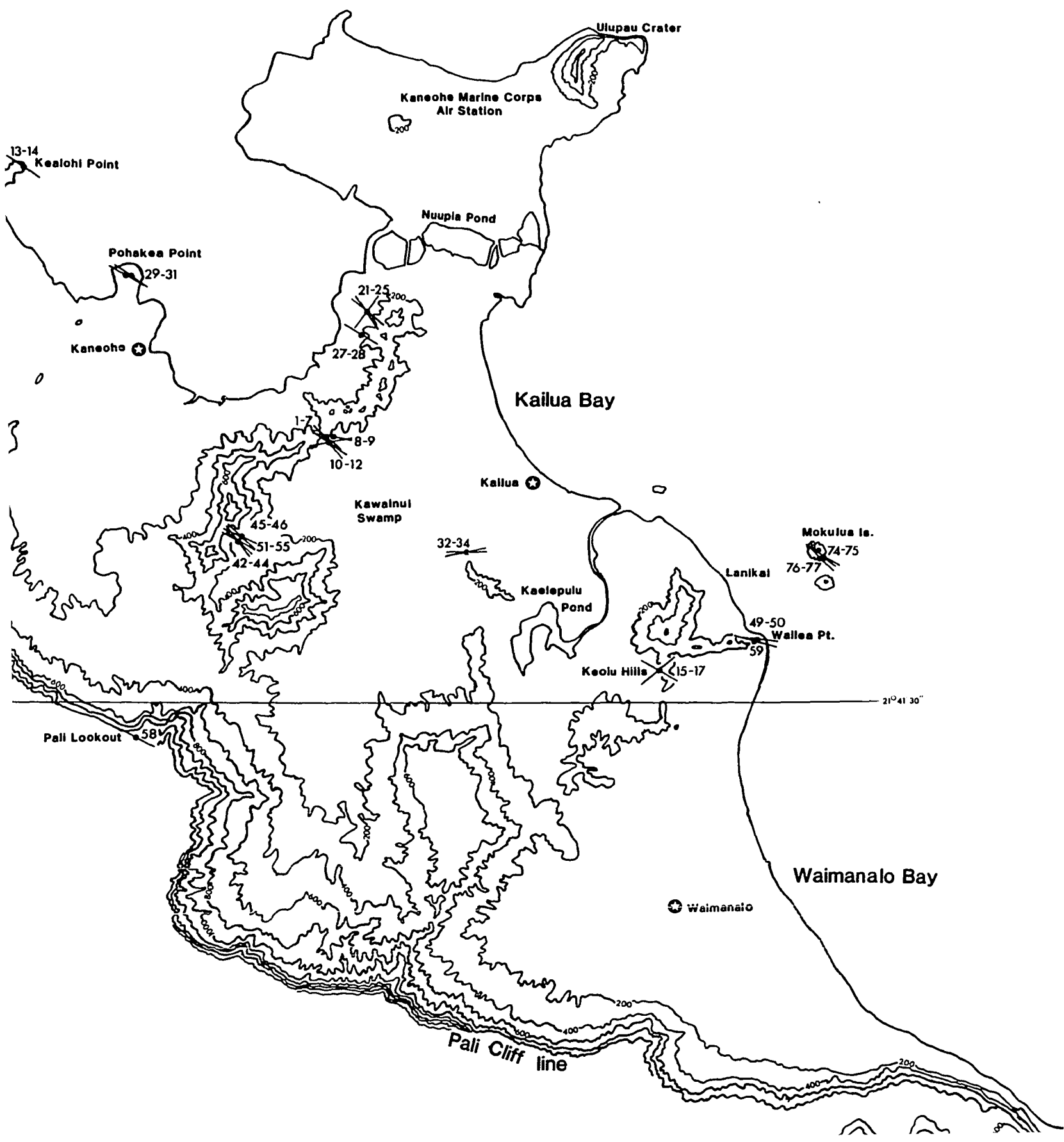
Pali Lookout

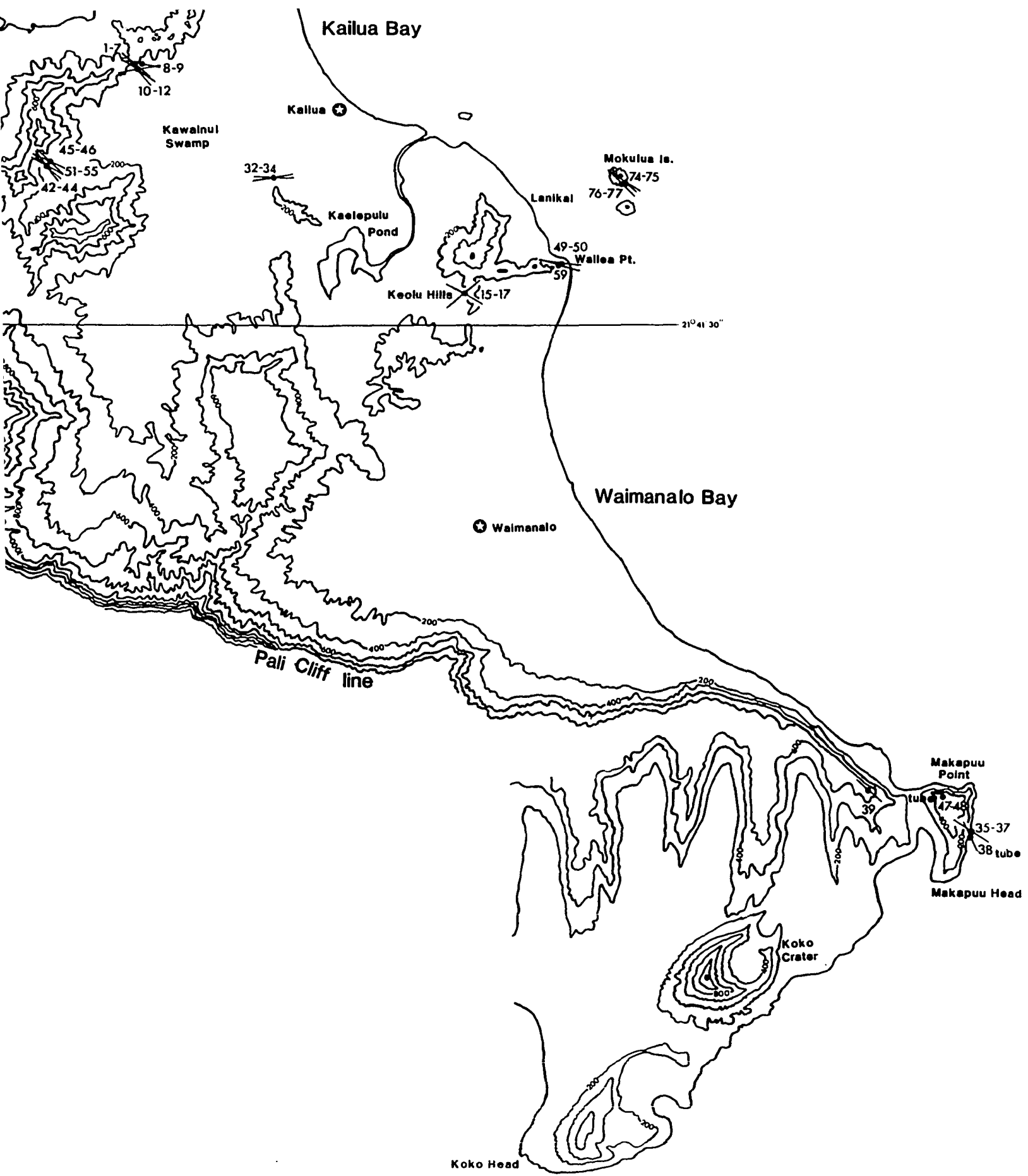
58

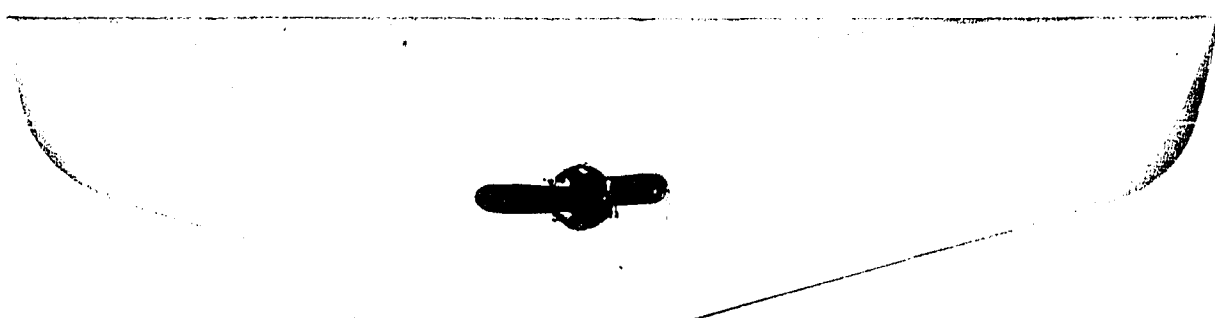
Pali Cliff



e Bay







**PLEASE NOTE:**

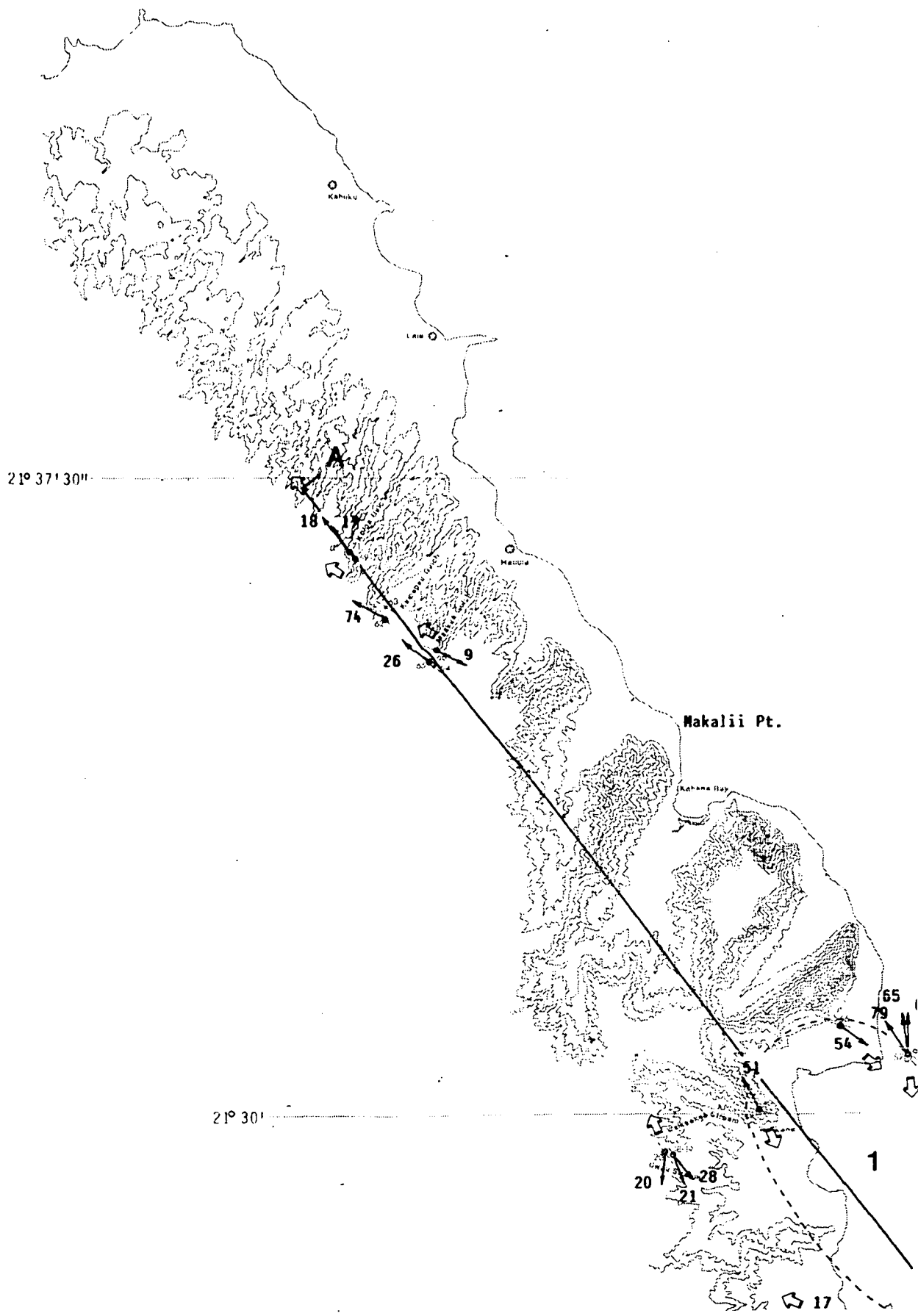
Oversize maps and charts are filmed in sections in the following manner:

**LEFT TO RIGHT, TOP TO BOTTOM, WITH SMALL OVERLAPS**

The following map or chart has been refilmed in its entirety at the end of this dissertation (not available on microfiche). A xerographic reproduction has been provided for paper copies and is inserted into the inside of the back cover.

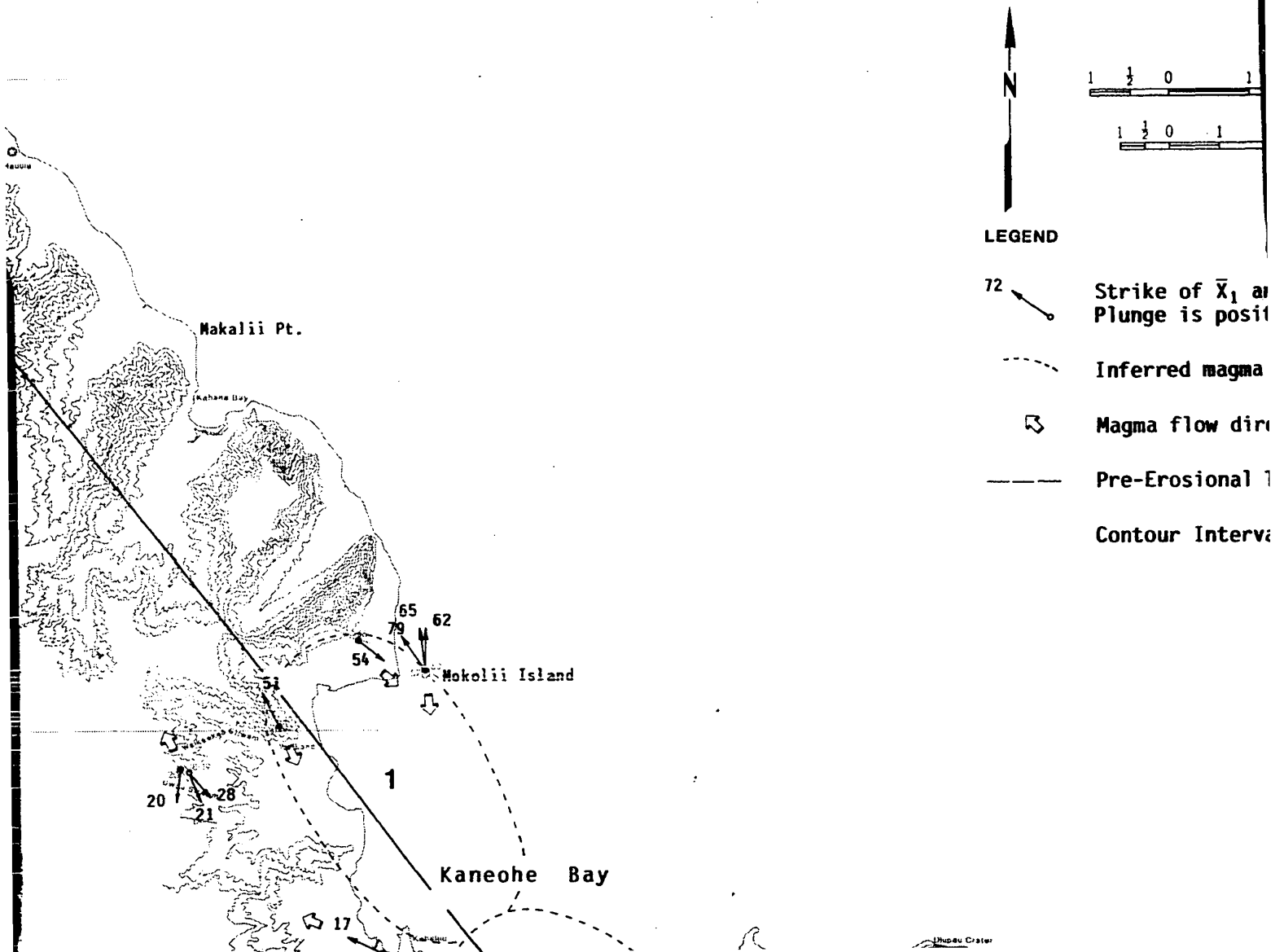
Standard 35mm slides or 17" x 23" black and white photographic prints are available for an additional charge.

**U·M·I**



# KOOLAU DIKE

Map of Mean Maximum  
of Dikes Measured, N



## LEGEND

- 72  Strike of  $\bar{X}_1$  at Plunge is positive
-  Inferred magma
-  Magma flow direction
-  Pre-Erosional
- Contour Interval

# KOOLAU DIKE COMPLEX

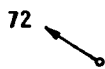
Map of Mean Maximum AMS Directions  
of Dikes Measured, Northeast Oahu



1 ½ 0 1 2 miles

1 ½ 0 1 2 3 kilometers

## LEGEND



Strike of  $\bar{X}_1$  and Angle of Plunge  
Plunge is positive downward



Inferred magma source



Magma flow direction



Pre-Erosional Topography of the Koolau Shield

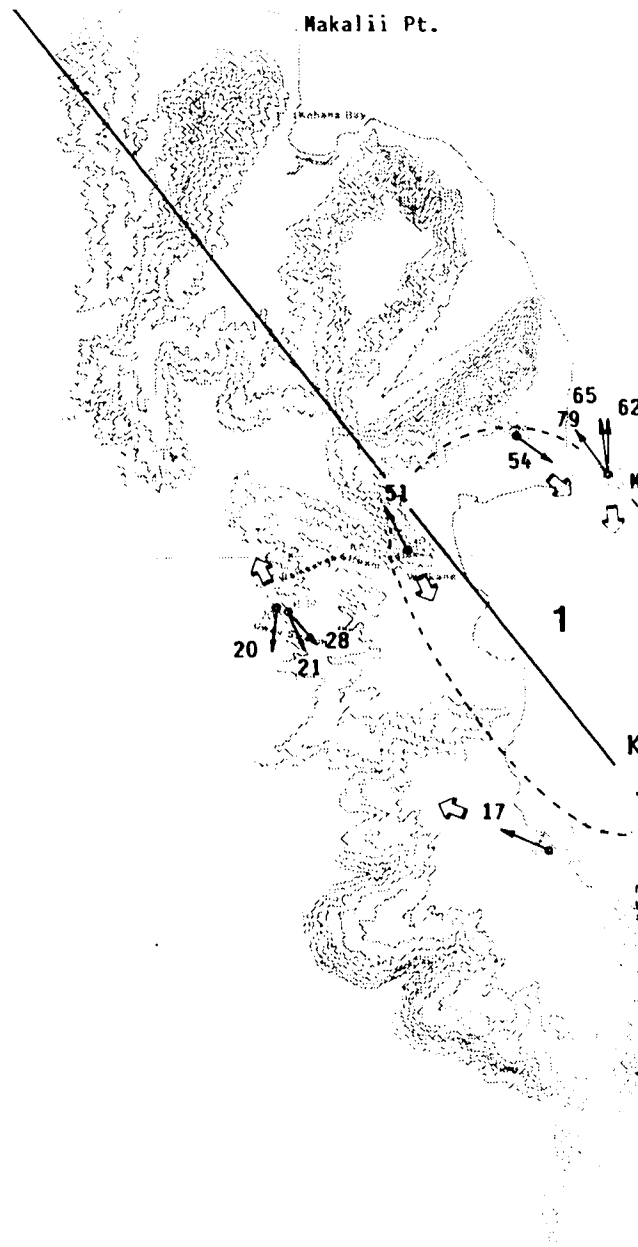
Contour Interval 200 feet

Makalii Pt.

Kohala Bay

21° 30'

21° 22' 30"



li Pt.

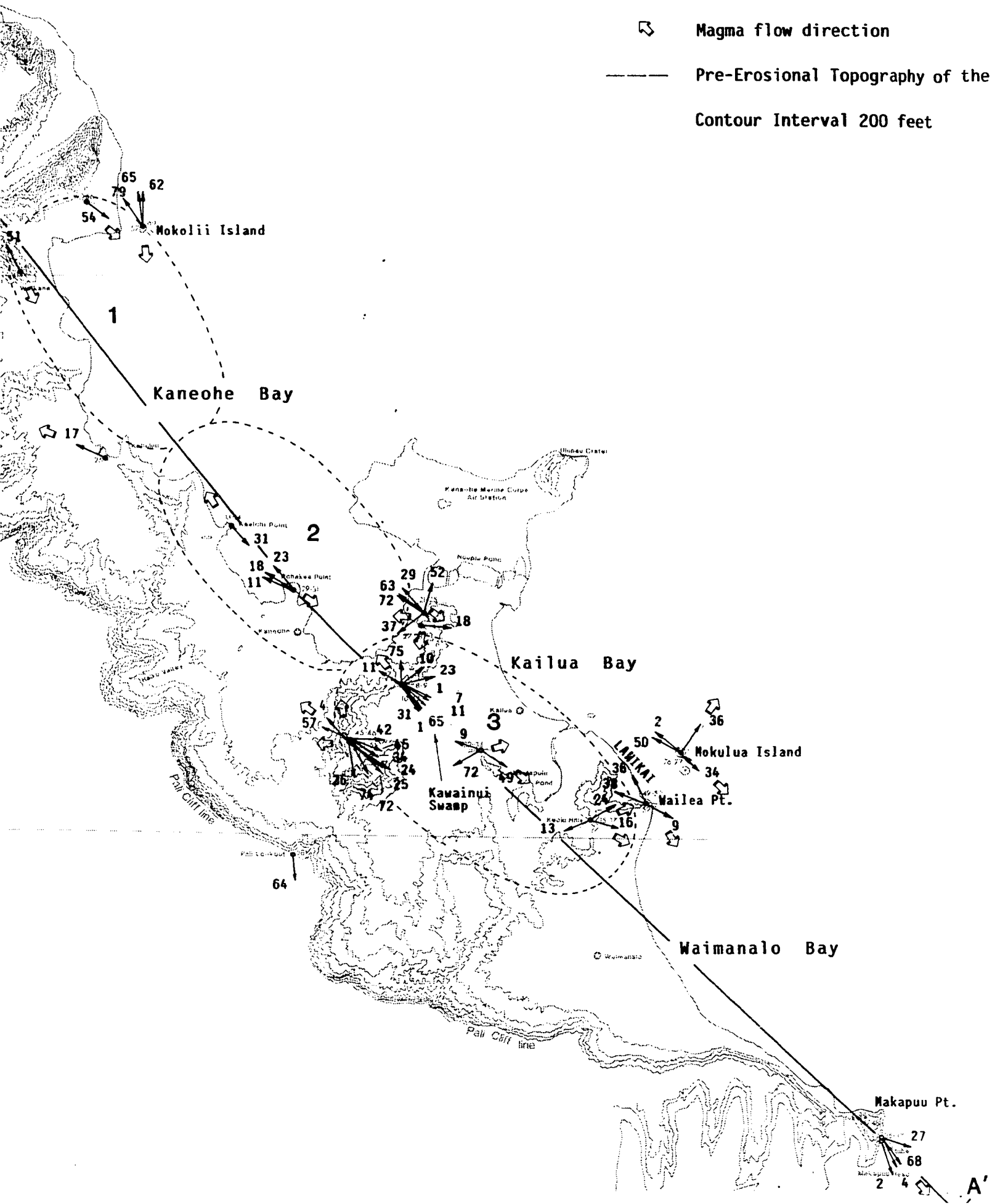
Strike or  $\alpha_1$  and Angle of Plunge  
Plunge is positive downward

Inferred magma source

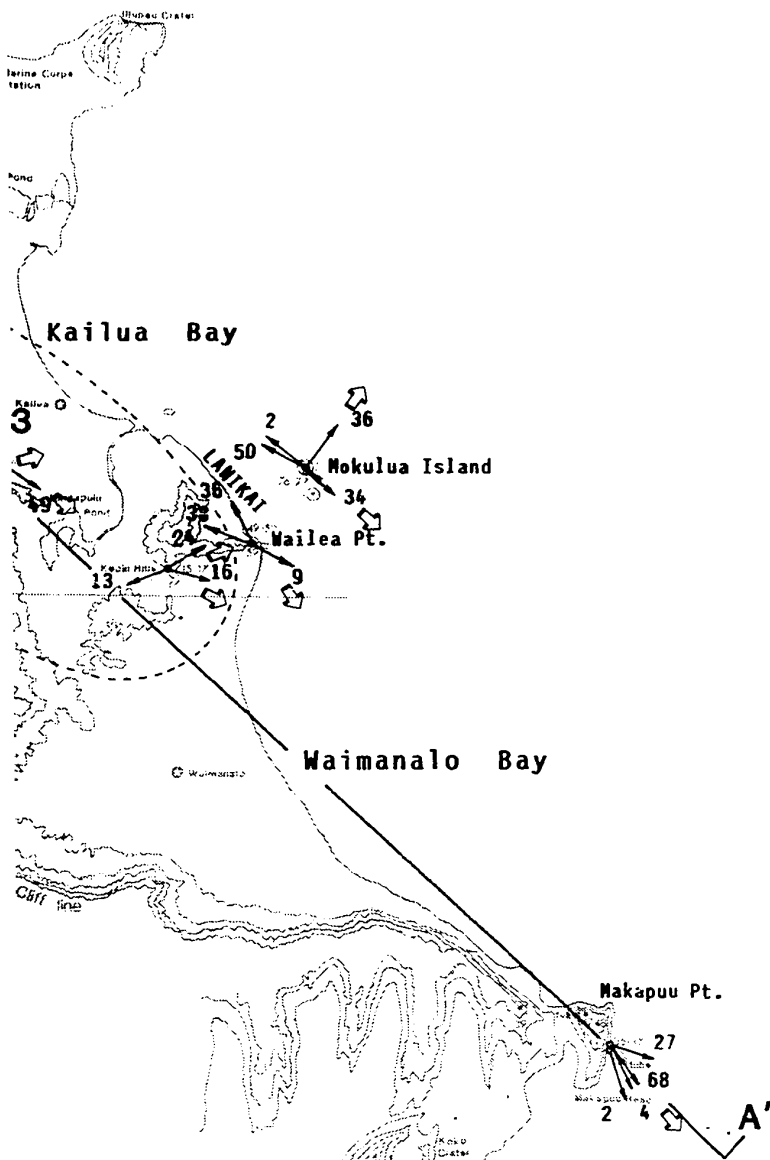
Magma flow direction

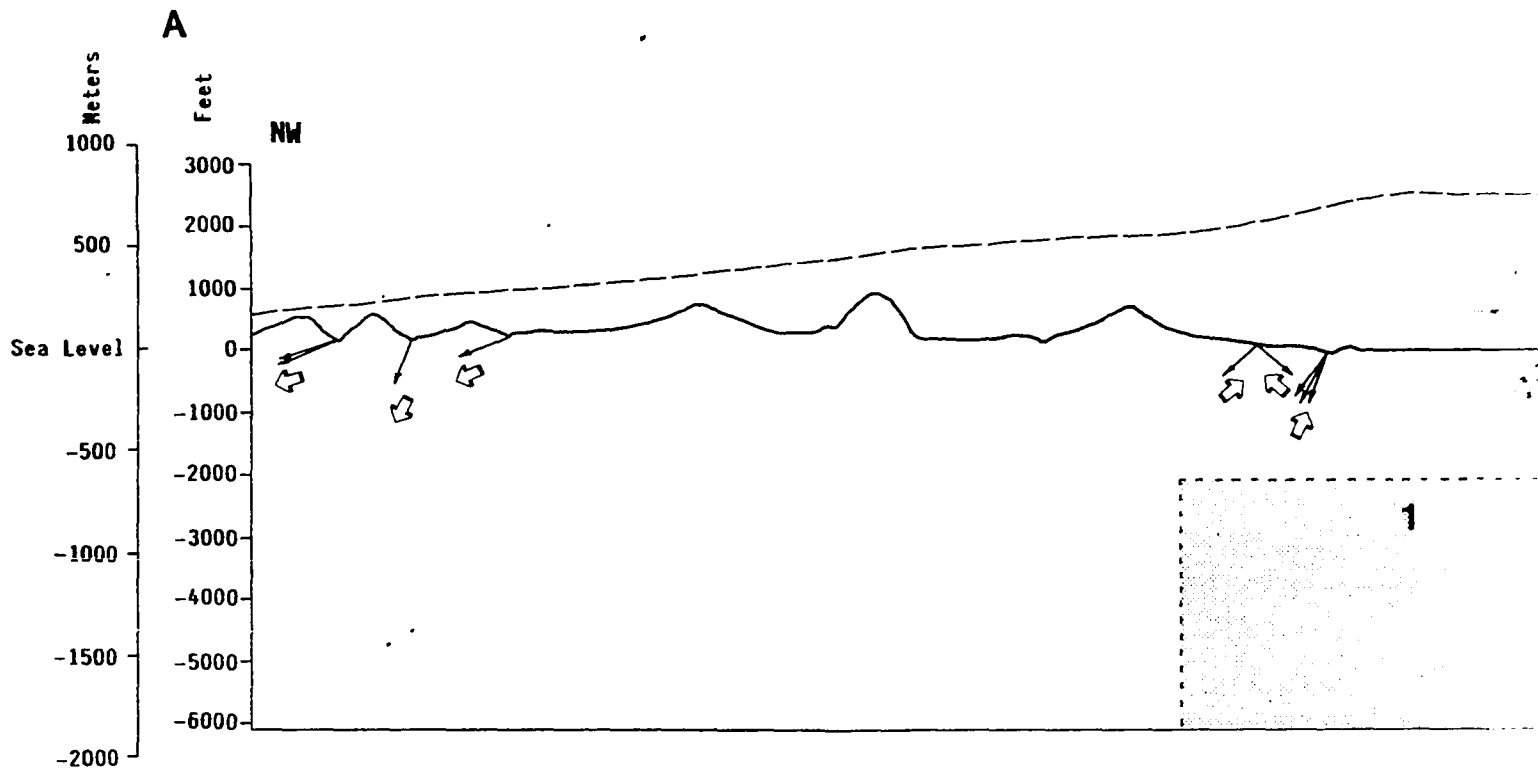
Pre-Erosional Topography of the K

Contour Interval 200 feet

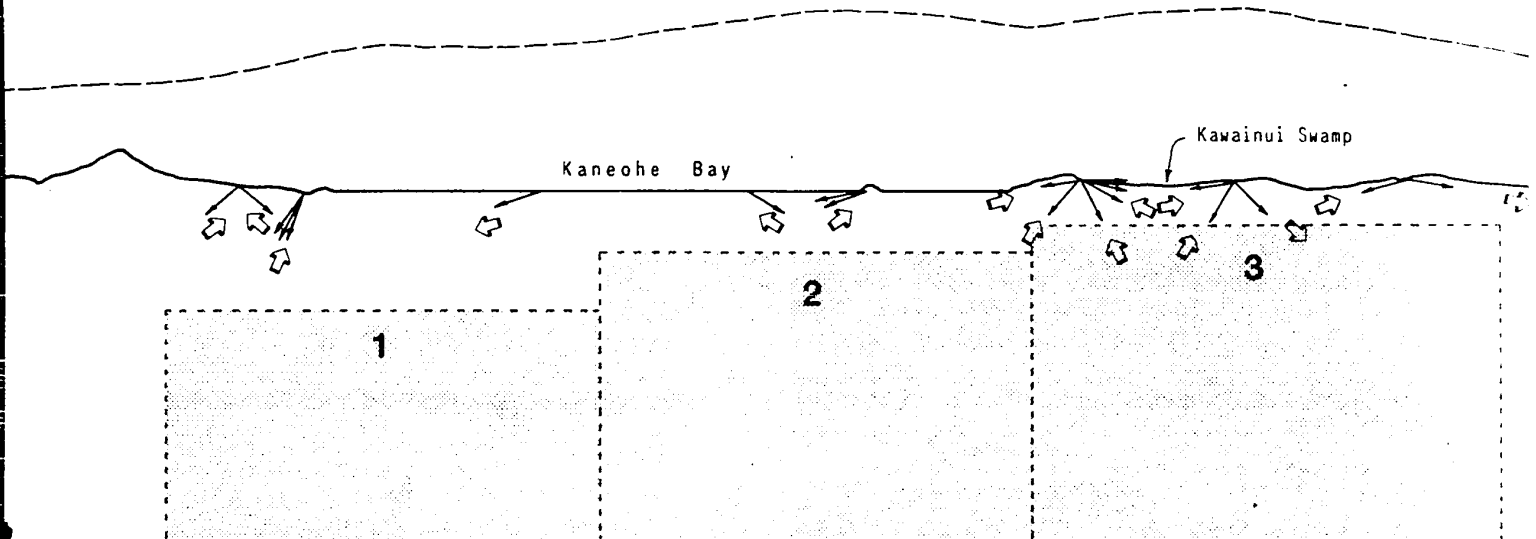
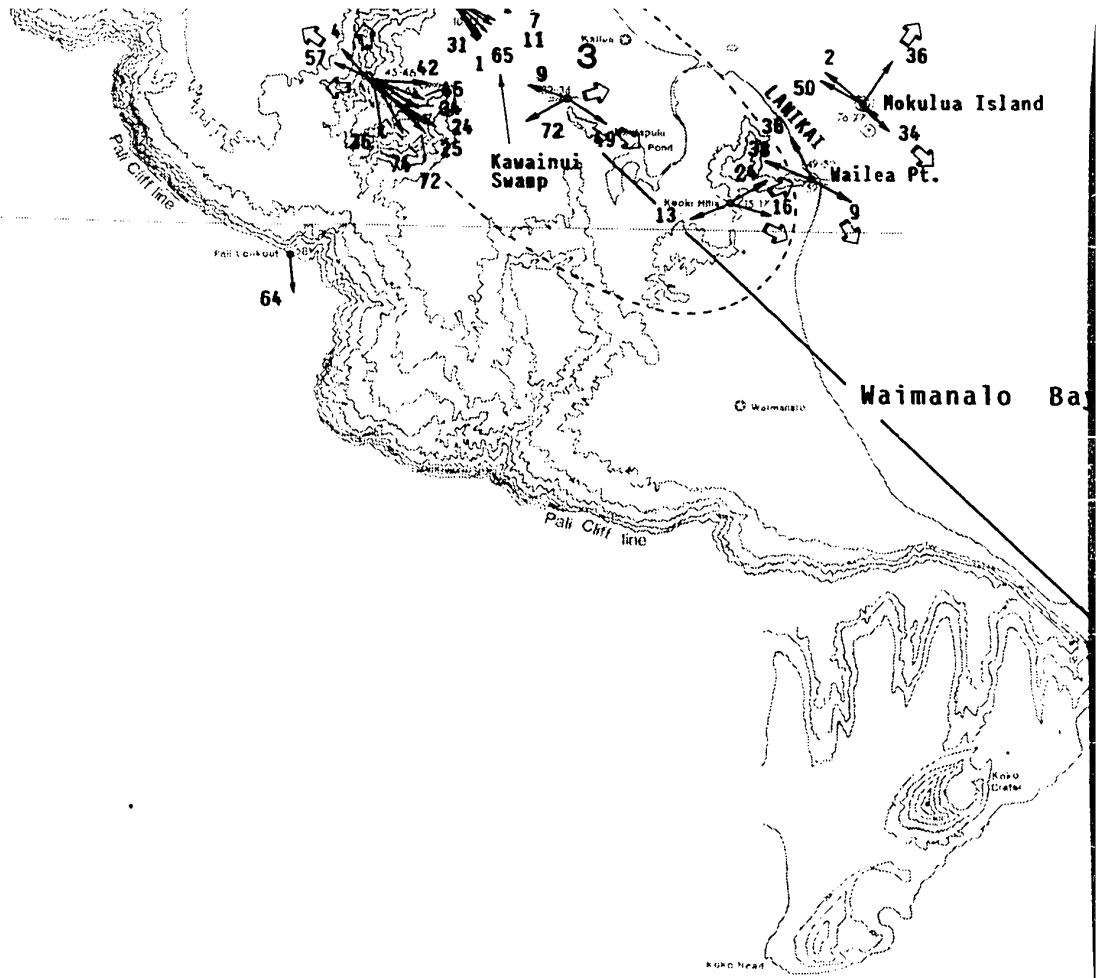


- ▽ Elevation is positive downward
  - - - Inferred magma source
  - ↻ Magma flow direction
  - Pre-Erosional Topography of the Koolau Shield
- Contour Interval 200 feet

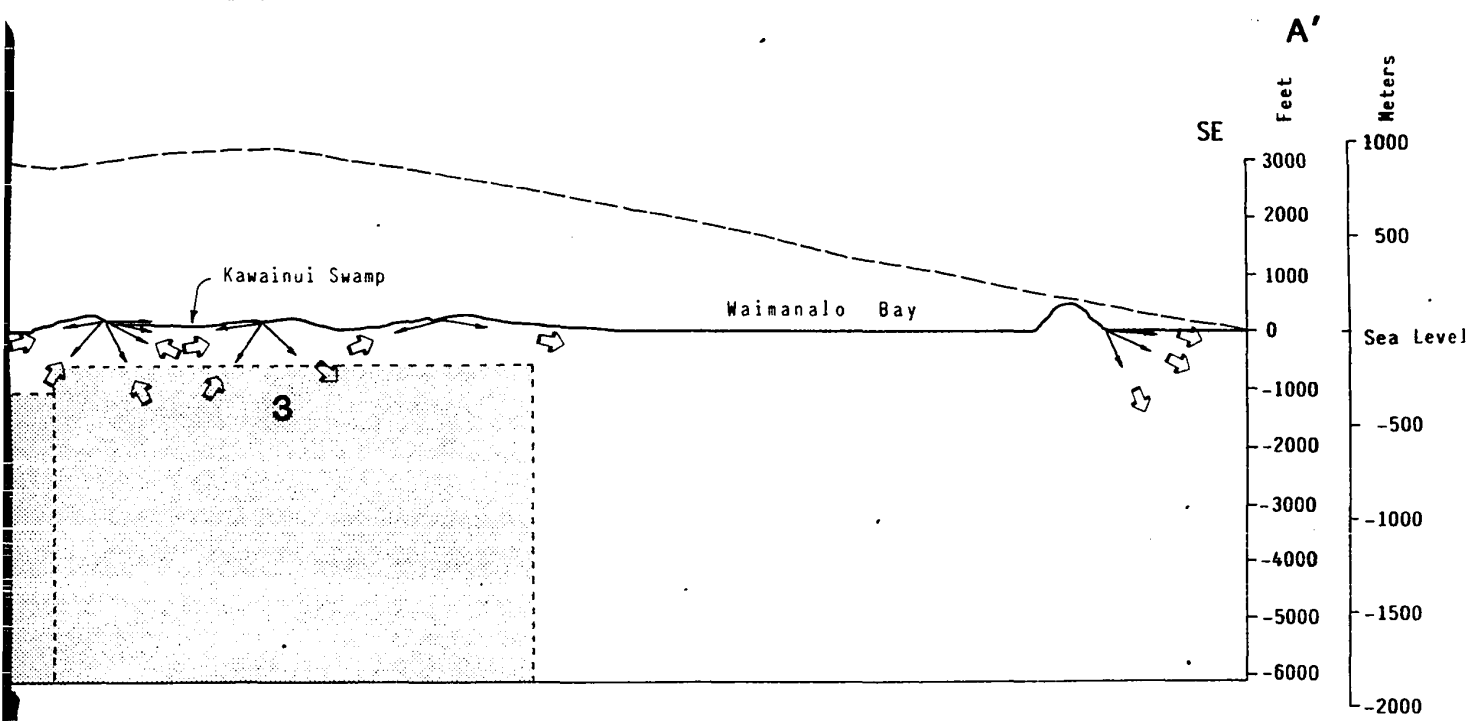
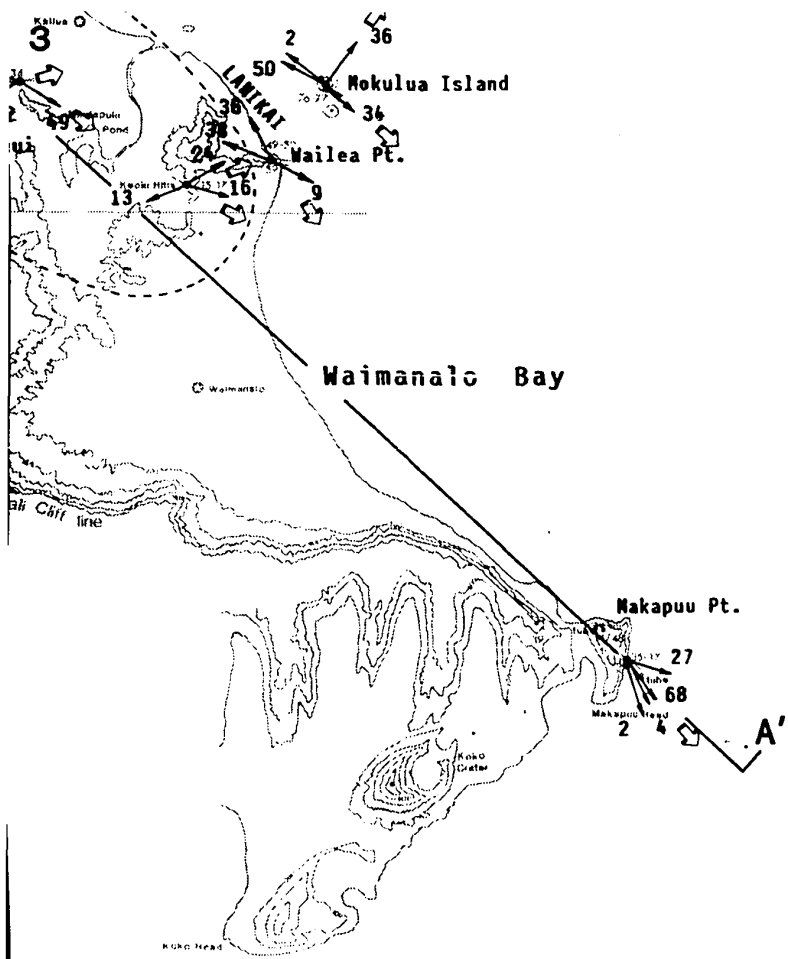


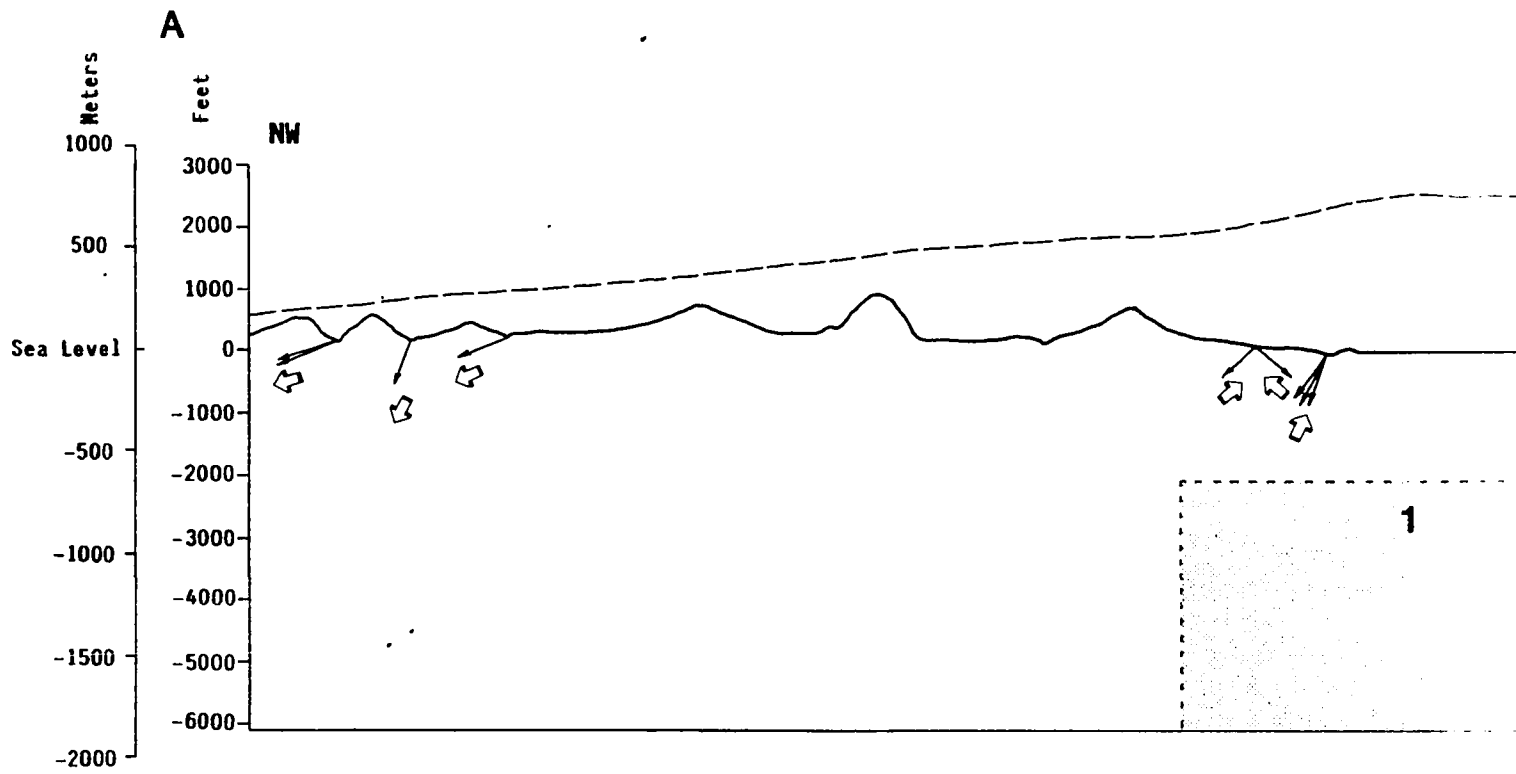


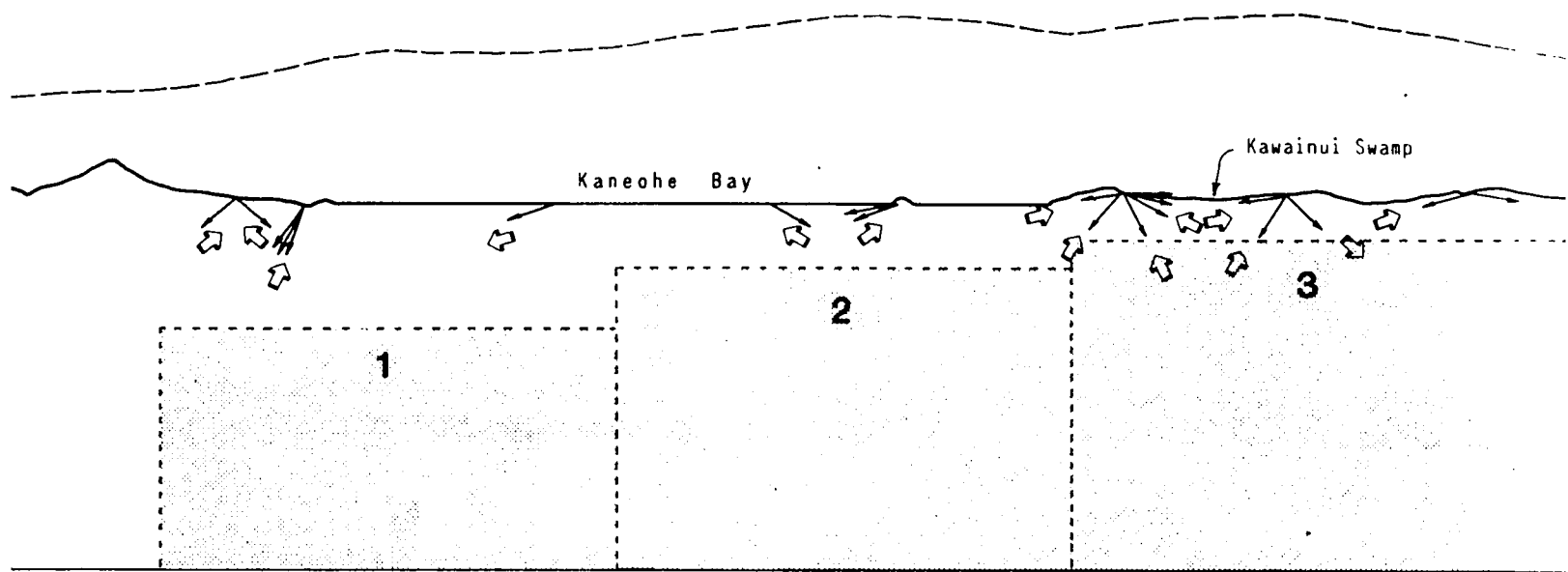
21° 22' 30"



CROSS SECTION A-A'







CROSS SECTION A-A'

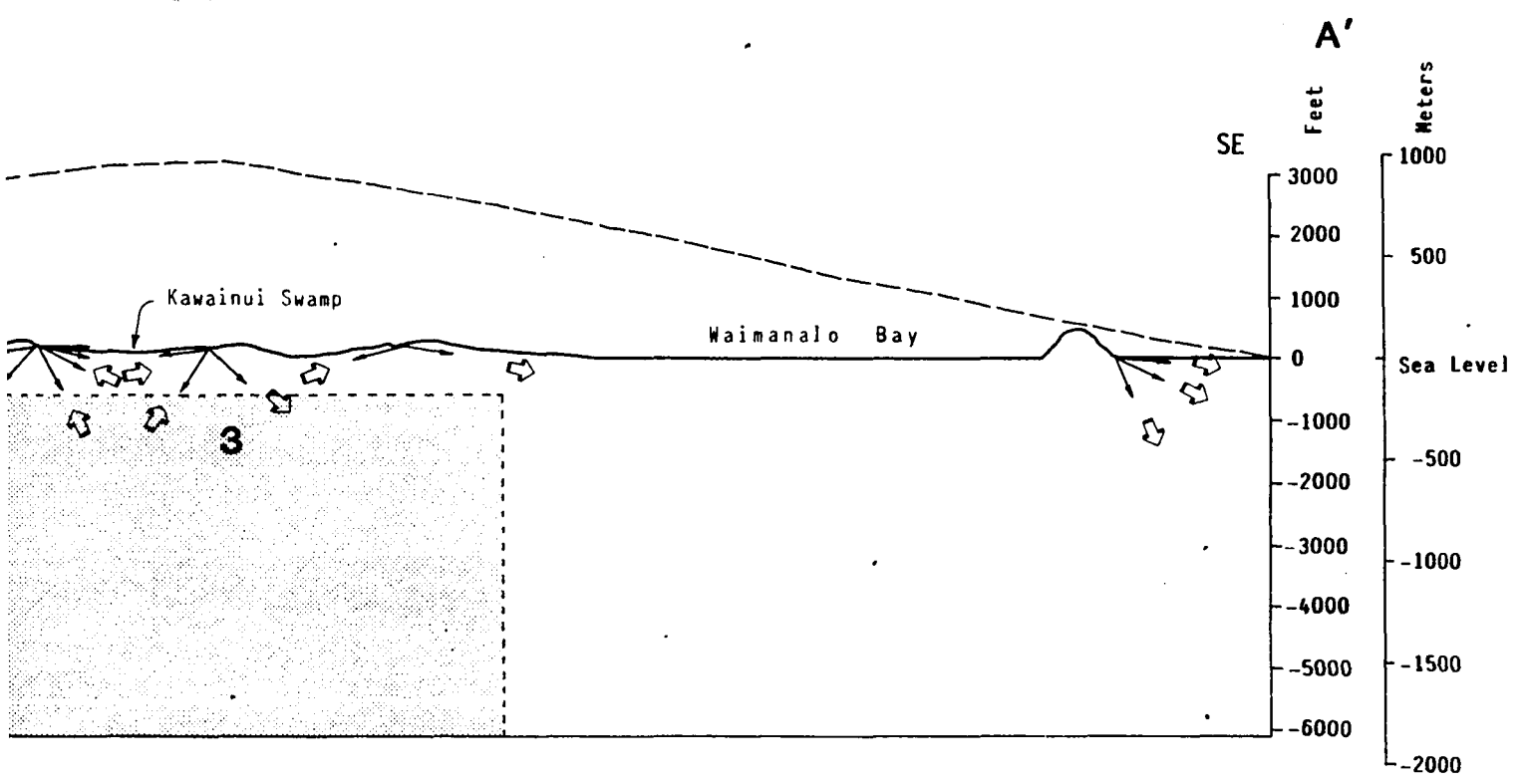
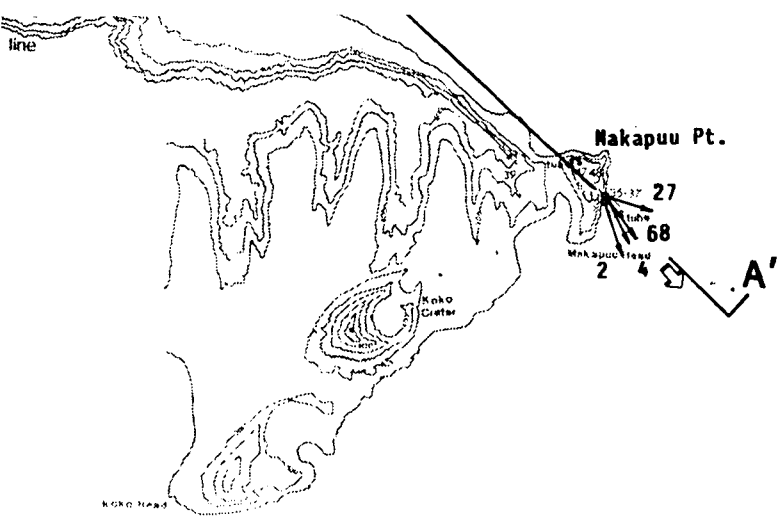


PLATE 2